ELECTROSTATIC INTERACTIONS AT DIELECTRIC INTERFACES: FROM MEMBRANES TO COLLOIDS

A Dissertation
Submitted to the Graduate Faculty
of the
North Dakota State University
of Agriculture and Applied Science

By

Guilherme Volpe Bossa

In Partial Fulfillment of the Requirements
for the Degree of
DOCTOR OF PHILOSOPHY

Major Department:
Physics

October 2017

Fargo, North Dakota

NORTH DAKOTA STATE UNIVERSITY

Graduate School

Title

ELECTROSTATIC INTERACTIONS AT DIELECTRIC INTERFACES: FROM MEMBRANES TO COLLOIDS

By

Guilherme Volpe Bossa

The supervisory committee certifies that this dissertation complies with North Dakota State University's regulations and meets the accepted standards for the degree of

DOCTOR OF PHILOSOPHY

SUPERVISORY COMMITTEE:

Dr. Sylvio May
Chair

Dr. Alan Denton

Dr. Andrew Croll

Dr. Indranil SenGupta

Approved:

10/27/2017
Date

Dr. Sylvio May
Department Chair

ABSTRACT

In this thesis we have investigated electrostatic interactions at dielectric interfaces using theoretical models based on the non-linear Poisson-Boltzmann theory and its extensions. We have focused on three major topics: (1) modeling the energetics and interactions of charged nanoparticles trapped at the air-water interface; (2) calculation of the line tension between domains in charged lipid membranes, lipid-lipid correlations, and how membrane curvature is influenced by charged peptides; and (3) extensions of the classical Poisson-Boltzmann theory by accounting for the influence of ion-specific solvent-mediated interactions. More precisely, ion-specificity has been accounted for using the Poisson-Helmholtz-Boltzmann formalism, which adds to the bare Coulombic interactions a Yukawa-like potential that accounts for the interacting hydration shells of ions. Motivated by recent experimental and computational results, all projects present here aim to provide a deeper understanding of fundamental physical properties of charged dielectric interfaces.

ACKNOWLEDGEMENTS

My most sincere “thank you” goes to Sylvio May who really contributed to make my PhD and time in Fargo very fruitful and has always been helpful, honest, enthusiastic, and patient. I am also thankful to Dr. Tereza Souza who bridged my Masters and PhD program, and Dr. Klemen Bohinc for all his help in several scientific projects.

I am grateful to my parents, Clavio and Rosana, my sister Caroline, Clara Bossa, my grandparents, and friends, in special: the 07 Fellowship, Carolina Tatiani, Dri Duarte, Ingrid Martins, Pedro Garcia, Tia Šimanović, and all the guys from “Galera do Age”.

I acknowledge the crucial financial support from CAPES Foundation/Brazil Ministry of Education under Grant No. 9466/13-4. I thank all committee members, Drs. Andrew Croll, Alan Denton and Indranil SenGupta, for reading and providing thoughtful comments on how to improve my work. Finally, I am also very grateful to the staff and faculty members from the Physics Department at North Dakota State University.

DEDICATION

To my old friends, grandpa and deceased master, the “amigões” Jercio Volpe and Augusto Agostinho Neto.

TABLE OF CONTENTS

LIST OF TABLES

LIST OF FIGURES

1. INTRODUCTION

Interfaces between media of different dielectric constants are omnipresent in cellular and molecular biology, pharmaceutical sciences, colloid chemistry, and biotechnology[8]. For example, all major classes of charged biomacromolecules (such as proteins, nucleic acids and lipid membranes) and many types of other macroions (including nanoparticles and colloids) can be represented by bodies of low inner dielectric constant that carry electric charges exclusively on their interface directly adjacent to an aqueous phase with high dielectric constant. Electric charges rarely reside inside these macroions because they would produce large electric fields with a correspondingly high energetic penalty. Translation of charges along the interface — instead of moving them into the region of low dielectric constant — is much less costly, implying that inhomogeneously charged interfaces should be abundant. In cellular biology, for example, this is indeed evident for lipid membranes, where charged lipids are frequently enriched within membrane domains, channels [9], or at proteins adsorption sites [10, 11]. A similar increase in the local charge density is also observed in lipid monolayers, which constitute a quasi two-dimensional model fluid that, depending on the applied lateral pressure [12, 13], is able to undergo phase separations at a dielectric boundary between air and water.

The long range of Coulomb interactions plays an important role for the structure of phase-separated systems. From an electrostatic point of view, the formation of a two-dimensional circular domain is less favorable than the formation of an elongated domain. The line tension between domains of a two-dimensional fluid, however, favors circular domains shapes. Hence, the competition between the two contributions — electrostatic and line tension — can be expected to produce complex patterns of domain shapes in lipid monolayers[14, 15], such as "the stripe phases" observed by Sriram and co-worker[16] in monolayers of lipid mixtures. Another interesting system are nanoparticles, which are often observed to partition into dielectric interfaces [17, 18, 19, 20, 21]. This tendency follows from a simple surface tension argument [22]: the surface tension tends to have a large magnitude in phase separated fluids of large dielectric mismatch. For example, the surface tension for an air-water interface at 300K is $\sim 1.75 k_B T/\mathrm{nm}^2$ (i.e., ~ 0.0072N/m). A wide range of nanoparticles are able to effectively lower the energy associated with the surface tension by partitioning to the interface [23, 24]. In some cases, the interplay of electrostatic interactions and surface tension leads to the formation of ordered structures such as two-dimensional arrays of nanoparticles [25, 26].

How electrostatic interactions affect particle partitioning remains a debated topic because modeling inhomogeneously charged dielectric interfaces is a challenging task. Different modeling approaches are available, but each of them involves approximations and comes with limitations. For example, the huge increase of computational power during the last decades has inspired the development of large-scale all-atom computer simulations that, although being based on classical (Newtonian) physics, accurately describe electrostatic interactions at dielectric interfaces [27]. However, limits with respect to accessible time and length scales remain; they still prohibit to study large-scale collective phenomena such as phase separations and self assembly. Coarse grained simulation approaches have further expanded the limits on simulation time and system size, but at the expense of ignoring properties of the solvent [28, 29, 30] and, hence, solvent-mediated interactions [31]. Besides that, most of the computational studies of fluids with non-homogeneous dielectric constants do not account for "dielectric effects" such as the formation of image charges [32] explicitly; instead, these effects are implicitly incorporated into effective charges and dielectric permittivities [33, 34]. Phenomenological modeling approaches — which are often carried out on the mean-field level, including the continuum Poisson-Boltzmann theory— purposely ignore as many details as affordable. Instead, they focus on a small number of "order parameters" such as local ion concentrations or the local dielectric constant [35, 36]. Although computationally far less costly, the risk of such an approach lies in the possibility of selecting an inappropriate set of order parameters. The advantage is that mean-field approaches provide a transparent formalism that can often be analyzed comprehensively and easily reveal the underlying physics, sometimes even leading to analytic expressions of optimal order parameters and minimal free energies [36]. Clearly, the different modeling approaches complement each other, and each of them can benefit from the presence of the others.

In this thesis we use the mean-field Poisson-Boltzmann theory (and extensions of it) to investigate electrostatic interactions at dielectric interfaces. We focus on three major scenarios: i) nanoparticles trapped at the interface between two media of distinct dielectric constants; ii) lipid membranes that can be phase separated or subject to changes in their curvature upon interaction with charged rod-like peptides; and iii) charged electrodes in contact with an aqueous solution containing monovalent ions which can interact among each other not only through the Coulomb potential but also by hydration-mediated non-electrostatic interactions. The following manuscripts that related to these major topics are listed below:

Topic: Nanoparticles at Dielectric Interfaces

- G. V. Bossa, J. Roth, K. Bohinc, S. May, The apparent charge of nanoparticles trapped at a water interface, Soft Matter 12 (18) (2016) 4229–4240. Role: contribution to project design and manuscript writing; discussion of the results; analytical and numerical calculations.

- G. V. Bossa, K. Bohinc, M. A. Brown, S. May, Dipole moment of a charged particle trapped at the air–water interface, J. Phys. Chem. B 120 (26) (2016) 6278–6285. Role: contribution to project design and manuscript writing; discussion of the results; analytical and numerical calculations.

Topic: Lipid Membranes

- G. V. Bossa, M. A. Brown, K. Bohinc, S. May, Modeling the electrostatic contribution to the line tension between lipid membrane domains using Poisson–Boltzmann theory, Int. J. Adv. Eng. Sci. Appl. Math. 8 (2) (2016) 101–110. Role: contribution to the manuscript writing; discussion of the results; analytical and numerical calculations.

- G. V. Bossa, J. Roth, S. May, Modeling lipid–lipid correlations across a bilayer membrane using the quasi-chemical approximation, Langmuir 31 (36) (2015) 9924–9932. Role: contribution to the manuscript writing and numerical calculations; discussion of the results.

- M. W. Lee, M. Han, G. V. Bossa, C. Snell, Z. Song, H. Tang, L. Yin, J. Cheng, S. May, E. Luijten, et al., Interactions between membranes and "metaphilic" polypeptide architectures with diverse side- chain populations, ACS Nano 11 (3) (2017) 2858–2871. Role: contribution to the mean-field modeling and results discussion.

Topic: Incorporation of Non-Electrostatic Interactions Potentials into Poisson-Boltzmann Theory

- K. Bohinc, G. V. Bossa, S. Gavryushov, S. May, Poisson-Boltzmann model of electrolytes containing uniformly charged spherical nanoparticles, J. Chem. Phys. 145 (23) (2016) 234901. Role: contribution to the mean-field modeling and results discussion.

- G. V. Bossa, J. Norris, S. May, Surface tension of a Yukawa fluid according to mean-field theory, J. Chem Phys. 146 (13) (2017) 134701. Role: contribution to project design and manuscript writing; discussion of the results; analytical and numerical calculations.

- M. A. Brown, G. V. Bossa, S. May, Emergence of a Stern layer from the incorporation of hydration interactions into the Gouy–Chapman model of the electrical double layer, Langmuir 31 (42) (2015) 11477–11483. Role: contribution to analytical and numerical calculations; discussion of the results.

- D. L. Z. Caetano, G. V. Bossa, V. M. de Oliveira, M. A. Brown, S. J. de Carvalho, S. May, Role of ion hydration for the differential capacitance of an electric double layer, Phys. Chem. Chem. Phys. 18 (40) (2016) 27796–27807. Role: contribution to project design and manuscript writing; discussion of the results; analytical and numerical calculations.

- D. L. Z. Caetano, G. V. V. Bossa, V. M. de Oliveira, M. Brown, S. J. de Carvalho, S. May, Differential capacitance of an electric double layer with asymmetric solvent-mediated interactions: Mean-field theory and Monte Carlo simulations, Phys. Chem. Chem. Phys. (19) (2017) 23971-23981. Role: contribution to project design and manuscript writing; discussion of the results; analytical and numerical calculations.

Other published works were not included here because they are either review papers or address subjects that only peripherally fit the scope of this thesis:

- S. Holzschuh, K. Kaeß, G. V. Bossa, C. Decker, A. Fahr, S. May, Investigations of the influence of liposome composition on vesicle stability and drug transfer in human plasma: a transfer study, J. Liposome Res. (2016) DOI:10.1080/08982104.2016.1247101. Role: contribution to the mean-field modeling and results discussion.

- T. P. de Souza, G. V. Bossa, P. Stano, F. Steiniger, S. May, P. L. Luisi, A. Fahr, Vesicle aggregates as a model for primitive cellular assemblies, Phys. Chem. Chem. Phys. 19 (30) (2017). Role: contribution to the mean-field modeling and results discussion. 20082–20092.

- K. Bohinc, G. V. Bossa, S. May, Incorporation of ion and solvent structure into mean-field modeling of the electric double layer, Adv. Colloid Interface Sci. (2017) DOI: 10.1016/j.cis.2017.05.001. Role: contribution to the manuscript writing and discussion of the results.

In the following we introduce each of the three research subjects.

1.1. Nanoparticles at Dielectric Interfaces

Nanoparticles have promising potential in industrial and biotechnological applications, being used in emulsion stabilizers [37], colloidosomes [38], bijels [39], and anti-reflective coatings [40, 41]. When trapped at dielectric interfaces, these particles are electrostatically stabilized and able to form ordered two-dimensional arrays [25, 26]. The pioneering works of Frank Stillinger [42], Alan Hurd [43], and Pawel Pieranski [17] have highlighted the dipole-like nature of the electrostatic interactions experienced by charged colloids placed at dielectric interfaces. In the specific case of an air-water interface, two main facts are noted: first, the colloid surface exposed to air usually carries fewer electric charges than the surface immersed in water; and second, the mobile ions in water screen the interaction and, cause a repulsive force that decays exponentially with the distance r between two colloids. Another factor that plays an important role in the interaction between interface-trapped particles are image charges. Both image charges and salt ions contribute to a total interaction that decays $\sim 1/r^3$ and is inversely proportional to the salt concentration in aqueous solution. In view of that, several recent studies have provided inconsistent evidence about the role played by the mobile ions in solution, with some groups reporting that the long-ranged repulsion between charged nanoparticles was insensitive to changes in salt concentration [37, 44], and others stating that such forces were weakly salt-dependent [45, 25].

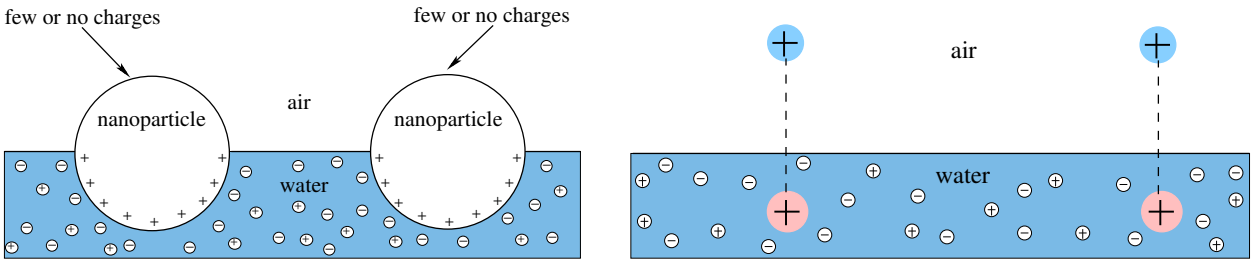

Figure 1.1. Schematic illustration of the systems studied in Part I of this thesis. On the left panel, charged spherical particles partition equatorially into the air-water interface. On the right panel, each hemisphere of a colloid is represented by a point charge placed at a fixed distance away from the air-water interface. In both cases, the aqueous solution contains monovalent anions and cations.

Part I of this thesis addresses the calculation of the electrostatic interaction between charged nanoparticles placed at an air-water interface (see Fig.1.1). Using a mean-field approach, we have first studied a spherical particle that partitions equatorially into the interface. By accounting for all the involved dielec-

tric media (i.e., air, water, and the inside of the colloid) and solving the corresponding coupled Poisson-Boltzmann and Laplace equations, we have found the electrostatic potential everywhere in the system. In addition to numerical calculations, we have obtained an analytical expression that allows to rationalize the role played by the dielectric constant inside the colloid and how it influences the effective charge density on the particle surface exposed to the air phase. In an extension of this project, we have generalized a model developed by Frank Stillinger [42] by representing each of the two hemispheres of an interface-trapped particle by a point charge. Then, we analyzed how different immersion depths — the distance from the point charges to the interface — affect the dipole-like nature of the interactions. Moreover, we have found that the force calculated by our model was similar to that reported by experimental works [46, 26].

1.2. Lipid Membranes

Lipid membranes are complex self-assembled structures that not only spatially organize cells and cellular organelles but also coordinate the trans-membrane communication, regulate permeability, and serve as reaction platform for biochemical and biophysical functions. Besides its primary role as a permeability barrier, lipid membranes can also form domains and rafts. Membrane rafts are heterogeneous dynamic regions of small spatial extension ($10-200$nm) enriched in raft-lipids such as sphingolipids and cholesterol [47, 48]. Furthermore, it is believed that rafts are involved in a multitude of biological processes, including signal transduction [49], protein targeting [50] and virus assembly [51]. The raft hypothesis has motivated many theoretical and experimental studies about domain formation in model membranes [52]. One of the conceptually most important parameters to characterize domains is the line tension between a domain and its immediate environment [52, 53, 54]. Line tensions have been measured for a number of different mixed lipid bilayers [53, 54] and protein decorated interfaces [55]. Although charged lipids are often accumulated in domains — regions where there is a discernible influence of electric charges on the line tension [53, 56] — no theoretical models have previously been proposed for quantifying the electrostatic contribution to the line tension [57]. One difficulty in modeling the line tension is that changing the electrostatic environment affects the line tension not only directly, but also indirectly through restructuring the arrangement of lipids at the domain boundary. This scenario is somewhat similar to the bending stiffness of a membrane, where electrostatic interactions also affect its non-electrostatic contribution [58, 59]. Another difficulty is related to the fact that most lipids have a large dipole moment that can also affect the line tension [56].

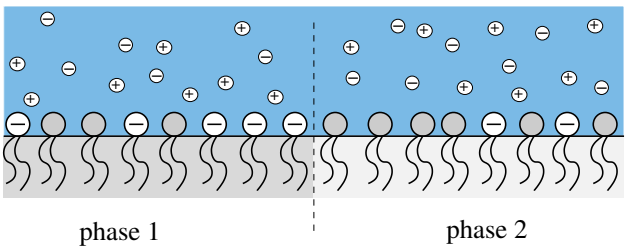

Figure 1.2. Schematic illustration of one of the systems studied in Part II of this thesis: a planar lipid layer composed of neutral and negatively charged lipids that undergoes phase separation, resulting in a highly and a weakly charged phase.

In part II of this thesis we present research projects that focus on lipid membranes. We have initially studied a planar lipid membrane composed only of neutral and negatively charged lipids (see Fig. 1.2). When this binary membrane undergoes phase separation, domains with distinct bulk lipid compositions will form. Concomitantly, an excess in the free energy per unit length of the boundary arises between the domains: the line tension. By means of a mean-field model based on the non-linear Poisson-Boltzmann equation, we have determined the electrostatic contribution to the line tension considering various boundary conditions related to the mobility of the lipids present in each phase. The values that we calculated are comparable to those reported experimentally for the *total* line tension, thus suggesting the crucial role played by electrostatic interactions. In addition to our numerical solutions, analytical expressions valid for the regime of weakly charged membranes were determined making use of the Kontorovich-Lebedev transformations [60]. Another topic investigated here was how the bending stiffness of a membrane is affected by electrostatic interactions. More precisely, we have employed the Poisson-Boltzmann theory to study how the membrane curvature is modified by the interaction with "metaphilic" polypeptides, a type of peptide characterized by a "bottlebrush" architecture consisting of a rigid hydrophobic core covered by mobile side chains terminated with hydrophobic or cationic terminal groups. In this project, our results demonstrated that the dynamic shape-changing properties of these peptides play an important role for their antimicrobial activity [61].

Besides the electrostatic interactions between charged lipids, structural features of lipid membranes are also affected by inter-leaflet coupling and lipid correlations. Experimentally, correlations along a membrane can be probed by the Nearest-Neighbor Recognition (NNR) method developed by Regen and coworkers [62]. More specifically, the NNR method uses the thiolate-disulfide interchange reaction to accurately quantify lipid pairing in mixed membranes. This pairing reflects lipid-lipid correlations and thus motivates

the comparison with theoretical predictions. However, the description of lipid correlations demands approaches beyond the mean-field level discussed so far. In view of that, we proposed a model that employs the quasi-chemical approximation[63] to describe the lipid-lipid correlations across a bilayer membrane. Using this model in conjunction with Monte Carlo simulations, we analyzed how the lipid distributions were affected by distinct lipid-lipid interaction parameters and salt concentrations [4].

1.3. Incorporation of Non-Electrostatic Interaction Potentials Into Poisson-Boltzmann Theory

In the previous sections, we have focused on the description of electrostatic interactions on phase separated systems and colloids with distinct charge distributions. However, the interaction of mobile ions with charged surfaces — such as electrodes, lipid membranes or macroions — is influenced not only by the bare Coulomb interactions, but also by effects due to structural features of the mobile ions. More precisely, these ion-specific effects include (but are not limited to) ionic size, shape, propensity to form hydration shells, and polarizability [64, 65, 66, 67, 68]. One of the most notorious experimental manifestations of ion specificity is the so-called Hofmeister effect [69, 66], which can arise not only from the finite size of ions but, more importantly, from the ion-induced ordering of water molecules [70]. Water molecules form hydration shells that depend on the size and charge distribution of the hydrated ions. Consequently, when ions interact mutually, the perturbation of their hydration shells contributes to an additional non-electrostatic interaction potential [65].

In recent years, a multitude of modeling studies – mostly employing computer simulations [65, 71, 67] – have improved our understanding of the origin and implications of ion specificity in systems of biological significance. Yet, there are also a number of phenomenological approaches that are based on accounting for the dipole potential of water and the ordering of water molecules at interfaces and near charged electrodes and/or macroions [72, 73, 74]. One of the approaches used to include ion specificity into the Poisson-Boltzmann formalism describes water by means of Langevin dipoles [75, 76, 77]; the other, leading to the Poisson-Helmholtz-Boltzmann model, introduces an additional Yukawa potential as effective solvent-mediated ion-ion interaction potential [31, 78], which adds to the Coulomb interaction[8,9,10]. In addition to solvent-mediated interactions, the classical Poisson-Boltzmann theory also ignores the non-vanishing steric size of ions. Consequently, the concentration of counter-ions at the immediate vicinity of a charged electrode (or macroion surface) is greatly overestimated. In order to overcome this issue, steric effects are

commonly incorporated into the Poisson-Boltzmann framework by means of non-ideal entropic contributions, with some of the most frequently used models accounting for excluded volume interactions either on the basis of a lattice gas model [79, 80] or using the Carnahan-Starling equation of state [81, 82, 83, 84].

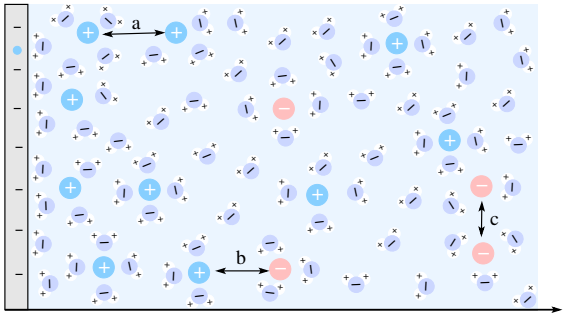

Figure 1.3. Schematic illustration of the type of systems studied in Part III of this thesis: a planar charged surface in contact with an aqueous solution containing monovalent cations and anions. In some of the projects considered here, the ions experience not only the electrostatic, but also solvent-mediated interactions. While the former are described by the Poisson-Boltzmann formalism, the latter are accounted for using ion-specific Yukawa pair potentials with strengths proportional to a set of parameters a, b, and c. Figure adapted from Ref. [9].

In part III of this thesis, we have explored extensions of the Poisson-Boltzmann theory by including hydration-mediated interactions, excluded volume interactions, and ions with spatially-extended charge distributions. We have predominantly considered a single flat charged surface exposed to an electrolytic solution in which the ions experience the combined action of Coulomb, hydration, and steric interactions (see Fig. 1.3). The structure of the ensuing electric double layer differs from the predictions of classical Poisson-Boltzmann theory. To characterize these differences, we computed the differential capacitance of the electric double layer and compared our mean-field results with detailed Monte Carlo Simulations performed in the NVT ensemble.

2. MATHEMATICAL METHODS

The present thesis investigates the role played by electrostatic interactions in a variety of systems, ranging from colloids placed at the air-water interface to charged lipid membranes at physiological conditions. All systems share one point in common: they involve the formation of an electric double layer, which is modeled on the level of the classical or a generalized version of the Poisson-Boltzmann theory. In the following we discuss the theoretical basis of the classical Poisson-Boltzmann theory and show how it can be extended to jointly describe electrostatic and non-electrostatic interactions at dielectric interfaces.

2.1. Poisson-Boltzmann Equation

The Poisson-Boltzmann (PB) theory neglects the solvent structure (apart from accounting for a uniform dielectric background) and, being a mean-field theory, it also ignores ion-ion correlations. These approximations render the PB theory mathematically simpler than more detailed approaches, but they still preserve the ability to describe the formation of an electric double layer in a meaningful way. For example, consider a macroion that carries a fixed surface charge density σ and is immersed in an aqueous solutions of dielectric constant ε_w containing monovalent ions (see Fig. 2.1). In the following we show how PB theory allows us to determine the electrostatic potential and, hence, how the mobile ions are distributed in the vicinity of the macroion. The basic idea of the classical PB theory relies on the assumption [35, 36] that the local concentration of cations, n_+, and anions, n_-, obey a Boltzmann distribution

$$n_\pm = n_0 \exp\left(\frac{\mp e\Phi}{k_B T}\right), \tag{2.1}$$

where Φ is the average local electric potential (in Volts), e the elementary charge, k_B the Boltzmann constant, T the absolute temperature and n_0 the bulk ionic concentration (that is, the concentration in the regions where the potential is zero). For a medium of uniform dielectric constant ε_w, the Poisson equation reads,

$$\nabla^2\Phi = -\frac{e(n_+ - n_-)}{\varepsilon_0 \varepsilon_w}, \tag{2.2}$$

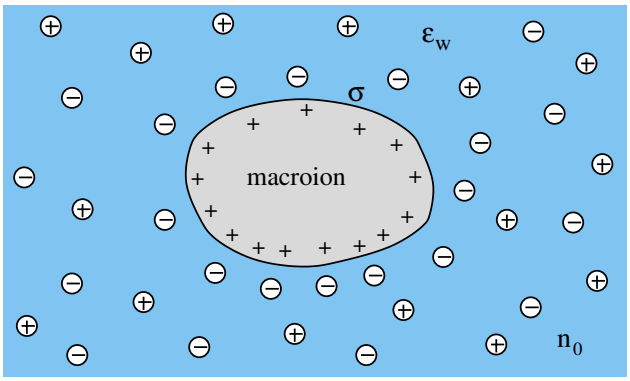

Figure 2.1. Schematic illustration of a macroion that carries a positive surface charge density σ and is embedded in an aqueous solution of dielectric constant ε_w containing monovalent salt ions of bulk concentration n_0. The charges on the macroion surface induce the formation of a diffuse layer of counter-ions at its vicinity.

where ε_0 and ∇^2 are the vacuum permittivity and Laplace operator, respectively. Upon inserting the Boltzmann distributions (eq. 2.1) into the Poisson equation (eq. 2.2) we arrive at the Poisson-Boltzmann equation

$$\nabla^2\Phi = \frac{2en_0}{\varepsilon_w\varepsilon_0}\sinh\left(\frac{e\Phi}{k_BT}\right). \tag{2.3}$$

The Poisson-Boltzmann equation is a non-linear, second-order partial differential equation for the electrostatic potential Φ, the complete solution of which demands a set of two boundary conditions. Often, one of them is the vanishing bulk potential, and the other is related to fixing the surface charge density, σ, or, for mobile surface charges, fixing their electrochemical potential μ.

2.2. Mean-Field Free Energy

The Poisson-Boltzmann equation can be derived by performing a functional minimization of the thermodynamic free energy with respect to all unconstrained parameters. For classical PB theory, the set of unconstrained parameters corresponds to the concentrations n_+ and n_-. Beyond the classical model, this approach also allows us to incorporate extensions, such as additional non-electrostatic ion-ion interactions. We start by writing the general Helmholtz free energy

$$F = U - TS, \tag{2.4}$$

where U is the energy due to particle-particle and particle-surface interactions (electrostatic interactions in the present case), and S accounts for the entropy associated with the motional degrees of freedom of the mobile ions. In the following we will discuss each term individually.

The electrostatic energy of the system, U, can be expressed as

$$\frac{U}{k_B T} = \frac{1}{2}\frac{l_B}{e^2}\int d^3\mathbf{r}\int d^3\mathbf{r}'\frac{\rho(\mathbf{r})\,\rho(\mathbf{r}')}{|\mathbf{r}-\mathbf{r}'|}\,, \tag{2.5}$$

where the local volume charge density is a function of the position vector $\mathbf{r}$, and the two integrations are carried out over the entire space. In addition, we have introduced in eq. 2.5 the Bjerrum length $l_B = e^2/(4\pi\varepsilon_0\varepsilon_w k_B T)$, which for an aqueous solution (i.e., $\varepsilon_w = 80$) at room temperature is $l_B = 0.7\,\text{nm}$. eq. 2.5 suggests the definition of a dimensionless electrostatic potential Ψ through

$$\Psi(\mathbf{r}) = \frac{l_B}{e}\int d^3\mathbf{r}'\frac{\rho(\mathbf{r})}{|\mathbf{r}-\mathbf{r}'|}, \tag{2.6}$$

which is connected to the regular electrostatic potential Φ via $\Psi = e\Phi/k_B T$. Although eq. 2.6 allows for the determination of the potential based on the ionic concentrations, a local representation of Ψ is often mathematically more convenient. A local representation of eq. 2.6 can be found upon applying the Laplace operator ∇^2 to both sides of eq. 2.6 and using its corresponding Green's function $\mathscr{G}(\mathbf{r}) = -1/(4\pi|\mathbf{r}|)$, which satisfies $\nabla^2\mathscr{G}(\mathbf{r}) = \delta(\mathbf{r})$. We find

$$\nabla^2\Psi(\mathbf{r}) = -4\pi\frac{l_B}{e}\rho(\mathbf{r}), \tag{2.7}$$

which is the Poisson equation and thus identical to eq. 2.2 but expressed in terms of l_B and the dimensionless potential Ψ. With this information at hand, we rewrite the electrostatic interaction energy in eq. 2.5 as

$$\frac{U}{k_B T} = -\frac{1}{8\pi l_B}\int d^3\mathbf{r}\;\Psi(\mathbf{r})\nabla^2\Psi(\mathbf{r}). \tag{2.8}$$

Then, the vector identity $-\Psi(\mathbf{r})\nabla^2\Psi(\mathbf{r}) = [\nabla\Psi(\mathbf{r})]^2 - \nabla\dot{[}\Psi(\mathbf{r})\nabla\Psi(\mathbf{r})]$ allows us to write

$$\frac{U}{k_B T} \;=\; \frac{1}{8\pi l_B}\int d^3\mathbf{r}\;\;[\nabla\Psi(\mathbf{r})]^2 - \frac{1}{8\pi l_B}\int d^3\mathbf{r}\;\;\nabla\dot{[}\Psi(\mathbf{r})\nabla\Psi(\mathbf{r})], \tag{2.9}$$

where, according to Gauss's law, the final integral can be written as a surface integral — carried out over the entire space — $\int d^2\mathbf{r}\Psi(\mathbf{r})\nabla\Psi(\mathbf{r})$. Let us discuss this surface integral. In regions far away from the

charge distributions, $\Psi(\mathbf{r}) \sim 1/|\mathbf{r}|$ and $\nabla\Psi(\mathbf{r}) \sim 1/\mathbf{r^2}$, while the area over which the integration is carried out grows proportionally to $\mathbf{r^2}$; roughly speaking, the entire surface integral decreases like $1/\mathbf{r}$. Hence, when we integrate over a sufficiently large space (thereby enclosing all the charges) this integral vanishes [85] and we arrive at the familiar expression for the electrostatic energy

$$\frac{U}{k_B T} = \int d^3\mathbf{r} \frac{(\nabla\Psi)^2}{8\pi l_B}. \tag{2.10}$$

Next, we focus on the entropic contribution to the system free energy. In the classical Poisson-Boltzmann theory, it is assumed that the N ions contained in any sub-volume V of the aqueous solution are point-like particles and, hence, on the mean-field level we arrive at the entropy of an ideal-gas

$$S = -k_B N \left[\ln\left(\frac{Nv}{V}\right) - 1 \right], \tag{2.11}$$

where v is a constant related to the thermal wavelength [86]. The Helmholtz free energy of an ideal gas $F_{ideal}(T,V,N) = -TS$ is a function of the temperature T, volume V, and particle number N. Although eqs. 2.10 and 2.11 can be used to find the relation between the local electrostatic potential and local ionic concentrations, many systems of biological and technological interest have the chemical potential, μ, fixed instead of the particle number N. A convenient way to account for this constraint and obtain $\tilde{F}_{ideal}(T,V,\mu)$ from $F_{ideal}(T,V,N)$ is by using the Legendre transformation:

$$\begin{aligned} \tilde{F}_{ideal}(T,V,\mu) &= F_{ideal}(T,V,N) - N\mu = F_{ideal}(T,V,N) - N \left.\frac{\partial F_{ideal}(T,V,N)}{\partial N}\right|_{T,V_0,N_0} \\ &= k_B T N \left[\ln\left(\frac{Nv}{V}\right) - 1 \right] - k_B T N \ln\left(\frac{N_0 v}{V_0}\right) = k_B T V n \left[\ln\left(\frac{n}{n_0}\right) - 1 \right], \end{aligned} \tag{2.12}$$

where N_0 is the number of ions in the bulk, V_0 is the bulk volume, and we have introduced the local ionic concentration $n \equiv N/V$ and its corresponding bulk value $n_0 = N_0/V_0$. The assumption that the mobile ions in solution behave like an ideal-gas allows us to extend eq. 2.12 to two ionic species by writing the total entropic contribution as the sum of two individual contributions, one for cations (n_+) and another for anions (n_-). Then, eq. 2.12 can conveniently be written as

$$\frac{\tilde{F}_{ideal}(T,V,\mu)}{k_B T V} = n_+ \ln\left(\frac{n_+}{n_0}\right) - n_+ + n_- \ln\left(\frac{n_-}{n_0}\right) - n_-. \tag{2.13}$$

Finally, by recalling eq. 2.10 the complete free energy of the system reads

$$\frac{F}{k_BT} = \int d^3\mathbf{r} \left[\frac{(\nabla\Psi)^2}{8\pi l_B} + n_+ \ln\left(\frac{n_+}{n_0}\right) - n_+ + n_- \ln\left(\frac{n_-}{n_0}\right) - n_- + 2n_0 \right], \tag{2.14}$$

where we have added the last term, the constant $2n_0$, to ensure that the free energy vanishes when $\Psi \to 0$ and $n_\pm = n_0$.

After having determined both the electrostatic and entropic contributions, we can carry out a functional minimization of F, that is, compute $\delta F(n_+, n_+)$ subject to the potential Ψ and ion concentrations obeying the Poisson equation (eq. 2.7). This results in

$$\frac{\delta F}{k_BT} = \int d^3\mathbf{r} \left\{ \delta n_+ \left[\Psi + \ln\frac{n_+}{n_0} \right] + \delta n_- \left[-\Psi + \ln\frac{n_-}{n_0} \right] \right\} + \int d^2\mathbf{r}\, \frac{\delta\sigma}{e} \cdot \Psi, \tag{2.15}$$

where we note that the final term vanishes if the surface charge density on the macroion, σ, is fixed. As thermal equilibrium demands $\delta F = 0$ (and $\delta n_\pm$ are arbitrary), each of the two expressions enclosed by square brackets in eq. 2.15 must vanish identically, i.e.,

$$\Psi + \ln\frac{n_+}{n_0} = 0, \qquad -\Psi + \ln\frac{n_-}{n_0} = 0, \tag{2.16}$$

implying the Boltzmann distributions

$$n_\pm = n_0 e^{\mp\Psi}. \tag{2.17}$$

Inserting n_+ and n_- into the Poisson equation (eq. 2.7), we obtain the Poisson-Boltzmann equation $\nabla^2\Psi(\mathbf{r}) = -4\pi l_B n_0 [e^{-\Psi(\mathbf{r})} - e^{\Psi(\mathbf{r})}]$. It is common to introduce the Debye screening length $l_D = (8\pi l_B n_0)^{-1/2}$. The PB equation can then be expressed as

$$l_D^2 \nabla^2 \Psi(\mathbf{r}) = \sinh\Psi(\mathbf{r}). \tag{2.18}$$

Note that eqs. 2.18 and 2.3 are equivalent. Assuming that $n_\pm$ fulfill the Boltzmann distributions given by eq. 2.17, we may use the differential form of the free energy in eq. 2.15 to compute F through a hypothetical charging process

$$\frac{F}{k_BT} = \int d^2\mathbf{r} \int_0^{\sigma/e} \frac{1}{e} d\bar{\sigma} \cdot \Psi(\bar{\sigma}/e). \tag{2.19}$$

In order to carry out the charging process according to eq. 2.19, we note that the relation $\Psi(\bar{\sigma}/e)$ is only needed at the macroion surface; this often simplifies the calculation of free energies.

The results above are valid for a macroion carrying a fixed surface charge density σ. However, quantities other than σ can be kept constant as, for example, the electrostatic potential Ψ_0 over the macroion surface. In order to account for this new constraint, we introduce a transformed free energy $\tilde{F}$ and carry out a Legendre transformation of eq. 2.15:

$$\frac{\tilde{F}}{k_BT} = \frac{F}{k_BT} - \int d^2\mathbf{r}\,\frac{\sigma}{e}\Psi. \tag{2.20}$$

Functional minimization of eq. 2.20 yields

$$\begin{aligned}\frac{\delta\tilde{F}}{k_BT} &= \frac{\delta F}{k_BT} - \delta\int d^3\mathbf{r}\,\frac{\sigma}{e}\Psi = \int d^3\mathbf{r}\left\{\delta n_+\left[\Psi + \ln\frac{n_+}{n_0}\right] + \delta n_-\left[-\Psi + \ln\frac{n_-}{n_0}\right]\right\} \\ &+ \int d^3\mathbf{r}\,\frac{\delta\sigma}{e}\cdot\Psi - \int d^2\mathbf{r}\,\frac{\delta\sigma}{e}\cdot\Psi - \int d^2\mathbf{r}\;\delta\Psi\cdot\frac{\sigma}{e}.\end{aligned} \tag{2.21}$$

With the local concentrations $n_\pm$ obeying eq. 2.17, the terms inside square brackets vanish and we arrive at $\delta\tilde{F}/k_BT = -\int d^2\mathbf{r}\;\delta\Psi\cdot\sigma/e$. Then, $\tilde{F}/k_BT$ can be written as

$$\frac{\tilde{F}}{k_BT} = -\int d^2\mathbf{r}\int_0^{\Psi_0} d\tilde{\Psi}\cdot\frac{\sigma(\tilde{\Psi})}{e}. \tag{2.22}$$

Here too, it is noteworthy that the relation between σ and $\tilde{\Psi}$ is only needed at the macroion surface.

Eqs. 2.19 and 2.22 have been used to study a lipid monolayer that consists of two separated phases, one kept at fixed surface charge density, and the other at fixed electrostatic potential; this scenario is further discussed in chapter 5.

2.3. Poisson-Boltzmann Equation in Planar Geometry

The non-linear Poisson-Boltzmann equation (eq. 2.18) and extensions of it underlie all projects presented in this thesis. Analytical solutions of this equation are available only for very few cases. One of these is a single, extended, planar electrode of area A that carries a surface charge density σ and is exposed to an electrolyte containing monovalent cations and anions of bulk concentration n_0. The planar geometry

implies that all properties of the system depend only on the distance x to the electrode; hence, we replace the argument $\mathbf{r}$ in eq. 2.18 by x. For the planar geometry, the first integration of the Poisson-Boltzmann equation can be carried out: $d\Psi/dx = -2l_D^{-1}\sinh(\Psi/2)$; therefore, at position $x = 0$

$$2\pi l_B \frac{\sigma}{e} = \frac{1}{l_D}\sinh[\Psi(x=0)/2], \tag{2.23}$$

where we have used the boundary conditions $(d\Psi/dx)_{x=0} = -4\pi l_B\sigma/e$ and vanishing of the potential (and its derivative) at $x \to \infty$. eq. 2.23 reveals a non-linear relation between the surface potential $\Psi_0 \equiv \Psi(x=0)$ and surface charge density σ. When expressed in terms of the surface potential, we arrive at the so-called Grahame equation [35, 87]

$$\Psi_0 = 2\text{arsinh}(2\pi l_B l_D \sigma/e). \tag{2.24}$$

We can integrate the PB equation once more to find the electrostatic potential at any point of the system [35]

$$\Psi(x) = -2\left[\frac{1-\tanh(\Psi_0/4)e^{-l_D x}}{1+\tanh(\Psi_0/4)e^{-l_D x}}\right], \tag{2.25}$$

with Ψ_0 according to eq. 2.24. For a charged planar surface placed at $x = 0$, in Fig. 2.2 we present the dimensionless potential $\Psi(x)$ given by eq. 2.25 (left panel) and the local concentrations (right panel) of cations (n_+, solid lines) and anions (n_-, dashed lines), respectively. Different colors correspond to different surface charge densities: $\sigma = 0.1e/\text{nm}^2$ (in black), $\sigma = 0.5e/\text{nm}^2$ (in red), and $\sigma = 1e/\text{nm}^2$ (in blue).

We can also find an analytical expression for the system free energy by applying the charging process according to eq. 2.19:

$$\frac{F}{Ak_BT} = \int_0^{\sigma/e} \frac{d\bar{\sigma}}{e}\Psi_0(\bar{\sigma}/e). \tag{2.26}$$

Then, upon using the surface potential $\Psi_0(\bar{\sigma}/e)$ given by the Grahame equation (eq. 2.24), eq. 2.26 yields

$$\frac{F}{Ak_BT} = 2\int_0^{\sigma/e} \frac{d\bar{\sigma}}{e}\text{arsinh}(2\pi l_B l_D \bar{\sigma}/e) = \frac{1}{\pi l_B l_D}[p\,\text{arsinh}(p) - \sqrt{1+p^2} + 1], \tag{2.27}$$

with $p \equiv 2\pi l_B l_D \sigma/e$.

Eq. 2.25 can be applied to a plethora of systems that exhibit planar symmetry, including charged lipid layers, metallic electrodes and colloidal suspensions. For applications that demand more sophisticated coordinates (e.g., spherical) and/or complex boundary conditions, solutions of the non-linear Poisson-

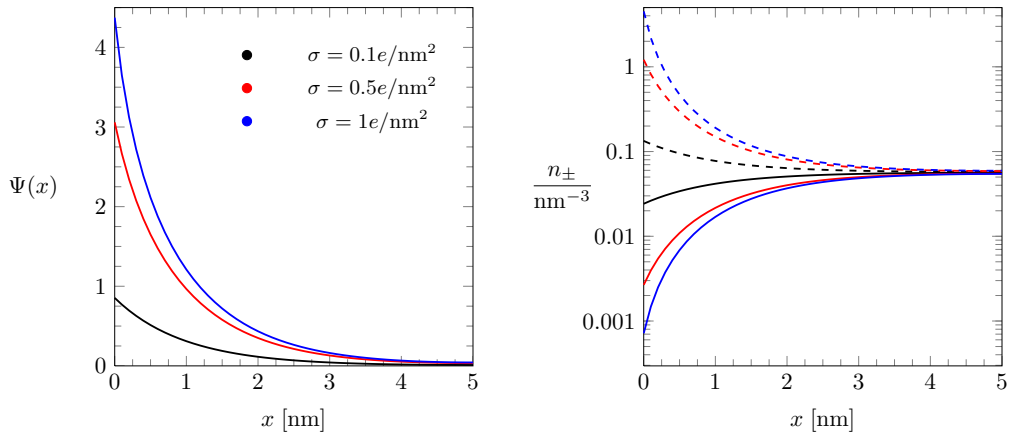

Figure 2.2. Left panel: Dimensionless electrostatic potential $\Psi(x)$ calculated via eq. 2.25. Right panel: Local concentration of cations (solid lines) and anions (dashed lines) according to the Poisson-Boltzmann theory. In both panels, different colors correspond to different surface charge densities: $\sigma = 0.1e/\mathrm{nm}^2$ (black), $\sigma = 0.5e/\mathrm{nm}^2$ (red), and $\sigma = 1e/\mathrm{nm}^2$ (blue). The remaining parameters are $n_0 = 0.056\mathrm{nm}^{-3}$ and $l_B = 0.7\mathrm{nm}$

Boltzmann equation are accessible only numerically. An efficient method to solve eq. 2.18 is the Newton-Raphson iteration scheme [56]. This method determines the solution of eq. 2.18 via solving an iterative sequence of linear differential equations

$$l_D^2 \nabla^2 \Psi_{n+1} = (\Psi_{n+1} - \Psi_n) \cosh \Psi_n + \sinh \Psi_n, \tag{2.28}$$

starting with $\Psi_n = 0$ in iteration step $n = 1$ and progressing until convergence is achieved for sufficiently large n (as convergence criterion one can use the stationarity $\Psi_{n+1} = \Psi_n$, or the minimization of the associated system free energy). Non-linear boundary conditions can also be incorporated into the Newton-Raphson iteration scheme [56].

2.4. Non-Ideal Entropic Contributions

The mathematical formalism presented so far has allowed us to derive the Poisson-Boltzmann equation from the functional minimization of the system free energy. One of the facts that renders this theory mathematically so simple is the modeling of the electrolyte as an ideal-gas composed of point-like ions. In order to account for deviations from ideal behavior —as for example, due to the finite size of ions— we add

to eq. 2.14 a non-ideal entropy contribution

$$\frac{F_{non-id}}{k_BT} = \int_V d^3\mathbf{r}\, \left[g(n_+ + n_-) - (n_+ + n_-)\, g'(2n_0) \right], \tag{2.29}$$

with the function $g(n_+ + n_-)$ appearing in the equation of state $pV/(Nk_BT) = 1 + g'(n) - g(n)/n$ of a gas that exerts a pressure p at fixed number N of particles kept at temperature T and confined to a volume V. We define $n = n_+ + n_- = N/V$ and a prime denotes a derivative with respect to the argument, that is, $g'(n) \equiv dg(n)/dn$. The system free energy now reads

$$\frac{F}{k_BT} = \int d^3\mathbf{r} \left[\frac{(\nabla\Psi)^2}{8\pi l_B} + n_+ \ln\left(\frac{n_+}{n_0}\right) - n_+ + n_- \ln\left(\frac{n_-}{n_0}\right) - n_- + 2n_0 \right. \tag{2.30}$$
$$\left. + g(n_+ + n_-) - (n_+ + n_-)\, g'(2n_0) \right].$$

Analogously to the ideal-gas case, functional minimization of this free energy yields

$$\begin{aligned} \frac{\delta F_{tot}}{k_BT} \;=\; & \int_V d^3\mathbf{r} \left\{ \delta n_- \left[-\Psi + \ln\frac{n_-}{n_0} + g'(n_- + n_+) - g'(2n_0) \right] \right. \\ & \left. +\; \delta n_+ \left[\Psi + \ln\frac{n_+}{n_0} + g'(n_- + n_+) - g'(2n_0) \right] \right\}. \end{aligned} \tag{2.31}$$

As exercised previously, the requirement that $\delta F = 0$ when thermal equilibrium is reached allows us to obtain the following relations between the local ionic concentrations $n_\pm$ and the electrostatic potential

$$\begin{aligned} -\Psi + \ln\frac{n_-}{n_0} + g'(n_- + n_+) - g'(2n_0) &= 0, \\ \Psi + \ln\frac{n_+}{n_0} + g'(n_- + n_+) - g'(2n_0) &= 0. \end{aligned} \tag{2.32}$$

Eqs. 2.32 are generally transcendental, but some specific choices of $g(n)$ yield analytic expressions for $n_+ = n_+(\Psi)$ and $n_- = n_-(\Psi)$. Clearly, the Boltzmann distributions shown in eq. 2.17 are recovered in the absence of non-ideal effects; that is, $g(n) = 0$. Another case where an analytic relation is available occurs when using a lattice-gas model [79, 80] to account for the finite size of ions. More precisely, assuming that all ions have the same diameter $2R$ and that each lattice cell can host no more than one single ion, the

function $g(n)$ reads

$$g^{LG}(n) = \frac{g_0^{LG} n + (1 - g_0^{LG} n)\ln(1 - g_0^{LG} n)}{g_0^{LG}}, \tag{2.33}$$

where $g_0^{LG} = (2R)^3$ corresponds to the volume of the lattice cell. Hence, upon inserting eq. 2.33 into 2.32 and solving for n_+ and n_- we find the Fermi-Dirac-like distributions

$$\begin{aligned} n_+ &= \frac{n_0 e^{\Psi}}{1 - 2\phi_0 + 2\phi_0 \cosh(\Psi)} \\ n_- &= \frac{n_0 e^{\Psi}}{1 - 2\phi_0 + 2\phi_0 \cosh(\Psi)}, \end{aligned} \tag{2.34}$$

with $\phi_0 \equiv n_0 (2R)^3$. Upon inserting these results back into the Poisson equation, we arrive at a modified [80] Poisson-Boltzmann equation

$$l_D^2 \nabla^2 \Psi = \frac{\sinh \Psi}{1 - 2\phi_0 + 2\phi_0 \cosh(\Psi)}. \tag{2.35}$$

eq. 2.35 recovers the "classical" Poisson-Boltzmann equation in the limit of point like-ions; that is, when $R \to 0$. It is also noteworthy that for large potentials ($\Psi \to \pm\infty$) the ionic profiles saturate, that is, they reach a plateau of constant value that does not change upon increasing $|\Psi|$ (see Fig. 2.3). Eqs. 2.33 -2.35 are used and further discussed in chapters 7-10. Besides the lattice-gas model, effects due to the finite size

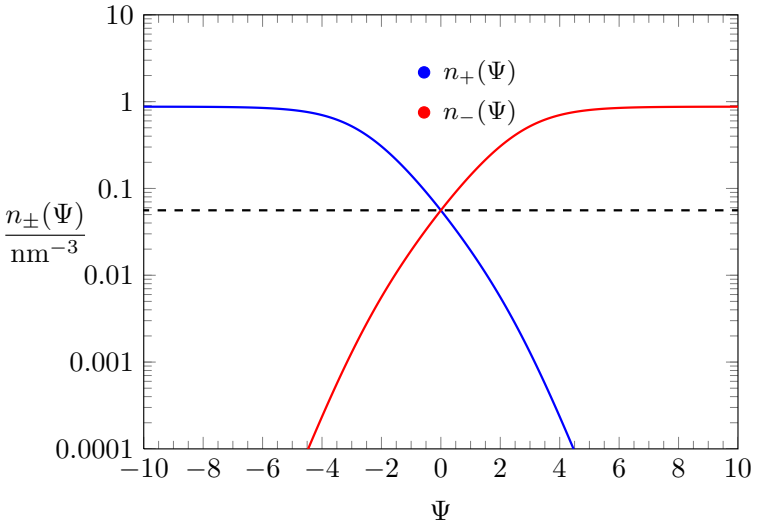

Figure 2.3. Distribution of cations (n_+, in blue) and anions (n_-, in red) as function of the electrostatic potential Ψ according to eqs. 2.34. Values obtained for particle radius $R = 0.2$nm and $n_0 = 0.057\text{nm}^{-3}$ (which, for $l_B = 0.7$nm, corresponds to ~ 100mM and is marked by a black dashed line).

of ions are frequently accounted for by means of phenomenological equations of states, such as the van der Waals [88] and the Carnahan-Starling equations of state [81, 89] for hard-sphere fluids (and a generalization to mixtures of spherical particles with different sizes, the so-called Boublik-Mansoori-Carnahan-Starling-Leland equation of state [81, 82, 83, 90, 91]). We now focus on the Carnahan-Starling equation of state; in order to use it in our formalism, we must first determine its corresponding function $g(n)$. Assuming that all ions in solution are spherical particles of the same radius, the Carnahan-Starling equation of state reads [81, 89]

$$\frac{PV}{Nk_BT} = \frac{1+\eta+\eta^2-\eta^3}{(1-\eta)^3}, \tag{2.36}$$

where the parameter η is defined by:

$$\eta = \frac{4\pi R^3 N}{3V} = \frac{4\pi R^3 (N_+ + N_-)}{3V}. \tag{2.37}$$

The finite size of ions will affect their distribution and, consequently, the overall entropic contribution to the Helmholtz free energy F. Here, these non-ideal effects are incorporated into a (still unknown) function $G(\eta)$, which is added to the ideal term (eq. 2.11):

$$\frac{F}{k_BT} = N\left[\ln\left(\frac{Nv}{V}\right) - 1\right] + NG(\eta). \tag{2.38}$$

From thermodynamics, we know that the pressure of a system can be determined by $P = -(\partial F/\partial V)|_{T,N}$, which, applied to eq. 2.38 and recalling that η is a function of V, yields:

$$\frac{P}{Nk_BT} = \frac{1}{V}\left[1 + \eta\frac{dG(\eta)}{d\eta}\right]. \tag{2.39}$$

Then, upon equaling eq. 2.39 to eq. 2.36,

$$\frac{1+\eta+\eta^2-\eta^3}{(1-\eta)^3} = 1 + \eta\frac{dG(\eta)}{d\eta}, \tag{2.40}$$

and solving this differential equation for $G(\eta)$, one finds

$$G(\eta) = \int_0^\eta \left[-1 + \frac{1+\tilde{\eta}+\tilde{\eta}^2-\tilde{\eta}^3}{(1-\tilde{\eta})^3}\right]\frac{d\tilde{\eta}}{\tilde{\eta}} = \frac{\eta(4-3\eta)}{(1-\eta)^2}, \tag{2.41}$$

where we have used the boundary condition $G(\eta = 0) = 0$. With this result, eq. 2.38 now reads

$$\frac{F}{k_B T} = N\left[\ln\left(\frac{Nv}{V}\right) - 1\right] + N\frac{\eta(4-3\eta)}{(1-\eta)^2}, \tag{2.42}$$

or, equivalently, in terms of $n = N/V$

$$\frac{F}{k_B T} = \int d^3\mathbf{r}\left[n\{\ln(nv) - 1\} + n\frac{\eta(4-3\eta)}{(1-\eta)^2}\right]. \tag{2.43}$$

Finally, based on the definition of η (eq. 2.37), we identify the function $g(n)$ according to the Carnahan-Starling equation of state as

$$g^{CS}(n) = nG(\eta) = \frac{g_0^{CS} n^2 (4 - 3g_0^{CS} n)}{(1 - g_0^{CS} n)^2}, \tag{2.44}$$

where we have used $\eta = g_0^{CS} N/V = g_0^{CS} n$ with $g_0^{CS} = 4\pi R^3/3$. The function $g^{CS}(N)$ is used and further discussed in Chapters 7-10.

2.5. Incorporation of Non-Electrostatic Pair Potentials

Deviations from the ideal-gas regime can be accounted for not only via non-ideal entropy terms, but also by means of non-electrostatic pair potentials that adds to the bare Coulomb potential. By denoting the former and latter potentials by u_n and u_e, respectively, in this section we present a field-based approach that allows the incorporation of non-electrostatic interactions into the Poisson-Boltzmann formalism. For a sake of simplicity, we initially assume that only one ion type n (e.g., cations, $n = n_+$) experiences the non-electrostatic potential. Hence, we recall the system free energy, $F = U - TS$, but with the total pair potential U now written as $U = U_e + U_n$, with U_e given by eq. 2.10 and U_n by

$$\frac{U_n}{k_B T} = \frac{1}{2}\int d^3\mathbf{r} \int d^3\mathbf{r}' n(\mathbf{r})\, n(\mathbf{r}') u_n(\mathbf{r} - \mathbf{r}'), \tag{2.45}$$

with the integrals being carried out over the entire space. Analogously to the previous section, based on eq. 2.45 we can define a corresponding non-electrostatic potential

$$\Psi_n(\mathbf{r}) = \int d^3\mathbf{r}' u_n(\mathbf{r}-\mathbf{r}')n(\mathbf{r}'). \tag{2.46}$$

Even with an unspecified $u_n(\mathbf{r}-\mathbf{r}')$, we can use the Green's function method to find the differential equations associated with the non-electrostatic potential, that is, we can follow the same steps that led us from eq. 2.6 to eq. 2.7. In line with this, we initially define an operator $\mathscr{A}(\mathbf{r})$ which, when acting on its associated Green's function $\mathscr{G}(\mathbf{r}-\mathbf{r}')$, yields $\mathscr{A}(\mathbf{r})\mathscr{G}(\mathbf{r}-\mathbf{r}') = -4\pi\delta(|\mathbf{r}-\mathbf{r}'|)$. Thus, using this operator in eq. 2.46 we find

$$\mathscr{A}(\mathbf{r})\Psi_n(\mathbf{r}) = \int d^3\mathbf{r}' \mathscr{A}(\mathbf{r})u_n(\mathbf{r}-\mathbf{r}')n(\mathbf{r}') = -4\pi n(\mathbf{r}). \tag{2.47}$$

2.5.1. Yukawa-like Potential

Let us now discuss some applications of the general result presented in eq. 2.47. For example, if $u_n(\mathbf{r}-\mathbf{r}')$ is Coulomb-like (i.e., $\sim 1/(|\mathbf{r}-\mathbf{r}'|)$), we must have $\mathscr{A}(\mathbf{r}) \sim \nabla^2$ and, hence, eq. 2.47 yields a Poisson equation similar to eq. 2.7. Another interesting case — which is employed and further discussed in chapters 8-10 — occurs when $u_n(\mathbf{r}-\mathbf{r}')$ takes the form of a Yukawa-like potential

$$u_n(\mathbf{r}-\mathbf{r}') = l_n \frac{e^{-\kappa|\mathbf{r}-\mathbf{r}'|}}{|\mathbf{r}-\mathbf{r}'|}, \tag{2.48}$$

where κ is a characteristic decay length and l_n is an interaction strength that plays the same role as l_B does for electrostatics. The operator $\mathscr{A}(\mathbf{r})$ associated with $u_n(\mathbf{r}-\mathbf{r}')$ is $\mathscr{A}(\mathbf{r}) = \nabla^2 - \kappa^2$. Then, with this information used in eq. 2.47, we find a Helmholtz-like differential equation with complex wave parameter and a source term

$$\nabla^2\Psi_n(\mathbf{r}) - \kappa^2\Psi_n(\mathbf{r}) = -4\pi l_n n(\mathbf{r}). \tag{2.49}$$

2.5.2. Oscillatory Yukawa Potential

The formalism presented so far can also be employed to describe an ion-specific damped oscillatory force between two flat surfaces [92, 93, 94]. In line with this, we modify eq. 2.48 by introducing an oscillatory term

$$u_n(\mathbf{r}-\mathbf{r}') = l_n \frac{e^{-\kappa\alpha|\mathbf{r}-\mathbf{r}'|}}{|\mathbf{r}-\mathbf{r}'|} e^{i(\kappa\beta|\mathbf{r}-\mathbf{r}'|+\phi)}, \tag{2.50}$$

where i is the imaginary unit, α and β are two real dimensionless constants that quantify the interaction range, and ϕ is a phase shift in the oscillations. We note that eq. 2.48 is recovered by setting $\alpha = 1$ and $\beta = \phi = 0$. Similarly to the previous case, the operator associated with eq. 2.50 is

$$\mathscr{A}_n = \frac{1+\gamma^2}{4\kappa^2}\nabla^4 + \nabla^2 - \kappa^2, \tag{2.51}$$

with ∇^4 being the bi-harmonic operator and γ a constant that specifies the values of α and β via

$$\alpha = \frac{\gamma}{\sqrt{1+\gamma^2+(1+\gamma^2)^{3/2}}}, \text{ and } \beta = \frac{\sqrt{1+\gamma^2+(1+\gamma^2)^{3/2}}}{1+\gamma^2}. \tag{2.52}$$

Hence, upon applying eq. 2.51 in 2.50 we obtain

$$\frac{1+\gamma^2}{4\kappa^2}\nabla^4\Psi_n(\mathbf{r}) + \nabla^2\Psi_n(\mathbf{r}) - \kappa^2\Psi_n(\mathbf{r}) = -2\pi(1-i\gamma)e^{i\phi} l_n n(\mathbf{r}). \tag{2.53}$$

It is noteworthy that only the real part of the above equations is of physical significance. Finally, we can use eqs. 2.53 and 2.45 and the Gauss law to write the non-electrostatic energy U_n as

$$\frac{U_n}{k_B T} = \int d^3\mathbf{r} \frac{-\frac{1+\gamma^2}{4\kappa^2}(\nabla^2\Psi_n)^2 + (\nabla\Psi_n)^2 + \kappa^2\Psi_n}{4\pi l_n(1-i\gamma)e^{i\phi}}. \tag{2.54}$$

Although written for non-electrostatic oscillatory interactions, eq. 2.54 represents a general result that can reproduce all the cases discussed here. For example, in the specific scenario where the pair-potential between particles does not exhibit oscillations — that is, $\alpha = 1$, $\beta = \phi = 0$, and $\gamma = i$ — eq. 2.54 yields

$$\frac{U_n}{k_B T} = \int d^3\mathbf{r} \frac{(\nabla\Psi_n)^2 + \kappa^2\Psi_n}{8\pi l_n}. \tag{2.55}$$

In addition, we note that eq. 2.55 becomes similar to the electrostatic energy (eq. 2.10) when $\kappa = 0$ and $l_n = l_B$.

2.5.3. Arbitrary Interaction Potentials and Laplace Transformation

In the preceding sections we have discussed how electrostatic and non-electrostatic potentials can be incorporated into the Poisson-Boltzmann formalism. We now go a step further and discuss a mean-field approach that allows us to account for any arbitrary pair-potential, $u_n(r)$. In view of that, we start by expressing the interaction potential $u_n(r)$ as a sum of Yukawa potentials [31] via

$$u_n(r) = \int_0^\infty d\kappa \; a(\kappa) \frac{e^{-\kappa r}}{r}, \tag{2.56}$$

with κ being an inverse decay length and $a(\kappa)$ the corresponding weight. In addition, we identify $r\,u(r) = \mathscr{L}[a(\kappa)]$ as a Laplace transformation; hence, once $u(r)$ is specified, we can find the coefficients $a(\kappa)$ through the inverse Laplace transformation $a(\kappa) = \mathscr{L}^{-1}[ru(r)]$. In terms of $u_n(r)$, the interaction energy of the system can be expressed as

$$\frac{U}{k_B T} = \frac{1}{2e^2} \int d^3\mathbf{r} \int d^3\mathbf{r}' \rho(\mathbf{r})\, \rho(\mathbf{r}') u(|\mathbf{r}-\mathbf{r}'|) = \frac{1}{2e} \int d^3\mathbf{r} \; \rho(\mathbf{r}) \int d\kappa \; a(\kappa) \Psi(\mathbf{r}, \kappa), \tag{2.57}$$

where we have used the auxiliary potential

$$\Psi(\mathbf{r}, \kappa) = \int d^3\mathbf{r}' \frac{\rho(\mathbf{r}')}{e} \frac{1}{|\mathbf{r}-\mathbf{r}'|} e^{-\kappa|\mathbf{r}-\mathbf{r}'|}. \tag{2.58}$$

For any choice of κ, the potential $\Psi(\mathbf{r}, \kappa)$ fulfills the differential equation $\nabla^2\Psi(\mathbf{r}, \kappa) - \kappa^2\Psi(\mathbf{r}, \kappa) = -4\pi\rho(\mathbf{r})$. With the energy U defined in a general form as in eq. 2.57, it is noteworthy to point out that the specific choice $a(\bar{\kappa}) = l_B \delta(\bar{\kappa} - 0)$ yields the familiar expression for the electrostatic energy

$$\frac{U}{k_B T} = \frac{1}{2e} \int d^3\mathbf{r} \; \rho(\mathbf{r}) \Psi(\mathbf{r}, \kappa = 0). \tag{2.59}$$

As exercised previously, by combining the energy U (eq. 2.57) with the entropic contribution (eq. 2.13) we can find the system free energy $F = U - TS$. The functional minimization of $F[\Psi(\mathbf{r})]$ then

yields the integro-differential equation

$$\nabla^2\Psi(\mathbf{r},\kappa)-\kappa^2\Psi(\mathbf{r},\kappa)=-4\pi n_0\left\{\exp\left[-\int_0^\infty d\bar{\kappa}a(\bar{\kappa})\Psi(\mathbf{r},\bar{\kappa})\right]+\exp\left[\int_0^\infty d\bar{\kappa}a(\bar{\kappa})\Psi(\mathbf{r},\bar{\kappa})\right]\right\}, \quad (2.60)$$

which has to be solved [31] for all κ that are necessary to produce $u(r)$ according to eq. 2.56. In the electrostatic regime, for example, we have only one discrete value of κ, which vanishes. More precisely, with $\kappa=0$ and recalling the "electrostatic coefficient" $a(\bar{\kappa})=l_B\delta(\bar{\kappa}-0)$ we find

$$\nabla^2\Psi(\mathbf{r},\kappa=0)=-4\pi n_0[e^{-l_B\Psi(\mathbf{r},\kappa=0)}+e^{l_B\Psi(\mathbf{r},\kappa=0)}]. \quad (2.61)$$

Upon defining $\Psi(\mathbf{r})\equiv l_B\Psi(\mathbf{r},\kappa=0)$, we finally obtain

$$\nabla^2\Psi(\mathbf{r})=-4\pi n_0[e^{-\Psi(\mathbf{r})}-e^{\Psi(\mathbf{r})}]=8\pi l_B n_0\sinh[\Psi(\mathbf{r})]=\frac{1}{l_D^2}\sinh[\Psi(\mathbf{r})], \quad (2.62)$$

which is the Poisson-Boltzmann equation.

3. THE APPARENT CHARGE OF NANOPARTICLES TRAPPED AT A WATER INTERFACE *

3.1. Introduction

Charged colloids or nanoparticles that partition into the dielectric interface between air and water (and similarly for oil and water) can arrange into ordered two-dimensional phases, which are stabilized by long-ranged repulsive electrostatic interactions. Such decorated interfaces offer promising applications, including emulsions stabilization [1, 95, 37, 96], antireflective coatings [41, 40], and optical devices. The two-dimensional nature of their electrostatically stabilized ordering render interface-trapped particles also interesting from a fundamental point of view.

Classical works by Stillinger [42] and Pieranski [17] highlight the dipole-like nature of the electrostatic interactions between charged particles at dielectric interfaces. Clearly, within a bulk aqueous solution the interaction is screened by mobile ions (salt, or H^+ and OH^- ions in the absence of salt) and thus decays exponentially whereas in a uniform dielectric medium without mobile ions a bare $1/r$-Coulomb potential as function of the distance r emerges. When trapped at an air-water (or oil-water) interface, image charges and the presence of mobile ions in the aqueous region render the long-range part of the interaction dipole-like, $1/r^3$, and inversely proportional to the salt concentration [43].

Charged colloids or nanoparticles often carry dissociable groups (phosphate or carboxyl moieties [97, 98, 99, 100]) that allow the surface charge density to adjust. When immersed in water the particle's surface charge density is much larger than that of a particle being exposed to air or oil [101]. Indeed, water has a large dielectric constant and contains mobile ions that provide an effective screeing of electrostatic interactions. In contrast, the high cost of forming electrostatic fields in media of low permittivity (air or oil) and the absence of mobile ions tend to oppose the accumulation of charge at charge-regulated surfaces. This results in charge densities that are high and low in the water-exposed and air- (or oil-) exposed regions of

*Reprinted from "G. V. Bossa, J. Roth, K. Bohinc, S. May, The apparent charge of nanoparticles trapped at a water interface, Soft Matter 12 (18) (2016) 4229–4240.". Reproduced by permission of The Royal Society of Chemistry. Copyright 2016 The Royal Society of Chemistry. This paper can be accessed online at `http://pubs.rsc.org/-/content/articlehtml/2016/sm/c6sm00334f`. The material in this chapter was co-authored by Guilherme V. Bossa, Joseph Roth, Klemen Bohinc and Sylvio May. G. V. Bossa contributed to the project design and manuscript writing. G.V.B. was responsible for the mathematical development, numerical and analytical solution of the equations, figures preparation, and discussion of the results.

the particle, respectively. However, the latter and not the former mediate long-ranged particle-particle interactions. In line with this, Aveyard *et al* [101] have reported that the ordered pattern formed by polystyrene latex particles covered by sulfate groups was insensitive to the electrolyte when they were placed at an oil-water interface. The authors concluded that the electrostatic repulsion emerged exclusively due to residual charges at the oil-exposed surface regions of the particles.

Based on the initially observed [101] electrolyte insensitivity and the perceived importance of the charges exposed to the oil, Danov et al. [102, 103, 104] have modeled the electrostatic force acting on charged colloids at the oil-water interface thereby imposing a scenario of no penetration of the electric field into the aqueous medium. Computational studies with a similar scope have been presented by Zhao *et al* [105] and Majee *et al* [106]. Both consider spherical particles that partition equatorially into the oil-water interface and compute electrostatic fields inside the aqueous and oil phases for asymmetric charge distributions on the particles (that is, different uniform surface charge densities on the oil- and water-exposed particle regions). While the two models accurately account for the particle shape and charge distribution, neither of them allows the electrostatic field to penetrate into the particle interior and thus to couple the electrostatic properties in the aqueous phase with those in the apolar medium.

Recent experiments have shown, however, that the repulsion between charged colloids at an oil-water interface is weakly dependent on the electrolyte concentration [26, 25, 45, 1], putting into question the sole responsibility of the oil-exposed charges for the long-range dipole interactions. As pointed out by Frydel *et al* [107], there is a possibility of the electric field produced by the charges on the water-facing side of a particles to propagate into the oil phase by passing though the particle interior instead of spreading exclusively into the aqueous phase. This idea has been pursued through a renormalization approach [107, 100, 108], where the charges on the water-facing side of a colloid give rise to an electrostatic potential in the air (or oil) phase that far away from the colloid can be matched with the potential produced by a dipole with an effective dipole moment. The effective dipole moment was determined from numerical solutions of the Poisson-Boltzmann and Laplace equations for spherical particles [107]. Yet, what was not accounted for is the possibility that, first, not only the water-facing side of the colloid but also its oil-facing side is charged and, second, the dielectric constant inside the colloid can be different from that in the air.

In the present work we analyze the electrostatic properties of a spherical particle (a colloid or a nanoparticle) that partitions equatorially into the air-water interface. We allow the particle to have different uniform charge densities on its water- and air-exposed regions. In contrast to previous studies we explicitly

include into our model the dielectric properties inside the particle. That is, we allow the electric field to propagate into the particle interior and thus to either enhance or diminish the electric field in the air. Hence, our model is designed to predict the salt dependence of the long-ranged dipolar particle-particle inteactions. Our calculations are carried out on the level of mean-field electrostatics. To this end, we solve Laplace equations in the air and inside the spherical particle, and the non-linear Poisson-Boltzmann equation in the water phase. Two approximations are adopted. First, we assume the radius of the particle is much larger than the Debye screening length of the aqueous solution and, second, the surface potential at the air-water interface is fixed and constant. We express our results in terms of an effective surface charge density at the air-exposed region of the particle, which generally differs from the bare charge density due to the contribution from the electric field inside the particle. Our calculations demonstrate that even with a small dielecric constant inside the particle, the charges at its water-exposed region can make a significant contribution to the long-ranged dipolar interactions between interfacially trapped particles. We analyze this behavior in terms of several paramters: the dielectric constant inside the particle, the salt content in the aqueous solution, and the potential drop at the air-water interface. We also show that a simple approximation – that of a planar capacitor – yields an explicit expression for the effective charge density at the air-exposed region of the particle, which is in qualitative agreement with our numerical calculations for the spherical geometry.

3.2. Theory

We consider a particle (a nanoparticle or a colloid) of uniform dielectric constant ε_n that partitions into the interface between air (with dielectric constant $\varepsilon_a = 1$) and water (with dielectric constant $\varepsilon_w = 80$ and in presence of monovalent salt with bulk concentration n_0). The surface of the particle carries a fixed surface charge density that we denote by σ_a for the air-exposed region and by σ_w for the water-exposed region; see Fig. 3.1. At this point we do not assume a specific shape of the particle, nor that the two surface charge densities σ_a and σ_w are uniform; both will be specified below. However, because we only target electrostatic interactions, we treat the air-water interface throughout this work as flat; i.e., we neglect surface perturbations due to capillary effects.

The present work is based on mean-field electrostatics, expressed in terms of the commonly used dimensionless electrostatic potential $\Psi = e\Phi/k_BT$, where Φ is the electrostatic potential, k_B the Boltzmann

constant, T the absolute temperature, and e the elementary charge. Note that $\Psi = 1$ corresponds to an electrostatic potential of $\Phi = 25\,\mathrm{mV}$ at room temperature. We use indices "a", "w", and "n" to label the three regions: air, water, and the inside of the nanoparticle. Hence Ψ_a, Ψ_w, and Ψ_n, denote the dimensionless potential in the air, water, and particle interior, respectively. With this, the electrostatic free energy, in units of k_BT, of the charged particle at the air-water interface can be expressed as

$$\begin{aligned}\frac{F_{el}}{k_BT} = {} & \varepsilon_a \int_{V_a} d\mathrm{v} \frac{(\nabla\Psi_a)^2}{8\pi l_B} + \varepsilon_w \int_{V_w} d\mathrm{v} \frac{(\nabla\Psi_w)^2}{8\pi l_B} + \varepsilon_n \int_{V_n} d\mathrm{v} \frac{(\nabla\Psi_n)^2}{8\pi l_B} \\ & + \int_{V_w} d\mathrm{v} \left[n_+ \ln \frac{n_+}{n_0} - n_+ + n_- \ln \frac{n_-}{n_0} - n_- + 2n_0 \right] \\ & - \int_{V_w} d\mathrm{v}\, \Psi_w^{(b)} (n_+ - n_-).\end{aligned} \tag{3.1}$$

The first three volume integrals, which run over the air (volume V_a), water (volume V_w), and nanoparticle (volume V_n) regions, account for the energy stored in the electrostatic field; $l_B = e^2/(4\pi\varepsilon_0 k_B T) = 56\,\mathrm{nm}$ is the Bjerrum length in vacuum (the permittivity of free space is denoted by ε_0). The fourth integral corresponds to the demixing free energy of two ideal gases, one for the mobile cations and the other for the mobile anions in the aqueous solution, expressed in terms of the local cation concentration, n_+, and local anion concentration, n_-. In the bulk of the aqueous phase $n_+ = n_- = n_0$.

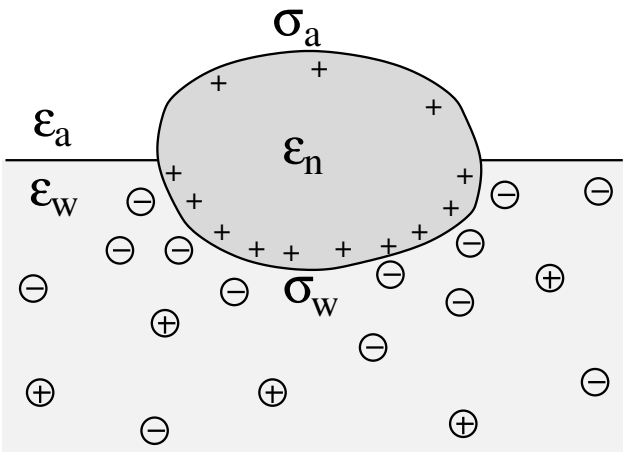

Figure 3.1. Schematic illustration of a charged particle (a nanoparticle or colloid, with dielectric constant ε_n), located at the interface between air (with dielectric constant $\varepsilon_a = 1$) and water (with dielectric constant $\varepsilon_w = 80$). The aqueous phase contains monovalent salt ions of bulk concentration n_0. The surface charge densities of the particle at its air-exposed and water-exposed regions are denoted by σ_a and σ_w, respectively.

We note that the electrostatic potential is believed to change when passing from air into the bulk of an aqueous solution. The potential difference likely reflects both the adsorption of ions (OH^- versus H^+) and the dipole potential from interface-induced water ordering. The magnitude and sign have been a matter of debate [109, 110], but a change from a more negative potential in the air to a more positive potential in bulk water finds wide experimental [111, 112] and some computational [113] support. In the present work we use the potential in the air, far away from the air-water interface and from the particle, as reference that we define as zero. Hence, in the bulk of the aqueous phase, the potential adopts a non-vanishing constant value that we denote by $\Psi_w^{(b)}$. The final term in Eq. 3.1 introduces $\Psi_w^{(b)}$ as a fixed (and yet unspecified) external potential in the aqueous medium. Indeed, minimization of F_{el} with respect to the local ion concentrations yields the Boltzmann distributions

$$n_\pm = n_0 e^{\mp(\Psi_w - \Psi_w^{(b)})}, \tag{3.2}$$

which recover $n_+ = n_- = n_0$ for $\Psi_w = \Psi_w^{(b)}$. When combined with the Poisson equation $\nabla^2\Psi_w = -4\pi l_B(n_+ - n_-)$, Eq. 3.2 gives rise to the Poisson-Boltzmann equation,

$$l_D^2\nabla^2\Psi_w = \sinh(\Psi_w - \Psi_w^{(b)}), \tag{3.3}$$

where $l_D = (8\pi l_B n_0/\varepsilon_w)^{-1/2}$ is the familiar Debye screening length. Minimization of F_{el} also produces the Laplace equations

$$\nabla^2\Psi_a = 0, \qquad \nabla^2\Psi_n = 0, \tag{3.4}$$

for the potentials in the air (Ψ_a) and inside the particle (Ψ_n). At the interfaces between the particle and air as well as between the particle and water, the change in the normal component of the electric displacement field equals the fixed surface charge density [114]. At the air-exposed surface A_a of the particle this reads

$$\varepsilon_a\left(\frac{\partial\Psi_a}{\partial N}\right)_{A_a} - \varepsilon_n\left(\frac{\partial\Psi_n}{\partial N}\right)_{A_a} = -4\pi l_B\frac{\sigma_a}{e}, \tag{3.5}$$

and similarly for the water-exposed surface A_w of the nanoparticle

$$\varepsilon_w\left(\frac{\partial\Psi_w}{\partial N}\right)_{A_w} - \varepsilon_n\left(\frac{\partial\Psi_n}{\partial N}\right)_{A_w} = -4\pi l_B\frac{\sigma_w}{e}, \tag{3.6}$$

where $\partial/\partial N$ denotes the derivative in the normal direction of the particle, pointing away from the particle's

interior. In the present work we assume the Debye screening length l_D is much smaller than the radius of curvature at any point of the particle. For example, a salt concentration of 1 mM gives rise to $l_D \approx 10\,\text{nm}$ so that we would assume $R \gg 10\,\text{nm}$ for a spherical nanoparticle of radius R. Generally, the assumption $R \gg l_D$ renders the solution of the Poisson-Boltzmann equation in the aqueous medium sufficiently close to that of a planar extended surface, allowing us to carry out the first integration [36]

$$\frac{\partial \Psi_w}{\partial N} = -\frac{2}{l_D} \sinh\left(\frac{\Psi_w - \Psi_w^{(b)}}{2}\right). \tag{3.7}$$

Eq. 3.7 is valid everywhere in the aqueous medium; when applying it to the water-exposed surface of the particle and using the continuity condition $\Psi_w|_{A_w} = \Psi_n|_{A_w}$, Eq. 3.6 reads

$$\varepsilon_w \frac{2}{l_D} \sinh\left(\frac{\Psi_n|_{A_w} - \Psi_w^{(b)}}{2}\right) + \varepsilon_n \left(\frac{\partial \Psi_n}{\partial N}\right)_{A_w} = 4\pi l_B \frac{\sigma_w}{e}. \tag{3.8}$$

Eq. 3.8 will serve us as one of the boundary conditions for solving the Laplace equation inside the particle.

Due to the presence of salt and the large dielectric constant of water it is a reasonable approximation to treat the aqueous solution as a perfect conductor, implying the condition $\Psi_a = 0$ at the air-water interface.

We also wish to calculate the electrostatic free energy. To this end, we insert the distributions for $n_\pm$ from Eq. 3.2 into Eq. 3.1, and then re-express F_{el} exclusively in terms of the particle's surface potentials using the Poisson-Boltzmann equation (Eq. 3.3) and the Laplace equations (Eq. 3.4) as well as the boundary conditions Eqs. 3.5 and 3.8,

$$\begin{aligned} \frac{F_{el}}{k_B T} &= \frac{1}{2e}\left[\int_{A_a} do\, \Psi_a \sigma_a + \int_{A_w} do\, \Psi_w \sigma_w\right] - \frac{\varepsilon_w}{8\pi l_B l_D} \int_{A_w} do \left[8 \cosh\left(\frac{\Psi_w - \Psi_w^{(b)}}{2}\right) - 8\right. \\ &- \left. 2\Psi_w \sinh\left(\frac{\Psi_w - \Psi_w^{(b)}}{2}\right)\right]. \end{aligned} \tag{3.9}$$

Here, the first integration runs over the particle's air-exposed surface region (A_a), and the second and third integrations run over the particle's water-exposed surface region (A_w).

The electrostatic problem is now fully defined; we need to solve the two Laplace equations in Eqs. 3.4, each in a medium with uniform but different dielectric constant, subject to the boundary conditions in Eqs. 3.5 and 3.8 (the latter one being nonlinear), and $\Psi_a = 0$ at both the air-water interface and at very large distance away from the particle. Once the potential at the surface of the particle is known, we may calculate

the corresponding electrostatic free energy using Eq. 3.9. In order to find explicit solutions for the potential we need to specify the shape of the particle. We will focus on a spherical particle of radius R that partitions equatorially to the air-water interface. However, prior to considering the spherical geometry explicitly, we investigate a planar capacitor-like geometry that serves us as an approximation for the spherical geometry and allows to compute simple analytical solutions for the potential.

3.2.1. Planar Capacitor Approximation

As we shall demonstrate in the Results and Discussion section, the planar capacitor displayed in Fig. 3.2 reproduces the electrostatic properties of a spherical, interface-trapped particle reasonably well.

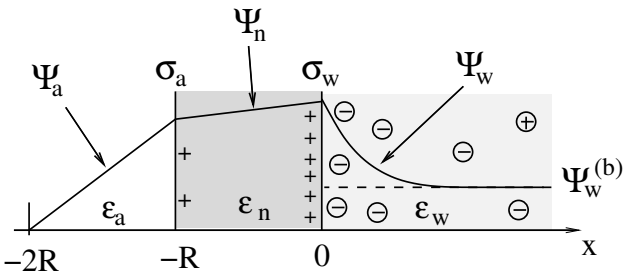

Figure 3.2. Illustration of the planar capacitor model that serves us as an approximation for a spherical particle of radius R. Three regions, air (for $-2R < x < -R$, with dielectric constant ε_a and dimensionless potential Ψ_a), the inside of the particle (for $-R < x < 0$, with dielectric constant ε_n and dimensionless potential Ψ_n), and water ($x > 0$, with dielectric constant ε_w and dimensionless potential Ψ_w), are separated by two planar surfaces, located at $x = -R$ and $x = 0$, that are oriented normal to the x-axis. The location $x = -2R$ is kept at fixed potential $\Psi_a = 0$, and the two surfaces at constant surface charge density: σ_a, at the surface exposed to the air and σ_w at the surface facing the aqueous medium. The dimensionless electrostatic potential in bulk water (at $x \to \infty$) is denoted by $\Psi_w^{(b)}$ (dashed line).

It consists of two planar surfaces with surface charge densities σ_a and σ_w that enclose a region of dielectric constant ε_n. The capacitor plates are located at positions $x = -R$ and $x = 0$, along the normal direction x. The region $x > 0$ models the water phase with its dielectric constant ε_w, whereas the region $-2R < x < -R$ has dielectric constant ε_a and represents the air region. We point out that there are no obvious choices for the linear extensions of the particle and air regions. Our assumptions $-R < x < 0$ and $-2R < x < -R$ both seem convenient but a more detailed model could attempt to further optimize these ranges. We denote the dimensionless electrostatic potential within the air, nanoparticle, and water

by $\Psi_a(x)$, $\Psi_n(x)$, and $\Psi_w(x)$, respectively. For the planar capacitor geometry the Laplace equations (see Eqs. 3.4), $\Psi_a''(x)=0$ and $\Psi_n''(x)=0$, yield the two solutions $\Psi_a(x)=\Psi_0^{(a)}(2+x/R)$ and $\Psi_n(x)=\Psi_0^{(a)}+(\Psi_0^{(w)}-\Psi_0^{(a)})(1+x/R)$, written in terms of the yet unknown surface potentials, $\Psi_0^{(a)}=\Psi_a(-R)=\Psi_n(-R)$ and $\Psi_0^{(w)}=\Psi_n(0)=\Psi_w(0)$, and fulfilling the condition $\Psi_a(-2R)=0$. It is convenient to define the two coupling parameters

$$H^a=\frac{\varepsilon_a l_D}{\varepsilon_w R}, \qquad\qquad H^n=\frac{\varepsilon_n l_D}{\varepsilon_w R}, \tag{3.10}$$

and express the surface charge densities σ_a and σ_w in terms of the dimensionless quantities

$$\bar{\sigma}_a=\frac{4\pi l_B l_D}{\varepsilon_w}\,\frac{\sigma_a}{e}, \qquad\qquad \bar{\sigma}_w=\frac{4\pi l_B l_D}{\varepsilon_w}\,\frac{\sigma_w}{e}. \tag{3.11}$$

Eqs. 3.5 and 3.8 then read for the planar capacitor model

$$\begin{aligned} H^a\Psi_a'(-R)-H^n\Psi_n'(-R) &= \frac{\bar{\sigma}_a}{R}, \\ \frac{2}{R}\sinh\left(\frac{\Psi_n(0)-\Psi_w^{(b)}}{2}\right)+H^n\Psi_n'(0) &= \frac{\bar{\sigma}_w}{R}. \end{aligned} \tag{3.12}$$

Upon inserting the potentials $\Psi_a(x)$ and $\Psi_n(x)$ we obtain two algebraic equations for the two surface potentials

$$\begin{aligned} H^a\Psi_0^{(a)}-H^n\left(\Psi_0^{(w)}-\Psi_0^{(a)}\right) &= \bar{\sigma}_a, \\ 2\sinh\left(\frac{\Psi_0^{(w)}-\Psi_w^{(b)}}{2}\right)+H^n\left(\Psi_0^{(w)}-\Psi_0^{(a)}\right) &= \bar{\sigma}_w. \end{aligned} \tag{3.13}$$

Note that for $H^n=0$ the air and water regions decouple and we immediately obtain

$$\Psi_0^{(w)}(H^n=0)=\Psi_w^{(b)}+2\left(\frac{\bar{\sigma}_w}{2}\right) \tag{3.14}$$

for the surface potential at the water-exposed plate. For $H^n \ll 1$ (that is, $\varepsilon_n l_D \ll \varepsilon_w R$) we can expand $\Psi_0^{(w)}=\Psi_0^{(w)}(H^n=0)+H^n\triangle\Psi_0^{(w)}$ up to linear order in H^n and thus re-express Eqs. 3.13 as a linear system

in terms of $\Psi_0^{(a)}$ and $\triangle\Psi_0^{(w)}$. The solution yields explicit relations for the two surface potentials

$$\begin{aligned}\Psi_0^{(w)} &= \frac{(H^a+H^n)\,q\left[\Psi_w^{(b)}+2\left(\frac{\bar{\sigma}_w}{2}\right)\right]+H^n\bar{\sigma}_a}{(H^a+H^n)\,q+H^aH^n},\\ \Psi_0^{(a)} &= \frac{H^n\,q\left[\Psi_w^{(b)}+2\left(\frac{\bar{\sigma}_w}{2}\right)\right]+(H^n+q)\bar{\sigma}_a}{(H^a+H^n)\,q+H^aH^n},\end{aligned} \tag{3.15}$$

where we have defined $q=\sqrt{1+\bar{\sigma}_w^2/4}$.

We are interested in the apparent surface charge density σ_a^{app} of the particle as observed from the air. We define σ_a^{app} as the surface charge density at the air-exposed region of the particle that preserves the electric field in the air while imposing $\varepsilon_n=0$. Similar to Eq. 3.11, we define a dimensionless apparent charge density $\bar{\sigma}_a^{app}=4\pi l_B l_D\sigma_a^{app}/(e\varepsilon_w)$, which we can compute according to Eq. 3.12 through $\bar{\sigma}_a^{app}=\bar{\sigma}_a+H^nR\Psi_n'(-R)$, or equivalently using Eq. 3.13, $\bar{\sigma}_a^{app}=H^a\Psi_0^{(a)}$. Hence, the surface potential at the air-exposed region of the nanoparticle determines the apparent surface charge density (in units of the elementary charge e)

$$\frac{\sigma_a^{app}}{e}=\frac{\varepsilon_a}{4\pi l_B R}\,\frac{H^n\,q\left[\Psi_w^{(b)}+2\left(\frac{\bar{\sigma}_w}{2}\right)\right]+(H^n+q)\bar{\sigma}_a}{(H^a+H^n)\,q+H^aH^n}. \tag{3.16}$$

Of course, for $H^n=0$ we recover $\sigma_a^{app}=\sigma_a$. Also, in the limit of large surface charge density at the water-exposed surface, $\bar{\sigma}_w\gg 1$, we obtain

$$\frac{\sigma_a^{app}}{e}=\frac{\frac{\sigma_a}{e}+\frac{\varepsilon_n}{4\pi l_B R}\left[\Psi_w^{(b)}+2\ln\left(\bar{\sigma}_w\right)\right]}{1+\frac{\varepsilon_n}{\varepsilon_a}}, \tag{3.17}$$

which exhibits additivity of the contributions from the bare surface charge density σ_a and from the field due to both the charges that face the aqueous medium and the potential difference $\Psi_w^{(b)}$ across the air-water surface. Moreover, if in addition we demand $\Psi_w^{(b)}=0$, $\bar{\sigma}_a=0$, and $\varepsilon_n=\varepsilon_a$, Eq. 3.16 reduces to $\sigma_a^{app}=\varepsilon_a\ln(\bar{\sigma}_w)/(4\pi l_B R)$, which is smaller by a factor of four than the prediction for the renormalized surface charge density at the particle-air interface that Oettel and Dietrich [100] have derived.

We note that the surface potentials in Eqs. 3.15 become an exact solution of Eqs. 3.13 if the scaled surface charge density $\bar{\sigma}_w\ll 1$ is sufficiently small. This case corresponds to the linear Debye-Hückel limit

of Poisson-Boltzmann theory, leading to

$$\begin{aligned}\Psi_0^{(w)} &= \frac{(H^a+H^n)\left(\Psi_w^{(b)}+\bar{\sigma}_w\right)+H^n\bar{\sigma}_a}{(H^a+H^n)+H^aH^n},\\ \Psi_0^{(a)} &= \frac{H^n\left(\Psi_w^{(b)}+\bar{\sigma}_w\right)+(H^n+1)\bar{\sigma}_a}{(H^a+H^n)+H^aH^n},\end{aligned} \tag{3.18}$$

and thus

$$\frac{\sigma_a^{app}}{e} = \frac{\varepsilon_a}{4\pi l_B R}\,\frac{H^n\left(\Psi_w^{(b)}+\bar{\sigma}_w\right)+(H^n+1)\bar{\sigma}_a}{(H^a+H^n)+H^aH^n}. \tag{3.19}$$

In the Results and Discussion section we will analyze and discuss the behavior of σ_a^{app} as predicted by the planar capacitor approximation.

3.2.2. Spherical Geometry

We now focus on the spherical geometry; that is, a spherical particle of radius R partitioning equatorially to the air-water interface as illustrated in Fig. 3.3. Recall that σ_a and σ_w denote the surface charge densities on the air-exposed and water exposed regions of the particle, respectively. In the following we assume that each of these two surface charge densities is uniform. We also recall that the potentials in the air, Ψ_a, and inside the particle, Ψ_n, fulfill the Laplace equation (see Eqs. 3.4), subject to the boundary conditions in Eqs. 3.5 and 3.8, and $\Psi_a = 0$ at both the air-water interface and at very large distance away from the particle. Due to the spherical geometry and because of the rotational symmetry with respect to an axis through the center of the sphere directed normal to the air-water interface, we can express the solutions for Ψ_a and Ψ_n in terms of Legendre polynomials $P_l(s)$ of order l through

$$\Psi_n(r,s) = \sum_{l=0}^{\infty} A_l P_l(s) r^l, \qquad \Psi_a(r,s) = \sum_{l'=1,3,5,\ldots}^{\infty} \frac{B_l P_l(s)}{r^{l+1}}, \tag{3.20}$$

where r is the distance to the center of the particle, $s = \cos\theta$ is the cosine of the angle with respect to the direction normal to the air-water interface, and A_l and B_l are yet to be determined sets of constants. Note that $\Psi_n(r,s)$ is defined for $0 \le r \le R$ and $-1 \le s \le 1$. Similarly, $\Psi_a(r,s)$ is defined for $r \ge R$ and $0 \le s \le 1$. Because we require the potential at the air-water interface $\Psi_a(r > R, s = 0) = 0$ to vanish, the sum in Eq. 3.20 runs only over uneven Legendre polynomials. Continuity $\Psi_a(R,s) = \Psi_n(R,s)$ at the air-exposed region of

the particle, i.e. for $0 \leq s \leq 1$, must allow us to express the coefficients A_l and B_l in terms of a single set of coefficients that we denote by C_l. Indeed continuity is ensured by choosing

$$\begin{aligned} A_l &= \frac{C_l}{R^l}, \\ B_l &= R^{l+1}(2l+1)\sum_{l'=0}^{\infty} C_{l'} g_{l'l}, \end{aligned} \tag{3.21}$$

where the numbers

$$g_{mn} = \int_0^1 ds\, P_m(s) P_n(s) \tag{3.22}$$

are defined for any combination of non-negative integers m and n. The integral in Eq. 3.22 yields [115]

$$g_{mn} = \begin{cases} 1/(2n+1) & m = n \\ 0 & m \neq n \quad \text{and } m+n \text{ even} \\ \bar{g}_{mn} & m \text{ even and } n \text{ odd} \\ \bar{g}_{nm} & n \text{ even and } m \text{ odd} \end{cases}$$

with

$$\bar{g}_{mn} = \frac{(-1)^{\frac{m+n+1}{2}}\, m!\, n!}{2^{m+n-1}(m-n)(m+n+1)\left[\left(\frac{m}{2}\right)!\right]^2\left[\left(\frac{n-1}{2}\right)!\right]^2}, \tag{3.23}$$

where m is an even and n an odd integer. The coefficients C_l in Eqs. 3.21 appear in an expansion of the dimensionless surface potential $\Psi_0(s) = \Psi_a(R,s) = \Psi_n(R,s)$ in terms of Legendre polynomials, $\Psi_0(s) = \sum_{l=0}^{\infty} C_l P_l(s)$ with $-1 \leq s \leq 1$.

In order to determine the coefficients C_l, which contain all the information needed to specify the electrostatic potential everywhere, we proceed as for the planar capacitor approximation (see the preceding section 3.1) by expanding the surface potential at the water-exposed region of the particle in terms of H^n up to first order. The two boundary conditions in Eqs. 3.5 and 3.8 then read

$$\begin{aligned} H^a \left(\frac{\partial \Psi_a}{\partial r}\right)_{r=R} - H^n \left(\frac{\partial \Psi_n}{\partial r}\right)_{r=R} &= -\frac{\bar{\sigma}_a}{R}, \\ \frac{q}{R}\left[\Psi_0(s) - \Psi_w^{(b)} - 2\left(\frac{\bar{\sigma}_w}{2}\right)\right] &= -H^n \left(\frac{\partial \Psi_n}{\partial r}\right)_{r=R}, \end{aligned} \tag{3.24}$$

where we have used the definitions in Eqs. 3.10 and 3.11 for H^n, H^a, $\bar{\sigma}_n$ and $\bar{\sigma}_a$. Also, $q = \sqrt{1 + \bar{\sigma}_w^2/4}$ as

previously defined. We point out that the first and second line in Eqs. 3.24 apply to $0 \leq s \leq 1$ and $-1 \leq s \leq 0$, respectively. Because Eqs. 3.24 are linear in the dimensionless potentials, we can use $\Psi_n(r,s)$ and $\Psi_a(r,s)$ from Eq. 3.20 together with the coefficients in Eq. 3.21 to extract the following linear system of equations

$$\begin{aligned} 0 &= -\bar{\sigma}_a g_l - (-1)^l g_l q \left[\Psi_w^{(b)} + 2\left(\frac{\bar{\sigma}_w}{2}\right)\right] + H^n \frac{2l}{2l+1} C_l + q \sum_{l'=0}^{\infty} C_{l'} (-1)^{l'+l} g_{l'l} \\ &+ H^a \sum_{l'=1,3,5,\ldots}^{\infty} (l'+1)(2l'+1) g_{l'l} \sum_{l''=0}^{\infty} g_{l'l''} C_{l''} \end{aligned} \tag{3.25}$$

for the coefficients C_l with $l = 0, 1, 2, \ldots$. In Eq. 3.25 we have introduced the definition $g_m = \int_0^1 ds\, P_m(s)$ for any non-negative integer m, which amounts to [115]

$$g_m = \begin{cases} 1 & m = 0 \\ 0 & m \neq 0 \quad \text{and } m \text{ even} \\ (-1)^{\frac{m-1}{2}} \frac{m!!}{m(m+1)(m-1)!!} & m \text{ odd.} \end{cases}$$

To derive Eq. 3.25 we have also used orthogonality $\int_{-1}^{1} P_m(x) P_m(x) dx = \delta_{mn} 2/(2m+1)$, where δ_{mn} denotes the Kronecker delta, and symmetry $\int_{-1}^{0} P_m(x) dx = (-1)^m \int_0^1 P_m(x) dx$ of the Legendre polynomials.

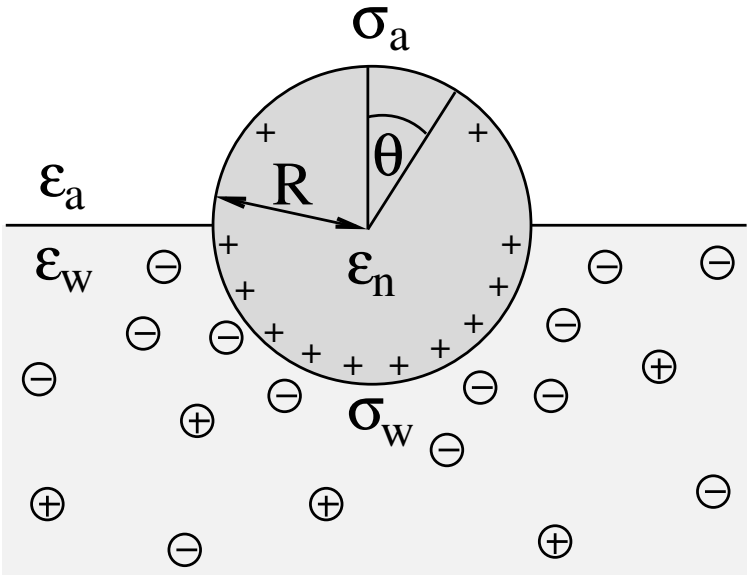

Figure 3.3. The same system as illustrated in Fig. 3.1 but for a spherical particle of radius R that partitions equatorially to the air-water interface; θ is the polar angle measured with respect to the normal direction as indicated.

Solutions of Eq. 3.25 can be found numerically for a finite set of coefficients C_l with $l = 0, 1, 2, \ldots, l_{max}$. The choice of l_{max} will determine the accuracy of the electrostatic potential. We will determine l_{max} such that the free energy $F_{el} = F_{el}(l_{max})$, calculated on the basis of the surface potential $\Psi_0(s) = \sum_{l=0}^{l_{max}} C_l P_l(s)$, converges to $F_{el}(l_{max} \to \infty)$ up to a certain numerical accuracy. Recall that F_{el} is fully determined by the surface potential; see Eq. 3.9. For spherical particle geometry, Eq. 3.9 reads

$$\begin{aligned}
\frac{F_{el}}{2\pi R^2 k_B T} &= \frac{1}{2e}\left[\sigma_a \int_0^1 ds\, \Psi_0(s) + \sigma_w \int_{-1}^0 ds\, \Psi_0(s)\right] \\
&- \frac{\varepsilon_w}{8\pi l_B l_D} \int_{-1}^1 ds \left[-8 + 8\cosh\left(\frac{\Psi_0(s) - \Psi_w^{(b)}}{2}\right)\right. \\
&- \left. 2\Psi_0(s)\sinh\left(\frac{\Psi_0(s) - \Psi_w^{(b)}}{2}\right)\right].
\end{aligned} \tag{3.26}$$

We finally investigate the linearized Debye-Hückel limit, valid if the dimensionless potential in the aqueous phase, measured with respect to the bulk, is sufficiently small, $|\Psi_w - \Psi_w^{(0)}| \ll 1$. In this case $q = 1$ and $2(\bar{\sigma}_w/2) = \bar{\sigma}_w$, and the system of equations, Eq. 3.25, reads

$$\begin{aligned}
0 &= -g_l\left[\bar{\sigma}_a + (-1)^l\left(\Psi_w^{(b)} + \bar{\sigma}_w\right)\right] \\
&+ H^n \frac{2l}{2l+1} C_l + \sum_{l'=0}^{\infty} C_{l'}(-1)^{l'+l} g_{l'l} \\
&+ H^a \sum_{l'=1,3,5,\ldots}^{\infty} (l'+1)(2l'+1) g_{l'l} \sum_{l''=0}^{\infty} g_{l'l''} C_{l''}.
\end{aligned} \tag{3.27}$$

The electrostatic free energy in the linearized Debye-Hückel limit becomes

$$\begin{aligned}
\frac{F_{el}}{2\pi R^2 k_B T} &= \frac{1}{2e}\left[\sigma_a \int_0^1 ds\, \Psi_0(s) + \sigma_w \int_{-1}^0 ds\, \Psi_0(s)\right] \\
&- \frac{\varepsilon_w}{8\pi l_B l_D} \int_{-1}^1 ds\, \Psi_w^{(b)}\left[\Psi_w^{(b)} - \Psi_0(s)\right].
\end{aligned} \tag{3.28}$$

3.3. Results and Discussion

We consider a spherical particle of radius $R = 50\,\text{nm}$, immersed at the interface between air (with dielectric constant $\varepsilon_a = 1$) and water (with dielectric constant $\varepsilon_w = 80$); see Fig. 3.3. We first compute the electrostatic free energy F_{el}, as specified in Eq. 3.26, as function of the number of coefficients l_{max} that are used to numerically solve the linear system in Eq. 3.25. Fig. 3.4 displays the free energy difference $\triangle F_{el}(\varepsilon_n, l_{max}) = F_{el}(\varepsilon_n, l_{max}) - F_{el}(\varepsilon_n = 5, l_{max} = 70)$ as function of l_{max} for a particle with representative surface charge densities of $\sigma_a = 3.2\,nC/\text{cm}^2$ and $\sigma_w = 3.2\,\mu C/\text{cm}^2$. Note that $3.2\,\mu C/\text{cm}^2$ corresponds to $0.2\,e/\text{nm}^2$. We have also chosen a Debye screening length $l_D = 5\,\text{nm}$ (which corresponds to a 4 mM concentration of monovalent salt cations and anions in the bulk), and a reference potential $\Psi_w^{(b)} = 0$ in the aqueous phase. The three different curves refer to the dielectric constants of $\varepsilon_n = 0$ (top), $\varepsilon_n = 2$ (middle), and $\varepsilon_n = 5$ (bottom) inside the spherical particle.

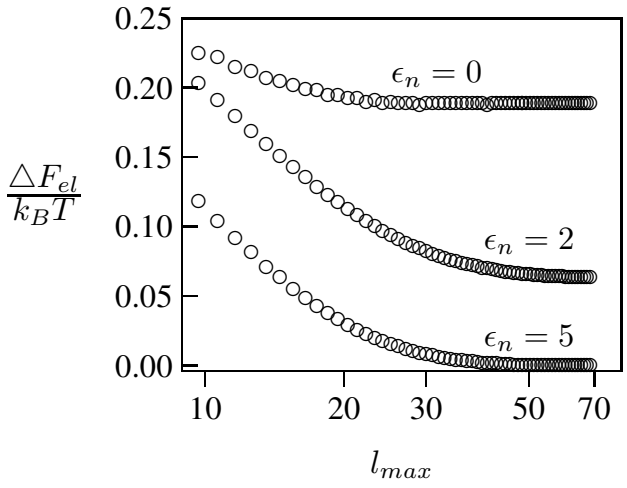

Figure 3.4. Electrostatic free energy difference $\triangle F_{el}(\varepsilon_n, l_{max}) = F_{el}(\varepsilon_n, l_{max}) - F_{el}(\varepsilon_n = 5, l_{max} = 70)$ as function of the number of coefficients l_{max} for a spherical particle of radius $R = 50\,\text{nm}$ with uniform surface charge densities $\sigma_a = 3.2\,nC/\text{cm}^2 = 0.0002e/\text{nm}^2$ at the air-exposed region and $\sigma_w = 3.2\,\mu C/\text{cm}^2 = 0.2e/\text{nm}^2$ at the water-exposed region. The three different curves refer to $\varepsilon_n = 0$ (top), $\varepsilon_n = 2$ (middle), and $\varepsilon_n = 5$ (bottom). The Debye screening length is $l_D = 5\text{nm}$.

Clearly, in the hypothetical limit of $\varepsilon_n = 0$ the inside of the particle becomes impenetrable to the electric field; this renders the electrostatic properties of the air-exposed and water-exposed regions of the particle independent from each other. Increasing ε_n allows the electric field to enter the particle and thus

decreases the free energy. The free energy also decreases with l_{max} because each C_l adds a degree of freedom to the system. Most importantly, $F_{el}(l_{max})$ converges to a fixed constant (within the thickness of the printed symbol) for a value of l_{max} smaller than about 70. Consequently, we have carried out all our calculations for $l_{max} = 70$. That is, we have solved Eq. 3.25 (in the nonlinear regime) and Eq. 3.27 (in the linear regime) for $l = 0 \ldots 70$, yielding the dimensionless surface potential $\Psi_0(s) = \sum_{l=0}^{70} C_l P_l(s)$ and thus, using Eqs. 3.21, the dimensionless potentials $\Psi_n(r,s) = \sum_{l=0}^{70} A_l P_l(s) r^l$ (with $r \le R$ and $-1 \le s \le 1$) inside the spherical particle and $\Psi_a(r,s) = \sum_{l=1,3,5,\ldots}^{69} B_l P_l(s)/r^{l+1}$ (with $r \ge R$ and $0 \le s \le 1$) in the air.

The main objective of the present work is to predict the apparent charge of the spherical particle on its air-exposed region. In addition to the bare charge, this renormalized charge contains a contribution from the electric field that penetrates through the particle's interior and determines the salt dependence of the long-ranged dipolar interactions among interface-trapped particles. For the planar capacitor approximation we have already defined in Eq. 3.16 the apparent surface charge density σ_a^{app}. In a similar manner we define the average apparent surface charge density

$$\sigma_a^{app} = -\frac{\varepsilon_a}{4\pi l_B} \int_0^1 ds \left(\frac{\partial \Psi_a(r,s)}{\partial r} \right)_{r=R} \tag{3.29}$$

of the air-exposed region for a spherical particle. Equivalently, we refer to $Q_a^{app} = 2\pi R^2 \sigma_a^{app}$ as the apparent total charge that the particle carries at its air-exposed region. With our particle radius $R = 50\,\mathrm{nm}$ this can be re-expressed as

$$\frac{Q_a^{app}}{e} = 0.98 \, \frac{\sigma_a^{app}}{\mathrm{nC\,cm^{-2}}}. \tag{3.30}$$

Hence, when measured in units of $\mathrm{nC/cm^2}$, the numerical value of σ_a^{app} is almost identical to the total number of elementary charges that appear to be attached to the air-exposed region of the $R = 50$ nm particle.

Fig. 3.5 shows two contour plots of the dimensionless electrostatic potential, calculated for particle radius $R = 50\,\mathrm{nm}$, Debye length $l_D = 5\,\mathrm{nm}$, surface charge density at the water-exposed region of the particle $\sigma_w = 3.2\,\mu\mathrm{C/cm^2} = 0.2\,e/\mathrm{nm^2}$, dielectric constant inside the particle $\varepsilon_n = 2$, and $\Psi_w^{(b)} = 0$.

The two diagrams are computed for surface charge densities at the air-exposed particle region $\sigma_a = 0$ (left) and $\sigma_a = 3.2\,\mathrm{nC/cm^2} = 0.0002\,e/\mathrm{nm^2}$ (right). At the water-exposed region, both particles possess an almost identical constant potential of $\Psi_0(s) = 4.36$, which is slightly smaller than the prediction from the Poisson-Boltzmann model for a planar isolated surface $\Psi_0(s) = \Psi_w^{(b)} + 2(\bar{\sigma}_w/2) = 4.37$ (the close proximity

is expected and, in fact, was our motivation for the expansion of the surface potential with respect to H^n, employed in the derivations of Eqs. 3.24 and 3.25). At the air-exposed surface, however, $\Psi_0(s)$ adopts a minimum at $s = 1$ when $\sigma_a = 0$ (left), whereas it adopts a maximum at $s = 1$ when $\sigma_a = 3.2\,\mathrm{nC/cm^2}$ (right). These differences result from the interplay between the charges attached to the water-exposed and air-exposed faces of the particle and the vanishing potential at the air-water interface. This interplay is also reflected in the apparent surface charge densities at the air-exposed region, for which we obtain according to Eq. 3.29 $\sigma_a^{app} = 3.6\,\mathrm{nC/cm^2}$ (left) and $\sigma_a^{app} = 5.9\,\mathrm{nC/cm^2}$ (right). We can thus state that, according to Eq. 3.30, the ≈ 3200 charges attached to the water-exposed region of the particle cause an increase in the number of apparent charges on the air-exposed particle region from zero to 3.6 for the left diagram in Fig. 3.5 and from 3.2 to 5.9 for the right diagram in Fig. 3.5. Of course, an isolated consideration of the two arbitrarily selected systems in Fig. 3.5 does not yield a systematic understanding of the relation between σ_a and σ_a^{app}. In the following we provide a more comprehensive analysis.

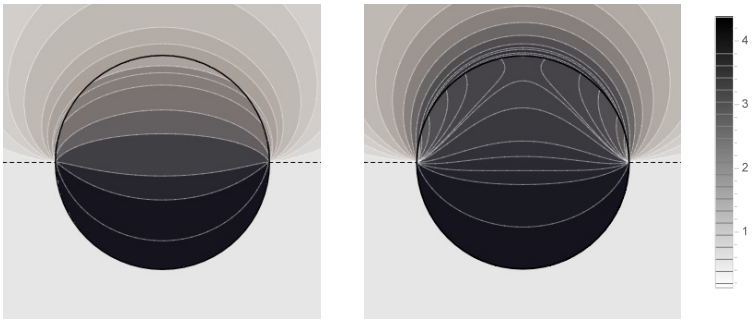

Figure 3.5. Contour plots of the dimensionless electrostatic potential, calculated for $\sigma_a = 0$ (left) and $\sigma_a = 3.2\,\mathrm{nC/cm^2} = 0.0002\,e/\mathrm{nm^2}$ (right). Both plots are computed for a particle radius $R = 50\,\mathrm{nm}$, Debye length $l_D = 5\,\mathrm{nm}$, surface charge density at the water-exposed region of the particle $\sigma_w = 3.2\,\mu\mathrm{C/cm^2} = 0.2\,e/\mathrm{nm^2}$, dielectric constant inside the particle $\varepsilon_n = 2$, and vanishing potential difference $\Psi_w^{(b)} = 0$ between bulk water and air. Darker shading corresponds to a more positive dimensionless potential Ψ as marked in the legend.

In Fig. 3.6 we show the results of a detailed analysis of σ_a^{app} as function of ε_n for eleven different choices of σ_a in each diagram. All results in Fig. 3.6 refer to a Debye screening length $l_D = 5\,\mathrm{nm}$ (that is, a 4 mM salt concentration in the aqueous medium). Each diagram corresponds to a specific combination of σ_w and $\Psi_w^{(b)}$, with $\sigma_w = 0$ in the left column and $\sigma_w = 3.2\,\mu\mathrm{C/cm^2}$ in the right column, as well as $\Psi_w^{(b)} = -2$ in the upper row of diagrams, $\Psi_w^{(b)} = 0$ in the middle row, and $\Psi_w^{(b)} = +2$ in the bottom row. All solid lines refer to calculations based on the nonlinear Poisson-Boltzmann model; see Eq. 3.25. The dashed

lines, visible only in the right column of diagrams are computed for the linearized Debye-Hückel model; see Eqs. 3.27. On the left column of diagrams, the dashed lines coincide with the solid lines and are thus not visible individually. In the limit $\varepsilon_n = 0$ there is no interaction between the air- and water-exposed regions of the particle, implying $\sigma_a^{app} = \sigma_a$. Hence, the value of σ_a for which each curve in Fig. 3.6 is derived corresponds to the value of σ_a^{app} at $\varepsilon_n = 0$. Note also that the two specific systems represented in Fig. 3.5 are marked in Fig. 3.6 by the symbol •.

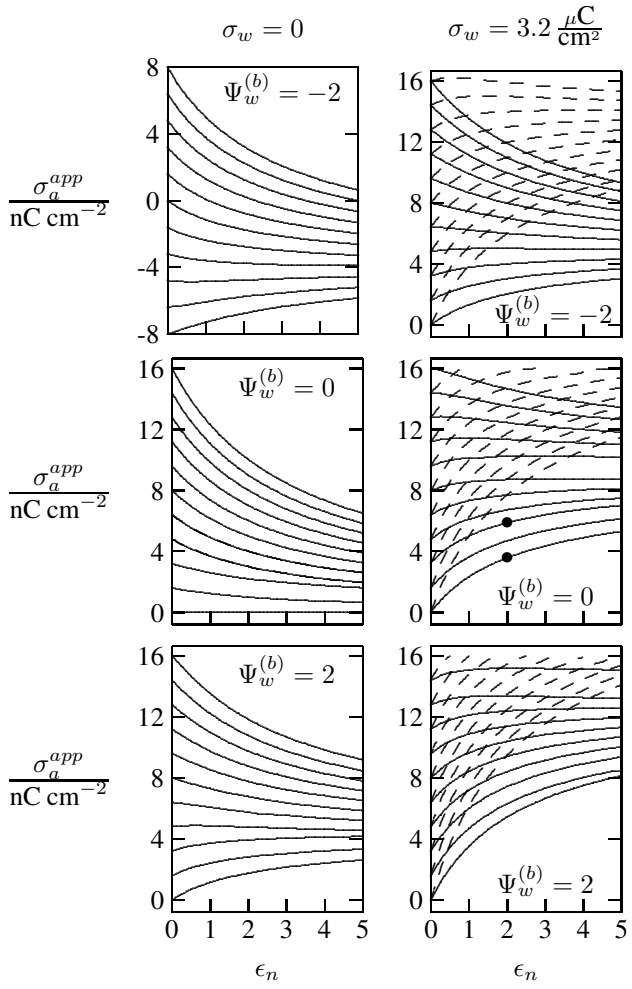

Figure 3.6. Apparent charge density σ_a^{app} at the air-exposed surface of a spherical particle as function of the particle's dielectric constant ε_n. Solid and dashed lines correspond, respectively, to results in the nonlinear Poisson-Boltzmann and the linear Debye-Hückel regimes. Different curves in each diagram refer to different $\sigma_a = \sigma_a^{app}(\varepsilon_n = 0)$. The two columns of diagrams are computed for $\sigma_w = 0$ (left) and $\sigma_w = 3.2\,\mu C/cm^2$ (right); The three rows refer to $\Psi_w^{(b)} = -2$ (top), $\Psi_w^{(b)} = 0$ (middle), and $\Psi_w^{(b)} = 2$ (bottom). All results are derived for $R = 50\,nm$ and $l_D = 5nm$. The two bullets in the middle-right diagram refer to the contour plots displayed in Fig. 3.5.

Let us now discuss the findings in Fig. 3.6. Consider first the middle diagram on the left column, derived for $\sigma_w = 0$ and $\Psi_w^{(b)} = 0$. For $\sigma_a = 0$ the particle is completely uncharged, the potential is zero everywhere, and thus $\sigma_a^{app} = 0$ for any choice of ε_n. For $\sigma_a > 0$ the apparent value σ_a^{app} decreases with growing ε_n because a part of the electric field propagates through the inside of the particle and interacts with negative charges in the aqueous solution that are polarized at the water-exposed region of the particle. This is more favorable than passing exclusively through the air and interacting with negative charges in the aqueous solution that are polarized at the air-water interface. We note that the ratio σ_a^{app}/σ_a reaches 50% roughly at $\varepsilon_n \approx 4$. We also note that the potential inside the aqueous phase, which is only caused by the few charges at the air-exposed region of the particle, is small so that it practically makes no difference to use the linear Debye-Hückel model or the nonlinear Poisson-Boltzmann approach.

Next, we consider the middle diagram on the right column, derived for $\sigma_w = 3.2\,\mu\mathrm{C/cm^2}$ and $\Psi_w^{(b)} = 0$. For $\sigma_a = 0$ all charges carried by the particle (about 3200) are attached to the water-exposed region. These charges are very effectively screened by the mobile salt ions in the aqueous solution, which are present with a bulk concentration of 4 mM. However, as ε_n grows, a small (but increasing) part of the electric field produced by σ_w is able to propagate through the particle interior into the air and thus appears as an apparent charge density σ_a^{app}. For example, at $\varepsilon_n = 2$, we find $\sigma_a^{app} = 3.6\,\mathrm{nC/cm^2}$, corresponding to an apparent number of 3.6 elementary charges attached to the air-exposed particle region. This, in fact is the example already presented in Fig. 3.5 (left diagram) and marked by the lower of the two bullets in the middle-right diagram of Fig. 3.6. Although few in number, these apparent charges are unscreened and thus highly effective in influencing the long-ranged interactions between interface-trapped particles. As σ_a grows, the increase in $\sigma_a^{app}(\varepsilon_n)$ becomes weaker and eventually reverses into a decreasing function. Indeed, with growing σ_a the particle-propagating part of the electric field produced by the air-exposed charges becomes stronger and eventually reverses the direction of the total electric field in the particle interior. The reversal occurs roughly at $\sigma_a = 12\,\mathrm{nC/cm^2}$. At this particular combination of charge densities – about 3200 charges at the water-exposed region and 12 charges at the air-exposed region of the particle – the dielectric constant ε_n becomes practically irrelevant and thus does not affect the interactions between interface-trapped particles. It is one of the central conclusions of the present work that the ability of the electric field to propagate into the particle interior can enhance or diminish the interaction strength of particles at the air-water (and similar for oil-water) interface. That is, already a few air-exposed charges will reverse the direction of the electric field inside the particle and thus qualitatively change the influence of the particle's dielectric constant on the

long-ranged particle-particle interactions.

As pointed out in the Introduction, sign and magnitude of the change in electrostatic potential upon crossing from air into bulk water have received significant attention in recent years [109, 110, 111, 112, 113]. The implications of this potential difference on the electrostatic properties of interface-trapped particles, however, have not been analyzed previously. We have therefore incorporated the presence of an arbitrary bulk potential $\Psi_w^{(b)}$ into our theoretical approach (recall that $\Psi_w^{(b)}$ denotes the difference of the dimensionless electrostatic potential in bulk water and in air, both far away from the air-water interface). Note that we have not introduced an additional change in potential when passing from the interior of the particle into the aqueous medium. In fact, there is no need to introduce such an additional change in potential if we interpret $\Psi_w^{(b)}$ as the difference in the change of the (dimensionless) electrostatic potential at the bare air-water interface and particle-water interface. We do not know the sign and magnitude of $\Psi_w^{(b)}$ but we can analyze its general impact on σ_a^{app}. This is shown in the upper and lower rows of Fig. 3.6 for $\Psi_w^{(b)} = -2$ and $\Psi_w^{(b)} = 2$, respectively. Our motivation to use the specific magnitude $|\Psi_w^{(b)}| = 2$ for the displayed examples goes back to a suggestion of Gehring and Fischer [112]. Yet, we emphasize that the actual value and sign of $\Psi_w^{(b)}$ remain a matter of debate. A negative value of $\Psi_w^{(b)}$ mimics the presence of additional negative charges at the water-exposed region of the particle, implying more negative slope of the function $\sigma_a^{app}(\varepsilon_n)$. This is most clearly seen for the case $\sigma_w = \sigma_a = 0$, where the increase of ε_n from 0 to 2 changes σ_a^{app} from 0 to about $-1.8\,\mathrm{nC/cm^2}$; see the upper-left diagram of Fig. 3.6. Hence, even a completely uncharged particle carries a small apparent negative charge on its air-exposed face. All curves (solid lines) in the two top and two bottom diagrams of Fig. 3.6 can be rationalized by translating a negative or positive bulk potential $\Psi_w^{(b)}$ into, respectively, an additional negative or positive charge at the water-exposed particle region. We add two comments. First, changing the magnitude of $|\Psi_w^{(b)}|$ from 0 to 2 (which corresponds to a change of 50 mV) typically causes Q_a^{app} to adjust by 2-5 elementary charges for a fixed ε_n in the region $2 < \varepsilon_n < 5$. Second, the relation $\sigma_a^{app}(\varepsilon_n)$ can pass through a local maximum (which, however, is not very pronounced). This implies that, perhaps somewhat unexpectedly, the apparent charge Q_a^{app} may be observed to first increase and then decrease as function of increasing ε_n.

We have carried out calculations of σ_a^{app} on the basis of the nonlinear Poisson-Boltzmann model (solid lines in Fig. 3.6) and the linearized Debye-Hückel approximation (dashed lines in Fig. 3.6). For $\sigma_w = 0$ (left column of diagrams in Fig. 3.6) both models yield virtually identical results, but for $\sigma_w = 3.2\,\mu\mathrm{C/cm^2}$ (right column of diagrams in Fig. 3.6) this is no longer the case. Indeed, the surface potential

at the water-exposed region of the particle is only slightly smaller than 4.37, implying that the linearization of the Poisson-Boltzmann equation is a poor approximation and, in fact, overestimates the magnitude of the surface potential [36]. Hence, in the linearized model, we expect the more positive surface potential at the water-exposed particle region to cause a larger σ_a^{app} than the nonlinear model predicts, and this is indeed what we observe in Fig. 3.6. Despite this overestimation, however, the qualitative nature of the results for σ_a^{app} is preserved in the linear Debye-Hückel approximation; this includes the reversal of the slope of the function $\sigma_a^{app}(\varepsilon_n)$ for sufficiently large σ_a as can be observed directly in the top-right diagram of Fig. 3.6 (at about $\sigma_a = 16\,n\mathrm{C}/\mathrm{cm}^2$).

Numerical results like those in Fig. 3.6 are computed for a specific set of parameters, of which some are kept constant and others varied across a small set of discrete values. Analytic expressions offer the advantage of allowing a systematic analysis and hence a clearer understanding of the relationships between parameters. In section 3.1 we have proposed a planar capacitor approximation and derived a simple expression for σ_a^{app}; see Eq. 3.16 (as well as Eq. 3.17 for large σ_w and Eq. 3.19 for small σ_w). Recall that the planar capacitor approximation is based on representing the interface-trapped spherical particle by the geometry of a planar capacitor; see Fig. 3.2. In Fig. 3.7 we present predictions for σ_a^{app} as function of ε_n according to the planar capacitor approximation for exactly the same set of parameters as in Fig. 3.6. Here too, solid lines refer to nonlinear Poisson-Boltzmann theory (calculated using Eq. 3.16), whereas the dashed lines correspond to the linear Debye-Hückel limit (calculated using Eq. 3.19). A comparison of Figs. 3.6 and 3.7 reveals good qualitative agreement. This includes (i) the slope-reversion of σ_a^{app} (that is, σ_a^{app} being a decreasing function for sufficiently large σ_a and an increasing function for sufficiently small σ_a), (ii) the down-shift of the point where the slope-reversion occurs for negative $\Psi_w^{(b)}$ and its up-shift for positive $\Psi_w^{(b)}$, (iii) the excellent agreement between the nonlinear and linear models for $\sigma_w = 0$, and (iv) the overestimation of σ_a^{app} for large σ_w when comparing the linear and nonlinear models. There are also notable differences between Figs. 3.6 and 3.7. First, the dependence of σ_a^{app} on ε_n tends to be stronger in the planar capacitor approximation as compared to the spherical geometry. For example, for $\sigma_w = 0$, $\Psi_w^{(b)} = 0$, $\sigma_a = 16\,\mu\mathrm{C}/\mathrm{cm}^2$, and $\varepsilon_n = 5$ our calculations predict $\sigma_a^{app} = 7\,\mu\mathrm{C}/\mathrm{cm}^2$ for spherical geometry and $\sigma_a^{app} = 3\,\mu\mathrm{C}/\mathrm{cm}^2$ for the planar capacitor approximation. A second difference is the lack of any local maxima of the function $\sigma_a^{app}(\varepsilon_n)$. Instead, at one specific value for σ_a (the slope-reversion point) the function $\sigma_a^{app}(\varepsilon_n)$ becomes independent of ε_n; the corresponding locations are marked by pairs of open circles in Fig. 3.7 (the two pairs of open circles on the diagrams refer to the nonlinear and linear models). From Eq. 3.16 we find the condition

$\sigma_a^{app} = \sigma_a$ to be fulfilled for

$$\begin{aligned} \frac{\sigma_a}{e} &= \frac{\varepsilon_a}{4\pi l_B R}\left[\Psi_w^{(b)} + 2\left(\frac{\bar{\sigma}_w}{2}\right)\right] \\ &= \frac{\varepsilon_a}{4\pi l_B R}\,\Psi_0^{(w)}(H^n = 0). \end{aligned} \tag{3.31}$$

This marks the point where for $\varepsilon_n = 0$ the potential produced by σ_a at the air-exposed surface is equal to the potential produced by σ_w at the water-exposed surface. The electrostatic properties of the air-exposed and water-exposed regions are then decoupled and thus do not depend on ε_n. A similar rationale applies to the slope reversion of spherical particles observed in Fig. 3.6.

As discussed in the Introduction, experimental investigations of how the salt concentration in the aqueous medium affects the observed long-ranged repulsive forces between interface-trapped colloidal particles have not led to conclusive results. A number of studies suggest the interaction is insensitive to the salt concentration [101, 18, 116], while others report a weak dependence [44, 26, 25, 45, 1]. Note that the force between two interface-trapped particles is proportional to the square of the apparent surface charge density σ_a^{app}, which depends on the salt concentration. In Fig. 3.8 we display the dependence of σ_a^{app} on the Debye screening length l_D for spherical particle geometry (left diagrams) and for the planar capacitor approximation (right diagrams).

The two sets of curves in each diagram ($\sigma_a = 0$ for dashed lines in upper diagrams, $\sigma_a = 3.2\,\mathrm{nC/cm^2}$ for solid lines in upper diagrams, $\sigma_a = 16\,\mathrm{nC/cm^2}$ for dashed lines in lower diagrams, and $\sigma_a = 32\,\mathrm{nC/cm^2}$ for solid lines in lower diagrams) refer to $\varepsilon_n = 0$ (symbol $\circ$), $\varepsilon_n = 1$ ($\triangleleft$), $\varepsilon_n = 2$ ($\bullet$), $\varepsilon_n = 5$ ($\triangleright$). We have placed the symbols $\circ$, $\triangleleft$, $\bullet$, $\triangleright$ at the position $l_D = 5\,\mathrm{nm}$, which corresponds to the results in Figs. 3.6 and 3.7. Note that for spherical geometry we only consider Debye lengths up to $l_D = 10\,\mathrm{nm}$ to ensure $l_D \ll R$.

All curves in Figs. 3.8 indicate nondecreasing behavior of σ_a^{app} as function of l_D. That is, adding salt is never predicted to increase the apparent particle charge (yet, it could do so in the hypothetical case that the bare charge densities σ_a and σ_w were of different sign). Let us discuss decreasing the salt concentration from 100 mM ($l_D = 1\,\mathrm{nm}$) to 1 mM ($l_D = 10\,\mathrm{nm}$) for a particle of dielectric constant $\varepsilon_n = 5$. For $\sigma_a = 0$ this induces an increase of σ_a^{app} from $2.0\,\mathrm{nC/cm^2}$ to $7.3\,\mathrm{nC/cm^2}$ and thus a 13.5-fold increase in the force between two particles (the force increase calculated within the planar capacitor approximation is 13.1). For large σ_a the absolute increase in σ_a^{app} is similar but the relative increase in the force is much lower. For example, $\sigma_a = 32\,\mathrm{nC/cm^2}$ leads to an increase in σ_a^{app} from $14.1\,\mathrm{nC/cm^2}$ to $19.5\,\mathrm{nC/cm^2}$, implying a 1.9-

fold increase of the force (and a 1.6-fold increase predicted by the planar capacitor approximation). Because the planar capacitor model makes reasonable predictions, we may insert the parameters used in our specific example into Eq. 3.17 (namely $\sigma_w = 3.2\,\mu\mathrm{C/cm^2}$, $R = 50\,\mathrm{nm}$, $l_B = 56\mathrm{nm}$, $\varepsilon_a = 1$, $\varepsilon_w = 80$, $\varepsilon_n = 5$, and $\Psi_w^{(0)} = 0$), yielding

$$\sigma_a^{app} = c_1\sigma_a + c_2\,\ln(c_3 l_D)\,, \tag{3.32}$$

with $c_1 = 0.17$, $c_2 = 0.75\,\mathrm{nC/cm^2}$, and $c_3 = 1.76/\mathrm{nm}$.

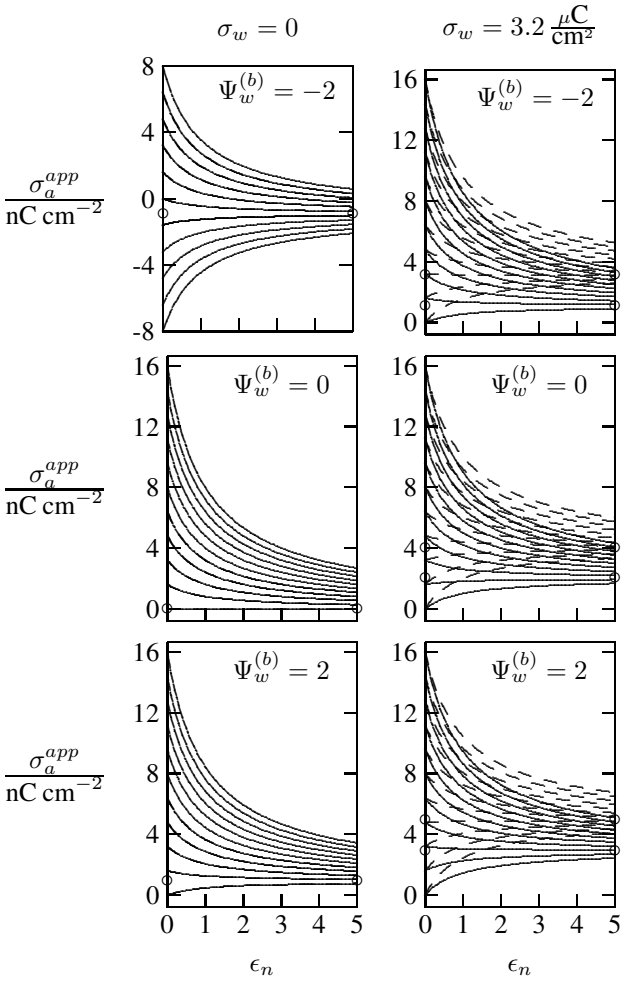

Figure 3.7. Apparent surface charge density σ_a^{app} at the air-exposed surface as function of ε_n according to the planar capacitor approximation, calculated according to Eq. 3.16 (solid lines) on the level of nonlinear Poisson-Boltzmann theory and according to Eq. 3.19 (dashed lines) in the linear Debye-Hückel limit. All results are computed for exactly the same set of parameters as in Fig. 3.6. Specifically, different curves in each diagram refer to different $\sigma_a = \sigma_a^{app}(\varepsilon_n = 0)$. The two columns of diagrams are computed for $\sigma_w = 0$ (left) and $\sigma_w = 3.2\,\mu\mathrm{C/cm^2}$ (right); The three rows refer to $\Psi_w^{(b)} = -2$ (top), $\Psi_w^{(b)} = 0$ (middle), and $\Psi_w^{(b)} = 2$ (bottom). All results are derived for $R = 50\,\mathrm{nm}$ and $l_D = 5\,\mathrm{nm}$.

Such a relation could, in principle, be used to estimate the bare charge density σ_a from the measured salt-dependence of the force between interface-trapped particles.

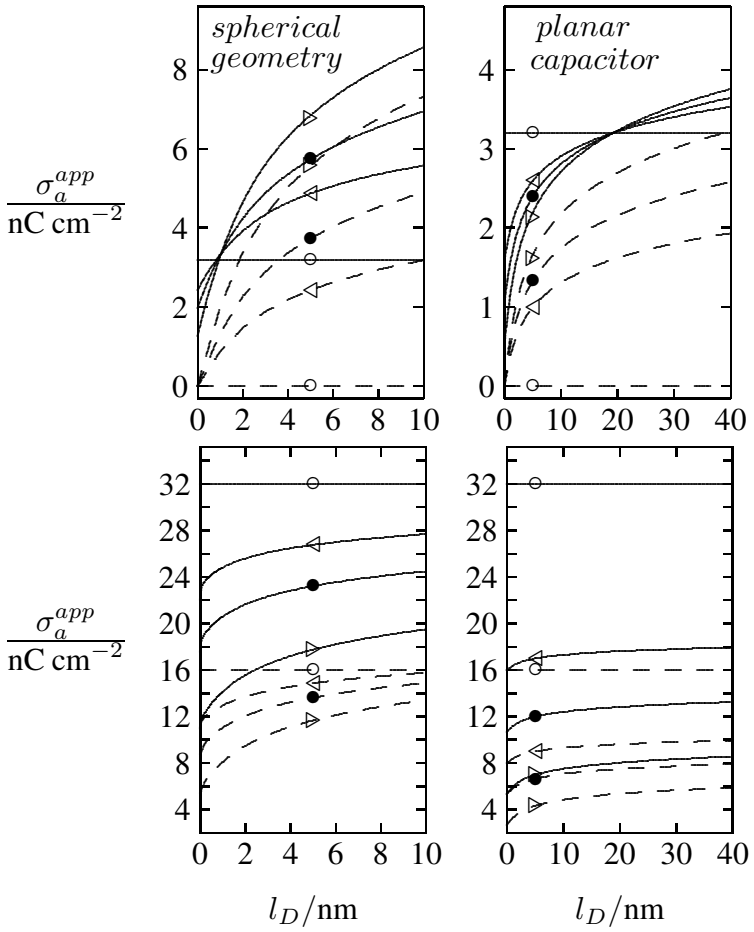

Figure 3.8. Apparent surface charge density σ_a^{app} at the air-exposed particle region as function of the Debye screening length l_D for fixed $\sigma_w = 3.2\,\mu\mathrm{C/cm^2}$, $R = 50\,\mathrm{nm}$, and $\Psi_w^{(b)} = 0$. Dashed and solid lines in the upper two diagrams refer to $\sigma_a = 0$ and $\sigma_a = 3.2\,\mathrm{nC/cm^2}$, respectively. Dashed and solid lines in the lower two diagrams refer to $\sigma_a = 16\,\mathrm{nC/cm^2}$ and $\sigma_a = 32\,\mathrm{nC/cm^2}$, respectively. Left and right diagrams correspond, respectively, to calculations for the spherical geometry (see Section 3.2) and the planar capacitor approximation (see Section 3.1). The four different curves for each set are derived for $\varepsilon_n = 0$ (symbol $\circ$), $\varepsilon_n = 1$ ($\triangleleft$), $\varepsilon_n = 2$ ($\bullet$), $\varepsilon_n = 5$ ($\triangleright$). We have placed the symbols at position $l_D = 5\,\mathrm{nm}$, for which all calculations in Figs. 3.6 and 3.7 were carried out.

To be specific, we attempt to model the salt concentration dependence of the force $F \sim (\sigma_a^{app})^2/r^4$ between charge-stabilized polystyrene particles ($R = 1.5\,\mu\mathrm{m}$, $\varepsilon_n = 2.5$, $\sigma_w = 9.1\,\mu\mathrm{C/cm^2}$) at a decane-water interface ($\varepsilon_a = 2.0$, $\varepsilon_w = 80$) as measured by Park *et al* [1]. For this system we obtain $c_1 = 0.44$, $c_2 = 2.03 \times 10^{-6}\,\mathrm{nC/cm^2}$, and $c_3 = 5.0/\mathrm{nm}$. Decreasing the salt concentration from 1 mM (implying

$l_D^{(1)} = 10$ nm) to 0.01 mM (implying $l_D^{(2)} = 100$ nm) at a particle-to-particle separation of $r = 9\,\mu$m was reported to increase the force from about $F_1 = 0.2$ pN to about $F_2 = 0.6$ pN. Using the dependence of the force F on σ_a^{app} together with Eq. 3.32 yields

$$\sigma_a = \frac{c_2}{c_1} \frac{\sqrt{F_1} \ln\left(c_3 l_D^{(2)}\right) - \sqrt{F_2} \ln\left(c_3 l_D^{(1)}\right)}{\sqrt{F_2} - \sqrt{F_1}} = 0.06 \frac{\text{nC}}{\text{cm}^2}. \tag{3.33}$$

This (very rough) estimate predicts the surface charge density at the oil-exposed region of the particle to be 150,000 times smaller than that at the water-exposed region. This implies the particle carries a total of about 50 elementary charges on its oil-exposed surface.

We finally point out that in Fig. 3.6 we had discussed the possibility of adjusting σ_a to render σ_a^{app} virtually independent of ε_n. Fig. 3.8 reveals that this may also be accomplished by adjusting the salt concentration. For example for $\sigma_a = 3.2\,\text{nC}/\text{cm}^2$ (see the upper left diagram in Fig. 3.8) the solid lines all intersect in a region close to $l_D = 1\,$nm, implying σ_a^{app} does not depend on ε_n. Note that the planar capacitor approximation also predicts such a point, yet fails to correctly predict the corresponding salt concentration.

3.4. Conclusion

This work has studied the electrostatic properties of a spherical nanoparticle with dielectric constant ε_n, trapped at an air-water interface using mean-field electrostatics. Our specific goal was to characterize how the interplay between the electrostatic properties in the aqueous medium and in the air influence each other and may lead to the observed weak salt dependence of long-ranged dipolar forces that stabilize ordered arrays of particles at dielectric interfaces. We have expressed this interplay by introducing an apparent surface charge density σ_a^{app} of the nanoparticle at its air-exposed region. Indeed, the apparent surface charge density is generally different from the bare surface charge density σ_a at the air-exposed region. The difference arises from the ability of the electric field to propagate through the particle interior; this may either enhance or diminish σ_a^{app}, depending on how large the surface charge density σ_w of the particle at its water-exposed region is and how effectively salt ions in the aqueous medium screen these charges. For a particle size of 100 nm with several thousands of charges attached to the water-facing side, decreasing the salt concentration from 100 mM to 1 mM increases the apparent number of elementary charges at the air-exposed region by only a few. Yet, these charges are unscreened and thus very effective in modulating

long-ranged dipolar interactions between particles. If the bare charge density σ_a on the air-exposed face of the particle amounts to not many more than those added apparent charges, a salt dependence should be observable experimentally. In fact the salt dependence may then be used to estimate σ_a in the first place. In order to facilitate calculations, we have introduced a simple planar capacitor approximation that allows to calculate an estimate of σ_a^{app} analytically. Note that our theoretical model makes significant approximations that we have adopted to simplify the mathematical formalism. They include equatorial partitioning of the particle and a constant electrostatic potential at the air-water interface. Note also that we have focused only on electrostatic interactions; capillary forces may further affect interactions between interface-trapped particles if the particles are sufficiently large. In addition, we have ignored ion-specific effects, which have been suggested to modify the salt concentration dependence of the interaction between interfacially trapped colloids [44, 26]. Interface-induced solvent polarization, which may further modulate this dependence [117], is approximately accounted for in our model through $\Psi_w^{(b)}$.

3.5. Acknowledgments

G.V.B. acknowledges a doctoral scholarship from CAPES Founda- tion/Brazil Ministry of Education (Grant No. 9466/13-4).

4. THE DIPOLE MOMENT OF A CHARGED PARTICLE TRAPPED AT THE AIR-WATER INTERFACE *

4.1. Introduction

Understanding the behavior of nanoparticles and colloids at liquid interfaces is not only of fundamental interest with regard to the physics of two-dimensional systems [118, 119, 120], it also is of importance for practical applications such as the stabilization of emulsions and foams [38, 121, 122, 123], for colloidal self-assembly [124, 125], and for electronic and optical devices [126, 127]. Charged particles at the air-water or oil-water interface are subject to long-range dipolar interactions, which can be exploited by forming colloidal arrays of very small surface concentration [128, 101, 45, 26]. The description of the physical properties of such arrays is, however, challenged by the complexity of electrostatic interactions near and across discontinuous dielectric interfaces [17, 129].

More than 50 years ago, Stillinger [42] used the linearized Poisson-Boltzmann approach – also known as Debye-Hückel model [130, 131] – to calculate the interaction free energy between two point charges q that are located at the interface between air and water with dielectric constants $\varepsilon_a = 1$ and $\varepsilon_w = 80$, respectively. The resulting expression was later decomposed by Hurd [43] into two contributions, a screened electrostatic decay that reflects the salt concentration n_0 in the aqueous phase (as expressed by the Debye screening length $l_D \sim n_0^{-2}$) and a dipolar repulsion that is mediated by the presence of the adjacent medium of low dielectric constant. The dipolar repulsion can be expressed in terms of two aligned dipoles that interact in air, each with a dipole moment $\mu = \sqrt{2}\, q\, l_D \varepsilon_a/\varepsilon_w$. Note that Stillinger's model predicts μ to strongly depend of the ambient salt concentration in the aqueous phase. In fact, the dipolar repulsion free energy scales directly with the Debye screening length l_D, with no residual interaction being left in the limit of large salt content, where $l_D \to 0$. However, experiments that have measured the interaction between interface-trapped colloids show diverse dependencies on the salt concentration, ranging from significant [1] over weak

*Reproduced with permission from "G. V. Bossa, K. Bohinc, M. A. Brown, S. May, Dipole moment of a charged particle trapped at the air–water interface, J. Phys. Chem. B 120 (26) (2016) 6278–6285". Copyright 2016 American Chemical Society. This paper can be accessed online at `http://pubs.acs.org/doi/abs/10.1021/acs.jpcb.6b02703`. The material in this chapter was co-authored by Guilherme V. Bossa, Klemen Bohinc, Matthew A. Brown, and Sylvio May. G. V. Bossa contributed to the project design and manuscript writing. G.V.B. was responsible for the mathematical development, numerical and analytical solution of the equations, figures preparation, and discussion of the results.

[18, 1, 26] to the virtual absence of a salt concentration dependence [101]. These different behaviors can be associated with the different charge densities on the air-exposed and water-exposed regions of the trapped particles, the former and latter being responsible for, respectively, the salt-independent [101, 102, 103] and salt-dependent contributions [107] to the dipolar repulsion.

Clearly, the inability of Stillinger's approach to produce different scenarios for the salt concentration dependence of the interaction between interface-trapped particles originates in the simplicity of the model, namely the point-like nature and interfacial position of the involved charges. It is no surprise that a multitude of follow-up modeling approaches have attempted to account in more detail for the spatial structure of the interface-trapped particles and the different charge densities of their air-exposed and water-exposed regions [132, 129, 103], for finite-size counterion effects [44], and for additional capillary forces [102]. These models typically yield numerical results but in some limiting cases, such as that of small distances between the interface-trapped particles [106] or for a multipole expansion of the particles [108], analytic results can emerge. A theoretical approach that extends the analysis of the above-mentioned dipole moment μ to a spatially extended charge distribution has, so far, not been presented.

In the present work we extend Stillinger's model from one single point charge that is attached to the air-water interface to two spatially separated point charges that reside on the different sides of the air-water interface. We propose this model to represent an interface-trapped particle, such as a nanoparticle or colloid, with the water-exposed and air-exposed surface charges of the particle being lumped into the water-immersed and air-immersed point charges, respectively. We seek to characterize the interaction between two particles, especially its residual dipolar component at large particle-to-particle distances. To this end, we numerically analyze the effective dipole moment μ and present a simple approximate expression that describes the dependence of μ on the particle size and salt content.

4.2. Theoretical Model

We consider a pair of two point charges with valencies z_a and z_w. The two charges are separated by a distance $x_a - x_w$ from each other. The charge with valence z_a is immersed in air and resides at distance x_a (with $x_a > 0$) above an air-water interface. The charge with valence z_w is immersed in the aqueous phase and is located at distance $-x_w$ (with $x_w < 0$) below the air-water interface. Hence, the pair is oriented perpendicular to the air-water interface and partially penetrates into each of the two coexisting phases as

illustrated in Fig. 4.1.

The aqueous solution is characterized by a dielectric constant ε_w and contains monovalent mobile cations and anions, each with bulk concentration n_0. The dielectric constant in the air is denoted by ε_a. We place the x-axis of a Cartesian coordinate system perpendicular to the air-water interface so that the two charges with valencies z_a and z_w correspond to the position vectors $\{x_a,0,0\}$ and $\{x_w,0,0\}$, respectively. In the following it is convenient to express the y- and z-coordinates of an arbitrary position vector $\mathbf{r} = \mathbf{x} + \mathbf{s}$ as the sum of a vector $\mathbf{x} = x\mathbf{e}_x$ normal to the air-water interface, where $\mathbf{e}_x$ is a unit vector in the x-direction, and a vector $\mathbf{s} = y\mathbf{e}_y + z\mathbf{e}_z$ parallel to the air-water interface, where $\mathbf{e}_y$ and $\mathbf{e}_z$ are unit vectors along the y- and z-directions, respectively.

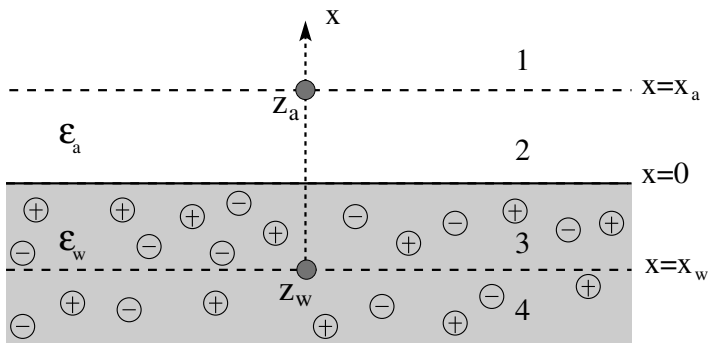

Figure 4.1. Two point charges with valencies z_a and z_w are located at distances x_a above and $-x_w$ below an air-water interface, respectively. Air has a dielectric constant $\varepsilon_a \approx 1$. Water (the shaded region) has a dielectric constant $\varepsilon_w \approx 80$ and contains a symmetric 1:1 electrolyte of bulk concentration n_0. Co-ions and counter-ions are represented schematically. The x-axis of a Cartesian coordinate system points normal to the interface. The three positions $x = x_a$, $x = 0$ (coinciding with the air-water interface), and $x = x_w$ divide space into four regions indexed 1,2,3,4.

To calculate the electrostatic potential at every point in space we employ the same approach as used by Stillinger [42] for one single point charge. To this end, we divide the space into four regions that are separated by three parallel planes located at $x = x_a$, $x = 0$, and $x = x_w$. We index the four regions $i = 1$ for $x \geq x_a$, $i = 2$ for $x_a \geq x \geq 0$, $i = 3$ for $0 \geq x \geq x_w$, and $i = 4$ for $x_w \geq x$. Instead of the electrostatic potential Φ, we will work with the dimensionless electrostatic potential $\Psi = e\Phi/k_BT$, where e denotes the elementary charge, k_B the Boltzmann constant, and T the absolute temperature. The dimensionless potential in the four regions is then denoted by $\Psi_i = \Psi_i(\mathbf{r})$ with $i = 1,2,3,4$. Clearly, in the air (regions 1 and 2) the potential

fulfills the Laplace equation

$$\nabla^2\Psi_1 = 0, \qquad \nabla^2\Psi_2 = 0. \tag{4.1}$$

The aqueous phase (regions 3 and 4) contains mobile ions, the presence of which could be described by the non-linear Poisson-Boltzmann approach. However, because we represent a charged object (such as a nanoparticle or colloid) by two point charges, our approach is not appropriate to model the potential near those two charges. We thus focus on large distances away from the two charges, where the potential is sufficiently small so that the linearized Debye-Hückel model becomes applicable. In regions 3 and 4 we then need to solve the equations

$$l_D^2\nabla^2\Psi_3 = \Psi_3, \qquad l_D^2\nabla^2\Psi_4 = \Psi_4, \tag{4.2}$$

where $l_D = (8\pi l_B n_0/\varepsilon_w)^{-1/2}$ is the Debye screening length. The Bjerrum length $l_B = e^2/(4\pi\varepsilon_0 k_B T)$ (where ε_0 is the permittivity of free space) corresponds to the distance at which two elementary charges in vacuum experience an electrostatic interaction equal to the thermal energy $k_B T$. At room temperature $l_B = 56$ nm. Note the Bjerrum length in water is $l_B/\varepsilon_w = 0.7$ nm. Solutions

$$\Psi_i(\mathbf{r}) = \frac{1}{(2\pi)^2}\int_{-\infty}^{\infty} dk_y \int_{-\infty}^{\infty} dk_z \Psi_i^{(k)}(\mathbf{r}) \tag{4.3}$$

for the total potential in all four regions $i = 1,2,3,4$ can be decomposed into solutions corresponding to individual wave vectors $\mathbf{k} = \{k_y, k_z\}$ of magnitude $k = \sqrt{k_y^2 + k_z^2}$. These particular solutions

$$\begin{aligned}
\Psi_1^{(k)}(\mathbf{r}) &= Ae^{-|k|x}e^{i\mathbf{k}\cdot\mathbf{s}}, \\
\Psi_2^{(k)}(\mathbf{r}) &= (Be^{-|k|x} + Ce^{|k|x})e^{i\mathbf{k}\cdot\mathbf{s}}, \\
\Psi_3^{(k)}(\mathbf{r}) &= (De^{-\sqrt{k^2+l_D^{-2}}x} + Ee^{\sqrt{k^2+l_D^{-2}}x})e^{i\mathbf{k}\cdot\mathbf{s}}, \\
\Psi_4^{(k)}(\mathbf{r}) &= (Fe^{\sqrt{k^2+l_D^{-2}}x})e^{i\mathbf{k}\cdot\mathbf{s}},
\end{aligned} \tag{4.4}$$

ensure vanishing of the potential far away from the air-water interface, namely for $\Psi_1(x \to \infty) = 0$ and $\Psi_4(x \to -\infty) = 0$). The six constants A, B, C, D, E, F in Eq. 4.4 must be determined from both continuity of the potential and from a set of appropriate boundary conditions. Regarding the former, continuity of the potential at positions $x = x_a$, $x = 0$, and $x = x_w$ entails the three conditions $\Psi_1(\{x_a, y, z\}) = \Psi_2(\{x_a, y, z\})$,

$\Psi_2(\{0,y,z\}) = \Psi_3(\{0,y,z\})$, and $\Psi_3(\{x_w,y,z\}) = \Psi_4(\{x_w,y,z\})$. The latter relate the normal derivative of the potential to the change in dielectric constant across the air-water interface

$$\varepsilon_a \left(\frac{\partial \Psi_2}{\partial x}\right)_{x=0} = \varepsilon_w \left(\frac{\partial \Psi_3}{\partial x}\right)_{x=0} \tag{4.5}$$

and to the surface charge densities σ_a at $x = x_a$ and σ_w at $x = x_w$,

$$\begin{aligned} \left(\frac{\partial \Psi_1}{\partial x}\right)_{x=x_a} - \left(\frac{\partial \Psi_2}{\partial x}\right)_{x=x_a} &= -4\pi \frac{l_B}{\varepsilon_a}\frac{\sigma_a}{e}, \\ \left(\frac{\partial \Psi_3}{\partial x}\right)_{x=x_w} - \left(\frac{\partial \Psi_4}{\partial x}\right)_{x=x_w} &= -4\pi \frac{l_B}{\varepsilon_w}\frac{\sigma_w}{e}. \end{aligned} \tag{4.6}$$

Note that the presence of the two discrete charges with valencies z_a and z_w translates into surface charge densities $\sigma_a(\mathbf{s}) = z_a\delta(\mathbf{s})$ at the surface $x = x_a$ and $\sigma_w(\mathbf{s}) = z_w\delta(\mathbf{s})$ at the surface $x = x_w$, where the Dirac delta peak at $\mathbf{s} = 0$ is related to the wave numbers $\mathbf{k}$ through

$$\delta(\mathbf{s}) = \frac{1}{(2\pi)^2} \int_{-\infty}^{\infty} dk_z \int_{-\infty}^{\infty} dk_y \, e^{i\mathbf{k}\cdot\mathbf{s}}. \tag{4.7}$$

Eqs. 4.3-4.7 together with the continuity conditions make the calculation of the constants A, B, C, D, E, F for every wave vector $\mathbf{k}$ straightforward. The resulting expressions for the potentials $\Psi_i(\mathbf{r})$ (with $i = 1,2,3,4$) become most convenient when expressing the components of the wave vector in polar coordinates, l and θ, through $k_y = (l/l_D)\cos(\theta)$ and $k_z = (l/l_D)\sin(\theta)$; this implies for the area element of the wave vector space $dk_y\,dk_z = (l/l_D^2)\,dl\,d\theta$. In fact, the resulting integration over the variable θ is of the form $\int_0^{2\pi} d\theta\, e^{is(l/l_D)\cos\theta} = 2\pi J_0(sl/l_D)$, where J_0 denotes the Bessel function of first kind and order zero, and thus can be carried out. Note that in the following we write the potential $\Psi_i(\mathbf{r}) \to \Psi_i(x,s)$ directly as function of x and $s = \sqrt{y^2+z^2}$. With this, the final expression for the potential in region 1 (where $x \geq x_a$) reads

$$\begin{aligned} \Psi_1(x,s) \;=\; & \frac{2z_a l_B}{\varepsilon_a l_D} \int_0^{\infty} dl \, \frac{e^{-\frac{x}{l_D}l} J_0\left(\frac{s}{l_D}l\right)}{\varepsilon_a l + \varepsilon_w\sqrt{1+l^2}} \left[\varepsilon_a l \cosh\left(\frac{x_a}{l_D}l\right)\right. \\ & + \left. \varepsilon_w\sqrt{1+l^2}\sinh\left(\frac{x_a}{l_D}l\right) + \varepsilon_a l \frac{z_w}{z_a} e^{\frac{x_w}{l_D}\sqrt{1+l^2}}\right]. \end{aligned} \tag{4.8}$$

For region 4 (where $x \leq x_w$) we obtain

$$\begin{aligned}\Psi_4(x,s) &= \frac{2z_w l_B}{\varepsilon_w l_D}\int_0^\infty dl\,\frac{e^{\frac{x}{l_D}\sqrt{1+l^2}}J_0\left(\frac{s}{l_D}l\right)}{\varepsilon_a l+\varepsilon_w\sqrt{1+l^2}}\left[\varepsilon_w l\frac{z_a}{z_w}e^{-\frac{x_a}{l_D}l}\right.\\ &- \varepsilon_a\frac{l^2}{\sqrt{1+l^2}}\sinh\left(\frac{x_w}{l_D}\sqrt{1+l^2}\right)\\ &+ \left.\varepsilon_w l\cosh\left(\frac{x_w}{l_D}\sqrt{1+l^2}\right)\right].\end{aligned} \tag{4.9}$$

Our objective is to calculate the interaction free energy

$$\frac{U_{el}(s)}{k_BT} = z_a\Psi_1(x_a,s)+z_w\Psi_4(x_w,s) \tag{4.10}$$

between two identical pairs of charges that are separated by a distance s. Using Eq. 4.8 and 4.9 we find

$$\frac{U_{el}}{k_BT} = 2\,\frac{l_B}{l_D}\int_0^\infty dl\,l\,\frac{J_0\left(\frac{s}{l_D}l\right)\left(c_{aa}z_a^2+2c_{aw}z_az_w+c_{ww}z_w^2\right)}{\varepsilon_a l+\varepsilon_w\sqrt{1+l^2}}, \tag{4.11}$$

with

$$\begin{aligned}c_{aa} &= e^{-\frac{x_a}{l_D}l}\left[\cosh\left(\frac{x_a}{l_D}l\right)+\frac{\varepsilon_w}{\varepsilon_a}\frac{\sqrt{1+l^2}}{l}\sinh\left(\frac{x_a}{l_D}l\right)\right],\\ c_{aw} &= e^{-\frac{x_a}{l_D}l}\,e^{\frac{x_w}{l_D}\sqrt{1+l^2}},\\ c_{ww} &= e^{\frac{x_w}{l_D}\sqrt{1+l^2}}\left[\cosh\left(\frac{x_w}{l_D}\sqrt{1+l^2}\right)-\frac{\varepsilon_a}{\varepsilon_w}\frac{l}{\sqrt{1+l^2}}\sinh\left(\frac{x_w}{l_D}\sqrt{1+l^2}\right)\right].\end{aligned} \tag{4.12}$$

Eqs. 4.11 and 4.12 are the major result of our theoretical model; they constitute a generalization of Stillinger's classical result [42] that we analyze and discuss in the following.

4.3. Results

Our main objective is to investigate the salt concentration dependence of the interaction free energy $U_{el}(s)$ as function of the distance s between the two pairs of point charges. Generally, the integral in Eq. 4.11 does not yield exact solutions. We therefore present in this section analytically accessible limiting cases followed by a discussion of numerical results. At the end we characterize the dipolar behavior of the

interaction in the limit of large s.

4.3.1. Analytic Solutions in Limiting Cases

The specific case $x_a = x_w = 0$ places both charges, the one with valence z_a and the other with valence z_w, directly at the air-water interface. This implies $c_{aa} = c_{aw} = c_{ww} = 1$ in Eqs. 4.11 and 5.16 and thus recovers Stillinger's classical result [42]

$$\frac{U_{el}}{k_B T} = 2\,(z_a + z_w)^2\,\frac{l_B}{l_D}\int_0^\infty dl\,l\,\frac{J_0\left(\frac{s}{l_D}l\right)}{\varepsilon_a l + \varepsilon_w\sqrt{1+l^2}}. \tag{4.13}$$

In the limit $\varepsilon_a \to 0$ we obtain from Eq. 4.13 the result $U_{el}/k_BT = 2(z_a+z_w)^2 l_B e^{-s/l_D}/(\varepsilon_w s)$, which is twice the screened (Yukawa-like) interaction energy between two point charges, each with effective valence $z_a + z_w$, in a bulk electrolyte of Debye screening length l_D. Similarly, twice the Coulomb interaction energy $U_{el}/k_BT = 2(z_a+z_w)^2 l_B/(\varepsilon_a s)$ between two point charges in a medium of dielectric constant ε_a is recovered from Eq. 4.13 in the limit $\varepsilon_w \to 0$. Note that both cases contain an additional factor of 2, which is a consequence of excluding the electric field from the space of vanishing dielectric constant or, equivalently, of doubling the charge at the interface due to its own identical image.

In a medium with uniform dielectric constant $\varepsilon_a = \varepsilon_w$ (and still with $x_a = x_w = 0$), Eq. 4.13 yields the exact result

$$\frac{U_{el}}{k_B T} = \frac{2}{\varepsilon_a}\,(z_a + z_w)^2\,l_B\,\frac{l_D^2}{s^3}\left[1 - \left(1 + \frac{s}{l_D}\right)e^{-s/l_D}\right], \tag{4.14}$$

which corresponds to a Coulomb interaction at small distances and to a dipolar interaction at large distances. More specifically, at small distances we recover the electrostatic interaction $U_{el}/k_BT = (z_a+z_w)^2 l_B/(\varepsilon_a s)$ between two charges of valence $z_a + z_w$ in a medium of uniform dielectric constant ε_a. At large distances s, the term in Eq. 4.15 that decays exponentially becomes small, leaving a dipolar repulsion energy $U_{el}/k_BT = l_B(\mu/e)^2/(\varepsilon_a s^3)$ with a dipole moment $\mu = \sqrt{2}\,e(z_a+z_w)l_D$.

Another, and more relevant, case within the scenario $x_a = x_w = 0$ is that of a strong dielectric discontinuity, $\varepsilon_a \ll \varepsilon_w$, which has been analyzed previously by Hurd [43], yielding the approximate relation

$$\frac{U_{el}}{k_B T} = \frac{2}{\varepsilon_w}\,(z_a + z_w)^2\,l_B\left[\frac{\varepsilon_a}{\varepsilon_w}\frac{l_D^2}{s^3} + \frac{e^{-s/l_D}}{s}\right]. \tag{4.15}$$

The first part in Eq. 4.15, valid in the limit of large s, corresponds to the interaction energy $U_{el}/k_BT = l_B(\mu/e)^2/(\varepsilon_a s^3)$ between two dipoles in air, each of dipole moment $\mu = \sqrt{2}\,e(z_a+z_w)l_D\varepsilon_a/\varepsilon_w$. The second part in Eq. 4.15, a screened (Yukawa-like) repulsion energy, is the dominating behavior of the exponentially decaying contribution to Eq. 4.13.

For $z_w = 0$ (with $z_a > 0$ and $x_a > 0$) we are left with a single point charge suspended in the air at a distance x_a away from the interface. In the two limits $\varepsilon_w \to \infty$ and $\varepsilon_w \to 0$ the water phase is impenetrable to the electric field, either with a fixed potential (for $\varepsilon_w \to \infty$) or with vanishing surface charge density (for $\varepsilon_w \to 0$) at the air-water interface; Eqs. 4.11 and 4.12 then yield

$$\frac{U_{el}}{k_BT} = z_a^2 \frac{l_B}{\varepsilon_a}\left[\frac{1}{s} \pm \frac{1}{\sqrt{s^2+(2x_a)^2}}\right], \tag{4.16}$$

where the plus and minus signs refer to $\varepsilon_w \to 0$ and $\varepsilon_w \to \infty$, respectively. The latter case implies a dipolar interaction energy $U_{el}/k_BT = 2l_B z_a^2 x_a^2/(\varepsilon_a s^3)$ for $x_a \ll s$. Similarly, for $z_a = 0$ (with $z_w > 0$ and $x_w < 0$) we are left with a single point charge suspended in the aqueous phase at a distance $-x_w$ away from the interface. The two limits $\varepsilon_a \to \infty$ and $\varepsilon_a \to 0$ now yield

$$\frac{U_{el}}{k_BT} = z_w^2 \frac{l_B}{\varepsilon_w}\left[\frac{e^{-s/l_D}}{s} \pm \frac{e^{-\sqrt{s^2+(2x_w)^2}/l_D}}{\sqrt{s^2+(2x_w)^2}}\right], \tag{4.17}$$

where the plus and minus signs refer to $\varepsilon_a \to 0$ and $\varepsilon_a \to \infty$, respectively. Clearly, Eqs. 4.16 and 4.17 describe the interaction between two point charges located close to a field-impenetrable medium, either with (the minus sign) or without (the plus sign) mobile charges on the surface of the field-impenetrable medium. Eqs. 4.16 and 4.17 are based on, respectively, an unscreened ($\sim 1/s$) and a screened ($\sim e^{-s/l_D}/s$) electrostatic interaction energy of two point charges in a bulk medium.

Still another exact result is available in the limit $l_D \to \infty$, which corresponds to the salt-free case $n_0 = 0$. Eqs. 4.11 and 4.12 then produce

$$\begin{aligned}\frac{U_{el}}{l_B k_B T} &= \frac{z_w^2}{\varepsilon_w}\left[\frac{1}{s} + \left(\frac{\varepsilon_w-\varepsilon_a}{\varepsilon_w+\varepsilon_a}\right)\frac{1}{\sqrt{s^2+(2x_w)^2}}\right] \\ &+ \frac{z_a^2}{\varepsilon_a}\left[\frac{1}{s} - \left(\frac{\varepsilon_w-\varepsilon_a}{\varepsilon_w+\varepsilon_a}\right)\frac{1}{\sqrt{s^2+(2x_a)^2}}\right] \\ &+ \frac{4z_a z_w}{\varepsilon_w+\varepsilon_a}\frac{1}{\sqrt{s^2+(x_a-x_w)^2}},\end{aligned} \tag{4.18}$$

which corresponds to the well-known result [114] for the interaction energy between two identical pairs of charges that span across a discontinuous dielectric interface. For $x_a = x_w = 0$, Eq. 4.18 simplifies to the Coulomb repulsion $U_{el}/k_BT = l_B(z_a + z_w)^2/(s\varepsilon_{av})$ with the average dielectric constant $\varepsilon_{av} = (\varepsilon_a + \varepsilon_w)/2$. For $z_a = -z_w = z$ the leading term $U_{el}/k_BT = [2l_B(z^2/s^3)\,(x_a/\varepsilon_a - x_w/\varepsilon_w)^2]/(1/\varepsilon_a + 1/\varepsilon_w)$ for small x_a and x_w is dipolar. Note that in a uniform dielectric medium with $\varepsilon_w = \varepsilon_a = \varepsilon_{av}$ this reduces to the familiar dipole-dipole interaction $U_{el}/k_BT = l_B z^2 (x_a - x_w)^2/(\varepsilon_{av} s^3)$.

4.3.2. Discussion of Numerical Results

Fig. 4.2 presents numerical results for the interaction between the two pairs of charges, in all cases with $x_w = -x_a$, $\varepsilon_a = 1$, and $\varepsilon_w = 80$. Our choice $x_w = -x_a$ mimics equatorial partitioning of an interface-trapped spherical particle. We plot $\sqrt{U_{el}/k_BT}$ as function of $s^{-3/2}$ because the slope of the resulting curves can inform us about the magnitude of a dipole moment that causes the interaction. Specifically, if the electrostatic interaction

$$\frac{U_{el}}{k_BT} = \frac{l_B}{\varepsilon_a}\left(\frac{\mu}{e}\right)^2 \frac{1}{s^3} \tag{4.19}$$

is effectively that between two aligned dipoles, each of dipole moment μ, in a uniform medium of dielectric constant ε_a, the slope equals $\sqrt{l_B/\varepsilon_a} \times \mu/e$. The three different diagrams in Fig. 4.2 correspond to the combinations $z_a = 20$ and $z_w = 0$ (top diagram), $z_a = 0$ and $z_w = 500$ (middle diagram), and $z_a = 20$ and $z_w = 500$ (bottom diagram). That is, the three diagrams refer, respectively, to a single point charge of valence 20 at distance x_a above the air-water interface (top diagram), to a single point charge of valence 500 at the same distance x_a below the air-water interface (middle diagram), and to the simultaneous presence of these two charges above and below the air-water interface (bottom diagram). Our choice for the valencies 20 and 500 is motivated by the typically vastly different surface charge densities of interface-trapped colloids at their air-exposed and water-exposed surface regions. Each diagram contains four sets of differently colored curves; they correspond to $x_a = 0$ (black), $x_a = 1\,\text{nm}$ (blue), $x_a = 2\,\text{nm}$ (red), and $x_a = 4\,\text{nm}$ (green). Each set of fixed color contains five curves; they are computed for different Debye screening lengths: $l_D \to \infty$, $l_D = 100\,\text{nm}$, $l_D = 10\,\text{nm}$, $l_D = 5\,\text{nm}$, and $l_D = 2\,\text{nm}$ (from top to bottom). The curves for $l_D \to \infty$ are shown as dashed lines. In addition, the upper diagram contains dotted curves, which apply to the limiting case of an infinite amount of added salt, $l_D \to 0$.

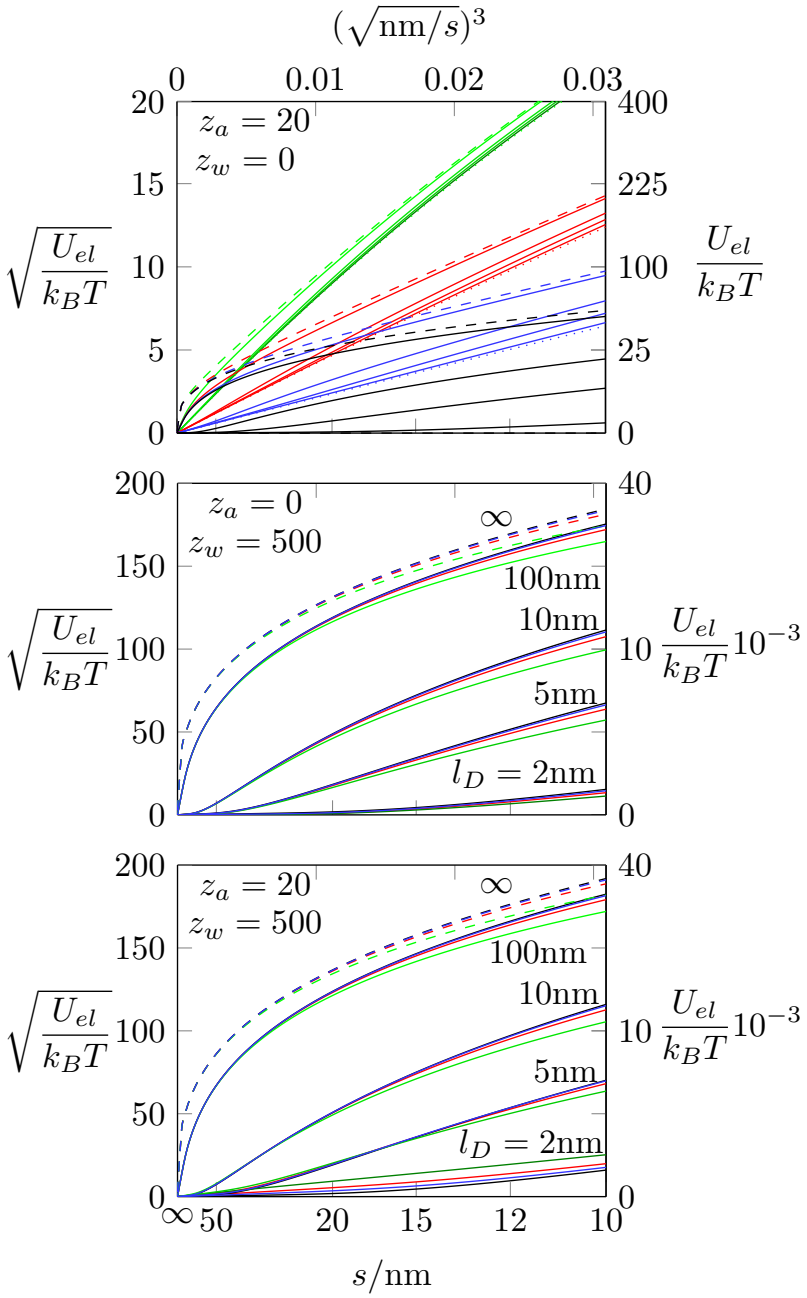

Figure 4.2. The square root of the electrostatic interaction free energy, $\sqrt{U_{el}/k_BT}$, of two pairs of point charges (see Fig. 4.1) as function of $\sqrt{1/s^3}$, where s is the distance between the two pairs along the air-water interface. All curves are derived using Eqs. 4.11 and 4.12 with $x_w = -x_a$, $\varepsilon_a = 1$, and $\varepsilon_w = 80$. The three diagrams correspond to $z_a = 20$ and $z_w = 0$ (top diagram), $z_a = 0$ and $z_w = 500$ (middle diagram), and $z_a = 20$ and $z_w = 500$ (bottom diagram). All curves are color-coded according to $x_a = 0$ (black), $x_a = 1\,\mathrm{nm}$ (blue), $x_a = 2\,\mathrm{nm}$ (red), and $x_a = 4\,\mathrm{nm}$ (green). Sets of curves of the same color in each diagram refer to $l_D \to \infty$, $l_D = 100\,\mathrm{nm}$, $l_D = 10\,\mathrm{nm}$, $l_D = 5\,\mathrm{nm}$, and $l_D = 2\,\mathrm{nm}$ (from top to bottom). The curves for $l_D \to \infty$ are shown as dashed lines. The upper diagram contains additional dotted curves (the bottom ones for green, red, and blue color), which correspond to the large salt limit, $l_D \to 0$.

Consider first the upper diagram, where a single positive point charge of valence 20 is suspended in air, at distance x_a above the air-water interface. When $x_a = 0$ (see the black curves in the top diagram of Fig. 4.2), the interaction is described by the Stillinger's result [42] in Eq. 4.13. In the additional absence of salt (the dashed curve in black) the interaction energy $U_{el}/k_BT = l_B z_a^2/(\varepsilon_{av} s)$ is Coulombic, with an effective dielectric constant $\varepsilon_{av} = (\varepsilon_a + \varepsilon_w)/2$. This also follows from Eq. 4.18 (with $z_w = 0$ and $x_a = 0$). The presence of salt renders the interaction for large s dipolar. Added salt also weakens the magnitude of the interaction until, in the limit $l_D \to 0$, it vanishes completely (that is $U_{el}(s) = 0$). This strong salt concentration dependence is a characteristic feature of Eq. 4.13 as is evident from Hurd's analysis [43] (see Eq. 4.15), which predicts $U_{el} \sim l_D^2$ for large s. For non-vanishing x_a, the limit of no added salt (see the blue, red, and green dashed curves in the upper diagram of Fig. 12.2) is again described by Eq. 4.18. Note that the dominating contribution to $U_{el}(s)$ remains Coulombic at large distances (hence, all dashed lines merge into one single curve $U_{el}^{1/2} \sim \left(s^{-3/2}\right)^{1/3}$ in the limit of large s). The next-order term is dipolar, as in Eq. 4.19, with an effective dipole moment $\mu = \sqrt{2}\, e z_a x_a \sqrt{(\varepsilon_w - \varepsilon_a)/(\varepsilon_w + \varepsilon_a)}$, or

$$\mu = \sqrt{2}\, e z_a x_a \tag{4.20}$$

for $\varepsilon_w \gg \varepsilon_a$. This dipolar contribution determines virtually all of the differences between the dashed lines in the upper diagram of Fig. 12.2. Lowering x_a or adding salt decreases the interaction energy U_{el}. However, even if an infinite amount of salt is added, the interaction always remains non-vanishing for any choice of x_a with $x_a > 0$. It is then given by the limit $\varepsilon_w \to \infty$, as specified in Eq. 4.16, which for large s implies a dipolar interaction as in Eq. 4.19 with an effective dipole moment again given by Eq. 4.20. The large salt limit, $l_D \to 0$, is displayed in the upper diagram of Fig. 4.2 by the blue, red, and green dotted lines. We emphasize that the entire salt concentration dependence is described by the differences between the dotted and dashed lines for the blue, red, and green sets of curves. These differences are small, which is in contrast to Stillinger's predictions in Eqs. 4.13 and 4.15 for the exact interfacial location ($x_a = 0$) of the charge. If we identify the point charge in our present model with the charge located at the air-exposed region of an interface-trapped particle, our model for $x_a > 0$ would predict a limited salt concentration dependence of the interaction free energy $U_{el}(s)$, which agrees with experimental observations but is in contrast to Eqs. 4.13 and 4.15.

Consider next the middle diagram of Fig. 4.2, where a single positive point charge of valence 500 is

suspended in the aqueous phase, at distance x_a away from air-water interface. As expected, the interaction energy $U_{el}(s)$ depends strongly on the presence of salt but is only moderately affected by the distance x_a. In fact, increasing x_a renders the interaction more favorable (as opposed to the charge being suspended in air). The reason is the sign of the charge and its image charge being the same if the charge is suspended in the medium with the higher dielectric constant, implying a repulsive interaction. Conversely, they have opposite sign if the charge is immersed in the medium with the lower dielectric constant, which implies an attractive interaction. In the limit $l_D \to \infty$ this is revealed immediately by Eq. 4.18; see the different signs in the first and second line of that equation. Again, the limit $l_D \to \infty$ renders the interaction Coulombic, whereas it is dipolar in the presence of salt. Hence, for any non-vanishing salt content the slopes of all solid lines in the middle diagram of Fig. 4.2 remain finite and non-vanishing in the limit of large s. As x_a grows and as more salt is added (smaller l_D), the dipole moment μ decreases.

Finally, consider the bottom diagram of Fig. 4.2. Here, both charges are present, the one with valence $z_a = 20$ immersed in air and the other with valence $z_w = 500$ immersed in water. Note that all the three terms, c_{aa}, c_{aw}, and c_{ww}, in Eq. 4.12 are now non-vanishing (including the coupling term c_{aw}). At vanishing salt content the interaction energy is described by Eq. 4.18, which due to the valence asymmetry $z_w \gg z_a$ is dominated by the interaction between the two water-immersed charges. This renders the interaction energies in the bottom diagram of Fig. 4.2 very similar to those in the middle diagram, given l_D is large or infinite. For large salt content (small l_D), electrostatic interactions in the water are screened and the interaction energies in the bottom diagram of Fig. 4.2 become similar to those in the upper diagram. Therefore, while for large l_D an increase in x_a decreases U_{el}, we observe that for small l_D an increase in x_a increases U_{el}. In between these these two limiting behaviors, there exists a specific distance for each given salt concentration (for example $s \approx 16\,\text{nm}$ if $l_D \approx 5\,\text{nm}$) for which the interaction becomes independent of x_a. Here, the changes in U_{el} due to increasing the distance of the air-immersed and water-immersed charge to the interface eliminate each other.

4.3.3. The Dipole Moment at Large Separations

After discussing the interaction $U_{el}(s)$ in general terms, we now analyze the residual dipole moment

$$\mu = e\sqrt{\frac{\varepsilon_a}{l_B}\left(\frac{dU_{el}/k_BT}{d(1/s^3)}\right)_{s\to\infty}}, \tag{4.21}$$

at large distances s. Fig. 4.3 shows the dipole moment as function of the Debye screening length l_D, in all cases with $x_w = -x_a$, $\varepsilon_a = 1$, and $\varepsilon_w = 80$, for the same three combinations of valencies [$z_a = 20$ and $z_w = 0$ (top diagram), $z_a = 0$ and $z_w = 500$ (middle diagram), and $z_a = 20$ and $z_w = 500$ (bottom diagram)] and the same coloring scheme [$x_a = 0$ (black), $x_a = 1\,\text{nm}$ (blue), $x_a = 2\,\text{nm}$ (red), and $x_a = 4\,\text{nm}$ (green)] as in Fig. 4.2.

Consider first the upper diagram of Fig. 4.3. The black solid curve results from a numerical calculation of Stillinger's integral in Eq. 4.13; i.e., a charge of valence $z_a = 20$ is located directly at the air-water interface, $x_a = 0$. The corresponding black dashed line is Hurd's [43] approximate expression $\mu = \sqrt{2}\,ez_a l_D\varepsilon_a/\varepsilon_w$, valid for $\varepsilon_w \gg \varepsilon_a$; see the discussion following Eq. 4.15. The linear relationship $\mu \sim l_D$ is an obviously excellent approximation over a wide range of Debye screening lengths. Deviations at large l_D indicate approaching the salt-free limit, where μ diverges; see Fig. 4.2. Growing separation x_a between the point charge and the air-water interface increases μ; the numerical results according to Eqs. 4.11 and 4.12 are shown as solid lines. The corresponding dashed lines show the approximate relation $\mu = \sqrt{2}\,ez_a(x_a + l_D\varepsilon_a/\varepsilon_w)$, which adds the dipole moment in the limit of high salt content as specified in Eq. 4.20, to Hurd's expression. Agreement with the full numerical result according to Eqs. 4.11 and 4.12 is excellent over a wide range of Debye screening lengths.

Consider next the middle diagram of Fig. 4.3. Here, only the water-immersed charge with valence $z_w = 500$ is present. The plotted quantity $\triangle\mu = \mu - \sqrt{2}\,ez_w l_D\varepsilon_a/\varepsilon_w$ is the difference between the actual dipole moment and Hurd's [43] approximate expression. The solid and dashed lines refer to the numerical integration of Eqs. 4.11 and 4.12 and to the expression $\triangle\mu = -\sqrt{2}\,ez_w x_a\varepsilon_a/\varepsilon_w$, respectively. For $x_a = 0$ the difference between the two curves (the two black curves in the middle diagram of Fig. 4.3) expresses the difference between Stillinger's integral expression in Eq. 4.13 and Hurd's approximation $\mu = \sqrt{2}\,ez_w l_D\varepsilon_a/\varepsilon_w$. This is analogous for the other pairs of curves (blue, red, and green), yet with Hurd's approximation extended to $\mu = \sqrt{2}\,ez_w(l_D - x_a)\varepsilon_a/\varepsilon_w$, which accounts for the non-vanishing separation x_a between the water-

immersed charge and the air-water interface. The middle diagram of Fig. 4.3 reveals that the approximation $\mu = \sqrt{2}\,e z_w (l_D - x_a)\varepsilon_a/\varepsilon_w$ works well for intermediate values of l_D, yet not in the limits $l_D \to 0$ and $l_D \to \infty$.

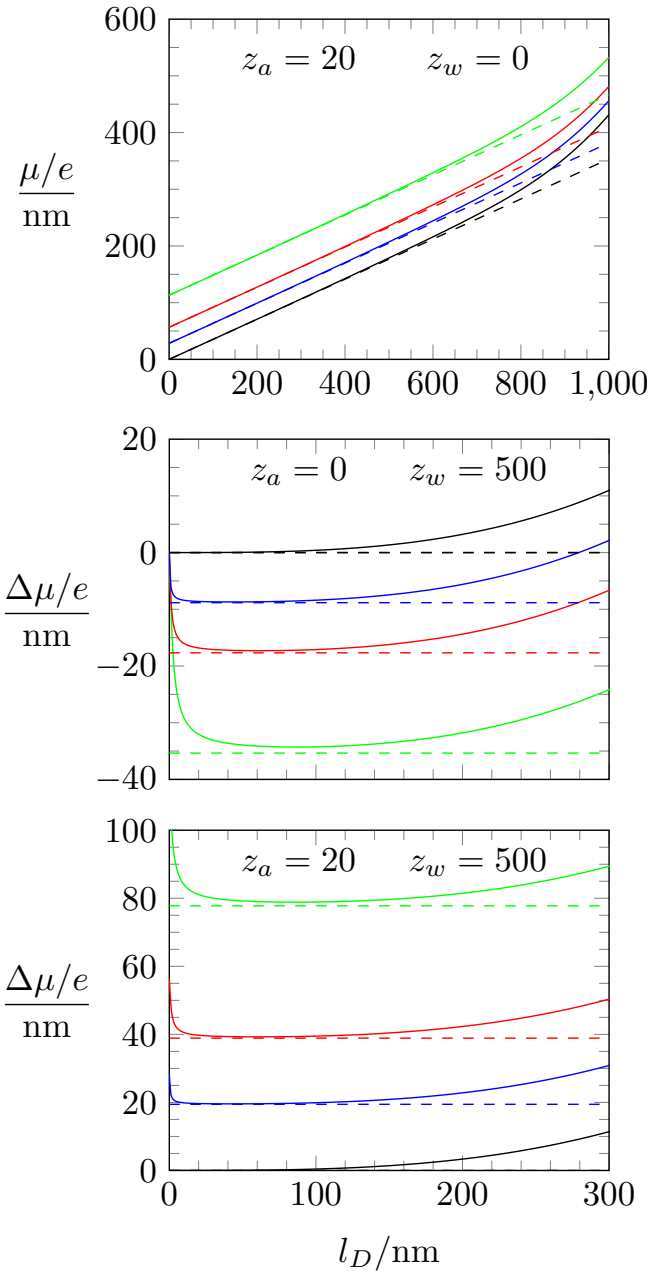

Figure 4.3. The dipole moment defined in Eq. 4.21 shown as function of the Debye screening length l_D (in all cases with $x_w = -x_a$, $\varepsilon_a = 1$, and $\varepsilon_w = 80$) for the same three combinations of valencies [$z_a = 20$ and $z_w = 0$ (top diagram), $z_a = 0$ and $z_w = 500$ (middle diagram), and $z_a = 20$ and $z_w = 500$ (bottom diagram)] and the same coloring scheme [$x_a = 0$ (black), $x_a = 1\,\text{nm}$ (blue), $x_a = 2\,\text{nm}$ (red), and $x_a = 4\,\text{nm}$ (green)] as in Fig. 12.2. The upper diagram displays μ; the middle and lower diagrams display $\triangle\mu = \mu - \sqrt{2}\,e(z_a + z_w) l_D \varepsilon_a/\varepsilon_w$. Solid lines refer to numerical calculations of μ according to Eqs. 4.11 and 4.12. Dashed lines show μ according to Eq. 4.22, implying a constant $\mu = \sqrt{2}\,e\,x_a(z_a - z_w\varepsilon_a/\varepsilon_w)$.

We finally consider the bottom diagram of Fig. 4.3, which applies to the combined presence of both the air-immersed and water-immersed charge. Here again we have plotted the difference $\triangle\mu = \mu - \sqrt{2}\,e(z_a+z_w)l_D\varepsilon_a/\varepsilon_w$ between the actual dipole moment μ and Hurd's approximation $\sqrt{2}\,e(z_a+z_w)l_D\varepsilon_a/\varepsilon_w$. The solid lines refer to the numerical integration of Eqs. 4.11 and 4.12. The dashed lines approximate the dipole moment by the simple expression

$$\mu = \sqrt{2}\,e\left[l_D\frac{\varepsilon_a}{\varepsilon_w}(z_a+z_w)+x_a\left(z_a-\frac{\varepsilon_a}{\varepsilon_w}z_w\right)\right]. \tag{4.22}$$

Even in this general case (non-vanishing z_a and z_w) the agreement is reasonable over a wide range of intermediate Debye screening lengths. Hence, we suggest μ according to Eq. 4.22 as a generalization of Hurd's limiting result [43] for the dipolar interaction at large distances between charged particles at the air-water interface. We note that in the limit of a large salt content, $l_D \to 0$, Eq. 4.22 should be replaced by $\mu = \sqrt{2}\,e\,x_a z_a$. This predicts a residual dipolar interaction that is determined solely by the air-exposed charge of the particle. We also note that Eq. 4.22 can easily be extended to the case where x_a and x_w are two independent variables (instead of assuming $x_w = -x_a$); it then reads $\mu = \sqrt{2}\,e\,[l_D(\varepsilon_a/\varepsilon_w)(z_a+z_w)+x_a z_a + x_w z_w(\varepsilon_a/\varepsilon_w)]$.

Our extension of Stillinger's model from one single point charge to two spatially separated point charges is subject to the same approximations as Stillinger's original model. One is the use of the linear Debye-Hückel model, which in comparison to the non-linear Poisson-Boltzmann approach overestimates electrostatic potentials near charged macroions. Even though we focus on large particle separations, where the interaction potentials are small enough to justify the use of the Debye-Hückel approximation, the prefactor of the interaction potential – namely the magnitude of the dipole moment μ in Eq. 4.19 – tends to be overestimated. Note that this nonlinear screening effect is salt dependent. To compensate for the overestimation, a salt-dependent charge-renormalization factor $g = g(l_D)$ can be introduced [107]. We obtain a simple approximation for g from a previously suggested electrostatic model of an interface-trapped charged colloid [133]. The colloid has a radius R, dielectric constant ε_n, and is assumed to partition equatorially to an air-water (or oil-water) interface. The numerical predictions for the apparent colloid charge (i.e., the apparent charge that determines the dipole moment μ as defined in Eq. 4.19) can be captured reasonably well using a planar capacitor model; see reference [133] for a detailed discussion of the planar capacitor model. The ratio between the predicted apparent colloid charge calculated on the basis of the non-linear Poisson-Boltzmann model (Eq. 16 in reference [133]) and the linear Debye-Hückel model (Eq. 19 in reference [133]), subject

to the assumptions $\varepsilon_w R \gg \varepsilon_n l_D$ and $l_B l_D z_w \gg \varepsilon_w R^2$, yields the estimate

$$g = \frac{\ln\left(\frac{2 l_B l_D z_w}{\varepsilon_w R^2}\right) + \frac{z_a l_B}{\varepsilon_n R}}{\frac{z_a l_B}{\varepsilon_n R} + \frac{z_w l_B l_D}{\varepsilon_w R^2}} \tag{4.23}$$

for the salt-dependent charge-renormalization factor. With the renormalization factor included, the dipole moment becomes $\mu_{renorm} = g\mu$, where μ is specified in Eq. 4.22.

Table 4.1. Comparison of the dipole moments $\mu_{experim}$, as derived from experiments of Park *et al* [1], with our theoretical prediction $\mu_{renorm} = g\mu$ for various salt concentrations.

dipole moment	salt concentration (mM)				
in units of e $\times 10^6$nm	1	0.5	0.1	0.01	no salt
$\mu_{experim}$	1.9	2.8	3.0	3.5	4.5
μ_{renorm}	2.4	2.7	3.2	3.7	4.1

As pointed out in the Introduction, the salt dependence of dipolar interactions between interface-trapped colloids has been measured previously. One of the most detailed data sets has been reported by Park *et al* [1] for spherical, charge-stabilized polystyrene particles of radius $R = 1.5\,\mu$m and $\varepsilon_n = 2.5$ at a decane-water interface. The forces between individual particles were observed to follow a dipolar $1/r^4$-behavior with a salt-dependent prefactor. From the measured forces (see Fig. 3 of reference [1]) we can extract the dipole moment $\mu = \mu_{experim}$ as defined in Eq. 4.19, with the Bjerrum length $l_B = 56\,$nm in vacuum and a dielectric constant $\varepsilon_a = 2$ of decane. These experiment-based values $\mu_{experim}$ for the dipole moment are specified in Table 4.1; they increase from $\mu = 1.9 \times 10^6\, e\,$nm for 1 mM salt to $\mu = 4.5 \times 10^6\, e\,$nm in the absence of salt. We have determined μ_{renorm} as defined in the preceding paragraph to fit the experimental values, using x_a and z_a as free parameters and fixing $\varepsilon_a = 2$, $\varepsilon_w = 80$, $z_w = 7.9 \times 10^6$, and $l_B = 56\,$nm. Note that the estimate for $z_w = 2\pi R^2 \sigma_w$ follows from the surface charge density $\sigma_w = 0.56\, e/\text{nm}^2$ of polystyrene particles in water. A fit of the values for $\mu_{experim}$ in Table 4.1 yields $x_a = 4.2\,$nm and $z_a = 1900$, where a Debye length $l_D = 600\,$nm was chosen to model the case of no added salt.

The resulting dipole moments μ_{renorm} (listed in Table 4.1) exhibit reasonable agreement with $\mu_{experim}$. We emphasize that our underlying approach of assuming point charges interacting according to the linearized Debye-Hückel model (yet with an added charge-renormalization factor) was designed to yield a simple ana-

lytic expression for μ rather than to accurately reproduce experimental results. In light of this, the agreement between μ_{renorm} and $\mu_{experim}$ appears satisfying but may also be fortuitous.

4.4. Conclusions

This work has presented a generalization of Stillinger's classical work [42] on how charged particles trapped at a dielectric interface such as air and water interact with each other. Instead of locating a single point charge directly at the interface we have considered two individual point charges that protrude into the two interfacing media. An integral expression for the interaction between two such pairs of point charges is derived based on the Debye-Hückel approach, analytically accessible solutions are discussed, and an approximate expression for the dipole moment in the limit of large separations between the charge pairs along the air-water interface is proposed. The dipole moment reflects not only the total charge but also its fractions located at the air-exposed and water-exposed particle faces, the particle size, and the salt content. We find a non-vanishing residual dipole moment even in the limit of large salt content, as long as the air-immersed charge remains at a non-vanishing distance away from the air-water interface. Our results are subject to the limitations of modeling individual point charges using the Debye-Hückel approach [129]. However, to account for nonlinear screening, we have also introduced a salt-dependent charge-renormalization factor and compared the predicted (renormalized) dipole moments with recent experimental results from Park *et al* [1]. Our model is susceptible to future extensions such as, for example, the consideration of more complex charge distributions or additional dielectric discontinuities.

4.5. Acknowledgments

M.A.B. acknowledges the Swiss National Science Foundation for an International Short Visit travel grant (Grant No. 162320) to North Dakota State University. G.V.B. acknowledges a doctoral scholarship from CAPES Foundation/Brazil Ministry of Education (Grant No. 9466/13-4).

5. MODELING THE ELECTROSTATIC CONTRIBUTION TO THE LINE TENSION BETWEEN LIPID MEMBRANE DOMAINS USING POISSON-BOLTZMANN THEORY *

5.1. Introduction

It is likely that one of the most significant events in the evolution of life was the advent of lipid membranes – structures able to spatially organize cells and coordinate the exchange of matter between the cytosplasm and extracellular space [134, 135, 136, 137]. Besides acting as a permeability barrier, lipid membranes are also able to form domains that have been suggested to be involved in a multitude of biological processes such as cell signaling, fusion, and defense [138, 48, 11, 139, 140]. Due to the structural complexity of biomembranes, the experimental characterization of their physical properties is often based on model membranes. Certain ternary lipid mixtures undergo phase transitions where large domains rich in cholesterol and lipids with saturated acyl chains form a liquid ordered phase (L_o) that coexists with a liquid disordered phase (L_d) composed of mostly unsaturated lipids [52, 54, 137, 141, 142, 143]. At the boundaries between these distinct phases, the mismatch between the membrane thickness of the L_o and L_d phases is one of the main factors that turns the interfacial region into an environment different from that experienced by the lipids in the bulk of each phase (i.e., far away from the phase boundary [144]). The varying microenvironment in the normal direction of the boundary region also leads to an adjusting local composition of the lipids as compared to their bulk values. The resulting line tension, Λ, reflects the minimal energy per unit length to link the two lipid domains to each other [53, 145, 139]. The line tension plays a crucial role in membrane phase separation, fission, budding, and vesicle formation [52, 146, 147]; its magnitude is sensitive to changes in the boundary structure such as, for example, binding of proteins, partitioning of surfactants, or membrane bending [144, 148, 149, 150, 151].

*Reprinted from Springer article "G. V. Bossa, M. A. Brown, K. Bohinc, S. May, Modeling the electrostatic contribution to the line tension between lipid membrane domains using Poisson–Boltzmann theory, Int. J. Adv. Eng. Sci. Appl. Math. 8 (2) (2016) 101–110" with permission of Springer. Copyright 2016. This paper can be accessed online at `https://link.springer.com/article/10.1007/s12572-015-0158-6`. The material in this chapter was co-authored by Guilherme V. Bossa, Matthew A. Brown, Klemen Bohinc, and Sylvio May. G. V. Bossa contributed to the project design and manuscript writing. G.V.B. was responsible for the mathematical development, numerical and analytical solution of the equations, figures preparation, and discussion of the results.

Typically about one third of all lipids present in biomembranes carry a negative excess charge. Consequently, we expect the line tension Λ between membrane domains to also reflect electrostatic properties. We point out that while Λ is positive the electrostatic contribution Λ_{el} to the line tension must be negative. The negative sign of Λ_{el} is a simple consequence of the repulsive nature of the (screened) electrostatic interactions between the anionic lipids in the membrane: close to the boundary between two phases – one with higher and one with lower surface charge density – a favorable electrostatic excess free energy (as compared to two unperturbed bulk phases) emerges. It originates in the larger electrostatic energy gain of the anionic lipids near the boundary of the phase with the higher surface charge density as compared to the electrostatic energy loss of the anionic lipids near the boundary of the phase with the lower surface charge density. The gain in electrostatic excess free energy is also signified by an increased spatial freedom that the diffuse counterion cloud in the vicinity of the domain boundary (with its abrupt change in the membrane surface charge density) has.

In the present work we use non-linear Poisson-Boltzmann theory to model a straight interfacial region between two large charged membrane domains that are in contact with an electrolyte solution and extract Λ_{el} as function of the average (bulk) lipid composition in each phase. In order to discuss the influence of lipid mobility on Λ_{el}, we analyze various combinations of boundary conditions related to fixing the local surface charge density, the electrostatic surface potential, and an electrochemical potential of the lipids in each phase. While fixing the surface charge density or electrostatic potential corresponds, respectively, to the two thermodynamic limits of no or completely unrestricted mobility of the surface charges on the membrane, the latter case of a fixed electrochemical potential accounts for lipid mobility subject to a demixing entropy penalty and is thus the most relevant scenario for fluid-like lipid domains. In addition to our numerical results valid within non-linear Poisson-Boltzmann theory, we also derive analytical expressions for Λ_{el}, valid in the linear Debye-Hückel regime for the two specific cases where one domain carries a fixed surface charge density and the other one has either a fixed electrostatic potential or a fixed surface charge density. Our modeling approach predicts Λ_{el} to be negative with a magnitude on the order of piconewton. Experimentally determined values of the total line tension are positive, with magnitudes also on the order of piconewton. This suggests electrostatic interactions to generally provide an important contribution to (in fact, lowering of) the total line tension Λ. An extraction of Λ_{el} from experimental results of Λ is, however, hampered by the intricate coupling between electrostatic and non-electrostatic interactions in a lipid membrane.

5.2. Theory

Consider a planar lipid layer that consists of a binary mixture of neutral and negatively charged lipids with ϕ being the local mole fraction (composition) of the latter. We assume the presence of two coexisting lipid phases, indexed 1 and 2, with mole fractions $\bar{\phi}_1$ and $\bar{\phi}_2$ of the anionic lipid in the bulk. The two phases are macroscopically large, separated by a straight interface along the $x = 0$ line of a Cartesian coordinate system. Phases 1 and 2 extend respectively into the $x < 0$ and $x > 0$ regions, as illustrated in Fig. 5.1, with $z = 0$ and an unrestricted range along the y-coordinate (which points outward the page). The two phases are in contact with a symmetric 1:1 electrolyte located within the half-space $z > 0$.

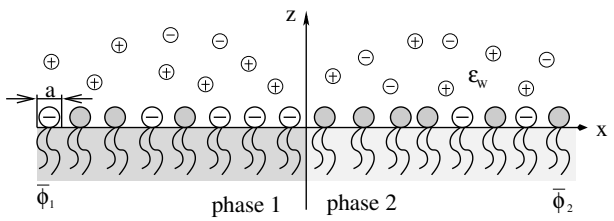

Figure 5.1. Schematic illustration of a planar lipid layer that bridges between two coexisting phases composed of a binary mixture of anionic and neutral lipids. The position $x = 0$ divides between the two phases, each with average mole fractions $\bar{\phi}_1$ (for $x < 0$) and $\bar{\phi}_2$ (for $x > 0$). The cross-sectional area per lipid, $a = 0.65\,\mathrm{nm}^2$, is assumed to be the same for both species. The lipid layer is facing an aqueous solution of dielectric constant $\varepsilon_W = 80$ that contains a symmetric 1:1 electrolyte of bulk concentration n_0. The diffuse ion cloud of monovalent co- and counter-ions is represented schematically.

Note that we only need to consider a single leaflet of the membrane because the low dielectric constant inside the membrane's hydrocarbon core effectively decouples the electrostatic properties of a lipid bilayer [152].

5.2.1. Electrostatic Free Energy

The electrostatic free energy of the coexisting phases can be expressed within classical Poisson-Boltzmann theory as the sum of an electrostatic energy and an ideal demixing entropy contribution of the

mobile ions in the aqueous solution; it reads

$$\begin{aligned} F_{el}^{(\sigma)} &= \frac{\varepsilon_W \varepsilon_0}{2} \int\limits_V dv (\nabla\Phi)^2 \\ &+ k_B T \int\limits_V dv \left[n_+ \ln \frac{n_+}{n_0} - n_+ + n_- \ln \frac{n_-}{n_0} - n_- + 2n_0 \right], \end{aligned} \tag{5.1}$$

where the two volume integrals $\int_V dv \to \int_{-\infty}^{\infty} dx \int_{-\infty}^{\infty} dy \int_0^{\infty} dz$ run over the aqueous solution (i.e., the half-space $z > 0$); Φ is the local electrostatic potential, k_B is the Boltzmann constant, T is the absolute temperature, n_+ and n_- are the local concentrations of mobile cations (the counterions) and anions (the coions), respectively, and $n_0 = n_+(z \to \infty) = n_-(z \to \infty)$ is their bulk value. Note that all local system properties depend only on the x-coordinate; $\Phi = \Phi(x)$, $n_\pm = n_\pm(x)$, and $\phi = \phi(x)$. Also, ε_0 is the vacuum permittivity and $\varepsilon_W = 80$ is the dielectric constant of water. The first term in Eq. 5.1 represents the energy stored in the electrostatic field, $-\nabla\Phi$, and the second term consists of the ideal mixing free energy of two ideal gases composed of either counterions or coions and kept at constant chemical potential to account for the existence of a bulk electrolyte. The local volume charge density of the electrolyte (for $z > 0$) is $\rho = e(n_+ - n_-)$; this allows us to express the Poisson equation as $\nabla^2\Phi = -e(n_+ - n_-)/(\varepsilon_0\varepsilon_W)$ where e denotes the elementary charge. The variation of $F_{el}^{(\sigma)} = F_{el}^{(\sigma)}[\Phi(n_+, n_-), n_+, n_-]$ with respect to n_+ and n_- and subject to satisfying Poisson's equation results in

$$\begin{aligned} \delta F_{el}^{(\sigma)} &= \int\limits_V dv\, \delta n_+ \left(k_B T \ln \frac{n_+}{n_0} + e\Phi \right) \\ &+ \int\limits_V dv\, \delta n_- \left(k_B T \ln \frac{n_-}{n_0} - e\Phi \right) + \int\limits_A da\, \tilde{\Phi} \delta\sigma, \end{aligned} \tag{5.2}$$

where the area integration $\int_A da = \int_{-\infty}^{\infty} dx \int_{-\infty}^{\infty} dy$ in the final term runs over the entire lipid layer ($z = 0$) and $\tilde{\Phi} = \Phi(z = 0)$ denotes the surface potential. The requirement that $\delta F_{el}^{(\sigma)} = 0$ in thermal equilibrium entails the Boltzmann distributions $n_\pm = n_0 \exp(\mp\Psi)$, which we express in terms of the local dimensionless potential $\Psi = e\Phi/k_B T$. The final term in Eq. 5.2 vanishes if the lipid layer carries a fixed surface charge density σ. Such a scenario is applicable to gel-phase or crystalline membranes where the lipids have no translational in-plane mobility [153]. On the other hand, if the lipid charges have completely unrestricted (metal-like) lateral mobility, the condition of a fixed and constant electrostatic surface potential $\tilde{\Phi}$ is implied and the thermodynamic free energy reads $F_{el}^{(\tilde{\Phi})} = F_{el}^{(\sigma)} - \int_A da \tilde{\Phi}\sigma$.

The two cases, immobile lipids (constant and fixed σ) and unrestricted lipid mobility (constant and fixed $\tilde{\Phi}$), constitute, respectively, upper and lower thermodynamic limits for the free energy (subject to the same reference state), implying the values obtained for any type of *partially* restricted lipid mobility (that is, a fixed electrochemical potential μ) must must lie in between them. A specific example for the latter case are fluid domains in which the lipids are not frozen at their positions but exhibit lateral mobility that is only subject to a demixing (but to no other energy) penalty. For the demixing penalty we conveniently adopt the ideal mixing free energy of a lattice gas [63] with a local mole fraction $\phi = \phi(x)$ of the anionic lipid

$$F_{mix} = \frac{k_B T}{a} \int_A da \left[\phi \ln \frac{\phi}{\bar{\phi}} + (1-\phi) \ln \frac{1-\phi}{1-\bar{\phi}} \right], \tag{5.3}$$

where a is the cross-sectional area per lipid headgroup (which we assume to be the same for both the anionic and neutral lipid). Following Fig. 12.1, the reference composition $\bar{\phi}$ in Eq. 5.3 is identified with the average composition in each phase by

$$\bar{\phi} = \begin{cases} \bar{\phi}_1, & \text{if } x < 0, \text{ phase 1} \\ \bar{\phi}_2 & \text{if } x > 0, \text{ phase 2.} \end{cases} \tag{5.4}$$

Note that employing the step-like function for $\bar{\phi}(x)$ in Eq. 5.4 assumes that in the absence of electrostatic interactions the phase boundary is infinitely sharp. Moving away from the phase boundary, lipids in each phase become less influenced by electrostatic interactions with lipids in the other phase, thus increasingly adopting bulk properties including the surface potential in the bulk $\tilde{\Phi}^{(b)} = \Phi(z = 0, x \to \pm\infty)$. The total free energy becomes $F_{el}^{(\mu)} = F_{el}^{(\sigma)} + F_{mix}$; its functional minimization predicts a constant electrochemical potential

$$\mu = -e\tilde{\Phi}^{(b)} = -e\tilde{\Phi} + k_B T \ln \left[\frac{\phi(1-\bar{\phi})}{\bar{\phi}(1-\phi)} \right] \tag{5.5}$$

of the anionic lipids in each of the phases 1 (where $\mu = \mu_1(\bar{\phi}_1)$) and 2 (where $\mu = \mu_2(\bar{\phi}_2)$). Rearranging Eq. 5.5 yields an explicit relation between local lipid composition $\phi = \phi(x)$ and local dimensionless electrostatic surface potential $\tilde{\Psi} = \tilde{\Psi}(x)$ of the lipid layer

$$\phi = \frac{1}{1 + \frac{1-\bar{\phi}}{\bar{\phi}} e^{-\tilde{\Psi} + \tilde{\Psi}^{(b)}}}, \tag{5.6}$$

with $\tilde{\Psi} \equiv e\tilde{\Phi}/k_B T$ and $\tilde{\Psi}^{(b)} = e\tilde{\Phi}^{(b)}/k_B T$. Note the dimensionless surface potential in the bulk $\tilde{\Psi}^{(b)}(\bar{\phi})$ is

different in phases 1 and 2. That is, $\tilde{\Psi}^{(b)} = \tilde{\Psi}_1^{(b)}$ in phase 1 ($x < 0$) and $\tilde{\Psi}^{(b)} = \tilde{\Psi}_2^{(b)}$ in phase 2 ($x > 0$); see below in Eq. 5.11 for an explicit relation.

In the following subsection we also consider the combination of different boundary conditions in phases 1 and 2 (fixed σ, fixed $\tilde{\Phi}$, or fixed μ). The only case that cannot be combined is that of two fixed but different surface potentials, $\tilde{\Phi}_1 = \tilde{\Phi}_1^{(b)}$ in phase 1 and $\tilde{\Phi}_2 = \tilde{\Phi}_2^{(b)}$ in phase 2, because the free energy then diverges to negative values with infinitely large magnitude.

5.2.2. Poisson-Boltzmann Equation and Boundary Conditions

Upon inserting the Boltzmann distributions for the mobile ion concentrations $n_\pm$ back into the Poisson equation, we arrive at the Poisson-Boltzmann equation,

$$l_D^2 \nabla^2 \Psi = \sinh \Psi, \tag{5.7}$$

with the Debye screening length given by $l_D = (8\pi l_B n_0)^{-1/2}$ for a symmetric 1:1 electrolyte. The Bjerrum length, l_B, is defined as the distance where the electrostatic interaction energy between two elementary charges is equal to the thermal energy unit $k_B T$. For an aqueous medium ($\varepsilon_W \approx 80$) at room temperature, $l_B = 0.7\,\mathrm{nm}$.

Solutions of Eq. 5.7 must fulfill appropriate boundary conditions which reflect the degree of charge mobility in each phase. In the present work we consider four distinct sets of boundary conditions that are imposed onto the two phases of the planar lipid layer depicted in Fig. 5.1:

I Each of the two phases is kept at constant (but not necessarily the same) surface charge density. This implies

$$\left(\frac{\partial \Psi}{\partial z}\right)_{z=0} = \frac{4\pi l_B}{a}\bar{\phi}, \qquad \text{for } -\infty < x < \infty \tag{5.8}$$

with $\bar{\phi}$ given in Eq. 5.6. Hence, the local composition $\phi(x) = \bar{\phi}$ is a step function, and the fixed surface charge densities are $\sigma_1 = -e\bar{\phi}_1/a$ in phase 1 and $\sigma_2 = -e\bar{\phi}_2/a$ in phase 2.

II Phase 1 carries a constant surface charge density $\sigma_1 = -e\bar{\phi}_1/a$ and phase 2 is kept at uniform and constant electrostatic surface potential $\tilde{\Psi}_2 = \tilde{\Psi}_2^{(b)} = \tilde{\Psi}_2^{(b)}(\bar{\phi}_2)$.

III Phase 1 carries a constant surface charge density $\sigma_1 = -e\bar{\phi}_1/a$ and phase 2 is kept at constant electro-

chemical potential, $\mu_2 = \mu_2(\bar{\phi}_2) = -k_B T \tilde{\Psi}_2^{(b)}(\bar{\phi}_2)$. This implies

$$\left(\frac{\partial \Psi}{\partial z}\right)_{z=0} = \frac{4\pi l_B}{a} \begin{cases} \bar{\phi}_1, & \text{for } x < 0 \\ \dfrac{1}{1 + \frac{1-\bar{\phi}_2}{\bar{\phi}_2} e^{-\tilde{\Psi} + \tilde{\Psi}_2^{(b)}}}, & \text{for } x > 0; \end{cases} \tag{5.9}$$

IV Phases 1 and 2 each have constant electrochemical potentials $\mu_1 = \mu_1(\bar{\phi}_1) = -k_B T \tilde{\Psi}_1^{(b)}(\bar{\phi}_1)$ and $\mu_2 = \mu_2(\bar{\phi}_2) = -k_B T \tilde{\Psi}_2^{(b)}(\bar{\phi}_2)$, respectively, implying

$$\left(\frac{\partial \Psi}{\partial z}\right)_{z=0} = \frac{4\pi l_B}{a} \frac{1}{1 + \frac{1-\bar{\phi}}{\bar{\phi}} e^{-\tilde{\Psi} + \tilde{\Psi}^{(b)}}}, \text{ for } -\infty < x < \infty. \tag{5.10}$$

In Eqs. 5.8-5.10 we have used the relation $\sigma = -e\phi/a$, combined with Eq. 5.6 if μ is fixed in either phase 1 or 2. Also recall that the z-axis points normal to the membrane plane into the electrolyte; see Fig. 12.1. Finally, the relation between surface charge density (or, equivalently, average mole fraction $\bar{\phi}$ of the anionic lipid) and dimensionless surface potential $\tilde{\Psi}^{(b)} = \Psi(z = 0, x \to \pm\infty)$ in the bulk is, according to non-linear Poisson-Boltzmann theory, given by [35]

$$\tilde{\Psi}^{(b)}(\bar{\phi}) = -2 \left(\frac{2\pi l_B l_D}{a} \bar{\phi} \right) \tag{5.11}$$

We highlight that $\bar{\phi}$ and $\tilde{\Psi}^{(b)}$ adopt the values $\bar{\phi}_1$ and $\tilde{\Psi}_1^{(b)}$ in phase 1 (for $x < 0$), and $\bar{\phi}_2$ and $\tilde{\Psi}_2^{(b)}$ in phase 2 (for $x > 0$).

Because of its non-linear nature, analytic solutions of Eq. 5.7 can be found only for a few specific geometries and boundary conditions, a fact that generally necessitates the use of approximations or numerical methods. An efficient method to numerically solve Eq. 5.7 for all four sets of boundary conditions listed above employs a Newton-Raphson iteration scheme which starts with $\Psi_n = 0$ for $n = 1$ and subsequently progresses from n to $n+1$ according to

$$l_D^2 \triangle \Psi_{n+1} = (\Psi_{n+1} - \Psi_n) \cosh \Psi_n + \sinh \Psi_n \tag{5.12}$$

until convergence (where $\Psi_{n+1} = \Psi_n$) is achieved for sufficiently large n. Note that Eq. 5.12 is linear in Ψ_{n+1} and can thus be solved for any given Ψ_n using standard methods. An analogous scheme can also be employed to linearize the boundary conditions of the type in Eqs. 5.9 or 5.10.

At large distances away from the phase boundary, $|x| \gg l_D$, the solution of the Poisson-Boltzmann equation approaches that of a bulk system where the composition $\phi(x) = \bar{\phi}$ is homogeneous in each phase and where the dimensionless surface potential $\tilde{\Psi}^{(b)}$ is that specified in Eq. 5.11. The corresponding electrostatic free energy per unit area A in each of the two bulk phases is

$$\frac{F_{el}^{(b)}}{Ak_BT} = -\frac{4\sinh^2(\tilde{\Psi}^{(b)}/4)}{2\pi l_B l_D} \tag{5.13}$$

if the electrostatic surface potential $\tilde{\Phi}^{(b)} = k_BT\tilde{\Psi}^{(b)}/e$ is fixed and

$$\frac{F_{el}^{(b)}}{Ak_BT} = 2\frac{\bar{\phi}}{a}\left[\frac{1-q}{p} + \ln(p+q)\right] \tag{5.14}$$

if the surface charge density $\sigma = -e\bar{\phi}/a$ or the electrochemical potential μ are fixed. For Eq. 5.14 we have used the definitions $p = 2\pi l_B l_D \bar{\phi}/a$ and $q = \sqrt{p^2+1}$.

5.2.3. Electrostatic Contribution to the Line Tension

The line tension Λ_{el} is defined as the electrostatic *excess* free energy (per unit length) due to the interactions of the anionic lipids in phase 1 with those in phase 2 including all secondary effects such as compositional modifications and changes in the structure of the diffuse counterion layer. From the total electrostatic free energy F_{el} (which we compute numerically and which we identify with $F_{el}^{(\sigma)}$, $F_{el}^{(\tilde{\Phi})}$, or $F^{(\mu)}$, depending on whether the surface charge density σ, surface potential $\tilde{\Phi}$, or electrochemical potential μ in a given phase is fixed) and the known bulk free energy (given by Eqs. 5.13 or 5.14) we extract the electrostatic line tension through

$$\Lambda_{el} = \frac{F_{el} - F_{el}^{(b)}}{L}, \tag{5.15}$$

where $F_{el}^{(b)}$ refers to the same combined total area of phases 1 and 2 in the lipid layer as F_{el} but treating both as bulk phases. In Eq. 5.15, L denotes the length of the domain boundary along the y-axis in which we solve the Poisson-Boltzmann equation. Of course Λ_{el} does not depend on the choice of L because the structure of

the phase boundary is invariant along the y-direction. Yet, we highlight that we assume the domain boundary to be straight. Bending the boundary would entail an additional energy cost and thus an increase in Λ_{el}.

5.3. Results and Discussion

We have solved the non-linear Poisson-Boltzmann equation, Eq. 5.7, for each of the four sets of boundary conditions specified above. Numerical solutions are computed in a region $x_{min} \leq x \leq x_{max}$, $0 \leq z \leq z_{max}$, and a unit length L along the y-direction, with $-x_{min} = x_{max} = z_{max} = 5l_D$. Using the numerical solutions $\Psi(x,z)$ we compute the corresponding free energy F_{el} and from Eq. 5.15 calculate Λ_{el} as function of $\bar{\phi}_1$, $\bar{\phi}_2$ and l_D. In all cases we used the Bjerrum length $l_B = 0.7\,\text{nm}$ and a cross-sectional area per lipid of $a = 0.65\,\text{nm}^2$. Our results for Λ_{el} as function of $\bar{\phi}_2$ are displayed in the diagrams of Fig. 12.2; different rows refer to different combinations of $\bar{\phi}_1$, different columns to different Debye screening lengths ($l_D = 1\,\text{nm}$ in the left column and $l_D = 3\,\text{nm}$ in the right column).

The four curves in each diagram correspond to our four sets of boundary conditions I-IV. Fig. 5.2 is the main result of the present work.

Fig. 5.2 reveals that Λ_{el} is always negative due to the electrostatic free energy gain at the interfacial region. When $\bar{\phi}_1 = \bar{\phi}_2$, both phases have the same bulk lipid composition and a boundary between them no longer exists. Then, the excess free energy vanishes and Λ_{el} becomes equal to zero for all types of boundary conditions I-IV. Each diagram in Fig. 12.2 displays four curves. The two solid curves correspond to the thermodynamic limits of immobile lipids (boundary condition I, upper solid curve) and unrestricted migration of charges in phase 2 (boundary condition II, lower solid curve). In between these two curves is a dotted curve that refers to boundary condition III, where the lipids in phase 2 have a constant electrochemical potential. As discussed above, thermodynamics requires that the dotted curves stay strictly in between the two solid ones. We note that in most cases the two solid curves stay close together, which indicates a limited influence of the charge mobility in phase 2. However, if $\bar{\phi}_1$ is large and $\bar{\phi}_2$ is small, lipid migration entails a significant influence on Λ_{el}; see the discussion below. Finally, the dashed curves in Fig. 5.2 correspond to constant electrochemical potential in both phases 1 and 2 (boundary condition IV). This is the physically most relevant set of boundary conditions if both phases are in the fluid state, thus containing mobile lipids with the corresponding demixing entropy penalty accounted for.

Besides our numerical approach, for boundary conditions I and II we have also calculated explicit

analytic expressions for Λ_{el} in the linear Debye-Hückel limit (which requires $|\Psi| \ll 1$ at each location within the aqueous phase). This approximation leads to a linearized Poisson-Boltzmann equation, $l_D^2 \nabla^2 \Psi = \Psi$,

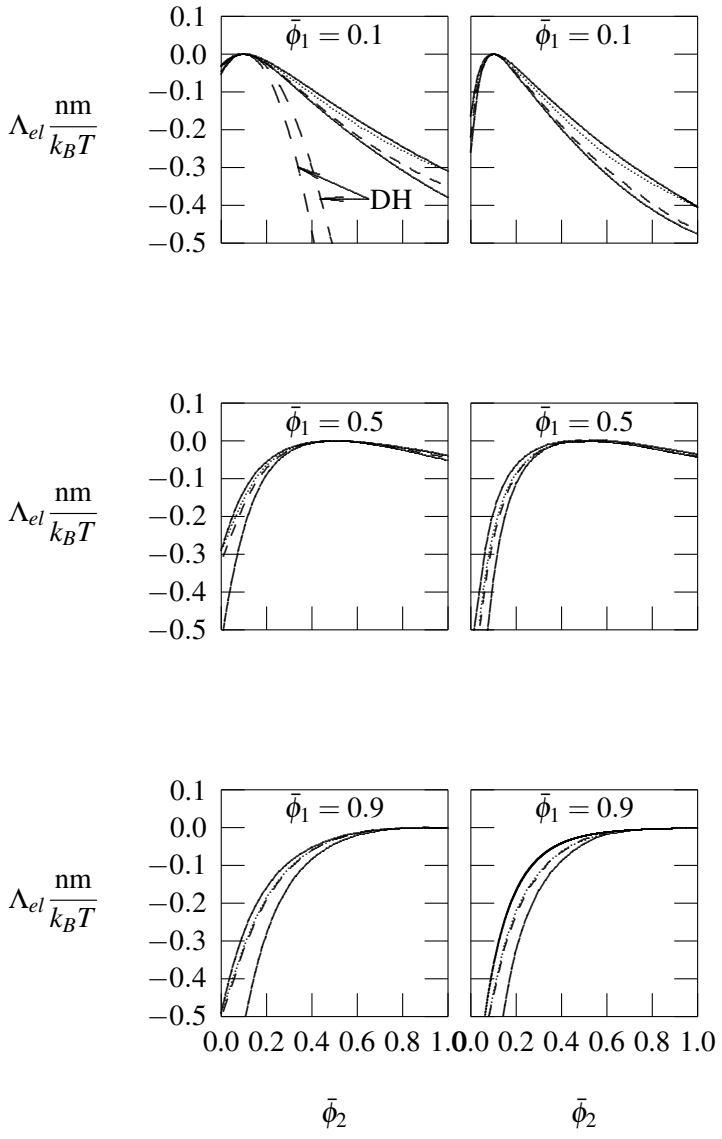

Figure 5.2. Electrostatic contribution to the line tension Λ_{el} plotted as function of the bulk lipid composition of phase 2, $\bar{\phi}_2$, for fixed $\bar{\phi}_1 = 0.1, 0.5, 0.9$. Upper solid lines correspond to fixed charge densities in both phases (case I); lower solid lines to phase 1 at constant electric potential and phase 2 at constant charge density (case II); dotted lines to constant charge density in one phase and constant chemical potential in the other (case III); and dashed lines to constant chemical potential in both phases (case IV). The long dashed lines in left-top diagram (indicated by DH), refer to results obtained in the Debye-Hückel limit. Left and right plots refer to $l_D = 1\,\text{nm}$ and $l_D = 3\,\text{nm}$, respectively. We have used a Bjerrum lenght $l_B = 0.7\,\text{nm}$ and a cross-sectional area per lipid $a = 0.65\,\text{nm}^2$ in all calculations.

which can be solved using the Kontorovich-Lebedev transformation [154, 60] and yields

$$\Lambda_{el} = -\frac{(\tilde{\Psi}_1^{(b)} - \tilde{\Psi}_2^{(b)})^2}{8\pi^2 l_B} \quad \text{for boundary condition I,} \tag{5.16}$$

$$\Lambda_{el} = -\frac{(\tilde{\Psi}_1^{(b)} - \tilde{\Psi}_2^{(b)})^2}{16\pi l_B} \quad \text{for boundary condition II,} \tag{5.17}$$

where $\tilde{\Psi}_{1,2}^{(b)} = \tilde{\Psi}^{(b)}(\bar{\phi}_{1,2}) = -4\pi l_B l_D \bar{\phi}_{1,2}/a$ are linearized versions of Eq. 5.11. Recall that boundary condition I refers to fixing the surface charge densities σ_1 and σ_2 in both phases; boundary condition II fixes σ_1 in phase 1 and the surface potential $\tilde{\Phi}_2$ in phase 2. As is required thermodynamically, Λ_{el} is larger (that is, less negative) in the former case as compared to the latter. The derivation of Eqs. 5.16 and 5.17 is outlined in the Appendix. The long dashed lines indicated by DH in the left-top diagram of Fig. 5.2 provide a comparison between the values obtained from Eqs. 5.16 and 5.17 (broken lines) and the corresponding outputs from our numerical solution in the non-linear regime (solid lines). We note that the linear and non-linear regimes coincide only for a very small compositional range when both $\bar{\phi}_1$ and $\bar{\phi}_2$ are small; higher charge densities render the assumption of small potentials no longer valid. For both boundary conditions (I and II), we point out that while in the linear regime Λ_{el} always adopts a quadratic behavior $\Lambda_{el} \sim (\bar{\phi}_1 - \bar{\phi}_2)^2$, no such symmetry is present in the non-linear case. This results from non-linear effects that are absent in the linear Debye-Hückel regime.

Upon decreasing the amount of salt in solution, electrostatic interactions become less screened and we expect larger magnitudes of Λ_{el}. Indeed, with a larger Debye length l_D (right column of diagrams in Fig. 5.2, calculated for $l_D = 3\,\text{nm}$), we see that Λ_{el} reaches more negative values. To illustrate this fact, for boundary condition II and $\bar{\phi}_1 = 0.9$ and $\bar{\phi}_2 = 0.025$ we obtain $\Lambda_{el} = -0.73\,k_BT/\,\text{nm}$ for $l_D = 1\,\text{nm}$ and $\Lambda_{el} = -1.25\,k_BT/\,\text{nm}$ when $l_D = 3\,\text{nm}$.

We now discuss the influence of lipid migration on the electrostatic line tension Λ_{el}. To this end, Fig. 5.3 shows the compositional profile $\phi(x)$ for the specific case $\bar{\phi}_1 = 0.75$, $\bar{\phi}_2 = 0.25$ and $l_D = 3\,\text{nm}$. The two solid curves refer to boundary conditions I and II, the dotted curve to boundary conditions III, and the dashed curve to boundary conditions IV. The corresponding four line tensions are $\Lambda_{el} = -0.10\,k_BT/\,\text{nm}$ (case I), $\Lambda_{el} = -0.17\,k_BT/\,\text{nm}$ (case II), $\Lambda_{el} = -0.13\,k_BT/\,\text{nm}$ (case III), and $\Lambda_{el} = -0.12\,k_BT/\,\text{nm}$ (case IV). Fig. 5.3 indicates that lipid migration tends to further enhance compositional differences in the vicinity

of a phase boundary. That is, the interfacial region is attractive and repulsive to lipids residing in the phase with larger and smaller $\bar{\phi}$, respectively. The domain boundary-induced compositional enhancement is largest if the mobility of charges in a given phase is unrestricted and becomes smaller if an additional demixing entropy penalty is present. The physical origin for the enhancement of compositional differences near a phase boundary is the same that renders Λ_{el} negative in the first place: anionic lipids in the more highly charged phase have fewer anionic lipids to interact with when close to the phase boundary. The corresponding gain in free energy is larger than the concomitant loss due to the fact that anionic lipids in the less highly charged phase have more anionic lipids to interact with when close to the phase boundary. Clearly then, the more highly charged phase further attracts anionic lipids to its boundary whereas the less highly charged phase repels them.

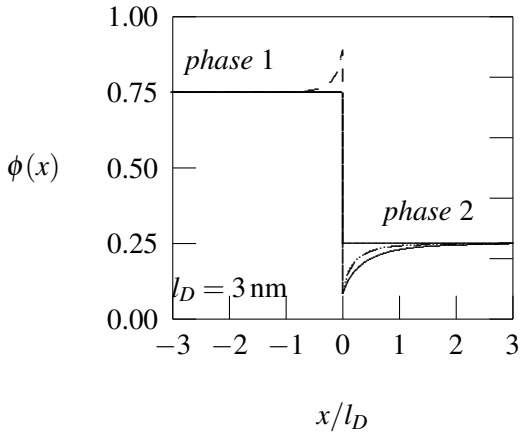

Figure 5.3. Lipid composition $\phi(x)$ normal to the phase boundary for $\bar{\phi}_1 = 0.25$ and $\bar{\phi}_2 = 0.75$. Straight solid lines correspond to fixed charge densities at both phases (case I); upper right solid line to phase 1 at constant electric potential and phase 2 at constant charge density (case II); dotted lines to constant charge density in one phase and constant chemical potential in the other (case III); and dashed lines to constant chemical potential in both phases (case IV). We have used a Bjerrum lenght $l_B = 0.7$ nm, a Debye length $l_D = 3$ nm, and a cross-sectional area per lipid $a = 0.65\,\mathrm{nm}^2$.

For the boundary conditions and lipid compositions analyzed here, the calculated magnitudes of Λ_{el} are generally on the order of $1\,k_BT/\mathrm{nm}$ ($\approx 4.1pN$), thus being comparable to values reported experimentally for the total line tension [155, 53]. For example, Tian *et al* [155] determined the line tension between coexisting L_o and L_d phases within giant unilamellar vesicles composed by mixtures of dioeoylphosphatidylcholine

(DOPC), cholesterol (Chol) and egg sphingomyeline (ESM). For a DOPC:Chol:ESM compositional ratio of 0.34:0.16:0.5 they measured an average total line tension of $\Lambda = 3.3\,\mathrm{pN} \approx 0.8\,k_BT/\mathrm{nm}$. If the ratio was 0.34: 0.4:0.26, which is closer to the critical point, the line tension dropped to $0.5\,\mathrm{pN} \approx 0.1\,k_BT/\mathrm{nm}$. Monolayers composed by dihydrocholesterol (Dchol, 15-25 mol%) and different lipids were investigated by Bischof and Wilke [53], yielding $\Lambda \approx 0.9\,\mathrm{pN}$ for Dchol:DPPE and $\Lambda \approx 0.15\,\mathrm{pN}$ for Dchol:DPPG binary mixtures. Here DPPE and DPPG refer to dipalmitoylphosphatidylethanolamine and dipalmitoylphosphatidylglycerol, respectively. We note that it is currently not possible to extract the electrostatic contribution Λ_{el} from the total measured line tension Λ. Even when comparing lipids with the same acyl chain structure (like DPPE and DPPG), the chemical differences of their headgroups imply different properties to form domains and thus different non-electrostatic contributions to the line tension. For example, the phosphatidylethanolamine headgroup of DPPE has an effectively smaller size than that of phosphatidylglycerol, which affects the cross-sectional area occupied by the lipid and induces a pronounced negative spontaneous curvature. Even experiments with identical lipid mixtures but distinct electrostatic properties (e.g., amounts of added salt) cannot be used straightforwardly to extract Λ_{el}, because electrostatic interactions modify the cross-sectional area per lipid and thus also affect the non-electrostatic contribution to Λ. Note there is a similar coupling between electrostatic and non-electrostatic interactions for the bending stiffness of a lipid bilayer [156].

5.4. Conclusions

The electrostatic contribution Λ_{el} to the total line tension Λ between two phases with distinct average charge density in a planar lipid membrane was determined using non-linear Poisson-Boltzmann theory. To this end, we have numerically solved the Poisson-Boltzmann equation for a set of four different boundary conditions that account for varying levels of lipid mobility. For two limiting thermodynamic cases we have also calculated Λ_{el} based on the linear Debye-Hückel regime by solving the linearized Poisson-Boltzmann equation. In this case, the use of the Kontorovich-Lebedev transformation provided us with analytical expressions for Λ_{el} which, due to their simplicity, may be used in subsequent membrane modeling approaches.

We generally find Λ_{el} to be negative with a magnitude below or on the order of $1 k_BT/\,\mathrm{nm}$ when the Debye length l_D is in the range $1-3\,\mathrm{nm}$. The negative values for Λ_{el} are a consequence of the favorable electrostatic conditions near the boundary of two phases with different average surface charge densities. Our theoretically predicted negative electrostatic contribution to Λ is on the same order than the positive

values deduced from experimental measurements. This clearly highlights the importance of electrostatic interactions for the ensuing line tension. Yet, we also emphasize that electrostatic and non-electrostatic contributions to Λ influence each other, which makes the extraction of Λ_{el} from experimentally reported values for Λ difficult.

5.5. Appendix : Calculation of Λ_{el} using the Kontorovich-Lebedev transformation

We solve the linearized Poisson-Boltzmann equation expressed in polar coordinates r and φ,

$$\frac{1}{r}\frac{\partial}{\partial r}\left(r\frac{\partial \Psi}{\partial r}\right)+\frac{1}{r^2}\frac{\partial^2 \Psi}{\partial \varphi^2}=\frac{\Psi}{l_D^2}, \tag{5.18}$$

for the dimensionless electrostatic potential $\Psi=\Psi(r,\varphi)$ within the region $0\le r\le\infty$ and $0\le\varphi\le\pi$ depicted in Fig. 5.4. Let us first consider the mixed case where one phase is kept at constant charge density σ_1 and the other at fixed and constant dimensionless surface potential $\tilde{\Psi}_2^{(b)}$. When expressed in polar coordinates, the boundary conditions specified in case II above read

$$\frac{1}{r}\left(\frac{\partial \Psi}{\partial \varphi}\right)_{\varphi=\pi}=4\pi l_B\frac{\sigma_1}{e}, \qquad \Psi(r,\varphi=0)=\tilde{\Psi}_2^{(b)} \tag{5.19}$$

and $\Psi(r\to\infty,\varphi)=0$. The first relation fixes the surface charge density $\sigma_1=-e\bar{\phi}_1/a$ of phase 1, and the second relation specifies the surface potential $\tilde{\Phi}_2^{(b)}=k_BT\tilde{\Psi}_2^{(b)}/e$ of phase 2.

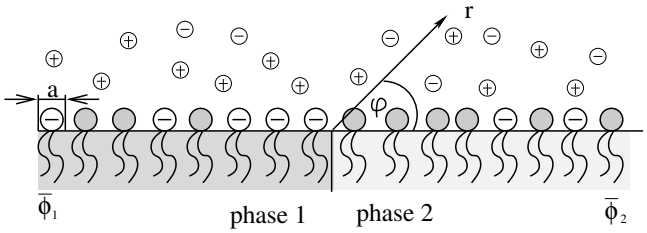

Figure 5.4. Schematic illustration of a planar lipid layer with two phases as in Fig. 12.1, yet described in terms of polar coordinates r and ϕ (instead of Cartesian coordinates). The aqueous phase corresponds to the range $0<r<\infty$ and $0<\phi<\pi$.

A convenient method to solve Eq. 5.18 and to calculate Λ_{el} employs the Kontorovich-Lebedev

transformation [154, 157, 158, 60] $\Psi(r,\varphi) \rightarrow \Upsilon(\lambda,\varphi)$, defined through

$$\Upsilon(\lambda,\varphi) = \int_0^\infty \frac{dr}{r} \Psi(r,\varphi)\, \mathrm{K}_{i\lambda}(r/l_D) \tag{5.20}$$

and its corresponding back-transformation

$$\Psi(r,\varphi) = \frac{2}{\pi^2} \int_0^\infty d\lambda\, \Upsilon(\lambda,\varphi)\, \mathrm{K}_{i\lambda}(r/l_D)\, \lambda\, \sinh(\pi\lambda) \tag{5.21}$$

where $K_{i\lambda}(x)$ is the modified Bessel function of the second kind of order λ and i is the imaginary unit. We note that the same method has been used previously by Duplantier [159] and Kang *et al* [60] for wedge-like geometries and boundary conditions of type I (yet not for type II). When expressed in terms of $\Upsilon = \Upsilon(\lambda,\varphi)$, Eq. 5.18 reads

$$\frac{\partial^2 \Upsilon}{\partial \varphi^2} = \lambda^2 \Upsilon \tag{5.22}$$

and the two boundary conditions in Eq. 5.19 become

$$\left(\frac{\partial \Upsilon}{\partial \varphi}\right)_{\varphi=\pi} = \frac{\pi \tilde{\Psi}_1^{(b)}}{2\cosh(\frac{\pi}{2}\lambda)}, \tag{5.23}$$

$$\Upsilon(\lambda, \varphi = 0) = \frac{\pi \tilde{\Psi}_2^{(b)}}{2\lambda \sinh(\frac{\pi}{2}\lambda)}. \tag{5.24}$$

with $\tilde{\Psi}_1^{(b)} = -4\pi l_B l_D \bar{\phi}_1 / a$. The condition $\Psi(r \rightarrow \infty, \varphi) = 0$ is consistently fulfilled due to the property $K_n(x \rightarrow \infty) = 0$ for all choices of n. The solution of Eq. 5.22 subject to the boundary conditions in Eqs. 5.23 and Eq. 5.24 is

$$\Upsilon = \frac{\pi}{2\lambda \cosh(\lambda\pi)} \left[\tilde{\Psi}_2^{(b)} \frac{\cosh[\lambda(\pi-\varphi)]}{\sinh(\frac{\pi}{2}\lambda)} + \tilde{\Psi}_1^{(b)} \frac{\sinh(\lambda\varphi)}{\cosh(\frac{\pi}{2}\lambda)} \right]. \tag{5.25}$$

Transforming back from $\Upsilon(\lambda,\varphi)$ to $\Psi(r,\varphi)$ according to Eq. 5.21 gives rise to

$$\begin{aligned}\Psi(r,\varphi) &= \frac{2}{\pi}\int_0^\infty d\lambda \frac{\mathrm{K}_{i\lambda}(r/l_D)}{\cosh(\lambda\pi)}\Bigg[\tilde{\Psi}_2^{(b)}\cosh\left(\frac{\pi}{2}\lambda\right) \\ &\times \cosh[\lambda(\pi-\varphi)]+\tilde{\Psi}_1^{(b)}\sinh\left(\frac{\pi}{2}\lambda\right)\sinh(\lambda\varphi)\Bigg].\end{aligned} \tag{5.26}$$

From the solution $\Psi(r,\varphi)$ in Eq. 5.26 we calculate the electrostatic line tension Λ_{el} as the *excess* free energy per unit length

$$\begin{aligned}\frac{\Lambda_{el}}{k_BT} &= \frac{\sigma_1}{2e}\int_0^\infty dr\left[\Psi(r,\pi)-4\pi l_B l_D\frac{\sigma_1}{e}\right] \\ &+ \frac{\tilde{\Psi}_2^{(b)}}{8\pi l_B}\int_0^\infty dr\left[\frac{1}{r}\left(\frac{\partial\Psi(r,\varphi)}{\partial\varphi}\right)_{\varphi=0}+\frac{\tilde{\Psi}_2^{(b)}}{l_D}\right].\end{aligned} \tag{5.27}$$

Instead of using σ_1, it is convenient to express the fixed surface charge density in phase 1 in terms of the corresponding surface potential $\tilde{\Psi}_1^{(b)}=4\pi l_B l_D\sigma_1/e$ far away from the boundary between the phases (that is $\tilde{\Psi}_1^{(b)}=\Psi(r\to\infty,\varphi=\pi)$). From Eq. 5.26 we can compute both $\Psi(r,\pi)$ and $(\partial\Psi/\partial\varphi)_{\varphi=0}$ and use these results to calculate the excess free energy according to Eq. 5.27. This leads to the expression for Λ_{el} as specified in Eq. 5.17.

When each of the two phases carries a fixed surface charge density (σ_1 in phase 1 and σ_2 in phase 2, as specified in boundary condition type I above), Eq. 5.19 reads

$$\frac{1}{r}\left(\frac{\partial\Psi}{\partial\varphi}\right)_{\varphi=\pi} = 4\pi l_B\frac{\sigma_1}{e},\ \ \frac{1}{r}\left(\frac{\partial\Psi}{\partial\varphi}\right)_{\varphi=0}=4\pi l_B\frac{\sigma_2}{e}. \tag{5.28}$$

The derivation of Λ_{el} follows the same steps as for the mixed boundary conditions, leading to the final result specified in Eq. 5.16.

We note that the result in Eq. 5.16 also appears as a special case of calculating Λ_{el} in a wedge-like geometry where the wedge subtends an angle α. For this case, Λ_{el} is given by

$$\Lambda_{el}(\alpha)=\frac{(\tilde{\Psi}_1^{(b)2}+\tilde{\Psi}_2^{(b)2})M_1(\alpha)-(\tilde{\Psi}_1^{(b)}-\tilde{\Psi}_2^{(b)})^2M_2(\alpha)}{4\pi l_B}. \tag{5.29}$$

The two functions $M_1(\alpha)$ and $M_2(\alpha)$ have been calculated previously by Kang *et al* [60]

$$M_1(\alpha) = \int_0^\infty d\omega \left[\frac{\tanh(\omega\alpha)}{\tanh(\omega\pi)} - 1\right] \tag{5.30}$$

and

$$M_2(\alpha) = \int_0^\infty d\omega \left[\frac{\tanh(\omega\alpha)}{\sinh(2\omega\pi)} - c\right] \tag{5.31}$$

with $c = 0$. We note a typo in the work of Kang *et al* [60], who state Eq. 5.31 with $c = 1$. For $\alpha = \pi$ we find $M_1(\alpha) = 0$ and $M_2(\pi) = 1/(2\pi)$, and Eq. 5.29 becomes the same as Eq. 5.16.

5.6. Acknowledgments

G. V. B. acknowledges a doctoral scholarship from CAPES Foundation/Brazil Ministry of Education (Grant No. 9466/13-4). M. A. B. acknowledges the Swiss National Science Foundation for an International Short Visit travel grant to North Dakota State University.

6. MODELING LIPID-LIPID CORRELATIONS ACROSS A BILAYER MEMBRANE USING THE QUASI-CHEMICAL APPROXIMATION*

6.1. Introduction

Biomembranes constitute an example par excellence for complex fluids: they are self-assembled structures consisting of lipids and proteins that exhibit no long-range order but form dynamically changing heterogeneities on the nanometer-scale due to a complex interplay of *lipid-based* interactions and *protein-based* scaffolding. The former and latter are often discussed in terms of two conceptual models, the "lipid raft" model [47, 160] and the "fence and picket" model [161], respectively. Lipid-based interactions, especially in the presence of cholesterol, have been studied extensively in the context of nonideal mixing, domain formation, and lateral phase separation in model membranes [162, 163, 164, 165].

One specific question that has attracted some interest is the interaction of domains *across* a lipid bilayer. Inter-leaflet coupling of solid-phase domains in fluid membranes has been demonstrated experimentally already more than two decades ago [166]. Spatial registration across the membrane exists also for fluid-phase domains in coexisting liquid-ordered and liquid-disordered phases. In a symmetric model membrane fluid-phase domains appear in spatial registration across the bilayer [167]. In an asymmetric membrane domain formation in one leaf can be induced or suppressed by the apposed leaf [168, 169]. Additional evidence of inter-leaflet coupling has been deduced, for example, from variations of phase separation temperatures in asymmetric versus symmetric bilayers [170] and from the dependence of protein sequestration into membrane domains on bilayer asymmetry [171]. The domains are large in all these cases, on the order of hundreds of nanometers or even micrometers, and thus reflect collective interactions of many lipids across the bilayer.

Evidence for inter-leaflet coupling exists also on the level of individual lipids. For example, the diffusion of particle-labeled lipids is affected by inter-leaflet coupling on the scale of a few nanometers [172].

*Reproduced with permission from "G. V. Bossa, J. Roth, S. May, Modeling lipid–lipid correlations across a bilayer membrane using the quasi-chemical approximation, Langmuir 31 (36) (2015) 9924–9932". Copyright 2015 American Chemical Society. This paper can be accessed online at `http://pubs.acs.org/doi/abs/10.1021/acs.langmuir.5b01719`. The material in this chapter was co-authored by Guilherme V. Bossa, Joseph Roth, and Sylvio May. G. V. Bossa contributed to the manuscript writing. G.V.B. was responsible for the mathematical development, simulation procedure, figures preparation, and discussion of the results.

An experimental method that probes correlations of lateral membrane organization on a molecular level is Nearest-Neighbor Recognition (NNR) developed by Regen and coworkers [62]. This method exploits a thiolate-disulfide interchange reaction to obtain a snapshot of nearest neighbor lipid distribution in a mixed membrane. NNR has originally been used to investigate molecular recognition between phospholipids but has recently also been applied to study interactions of phospholipids with cholesterol [173] and lipidated peptides [174]. A specific system designed to accentuate inter-leaflet correlations is a binary lipid membrane that contains lipids with two different hydrocarbon chain lengths: a short-chain and a long-chain lipid. To avoid the creation of a hydrophobic mismatch [175, 176] between long and short acyl chains, the lipids can be expected to arrange complementarily across the bilayer (i.e. a short-chain lipid in one leaf facing a long-chain lipid in the apposed leaf). Indeed, using NNR Regen and coworkers have been able to demonstrate and quantify such correlations [177, 178, 2].

We note that the NNR experiments have motivated a number of computer simulation studies based either on atomistic or coarse grained lipid models. Molecular Dynamics simulations have yielded a significant degree of complementarity for a mixture of gel and fluid phase lipids [179] and for small lipid domains [180]. A Monte Carlo simulation study [181] has identified entropy-driven clustering and complementary matching, arising from the steric hindrance of long-chain lipids across the bilayer. Finally, a weak degree of complementary matching was predicted by a hybrid method [182] for a mixture of two fluid phase forming lipids of different hydrocarbon chain lengths. In addition to these simulation works, Williamson and Olmsted [183] have recently presented a lattice model to study the registration versus anti-registration of domains during phase separation. The model aims to describe sufficiently large domains, but it also incorporates chain packing aspects on the level of individual lipids, including the tendency to avoid hydrophobic mismatch through complementary lipid packing across the bilayer. The authors analyze their model on the mean-field level, thereby predicting interesting kinetic scenarios where small anti-registered metastable domains may form initially and then nucleate to reach a stable thermodynamic equilibrium of large registered domains.

The present theoretical work was motivated by one of the above-mentioned NNR studies, where Zhang *et al* [2] have determined the degree of *cross talk* between the two leaves of a binary lipid bilayer. To briefly discuss that study, consider the probability of the two lipid types, in the following labeled 1 and 2, to form (11), (12), and (22) pairs in an equimolar $1:1$ lipid bilayer. Here, pair formation refers to lipids residing in the same leaflet, where their headgroups are in close contact and able to engage in a chemical

reaction that results in disulfide bridging. NNR measures these probabilities by taking a snapshot of nearest neighbor contacts. That is, it determines the concentrations [11], [12], and [22] of lipid-lipid pairs. From this, Zhang *et al* [2] calculated the equilibrium constant $K = [12]^2/([11][22])$, corresponding to the chemical reaction scheme $(11) + (22) \rightleftharpoons 2\,(12)$. For an ideal mixture $[12]/2 = [11] = [12]$ and thus $K = 4$. For $K \neq 4$ the mixing is nonideal: $K > 4$ favors an alternating checkerboard-like lipid arrangement and $K < 4$ manifests effective attraction between lipids of the same type, the latter favoring domain formation and possibly even phase separation. Zhang *et al* [2] have investigated two different versions of lipids of types 1 and 2, one with shorter (index "*s*") and one with longer (index "*l*") hydrocarbon chains (yet, each lipid variation 1_s and 1_l as well as 2_s and 2_l with the same headgroup structure). The corresponding equilibrium constants for the three equimolar lipid mixtures 1_s2_s, 1_l2_l, and 1_s2_l, were found to be $K_{ss} = 6.55 \pm 0.36$, $K_{ll} = 6.76 \pm 0.16$, and $K_{sl} = 6.92 \pm 0.47$, respectively. Here, the presence of a mismatch in the lipid's hydrocarbon chain lengths did not significantly affect the degree of nonideality as compared to having no mismatch. We note that all three equilibrium constants were larger than 4, which likely resulted from the fact that one lipid type was carrying a negative excess charge. The corresponding electrostatic interaction leads to an effective repulsion between lipids of the same type implying $K > 4$. It is worth pointing out, however, that the excess charge is only one among a multitude of often opposing factors in determining the mixing properties of lipid membranes [184].)

In another set of experiments, Zhang *et al* [2] added the divalent cationic ligand hexamethyl-1,6-hexanediammonium dichloride to each of the three mixtures 1_s2_s, 1_l2_l, and 1_s2_l. Because of its two positive charges the ligand tends to bind to (and thus bring into close proximity) two charged lipids. Hence, the equilibrium constant is expected to decrease. Indeed, the authors find $K_{ss} = 4.88 \pm 0.27$, $K_{ll} = 4.86 \pm 0.09$, and $K_{sl} = 3.84 \pm 0.12$, all being smaller than their corresponding values in the absence of the ligand. In fact, the presence of the divalent ligand renders all three mixtures more ideal and, most importantly, introduces a significant difference for matching and non-matching lipid chain lengths. Consequently, the additional decrease of the equilibrium constant for the lipid mixture with non-matching lipid chains was interpreted by Zhang *et al* [2] as an indication of cross talk across the bilayer. We point out that it is not obvious to rationalize why cross talk across the bilayer is only observed in the presence of the ligand but not in its absence. Ligand-induced modifications of lipid-lipid interactions within each leaflet seem to affect lipid-lipid recognition across the bilayer.

In this work we propose a theoretical model for the interaction of lipids within and across a lipid

bilayer. To account for nearest neighbor correlations between lipids within and across lipid layers we need to go beyond the often used Landau or Landau-Ginzburg mean-field theory. Because the analysis by Zhang *et al* [2] of their NNR experiments is carried out in terms of a chemical reaction scheme, we find it appropriate to employ a similar modeling approach, namely the quasi-chemical approximation (QCA). To this end we apply QCA to a system of two coupled 2D lattice models (that represent the two macroscopically homogeneous leaves of a lipid bilayer). Although QCA (and modifications of it) is a frequently used method in statistical mechanics of weakly correlated systems to factorize contact probabilities [185, 186], it has rarely [187] been adapted to the context of lipid bilayers. Here, we apply QCA to a macroscopically homogeneous binary lipid bilayer that does not undergo lateral phase separation but exhibits lipid-lipid correlations on molecular scales both within and across its two leaflets.

Our model introduces three interaction parameters. The first (denoted below by ω) accounts for lipid-lipid interactions within each leaf. Because our model does not target phase transitions, ω does not need to carry a positive sign. In fact, a negative sign, which reflects an effective repulsion between lipids of the same type, will be most appropriate to model the experiments by Zhang *et al* [2]. The second interaction parameter (denoted below by η) describes lipid-lipid interactions across the membrane. Both ω and η reflect pairwise lipid-lipid interactions. The third parameter (denoted below by ε) accounts for the hydrophobic mismatch associated with lipids of different chain lengths, which involves multi-body interactions (that is, interactions involving four lipids on the level of QCA). We demonstrate that the observed presence of cross talk can be rationalized by QCA, but only if the hydrophobic mismatch parameter ε is included in the analysis.

6.2. Theory

6.2.1. Reminder of QCA

We briefly recall the basic idea behind QCA; further details can be found in textbooks [188, 189]. A binary lattice gas with nearest neighbor interactions can be analyzed using QCA by assuming that pairs of nearest neighbors are statistically uncorrelated. Consider a lattice of coordination number z with $N = N_1 + N_2$ sites of which N_1 and N_2 are occupied by molecules of type 1 and 2, respectively. Our notion of molecules is general but in this work we will identify them with lipids. Fig. 6.1 displays an example, a one-dimensional

system with $z = 2$.

We denote by $N_{11}, N_{12}, N_{21}, N_{22}$ the numbers of (11), (12), (21), (22) pairs, respectively. Conservation of N_1 and N_2 implies the relations $(z/2)N_1 = N_{11} + N_{12}$ and $(z/2)N_2 = N_{21} + N_{22}$. (Note that the periodic boundary conditions used to express these relations become irrelevant in the thermodynamic limit $N \to \infty$.) In addition, each (12) pair must be matched by a corresponding (21) pair, implying $N_{12} = N_{21}$. There is thus only one single degree of freedom left to the system, which we denote by the sum $\bar{N} = N_{12} + N_{21}$ of (12) and (21) pairs.

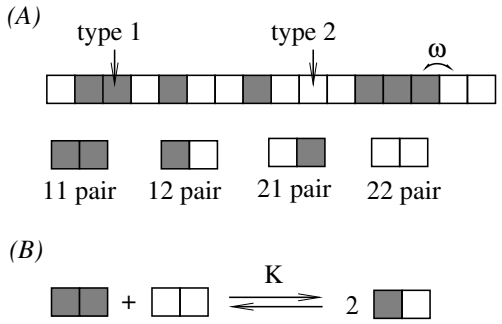

Figure 6.1. *A*: Schematic illustration of a one-dimensional lattice (of coordination number $z = 2$) with $N = 16$, $N_1 = 7$, $N_2 = 9$. The displayed example configuration has $N_{11} = 3$, $N_{12} = 4$, $N_{21} = 4$, $N_{22} = 5$ (assuming periodic boundaries). The interaction energy between a (12) or (21) pair is denoted by ω. Hence, the total interaction energy of the displayed configuration is $(N_{12} + N_{21})\omega = 8\omega$. *B*: The reaction scheme invoked by Eq. 6.4 is characterized by an equilibrium constant K.

We assume nearest neighbor interactions with a corresponding interaction energy ω between any two neighboring lattice sites that are occupied by different types of molecules. Hence, any given microstate entails an interaction energy $u = \omega(N_{12} + N_{21})$. The Helmholtz free energy is then

$$F = -\ln\left[\sum_{\{ij\}} e^{-u(\{N_{ij}\})}\right] \tag{6.1}$$

where the sum runs over all microstates; i.e., all possible distributions of (11), (12), (21), (22) pairs. Note also that everywhere in the present work we express the free energy (and, in fact, all energies) in units of the thermal energy $k_B T$ where k_B is Boltzmann's constant and T the absolute temperature. For sufficiently large system size (that is, in the thermodynamic limit $N \to \infty$) the sum in Eq. 6.1 can be approximated by its largest contribution. The quasi-chemical approximation offers a simple way to calculate that contribution

by assuming nearest neighbor pairs are uncorrelated. Indeed, accounting for pairwise (but no higher-order) correlations is the one step that QCA goes beyond the mean-field model. This allows us to write the free energy $F = F(N_{11}, N_{12}, N_{21}, N_{22})$ in Eq. 6.1 explicitly as

$$\begin{aligned} F &= F_0 + N_{11}\ln N_{11} + N_{12}\ln N_{12} \\ &+ N_{21}\ln N_{21} + N_{22}\ln N_{22} + \omega(N_{12} + N_{21}) \end{aligned} \tag{6.2}$$

where F_0 is a constant. As pointed out above, the N_{ij}'s are not all independent but can be expressed in terms of the single degree of freedom $\bar{N}$ through $N_{11} = (zN_1 - \bar{N})/2$, $N_{22} = (zN_2 - \bar{N})/2$, and $N_{12} = N_{21} = \bar{N}/2$. Inserting these equations into Eq. 6.2 yields $F(\bar{N})$ which must adopt a minimum in thermal equilibrium. From $(dF/d\bar{N})_{N_1,N_2} = 0$ we find

$$\frac{\bar{N}^2}{(zN_1 - \bar{N})(zN_2 - \bar{N})} = \frac{N_{12}N_{21}}{N_{11}N_{22}} = e^{-2\omega} \tag{6.3}$$

which constitutes a quadratic equation for $\bar{N}$. Eqs. 6.2 and 6.3 establish the framework for the extended model of the present work. We proceed with several remarks. First, although pairs (12) and (21) are microscopically distinguishable, they contribute the same to the averaged behavior of the system; it is therefore useful to rewrite Eq. 6.3 as

$$\frac{\bar{N}^2}{N_{11}N_{22}} = \frac{(N_{12} + N_{21})^2}{N_{11}N_{22}} = 4e^{-2\omega} = K \tag{6.4}$$

which can be viewed as resulting from the chemical reaction illustrated in Fig. 6.1B (hence the notion of the *quasi-chemical* approximation). The corresponding equilibrium constant is $K = 4\exp(-2\omega)$. Second, the limit $\omega \to 0$ leads to a non-interacting lattice gas, resulting in an equilibrium constant $K = 4$ as well as in $N_{11} = zN_1^2/N$, $N_{12} = N_{21} = (z/2)N_1N_2/N$, and $N_{22} = zN_2^2/N$. Third, consistency with the ideal gas limit determines the constant $F_0 = (1-z)[N_1\ln(N_1/N) + N_2\ln(N_2/N)] - (z/2)N\ln N$. Fourth, for $z = 2$ the quasi-chemical approximation represents the exact solution of the one-dimensional Ising model with conserved magnetization. Finally, calculation of the free energy upon insertion of F_0 and $\bar{N}$ (the solution of Eq. 6.3) is straightforward and leads to a well-known [188, 189] analytic expression for the free energy F.

6.2.2. QCA for Two Coupled Layers

We extend QCA to the case of two coupled lattice gases that represent the two leaflets of a lipid bilayer. The two lattice gases are referred to as external (E) and internal (I); both have the same size N and the same coordination number z. The external lattice contains N_1^E sites occupied by molecules of type 1 (and consequently $N_2^E = N - N_1^E$ sites occupied by molecules of type 2). Similarly, the internal lattice contains N_1^I sites occupied by molecules of type 1 (and consequently $N_2^I = N - N_1^I$ sites occupied by molecules of type 2). The two lattice gases reside on top of each other: each lattice site on one lattice is neighbor to a single corresponding site on the other, apposed, lattice. A specific microstate for a one-dimensional case (with $z = 2$) is illustrated in Fig. 6.2A.

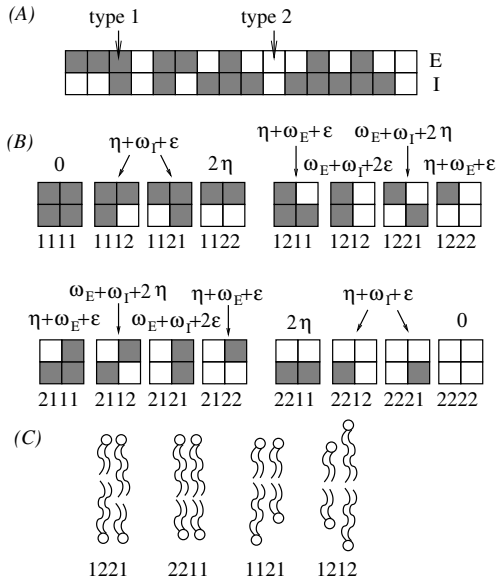

Figure 6.2. *A*: Schematic illustration of two coupled one-dimensional binary lattice gases (of coordination number $z = 2$) with $N = 16$, $N_1^E = 8$, $N_1^I = 10$. The displayed bilayer microstate has $N_{1122} = N_{1121} = N_{1212} = N_{2121} = N_{1112} = N_{1221} = N_{2221} = N_{2122} = 1$, $N_{2212} = 2$, and $N_{2111} = N_{1211} = 3$. The remaining N_{ijkl}'s vanish. The interaction energy for this particular example is $10\omega_E + 8\omega_I + 8\eta + 16\varepsilon$. *B*: All 16 distinct double pair conformations with their corresponding interaction energies. Here, ω_E and ω_I are nearest neighbor interaction energies within the external (E) and internal (I) layer, η is the interaction energy across the bilayer, and ε denotes the hydrophobic mismatch energy. *C*: Lipids with different chain length may or may not create hydrophobic mismatch. The identification of molecule types 1 and 2 with short and long chain lipids provides our motivation for the different mismatch energies. The displayed examples, (1221), (2211), (1121), and (1212), have mismatch energies of 0, 0, ε, and 2ε, respectively.

Our numerical calculations below are carried out for two-dimensional lattices with $z = 6$. To specify the microscopic state of the two coupled lattice gases, we introduce the notation $(ijkl)$ for a given double pair where each index can adopt the value 1 or 2. Here, the letters ij denote two neighboring sites in the external layer and kl two neighboring sites in the internal layer such that pairs ik and jl are spatially apposed across the layer. All $2^4 = 16$ different double pair conformations are illustrated in Fig. 6.2B.

Each double pair conformation is assigned a microscopic interaction energy. We account for four different contributions. First, nearest neighbors of type 1 and 2 in the external layer interact with energy ω_E. Second, nearest neighbors of type 1 and 2 in the internal layer interact with energy ω_I. Below we will set both interaction parameters equal, which is appropriate when modeling the experimental setup of Zhang *et al* [2]. Keeping ω_E and ω_I initially separate facilitates the discussion of the free energy contributions below and preserves applicability of our model to more general situations such as supported bilayers or a membrane whose two leaflets face different electrolytes. Third, there is an interaction energy η of nearest neighbors of type 1 and 2 across the two layers. Fourth, we assign an interaction energy ε to all double pairs that contain a 3:1 or 1:3 ratio of molecules of type 1 and 2, and an interaction energy 2ε to the double pairs (1212) and (2121). Our motivation for the fourth energy contribution is the *hydrophobic mismatch* penalty that two lipids of different chain length in a lipid bilayer incur; see the illustration in Fig. 6.2C. We note that the doubling of the hydrophobic mismatch penalty, when comparing conformations such as (1212) with (1211) represents a reasonable assumption; a more general model would assign two independent energy constants.

As an example consider the double pair (1121). It has an interaction energy $\eta + \omega_I + \varepsilon$ because the two lattice sites belonging to the internal layer interact with each other, there is one pair of different lipids interacting across the two layers, and the change in bilayer thickness implies a hydrophobic mismatch penalty. Note that while ω_E, ω_I, and η refer to two-body interactions, the hydrophobic mismatch energy ε emerges from a four-body interaction. We also point out that the two states (1221) and (2112) each have an energy $\omega_E + \omega_I + 2\eta$ and thus do not contain a hydrophobic mismatch penalty. This is a consequence of chain interdigitation across the midplane of the lipid bilayer as illustrated in Fig. 6.2C for the double pair (1221).

We denote by N_{ijkl} the number of double pairs that exhibit conformation $(ijkl)$. The 16 different N_{ijkl}'s are not all independent. The relations that exist between the N_{ijkl}'s can conveniently be expressed using the following summation convention: $N_{ijk\bullet} = N_{ijk1} + N_{ijk2}$ and analogously for any other index. That

is, appearance of the symbol $\bullet$ indicates summation over all combinations of the two possible values 1 and 2. For example, $N_{1\bullet 2\bullet} = N_{1121} + N_{1122} + N_{1221} + N_{1222}$, etc. Conservation of the numbers of lipids of type 1 and 2 in each layer then implies

$$\frac{z}{2} N_1^E = N_{1\bullet\bullet\bullet}, \quad \frac{z}{2} N_1^I = N_{\bullet\bullet 1\bullet}, \quad \frac{z}{2} N = N_{\bullet\bullet\bullet\bullet} \tag{6.5}$$

There are only three (and not four) independent conservation relations because the number of lattice sites (N) is the same for both layers. Furthermore, in each layer each pair (12) must be matched by a corresponding pair (21) in that same layer. This gives rise to the two relations

$$N_{12\bullet\bullet} = N_{21\bullet\bullet}, \qquad N_{\bullet\bullet 12} = N_{\bullet\bullet 21} \tag{6.6}$$

Eq. 6.6 can be viewed as symmetry relations that follow from the lateral isotropy of both lattices. In fact, four additional independent symmetry relations can be identified,

$$\begin{aligned} N_{1221} &= N_{2112}, \qquad N_{1212} = N_{2121} \\ N_{1121} &= N_{1112}, \qquad N_{1\bullet 1\bullet} = N_{\bullet 1\bullet 1} \end{aligned} \tag{6.7}$$

There is no other independent symmetry relation that would add to those in Eqs. 6.6 and 6.7. Hence, Eqs. 6.5, 6.6 and 6.7 comprise a set of 9 relations that reduce the number of degrees of freedom from 16 to 7. The free energy of the two coupled lattices can be written in analogy to Eq. 6.1 as

$$F = -\ln \left[\sum_{\{ijkl\}} e^{-u(\{N_{ijkl}\})} \right] \tag{6.8}$$

where $u = u(\{N_{ijkl}\})$ denotes the interaction energy for a given set $\{N_{ijkl}\}$ of double pairs and where the summation runs over all possible microstates $\{ijkl\}$. With the interaction scheme in Fig. 6.2B we can

express the interaction energy of any given bilayer microstate as

$$\begin{aligned} u &= (N_{1112}+N_{1121}+N_{2212}+N_{2221})(\eta+\omega_I+\varepsilon) \\ &+ (N_{1211}+N_{1222}+N_{2111}+N_{2122})(\eta+\omega_E+\varepsilon) \\ &+ (N_{1122}+N_{2211})\,2\eta \\ &+ (N_{1212}+N_{2121})(\omega_E+\omega_I+2\varepsilon) \\ &+ (N_{1221}+N_{2112})(\omega_E+\omega_I+2\eta) \end{aligned} \tag{6.9}$$

For example, the microstate displayed in Fig. 6.2A has $u = 10\omega_E + 8\omega_I + 8\eta + 16\varepsilon$. Using QCA renders all double pairs statistically independent and thus allows us to express the free energy of a sufficiently large system as

$$F = F_0 + u(\{N_{ijkl}\}) + \sum_{i=1}^{2}\sum_{j=1}^{2}\sum_{k=1}^{2}\sum_{l=1}^{2} N_{ijkl}\ln N_{ijkl} \tag{6.10}$$

where the constant F_0 is independent of the N_{ijkl}'s. We highlight that the statistical independence of the double pairs that enter Eq. 6.10 means all correlations between the 4 lipids that constitute a double pair can be accounted for; these include both pairwise and multi-body correlations. As pointed out, the system has 7 independent degrees of freedom. The derivative of the free energy with respect to all 7 degrees of freedom must vanish in thermal equilibrium. This gives rise to the following 7 equations

$$\begin{aligned} \frac{N_{1222}N_{2221}}{N_{1221}N_{2222}} &= e^{-2\varepsilon}, \\ \frac{N_{1112}N_{2111}}{N_{1111}N_{2112}} &= e^{-2\varepsilon}, \\ \frac{N_{1222}N_{2122}}{N_{1122}N_{2222}} &= e^{-2(\omega_E+\varepsilon)}, \\ \frac{N_{2212}N_{2221}}{N_{2211}N_{2222}} &= e^{-2(\omega_I+\varepsilon)}, \\ \frac{N_{2112}N_{1222}}{N_{1112}N_{2222}} &= e^{-2(\omega_E+\eta)}, \\ \frac{N_{2112}N_{2221}}{N_{2111}N_{2222}} &= e^{-2(\omega_I+\eta)}, \\ \frac{N_{1222}N_{2221}}{N_{1212}N_{2222}} &= e^{-2\eta} \end{aligned} \tag{6.11}$$

The reaction scheme invoked by Eqs. 6.11 is schematically displayed in Fig. 6.3. Note that Eqs. 6.5, 6.6 and 6.7 together with Eqs. 6.11 constitute a set of 16 equations for the occupation numbers N_{ijkl} of the 16

double pair conformations. For any given set of numbers N, N_1^E, N_1^I, ω_E, ω_I, η, ε the 16 different N_{ijkl}'s can easily be computed numerically.

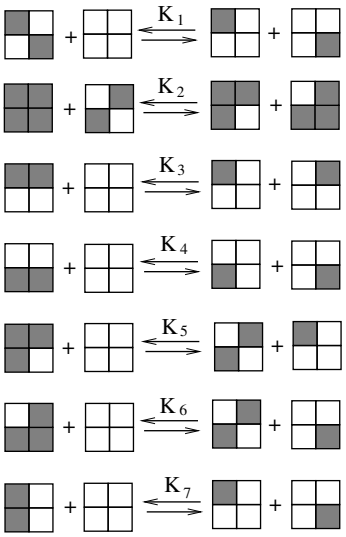

Figure 6.3. The reaction scheme invoked by Eqs. 6.11. The equilibrium constants are $K_1 = K_2 = e^{-2\varepsilon}$, $K_3 = e^{-2(\omega_E+\varepsilon)}$, $K_4 = e^{-2(\omega_I+\varepsilon)}$, $K_5 = e^{-2(\omega_E+\eta)}$, $K_6 = e^{-2(\omega_I+\eta)}$, and $K_7 = e^{-2\eta}$.

6.3. Results and Discussion

Our objective is to compute the numbers of (11), (12), and (22) pairs in each layer individually. To characterize the corresponding distributions we define (in analogy to Eq. 6.4) the apparent equilibrium constants

$$K^E = \frac{(N_{12\bullet\bullet} + N_{21\bullet\bullet})^2}{N_{11\bullet\bullet} N_{22\bullet\bullet}}, \quad K^I = \frac{(N_{\bullet\bullet 12} + N_{\bullet\bullet 21})^2}{N_{\bullet\bullet 11} N_{\bullet\bullet 22}} \tag{6.12}$$

in the external and internal layer, respectively. In the experiments by Zhang *et al* [2] the lipid membrane was macroscopically homogeneous and symmetric; i.e. both bilayer leaves consisted of an equimolar 1 : 1 lipid mixture of types 1 and 2. This implies $\omega_E = \omega_I$ and $N_1^E/N = N_1^I/N = 0.5$. For $\omega_E = \omega_I$ symmetry gives rise to $K^E = K^I$. It is thus convenient to define $\omega = \omega_E = \omega_I$ and $K = K^E = K^I$. Hence, the function $K = K(\omega, \eta, \varepsilon)$ completely specifies the pair distribution in each of the two layers as function of the lipid-lipid interaction strengths within (ω) and across (η) membrane leaflets and as function of the hydrophobic mismatch penalty (ε). We have calculated $K = K(\omega, \eta, \varepsilon)$ from solutions of the equations for the various N_{ijkl} as discussed in the previous section.

6.3.1. Discussion of Limiting Cases

We discuss combinations of limiting cases for the hydrophobic mismatch penalty parameter $\varepsilon = \{0, +\infty\}$ and the inter-leaflet lipid-lipid interaction parameter $\eta = \{-\infty, 0, +\infty\}$. A summary of the results, valid for arbitrary choices of the nearest neighbor lipid-lipid interaction parameter ω is displayed in Table 6.1.

Table 6.1. Equilibrium constants K predicted for the six combinations of $\varepsilon = \{0, +\infty\}$ and $\eta = \{-\infty, 0, +\infty\}$. Each result is valid for arbitrary ω.

	$\eta \to -\infty$	$\eta = 0$	$\eta \to +\infty$
$\varepsilon = 0$	$K = 4\,e^{-4\omega}$	$K = 4\,e^{-2\omega}$	$K = 4\,e^{-4\omega}$
$\varepsilon \to +\infty$	$K = 4\,e^{-4\omega}$	$K = e^{-4\omega}$	$K = 0$

Each case can be rationalized by considering the conformations $(ijkl)$ that are adopted with non-vanishing probability:

$\varepsilon = 0$ and $\eta = 0$: The two leaflets are completely decoupled and, hence, the single-layer result $K = 4e^{-2\omega}$ according to Eq. 6.4 is adopted.

$\varepsilon = 0$ and $\eta \to +\infty$: The two apposed leaflets are strongly coupled into symmetric pairs, leaving only the four distinct conformations (1111), (2222) (each with vanishing energy) and (1212), (2121) (each with an energy of 2ω). This effectively doubles the interaction energy $\omega \to 2\omega$ as compared to $\eta = 0$. Hence $K = 4e^{-4\omega}$.

$\varepsilon = 0$ and $\eta \to -\infty$: The two apposed leaflets are strongly coupled into anti-symmetric pairs, leaving only the four distinct conformations (1122), (2211) (each with vanishing energy) and (1221), (2112) (each with an energy of 2ω). As in the preceding case, this effectively doubles the interaction energy $\omega \to 2\omega$ as compared to $\eta = 0$. Hence $K = 4e^{-4\omega}$.

$\varepsilon = +\infty$ and $\eta = 0$: There can be no mismatch, leaving only the six conformations (1111), (1122), (2211), (2222) (all with vanishing energy) and (1221), (2112) (both with an energy of 2ω). With the definition of the equilibrium constant in Eq. 10.9 and the Boltzmann factor for the interaction energy ω we

obtain

$$K = \frac{(e^{-2\omega} + e^{-2\omega})^2}{2 \times 2} = e^{-4\omega} \tag{6.13}$$

$\varepsilon = +\infty$ and $\eta = \rightarrow +\infty$: Here, the only surviving states are (1111) and (2222), implying $K = 0$. Note that in this limit the bilayer would separate into pure phases of type 1 and type 2, irrespective of ω.

$\varepsilon = +\infty$ and $\eta = \rightarrow -\infty$: Here, the surviving four states are (1122), (2211) (both with vanishing energy) and (1221), (2112) (both with an energy of 2ω). This implies $K = 4e^{-4\omega}$.

6.3.2. Discussion of Numerical Results

Next, in Fig. 6.4, we display numerical results for $K(\omega, \eta, \varepsilon)$ as function of η. Note that K is plotted logarithmically. We first consider the special case $\varepsilon = 0$, thus ignoring the hydrophobic mismatch energy penalty. The three solid lines in Fig. 6.4 all refer to $\varepsilon = 0$, with $\omega = 0$ for curve a, $\omega = 0.2$ for curve b, and $\omega = -0.2$ for curve c. We note that the formulation of our model only in terms of ω and η (that is, with $\varepsilon = 0$) retains all nearest neighbor interactions, lateral in each leaflet and across the membrane, yet ignores any multi-body interactions. For $\omega = 0$, lipids within the two leaflets do not interact with each other. The lipid mixture in each leaflet is then random, implying $K = 4$ as discussed following Eq. 6.4. The random distribution for $\omega = 0$ is not affected by η (the solid curve a in Fig. 6.4). For $\omega = 0.2$ (the solid curve b in Fig. 6.4) lipids of types 1 and 2 effectively attract each other. This leads to $K < 4$. In the complete absence of inter-leaflet interactions, $\eta = 0$, we obtain $K = 4\,e^{-2\omega} = 2.68$ according to Eq. 6.4. Increasing the magnitude of η enhances the effective lipid-lipid attraction strength within each leaflet and thus must further decrease K. The decrease is invariant with respect to the sign of η. We have discussed this already in Table 6.1 for the limit $|\eta| \rightarrow \infty$, where apposed lipids are forced to interact via symmetric (for $\eta \rightarrow +\infty$) or antisymmetric (for $\eta \rightarrow -\infty$) pairs across the bilayer and thus double their effective attraction strength from $\omega = 0.2$ to $2\omega = 0.4$, implying $K(|\eta| \rightarrow +\infty) = 4\,e^{-4\omega} = 1.80$. For $\omega = -0.2$ (the solid curve c in Fig. 6.4) lipids of types 1 and 2 effectively repel other lipids or their own species, implying $K > 4$. For $\eta = 0$ we obtain $K = 4\,e^{-2\omega} = 5.97$, which according to Table 6.1 further increases with growing $|\eta|$ up to $K = 4\,e^{-4\omega} = 8.90$ in the limit $|\eta| \rightarrow \infty$. Here again, inter-leaflet coupling enhances the effective lipid-lipid attraction strength within each leaflet.

Switching on the hydrophobic mismatch energy ε renders the curves in Fig. 6.4 asymmetric with

respect to the sign of η. The physically relevant case is $\varepsilon > 0$, where mismatch implies a penalty and not an energy reward. The three dashed lines in Fig. 6.4 all refer to $\varepsilon = +0.2$, again with a $\omega = 0$ for curve a, $\omega = 0.2$ for curve b, and $\omega = -0.2$ for curve c. Generally, K decreases if ε is increased from $\varepsilon = 0$ to $\varepsilon = 0.2$ (see also the left and right diagrams in Fig. S1 of the Supporting Information). This is expected because growing ε favors the zero-mismatch states, 1111, 1122, 1221, 2222, 2211, 2112. Two of these states have lipids of different types in each leaflet (1221 and 2112), and the remaining four (1111, 1122, 2222, 2211) have lipids of the same type in each leaflet. This implies a stronger statistical weight of configurations with neighboring lipids of the same type in each leaflet and, hence, the decrease of K.

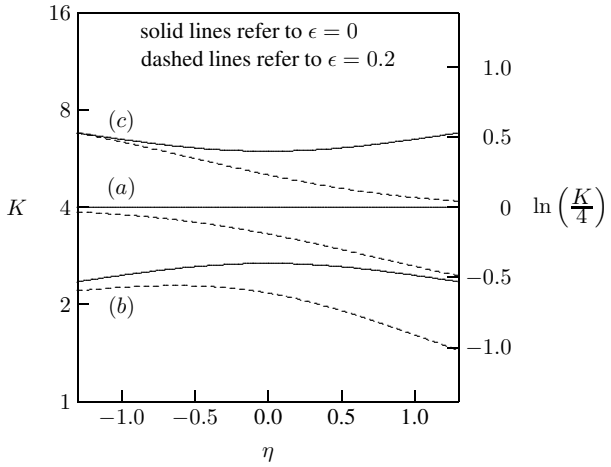

Figure 6.4. Equilibrium constants K predicted by the quasi-chemical approximation, plotted as function of the interaction energy across the lipid bilayer η. The three sets of curves correspond to different lipid-lipid interaction energies $\omega = 0$ (a), $\omega = 0.2$ (b), and $\omega = -0.2$. (c). Each set contains two different curves, calculated for a mismatch energy $\varepsilon = 0$ (solid lines) and $\varepsilon = 0.2$ (dashed lines).

We note an additional consequence: if only the states 1122, 1221, 2211, 2112 were populated, all lipids would face a lipid of opposite type on the other side of the bilayer. In this hypothetical scenario one leaflet would form a perfect hydrophobic template for the other one. The additional statistical preference of the two other states, 1111 and 2222, leads to the observed decrease of K in Fig. 6.4 for growing ε. Because a transition away from either one of these two states is not possible without hydrophobic mismatch, population of the state 1111 (and equivalently for 2222) must give rise to spatial clusters, implying registered domains of lipids of type 1 (and equivalently for type 2). These clusters are illustrated in the Table of Contents entry.

The tendency that K decreases with growing ε is further modulated by η. Growing η disfavors four

of the six states, leaving only 1111 and 2222 unaffected; this gives rise to a further decrease of K. On the other hand, increasingly negative values of η leave the four states 1122, 1221, 2211, and 2112 unaffected, and thus oppose the statistical bias introduced by increasing ε. As a consequence, the values of K for $\varepsilon = 0$ and $\varepsilon = 0.2$ approach each other if η becomes more and more negative. These trends are all consistent with the entries in Table 6.1.

6.3.3. Monte Carlo Simulations

In order to verify that the trends predicted by QCA are not artifacts of neglecting correlations between the 16 double pair conformations, we have carried out Monte Carlo simulations of two coupled two-dimensional cubic lattices, each with 20×20 lattice sites and the same interactions as defined in Fig. 6.2B. The results are displayed in Fig. 6.5.

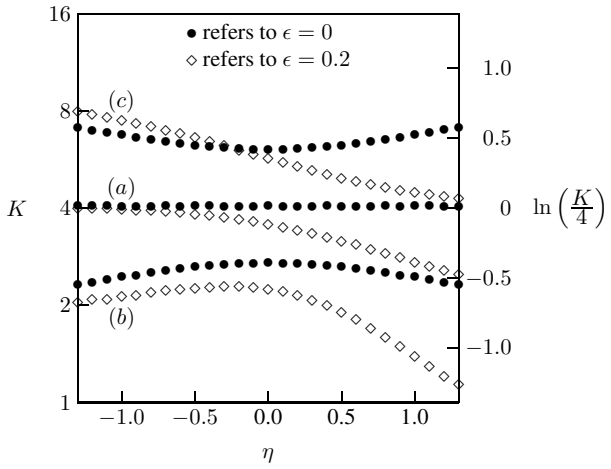

Figure 6.5. Equilibrium constants K predicted by Monte Carlo simulations of two coupled two-dimensional cubic lattices (each of 20×20 lattice sites) with interaction parameters identical to those used in QCA. Figs. 6.4 and 6.5 are derived for the same interaction parameters, the former using QCA and the latter using Monte Carlo simulations. Specifically, the three sets of curves correspond to different lipid-lipid interaction energies $\omega = 0$ (a), $\omega = 0.2$ (b), and $\omega = -0.2$. (c). Each set contains two different curves (marked by data points), calculated for a mismatch energy $\varepsilon = 0$ (marked by the symbol •) and $\varepsilon = 0.2$ (◇).

Clearly, there is qualitative agreement between the data in Figs. 6.4 and 6.5. Deviations of K from $K = 4$ tend to be somewhat stronger in the Monte Carlo simulations as compared to QCA, which is the expected consequence of neglecting correlations in QCA.

6.3.4. Comparison with Experimental Results

We compare the predictions of QCA with the experimental results of Zhang *et al* [2]. Here, NNR was used to demonstrate the presence of cross talk between the two leaflets of a fluid lipid bilayer. As discussed in the Introduction, equimolar lipid mixtures with different combinations of short and long chains, 1_s2_s, 1_l2_l and 1_s2_l, yielded equilibrium constants $K_{ss} = 6.55 \pm 0.36$, $K_{ll} = 6.76 \pm 0.16$, and $K_{sl} = 6.92 \pm 0.47$ in the absence of a divalent ligand as well as $K_{ss} = 4.88 \pm 0.27$, $K_{ll} = 4.86 \pm 0.09$ and $K_{sl} = 3.84 \pm 0.12$ in the presence of the divalent ligand. The decrease of the equilibrium constant for the short-chain and long-chain lipid mixture (1_s2_l) in the latter case was interpreted as evidence of a hydrophobic templating effect across the two apposed leaflets of a fluid lipid membrane (referred to as "cross talk" by Zhang *et al* [2]). Note that the observed equilibrium constants are marked in Fig. 6.6 (left and right diagrams refer to absence and presence of the ligand, respectively).

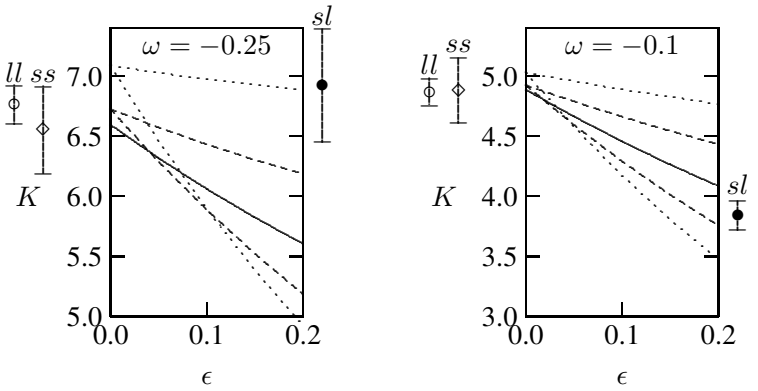

Figure 6.6. Equilibrium constants K predicted by the quasi-chemical approximation, plotted as function of the mismatch energy ε for $\omega = -0.25$ (left diagram) and $\omega = -0.1$ (right diagram). These two choices of ω model, respectively, the absence and presence of the divalent ligand in the experiments of Zhang *et al* [2]. Solid lines refer to $\eta = 0$, dashed lines to $\eta = \pm 0.4$, and dotted lines to $\eta = \pm 0.8$. For each pair of broken or dotted lines, the upper curve refers to negative η and the lower curve to positive η. Experimentally observed equilibrium constants [2], including their error bars, are indicated on the left-hand side (*ll* and *ss*) and right-hand side (*sl*) of each diagram.

Consider the presence of the divalent ligand (right diagram of Fig. 6.6). For the 1_s2_s and 1_l2_l systems, where all lipids have the same chain length, neither direct lipid-lipid interactions across the membrane nor hydrophobic mismatch penalties are expected to be relevant, implying $\eta = \varepsilon = 0$. (Strictly, even for the 1_s2_s and 1_l2_l systems there could be some degree of hydrophobic mismatch and a non-vanishing lipid-lipid

interaction across the membrane, namely if the different headgroups occupy different cross-sectional areas. The importance of this scenario is difficult to assess because no experimental data for the cross-sectional areas of the exchangeable phospholipids used in the experiments of Zhang *et al* [2] are available.) The two layers in the QCA model then decouple and the equilibrium constant is $\omega = -(1/2)\ln(K/4) = -0.1$ for the experimentally observed $K \approx 4.9$. For the 1_s2_l system we need to include the influence of η and/or ε. The solid line in the right diagram of Fig. 6.6 shows the influence of ε for $\eta = 0$. Clearly, the hydrophobic mismatch penalty ε lowers K and can thus rationalize the experimentally observed decrease of K_{sl} as compared to K_{ss} and K_{ll}, which was interpreted as evidence for the presence of "cross talk". The reduction of K results from the zero-mismatch states having twice as many lipid neighbors of the same type (1111, 1122, 2211, and 2222) than of different type (1221 and 2112). In addition, the most unfavorable high-mismatch states 1212 and 2121 have lipid neighbors of different type. Hence, avoiding mismatch tends to induce effective attraction between lipids of the same type. The reason behind this tendency is that the mismatch-induced energy bias ε favors the clustering of states for which the membrane does not change its thickness: states that are either complementary across the membrane (1122, 2211, 1221 and 2112) or represent domains of lipid type 1 (1111) or lipid type 2 (2222). The latter two are responsible for the decrease in K for growing ε. Note that "cross talk" is not the result of direct lipid-lipid interactions across the membrane. Indeed, K increases with growing magnitude of η (the same for positive or negative η), given $\varepsilon = 0$ and $\omega < 0$.

Let us estimate the interaction parameters ε and η. A crude estimate for an upper bound of ε can be obtained by assuming each lipid chain adopts its optimal length, but at the cost of the long chains exposing some of their hydrocarbon segments to the aqueous phase if mismatch is present; see for example the illustration of the conformation 1121 in Fig. 6.2C. The corresponding energy cost should be on the order $\gamma\,\delta h\,a/z$ where $\gamma = 12 k_B T/\mathrm{nm}^2$ is the hydrocarbon chain-water interfacial tension [190], $a \approx 0.65\,\mathrm{nm}^2$ is the cross-sectional area of a (double tail) lipid, $\delta h \approx 0.3\,\mathrm{nm}$ is the length of the chain segment that is exposed to aqueous solvent, and $z = 4\ldots6$ is the coordination number of the lattice. With this we obtain a mismatch energy of $\varepsilon \lesssim \gamma\,\delta h\,a/(z k_B T) = 0.6\,k_B T$. Another upper bound for ε can be estimated by assuming the membrane thickness stays constant, but at the cost of a corresponding stretching/compressing deformation of the lipids, as characterized by the compressional modulus $K_c = 40\,k_B T/\mathrm{nm}^2$ of a lipid membrane [191]. For example, consider the conformation 1121 and denote the optimal chain lengths of the short and long chains by h_S and h_L. If the actually adopted chain lengths for the 1121 conformation are h_1, h_2, h_3 and h_4,

we can write for the free energy per lipid double pair (of total cross-sectional area $2a$)

$$\begin{aligned} \frac{F}{k_B T} &= a\frac{K_c}{2}\left[\left(\frac{h_1}{h_S}-1\right)^2+\left(\frac{h_2}{h_S}-1\right)^2\right. \\ &+ \left.\left(\frac{h_3}{h_L}-1\right)^2+\left(\frac{h_4}{h_S}-1\right)^2\right] \end{aligned} \tag{6.14}$$

We fix the thickness $D = h_1 + h_3 = h_2 + h_4$ of the lipid double pair and define the two chain length relaxation parameters $\eta_1 = h_1/h_3$ and $\eta_2 = h_2/h_4$. Then, optimizing $F(D, \eta_1, \eta_2)$ yields $F = a(K_c/2)(h_S - h_L)^2/(3h_S^2 + h_L^2)$. With $h_S = 0.8h_L$ we obtain the upper bound estimate $\varepsilon \lesssim F/k_BT = 0.18$. The actual value of ε is expected to result from an optimization of the two mechanisms, variations of the membrane thickness and partial lipid chain protrusions into the aqueous phase; we expect it to be smaller but still on the same order of magnitude than the lower of our two estimates. This justifies our choice of the range $0 \leq \varepsilon \leq 0.2$ in Fig. 6.6.

The extent of lipid interactions across a lipid bilayer has been estimated recently by Collins [192] using a simple membrane line tension argument to be, very roughly, on the order of $0.1 \ldots 1\, k_BT/\mathrm{nm}^2$. A much more detailed coarse grained Molecular Dynamics simulation by Risselada and Marrink [193] of a ternary mixture of dipalmitoylphosphatidylcholine, dilinoleoylphosphatidylcholine, and cholesterol, which form coexisting liquid-disordered and liquid-ordered lipid phases, yielded $0.1 \ldots 0.2\, k_BT/\mathrm{nm}^2$. Measured per lipid cross-sectional area the latter corresponds to $\eta = 0.05 \ldots 0.1$. However, for coexisting liquid-disordered and liquid-ordered phases of ternary lipid mixtures with cholesterol η is likely much larger than for binary lipid mixtures where the lipids are all in the liquid-disordered state. Indeed, the different material stiffness of the disordered and ordered lipid phases has been suggested to determine the magnitude of η [194]. Hence, for binary lipid mixtures in their fluid state we can assume $\eta < 0.1$. The influence of η on the equilibrium constant K is then negligible (see Figs. 6.5,6.6, and S1). We speculate that the predicted lack of direct coupling, as expressed by the weak dependence of K on η, might be related to the experimentally observed insensitiveness of the gel-to-liquid phase transition temperature on the degree of externally induced inter-leaflet asymmetry [195, 196].

Our estimates of η and ε indicate that Fig. 6.6 (especially the solid line in each diagram, which corresponds to $\eta = 0$) is likely to capture the relevant regimes for the experiments of Zhang *et al* [2]. Recall that the right diagram refers to the system containing the divalent ligand for which "cross talk" was observed experimentally, as evidenced by the decrease of the equilibrium constant K_{sl} as compared to K_{ss}

and K_{ll}. Clearly our model reproduces the experimental findings and provides a physical explanation for why K_{sl} is reduced. Yet, we also point out that in the absence of the ligand (left diagram in Fig. 6.6) there was no experimental indication of a "cross talk" between the two leaflets whereas our model would still predict a decrease of K_{sl}. Even for a different set of interaction parameters our model would not be able to fit all six experimental equilibrium constants at the same time. A possible reason could be that the divalent ligand acts beyond merely increasing the attractive interaction between two charged lipids as we have assumed in our model. Consider, for example, that the size of the divalent ligand exceeds the headgroup-to-headgroup distance between two neighboring anionic lipids. To reduce its effective length, the ligand could then bind in an oblique orientation which induces a height mismatch and this affects the interaction parameter ε. Another possibility is that binding of the ligand alters the cross-sectional area per lipid. A smaller cross-sectional area imparts a thickening of the bilayer, which again affects the mismatch energy ε. Still another possible scenario is that the ligand, when bound, forms a tight complex with two anionic lipids, which enhances its propensity to serve as template across the bilayer by increasing the effective lipid size. Our present level of QCA does not capture this effect, unless the ligand is explicitly incorporated into the microstates of the lipid double pair (see Fig. 6.2). The number of microstates for each individual lipid double pair would then increase significantly due to the possible presence or absence of the ligand, which exceeds the scope of the present work but would be an interesting extension. However, the principal physical mechanism of how "cross talk" is induced across a lipid bilayer through hydrophobic templating is already captured by the present model.

6.4. Conclusions

Modeling of the coupling between the two leaflets of a mixed lipid bilayer has focused in the past on mean-field models [197, 198] and computer simulations [179, 193, 180]. The former neglect lipid-lipid correlations, rendering them useful in describing the inter-leaflet coupling of entire phase-segregated domains but incapable of characterizing the coupling on the level of individual lipids. The latter are powerful in describing any type of coupling, often however without allowing for a straightforward extraction of the underlying physical mechanism behind the coupling.

The present work was motivated by NNR experiments from Zhang *et al* [2], who predict "cross talk" through a hydrocarbon chain length-mediated hydrophobic templating effect on the level of individual

lipids. To describe the cross talk on this level, we needed to go beyond the mean-field approximation. To this end, we have included lipid-lipid correlations using the quasi-chemical approximation scheme of a lattice gas model of a lipid bilayer. Our theoretical approach employs the notion of "chemical reactions" as a tool to describe nearest neighbor correlations. This mimics the experimental NNR approach of Zhang *et al* [2], which takes a snapshot of a binary membrane and then describes nearest neighbor correlations in terms of a chemical reaction and a corresponding equilibrium constant. A smaller equilibrium constant reflects a larger probability that two neighboring lipids in a given leaflet are of the same type. According to our theoretical model and supporting Monte Carlo Simulations, the experimentally observed reduction of the equilibrium constant for binary mixtures of long and short chain lipids in their fluid state (as compared to having no chain length mismatch) results from the tendency of the membrane to maintain a constant thickness, implying an enhanced probability of lipids of the same type (that is, the same chain length) to be located at close proximity. In addition, we find that two interaction parameters, accounting for lipid-lipid pair interactions within each leaflet and for hydrophobic mismatch, are crucial to reproduce the experimentally observed cross talk whereas direct lipid-lipid pair interactions across the membrane are not needed and are likely to be negligible for binary lipid membranes in their fluid state.

6.5. Acknowledgments

The authors would like to thank Dr. Steven Regen for illuminating discussions. G.V.B. acknowledges a doctoral scholarship from CAPES Foundation/Brazil Ministry of Education (Grant No. 9466/13-4).

7. INTERACTIONS BETWEEN MEMBRANES AND "METAPHILIC" POLYPEPTIDE ARCHITECTURES WITH DIVERSE SIDE-CHAIN POPULATIONS*

7.1. Introduction

The functions of proteins or peptides, such as molecular recognition, enzymatic reactions, and allosteric regulation, are determined by their structures and their internal motions: Proteins or peptides can fold into structures that present specific chemical patterns on their molecular surfaces. These nanoscopically defined patterns of charge, hydrogen bonding, and/or hydrophobicity, which strongly influence peptide or protein interactions, are known to be partly smeared out by thermal fluctuations. For protein configurations structurally cognate to the native folded state, the protein energy surface, which controls protein dynamics, can have multiple minima, and proteins exhibit harmonic motions within these minima as well as crossing of potential barriers between them. In general, however, molecular thermal motions are not large compared to the dimensions of the molecule. Moreover, single-molecule experiments show that folded proteins typically have Young's moduli of$\approx 1 \times 10^8$ Pa [199, 200, 201], which give the protein a solid-like rigidity. There is a rich literature showing that in the low-temperature limit, proteins can undergo a dynamic transition to a glass-like solid state with small fluctuations [202, 203]. Taken together, the surface structure, shape, and elasticity of a protein determine the resultant presentation of surface chemistry, and thereby enable or limit its interactions. It would be interesting to start with the functional requirements for a given protein or peptide class, and explore the opposite limit, where patches of surface chemistry can be mobile.

Both antimicrobial peptides (AMPs) and cell-penetrating peptides (CPPs) are short (generally < 50 amino acids) peptides that exert their functions by interacting with and permeating membranes. As part of the innate host defense, AMPs collectively exhibit broad spectrum antimicrobial activity [204, 205, 206]

*Reproduced with permission from "M. W. Lee, M. Han, G. V. Bossa, C. Snell, Z. Song, H. Tang, L. Yin, J. Cheng, S. May, E. Luijten, et al., Interactions between membranes and "metaphilic" polypeptide architectures with diverse side- chain populations, ACS Nano 11 (3) (2017) 2858–2871". Copyright 2017 American Chemical Society. This paper can be accessed online at `http://pubs.acs.org/doi/abs/10.1021/acsnano.6b07981`. The material in this chapter was co-authored by Michelle W. Lee, Ming Han, Guilherme V. Bossa, Carly Snell, Ziyuan Song, Haoyu Tang, Lichen Yin, Jianjun cheng, sylvio May, Erik Luijten, and Gerard C. L. Wong. G. V. Bossa contributed to the mean-field modeling, figures preparation, writing and discussion of the results.

typically through the disruption and permeabilization of bacterial membranes [205, 206, 207]. Although AMPs are abundant and diverse in sequence and structure, they share some common features. Most AMPs are cationic and characterized by facially amphiphilic patterns of hydrophobicity and charge [205, 204, 206, 208, 209]. CPPs are capable of efficiently translocating across cell membranes and can mediate the uptake of conjugated cargos [210, 211, 212]. CPPs are generally cationic, but can also be amphiphilic, with the arginine-rich CPPs comprising the most widely studied group [210, 212, 213, 214, 215, 216]. Many CPP sequences are derived from natural proteins and peptides; however, research groups have also developed synthetic CPPs [210, 215]. While cationic charge and amphiphilicity are characteristics often found in both AMPs and CPPs, it has been noted that these properties can be found in many other membrane-remodeling peptides [217], including viral budding peptides [218] and viral fusion peptides [219]. While the vast majority of AMPs and CPPs are composed of linear amino acid sequences, a number of research groups have recently explored unconventional nanoscopic architectures in the design of polymer-based antimicrobial and cell-penetrating agents that are also characterized by cationic charge and hydrophobicity, including circular peptides, and especially an extensive taxonomy of side chain-rich comb, brush, or dendrimer architectures [220, 221, 222, 223, 224, 225]. In this work, we systematically investigate a prototypical class of peptides with side chain-rich architectures. These peptides consist of a rigid helical core decorated with mobile and flexible side chains that are terminated by cationic and hydrophobic groups, an arrangement that allows cationic and hydrophobic end groups to undergo large displacements, reminiscent of the Lindemann criterion for melting [226, 227]. Therefore, these molecules have unusually chemically adaptable and quasi-liquid surfaces. Although one might expect that the loss of well-defined spatial relations between cationic and hydrophobic patches on a highly evolved peptide or protein leads to a degradation of activity, we surprisingly find the opposite. We show that the membrane- permeating activity of AMPs and CPPs, both commonly characterized by anchored cationic and hydrophobic groups, can be significantly enhanced by the highly adaptable side chain-rich architecture: Like organisms that adapt to different colored environments via metachrosis, these molecular architectures adapt to different solvent environments (water, amphiphilic interface, hydrophobic membrane core) by being "metaphilic" rather than statically amphiphilic. In a sense, these metaphilic peptides are a molecular analogue of recently engineered omniphilic/omniphobic surfaces [228, 229, 230]. Computer simulations indicate that the quasi-liquid surface of the peptide allows it to adapt to environmental change by rearranging the flexible side chains, a capability that plays a key role in enabling unusual interactions with membranes. Specifically, these metaphilic peptides are able to induce

membrane-destabilizing curvature necessary for permeation, which we determine using X-ray measurements. Furthermore, because these metaphilic molecules can adapt their surface chemistry, we can control their charge and hydrophobicity over a broad range and still maintain water solubility, unlike many AMPs and CPPs [231, 232, 233, 234, 235]. This allows us to show how the activity of these metaphilic peptides is amplified with hydrophobicity and cationic charge, and we rationalize these results using a quantitative mean-field theory. One goal of this paper is to develop a general conceptual vocabulary to analyze how molecules of different architectures beyond linear peptides interact with membranes, and how these architectures consequently allow small quantitative changes in structural parameters to lead to qualitative differences in membrane interactions.

7.2. Results and Discussion

7.2.1. Methaphilic Membrane-Active Peptides

We previously developed a series of bottlebrush-like, radially amphiphilic peptides, where hydrophobic side chains that terminate in a cationic group are attached to a rigid core [236, 237].

Here we generalize this design and also create peptides with side chains having heterogeneous distributions of cationic and hydrophobic end groups. The surfaces of these brush-like molecules can mimic the chemical surfaces of natural AMPs, but maintain the mobility of cationic and hydrophobic patches so that they can rearrange in response to environmental changes. Specifically, these metaphilic molecules are water-soluble -helical poly(arginine)-based polypeptides [238] (7.1), which include both homopolymers and random copolymers. The metaphilic peptide monomer features a long hydrophobic side chain with either a terminal guanidinium or alkyl chain that is positioned distally (1318 σ-bonds away) from the backbone. Increasing cationic residues in a prototypical peptide has been shown to reduce helical stability due to greater electrostatic repulsion between side chains [231, 232] and increasing hydrophobicity leads to poor water solubility and aggregation [233, 234, 235].In the current architecture, charges are positioned at a significant distance away from the helical backbone to decrease the surface charge density and side chain repulsion, which promotes their stable -helical conformation in an aqueous environment [238]. In addition, the charged exterior shell formed by the terminal guanidinium groups around the helical backbone enables the metaphilic peptides to maintain water solubility by shielding the hydrophobic carbon side chains and helical core from

solution. All metaphilic peptides were synthesized through ring-opening polymerization of γ-chloroalkyl-L-glutamate based N-carboxyanhydrides, followed by the conversion of the side chain chloro groups into azido groups, and the subsequent copper-catalyzed Huisgen click chemistry with propargyl guanidines to attach guanidinium groups at the side chain terminus [238]. This robust and efficient synthesis enables the control of the side chain hydrophobicity in two different ways: (1) the variation of methylene spacer lengths between the pendant triazoles and esters through selecting different amino acid precursors (P1,P5, P6); (2) the introduction of additional hydrophobic moieties by coconjugating long chain alkynes together with the propargyl guanidines (P10P12). The latter also enables the control of charge density by varying the feeding ratios of propargyl guanidines and long chain alkynes (P11, P13, P14).

7.2.2. Metaphilic Peptides Exhibit Adaptable Amphiphilicty upon Interaction with Membranes

We performed generic coarse-grained molecular dynamics simulations to investigate the behavior of these metaphilic peptides as they interact with lipid membranes in an aqueous environment. Specifically, we were interested in the process in which a metaphilic peptide (with either 50% or 100% of its side chains terminated by a cationic end group) approaches a negatively charged membrane surface and subsequently inserts and organizes itself within the phospholipid bilayer.

The adaptation of the peptide configuration and its free-energy variation were quantitatively explored in a steered landing process, as illustrated in Fig. 7.2. At large separation, the peptide barely interacts with the oppositely charged membrane due to electrostatic screening by the ions (Fig. 7.2A), and its backbone effectively behaves as a neutral rod, randomly orienting with an average tilt angle $\theta = \pi/2 - 1$ toward the membrane (Fig. 7.2B). Its affinity to the membrane emerges at separations $z < 68$Å (defined as the distance between the peptide center and the membrane outer leaflet), around one peptide length. The peptide backbone begins to orient more orthogonally so that some of the charged side chains are able to reach the membrane. Apart from reorienting, the peptide also reorganizes its mobile side chains with their charged end groups extending toward the membrane, giving rise to an asymmetric charge distribution. This asymmetry is reflected in and quantified by the average deviation Δz of the charged end groups from the peptide center (Fig. 7.2C). The tilted peptide touches the membrane and starts to settle at $z = 50$Å; it fully lies down at $z \approx 40$Å, reaching its strongest asymmetry. Completion of this "landing" process is marked by the distance at which the forces on the peptide are balanced, near z landing $= 36$Å. The free-energy changes

for the peptides with 50% and 100% charge coverage upon landing are $4.9k_BT$ and $8.4k_BT$, respectively (Fig. 7.2D).

Furthermore, we also simulated the free (i.e., nonsteered) landing and insertion process of a peptide with 100% charge coverage, as illustrated in Fig. 7.2E. Initially, the peptide indeed tilts toward the membrane with charged end groups shifted downward, confirming our findings. After landing, the hydrophobic parts of the side chains tend to merge into the hydrophobic interior of the membrane, whereas the charged end groups tend to stay outside. The peptide first "anchors" to the membrane by bending a side chain and partially inserting its hydrophobic part into the membrane. Such a side chain can then further minimize its energy by "tunneling" of its charged end group toward the membrane surface on the inner leaflet. This process provides a strong driving force for the second stage, namely insertion of the peptide to completely span the membrane bilayer.

The insertion process exhibits a strong dependence on side chain length. From simulations we found that peptides with twice shorter side chains fail to insert (Fig.7.2F). These side chains are too short to undergo significant adaption required by the "anchoring" and "tunneling" stages. As a consequence, the hydrophobic parts of the peptide side chains are shielded by the charged end groups and unable to interact with the membrane. This obstacle, however, can be overcome by reducing the charge coverage. As shown in Fig. 7.2G, a peptide with reduced charge coverage of 50% and short side chains can successfully anchor to the interior of the membrane via its uncharged side chains. Having uncharged, hydrophobic side chains is sufficient to facilitate insertion and span the membrane. This indicates that membrane insertion is less efficient with shorter cationic side chains. However, it is possible to optimize the efficiency of the peptide by combining high charge coverage to achieve a large landing rate and a finite fraction of uncharged side chains to assist in the hydrophobic insertion process.

7.2.3. Dynamic Adaptability of Metaphilic Peptides Can Enhance Membrane Permeation

Previous studies have suggested that penetration of amphiphilic helical peptides into a bilayer perturbs the hydrophobic interactions of the membrane core, thus leading to membrane destabilization. This process depends on both the hydrophobic content of the peptide and membrane penetration depth. Indeed, the reduction of membrane activity of cationic amphiphilic α-helices has been found to correlate with decreased hydrophobicity [239, 240]. Accordingly, the relative sizes of the polar and hydropho-

bic faces of an amphiphilic helical peptide have been shown to affect the induced membrane curvature [208, 241, 242, 243, 244, 245, 246]. For metaphilic peptides, there is a wider range of possibilities. Although sometimes AMPs can become amphiphilic and α-helical as they touch down on a membrane, the simulation model here predicts that the metaphilic peptide will undergo a series of structural transitions as it engages the membrane that are not possible for most proteins or peptides: it has uniformly distributed side chains in bulk aqueous solution far from a membrane, but adopts a facially amphiphilic structure near a membrane, with cationic end groups arranged to face toward the membrane surface. Once adsorbed onto the membrane surface, the peptide reorganizes its side chain components to invert its facial amphiphilicity with cationic end groups associated with the polar lipid head groups at the surface, while the hydrophobic moieties penetrate further into the membrane core. Depending on the length of the side chains relative to the membrane thickness, terminal groups of the side chains can diffuse through the membrane, so that it is possible for a single metaphilic peptide to present guanidinium groups to polar lipid head groups on *both* leaflets of the membrane, which is not possible for AMPs. These effects lead to two interesting consequences. It is known that details of amphiphilic conformation can play important roles in peptidemembrane interactions necessary for function [242, 247, 248, 249]. The ability of metaphilic peptides to invert their facial amphiphilicity via progressive side chain migration suggests a direct translocation mechanism with no analogue in natural peptides. Moreover, simultaneous presentation of curvature-generating guanidinium groups to both membrane leaflets may lead to significantly enhanced membrane curvature generation [218, 250, 251, 252, 253, 254] which we explore in the next section.

7.2.4. Metaphilic Peptides Can Induce Negative Gaussian Curvature Necessary for Membrane Permeation

To assess the membrane-permeating mechanism of these peptides, we used high-resolution synchrotron small-angle X-ray scattering (SAXS) to quantitatively characterize the membrane deformations induced by metaphilic peptide variants. Small unilamellar vesicles (SUVs) were prepared from a phospholipid mixture of 1,2-dioleoyl-sn-glycero-3-phospho-L-serine (DOPS) and 1,2-dioleoyl-sn-glycero-3- phosphoethanolamine (DOPE) at a molar ratio of 20/80. Each metaphilic peptide was incubated with SUVs at a specified peptide-to-lipid (P/L) molar ratio corresponding to an electroneutral P/L charge ratio and the resulting membrane structures were characterized using SAXS.

We found that all α-helical metaphilic peptides (P1, P4P6, P10P14) resulted in the restructuring of the lipid vesicles into phases rich in negative Gaussian curvature (NGC) (Fig. 7.3 A,B), whereas control samples of SUVs only exhibited a broad characteristic feature consistent with the form factor of unilamellar vesicles. For every helical peptide, we typically observed a coexistence of phases: (1) one set of peaks with integral Q-ratios, which indexed a lamellar (L_α) phase with periodicity in the range of 5.5 to 7.4 nm; (2) a second set of correlation peaks with Q-ratios $\sqrt{1} : \sqrt{3} : \sqrt{4} : \sqrt{7} : \sqrt{9}$, consistent with an inverted hexagonal (HII) phase with a lattice parameter of 6.8 to 8.0 nm; (3) a third set of peaks with characteristic Q-ratios that indexed either a Pn3m "double-diamond" or an Im3m "plumber's nightmare" cubic (QII) lattice, or a coexistence of both. Q-ratios of $\sqrt{2} : \sqrt{3} : \sqrt{4} : \sqrt{8} : \sqrt{9}$ and $\sqrt{2} : \sqrt{4} : \sqrt{6} : \sqrt{8}$ correspond to Pn3m and Im3m cubic phases, respectively. In our experiments, cubic phase lattice parameters were found to range from 15.4 to 28.2 nm for Pn3m and 20.9 to 24.8 nm for Im3m (Fig. 7.3 C,D). For coexisting Pn3m and Im3m cubic phases, the ratio of their lattice parameters was close to the Bonnet ratio of 1.279 [255], indicating that the amount of curvature is balanced across the cubic phases, and thus implying that they are close to equilibrium. A bicontinuous cubic phase, such as Pn3m and Im3m, consists of two nonintersecting aqueous regions separated by a lipid bilayer that traces out a periodic minimal surface. All points along this minimal surface have NGC, which is also known as saddle-splay curvature due to its shape and the surface bends upward in one direction and bends downward in the orthogonal direction. NGC is topologically required for processes such as pore formation, budding, blebbing, and vesicularization [218, 252, 253, 256], all of which destabilize and compromise the barrier function of membranes. In fact, for molecules and peptides with functions determined by their membrane-disrupting activity, a strong correlation has been identified between NGC generation and their activity. For example, AMPs generally kill bacteria by inducing membrane permeabilization [204, 205, 206, 257, 258]. Recent studies have shown the trend of NGC generation and membrane permeation for a large number of $\alpha-$helical AMPs [218, 252], AMP mutants,and synthetic AMP analogues [259, 207]. Similarly, this trend has also been observed for a range of CPPs and transporter sequences [250, 251, 253, 254]. We found that the amounts of NGC generated by the present metaphilic peptides are comparable to those generated by AMPs [218, 252] and CPPs [250, 251, 253, 254]. From the simulation data, it is clear that metaphilic peptides can interact with membranes in ways that many peptides cannot. However, the SAXS results above show that metaphilic peptides retain the ability to permeabilize membranes like AMPs and CPPs.

We find that the inducible asymmetric shape of these metaphilic peptides is necessary in facilitating

NGC and membrane permeation activity. Nonhelical P3, a random-coil peptide synthesized from racemic monomers [238] and cognate to metaphilic peptides considered here, was not able to generate NGC, although it is able to interact with the membrane to induce lamellar and inverted hexagonal phases (Fig. 7.3A). Consistent with this, P3 demonstrated significantly lower membrane permeability [238]. Together, these results suggest that the asymmetric elongated shape stabilized by the rigid helical backbone is important for membrane permeation.

7.2.5. A Critical Comparison of Membrane Activity of Metaphilic Peptides, AMPs, and CPPs

We assessed the membrane permeation of a broad range of metaphilic peptides displaying different side chain lengths, types, and distributions. Peptide uptake alone and fluorescein isothiocyanate (FITC) uptake, when coincubated with peptide, were measured in HeLa cells in previous experiments [238]. FITC, a membrane impermeable fluorophore, has been used to evaluate peptide- induced pore formation in cell membranes, as the presence of pores allows molecules to enter cells via diffusion [260, 261]. The results show that all of the -helical metaphilic peptides exhibited membrane permeability, which is in agreement with our SAXS measurements showing that they are able to induce the curvature required for such membrane activity. In addition, the membrane permeabilities of the peptides were all found to be higher than those of well-known arginine-rich CPPs such as a domain of the human immunodeficiency virus type 1 tranactivator of transcription protein (HIV-TAT) and nona-arginine (R9) [238].

Among the helical homopolypeptides (P1, P4P6), P6 had the longest charged side chains and resulted in the highest FITC and peptide uptake levels [238]. We hypothesize that this is due in part to its metaphilic presentation of guanidinium groups to the lipid head groups of both inner and outer leaflets, which can promote efficient generation of curvature at both membrane locations [218, 250, 251, 252, 253, 250, 254]. The longer hydrophobic side chains also allow deeper membrane penetration and membrane spanning, which can further facilitate membrane curvature and destabilization. Previous work has similarly suggested that a greater number of arginines results in stronger membrane curvature effects [218, 250, 251, 261] and that arginine side chains can penetrate into the membrane interior due to attraction to the phosphate groups on the distal leaflet of the bilayer, leading to the formation of transient pores [261, 262, 263, 264]. Consistent with this picture, metaphilic peptides with shorter side chains that cannot span the membrane generally have lower uptake activity.

We specifically compared helical metaphilic peptides with similar degrees of polymerization and cationic charge (P1, P5,P6) and found that both their FITC and peptide uptake levels racked with their hydrophobic volumes (Fig. 7.4 A,C) (For details about the Methods, see Ref. [5]). Among metaphilic peptides with similar levels of hydrophobic volume (P10P14), we observed that membrane permeation activity increased with increasing cationic charge (Fig. 7.4 B,D). We further identified a more general relation among all tested helical metaphilic peptides, namely, that increases in the hydrophobic volume resulted in a higher ratio of FITC uptake to peptide uptake (Fig. 7.4 E). We hypothesize that these identified trends can be explained by differences in AMP vs CPP behavior, and differences in how free dyes and free peptides translocate into cells.

In these experiments, FITC molecules and peptides are not conjugated to one another, so both can diffuse independently in solution when coincubated with cells. In order for FITC molecules to enter cells, the peptides need to form sufficiently stable pores in the membrane to allow free FITC to pass through. AMPs typically permeate membranes by forming transmembrane pores [265, 266], and therefore, free molecules of AMPs or FITC are able to gain access to the cell interior through those pores. The membrane-associated peptides that create the pores themselves can also stochastically translocate into the cell as the pores close [265, 267]. In general, the lifetimes of membrane pores can vary greatly [263, 265] with transient pores allowing only a few peptides to translocate before closing, and more persistent pores allowing both membrane-associated peptides and free molecules through [262]. AMPs generally contain more hydrophobic residues than CPPs and generate stable membrane pores whereas CPPs are less hydrophobic and cross membranes quickly via transient pores. Therefore, synthetic peptides that have sufficient hydrophobicity can exhibit AMP-like behavior and insert into the membrane to create transmembrane pores that allow transport across membranes. In contrast, synthetic peptides with low hydrophobicity can behave like CPPs, which are able to translocate across membranes via transient membrane permeation [212, 251, 261, 268, 269].

We observed that greater peptide hydrophobic volume generally results in increased uptake of both FITC and peptide. Previous work has shown that increasing the hydrophobicity of CPPs enhances their interaction with the membrane, in turn affecting their behavior, which can change from rapid translocation across membranes to inducing slow leakage of dye from vesicles [250, 270, 271]. This finding suggests that hydrophobicity, which increases affinity for the membrane core and promotes deeper membrane penetration, can aid in stabilizing peptide-induced pore formation and yield longer pore lifetimes. By increasing the time that a membrane pore remains open, small molecules such as FITC, as well as free peptides in solution

that are not membrane-associated, can flow through into the cell. However, there is the potential trade-off between stable pore formation and translocation across a bilayer. As hydrophobicity enhances association of the peptide with the membrane interior to create a stable pore, it also impairs internalization of the peptide due to the greater chance of being retained in the membrane core [215, 250, 262, 271, 272]. This reciprocity provides a hypothesis as to why we see the ratio of FITC uptake to peptide uptake generally being higher for peptides with greater hydrophobic volume. As previously mentioned, increased peptide hydrophobicity predominately facilitates increased uptake of both FITC and free peptides, yet attenuates the translocation of lipid-associated peptides that compose the pores. Conversely, we expect lower hydrophobicity to inhibit the uptake of free molecules, and instead, promote internalization of membrane-associated peptides. Thus, a compensatory exchange exists between free peptide uptake and lipid-associated peptide uptake, which together constitute the total measured peptide uptake. Understandably, because FITC uptake requires stable pores, the effects of peptide hydrophobicity would be more prominent for FITC uptake in comparison to peptide uptake. As a result, the observed relationship between hydrophobic volume and the ratio of FITC uptake to peptide uptake will reflect that of hydrophobicity and FITC uptake. We also found that both FITC and peptide uptake increased with increasing cationic charge. The initial step for cellular entry of either molecule involves electrostatic interactions between the peptide and the membrane surface [212, 273, 274, 275]. Therefore, increased positive charge can promote more efficient binding of the peptide to the negative charges on the cell surface, which can subsequently enhance overall membrane permeation and cellular uptake. Finally, it is important to note that the cationic charge specifically for the metaphilic peptides originates from their guandinium groups. Interestingly, the guanidinium group of arginine has been found to play a key role in CPP membrane permeation [276, 277], and an increased number of arginines increases both the ability to generate NGC and cellular up- take [213, 218, 250, 251, 261, 277, 278] All of these findings are in agreement with our observations here.

7.3. Metaphilic Peptide Behavioral Trends Consistent with Mean-Field Description

We further characterized the ability of metaphilic peptides to induce NGC by a simple mean-field model. The model is an extension of the opposing-forces model [279, 280] supplemented by a hydrocarbon chain free energy that reflects the packing of the lipid tails in a bilayer geometry [281, 282]. Specifically, each lipid is characterized by its cross-sectional area a_i at the polarapolar interface, its cross-sectional area a_h

at the headgroup region (measured at fixed distance l_h away from the polarapolar interface), and the effective hydrocarbon chain extension b; see Fig. 7.5 A. The lipid free-energy model (see the section Methods below) features "opposing forces" due to the presence of repulsive interactions between lipid head groups and a chain-stretching penalty, which are both counterbalanced by a surface tension that acts at the polarapolar interface.

For any membrane curvature, the conformation of the membrane can be energetically optimized, subject to conservation of the hydrophobic lipid volume v_L. This allows calculation of the Gaussian modulus $\bar{\kappa}$. Note that negative $\bar{\kappa}$ implies a stable bilayer. When $\bar{\kappa}$ becomes positive, the membrane tends to spontaneously adopt saddle-like conformations that are characterized by NGC. We chose model parameters of our molecular free energy that are typical for a lipid bilayer with 20 mol % charged lipids ($\phi = 0.2$), obtaining a Gaussian modulus $\bar{\kappa} = -3.1 k_B T$ Inserting metaphilic peptides into the lipid bilayer with a peptide-to-lipid ratio P/L will perturb the host lipid bilayer and thus alter $\bar{\kappa}$. Within our mean-field framework, we account for two different types of perturbation. The first originates from insertion of the hydrophobic moieties of the peptide into the hydrocarbon core of the lipid bilayer, and the second relates to the electrostatic interactions of the charged terminal groups of the peptide side chains with the anionic lipid head groups. Our model describes the former as an effective increase of the hydrophobic lipid volume $v_L \to v_L + v_P P/L$ where v_P is the hydrophobic volume of the peptide. The latter is quantified based on the Poisson-Boltzmann model, which describes free energies of charged surfaces in an electrolyte solution as a function of their effective surface charge density.

We used model parameters that reflect a typical experimental situation, with $\phi = 0.2$, a hydrophobic peptide volume $v_L = 15\text{nm}^3$, and $z_c = +35$ charges per peptide. Fig. 7.5B shows the Gaussian modulus $\bar{\kappa}$ as a function of P/L from $P/L = 0$ to $P/L = 1/175$. The maximal value $P/L = \phi/z_c = 1/175$ reflects electroneutrality of the membrane. Membrane destabilization is absent when the hydrophobic volume of the peptide is assumed to vanish (dash-dotted line) or when electrostatic interactions are ignored (dashed line). However, when both perturbation modes are accounted for (solid line), the Gaussian modulus adopts a positive sign.

Deep insertion of the peptide into the hydrocarbon core of the membrane tends to not only increase the membrane thickness, but also increase the cross-sectional area per lipid. Yet, a larger cross-sectional lipid area implies weaker mutual headgroup repulsion and an increased surface tension energy at the polarapolar interface. Hence, we expect the membrane to seek a deformation mode that decreases a_i even if at the

same time ah increases. This is accomplished by a saddle deformation. The electrostatic neutralization of the anionic lipid head groups by the terminal groups of the metaphilic peptide side chains further lowers the headgroup repulsion strength and, therefore, even more so enhances the tendency of the membrane to minimize its free energy by adopting NGC.

In our mean-field description above, we found that their facially amphiphilic structural organization allows metaphilic peptides to penetrate deeply into the membrane and render the Gaussian modulus less negative. In addition, peptides with cationic charges also shift the Gaussian modulus to less negative values. Both of these changes in the membrane Gaussian modulus are destabilizing and promote NGC generation, which is necessary for membrane permeation. These mean-field trends are in agreement with SAXS measurements and cell uptake results. In fact, these trends are strikingly similar to those observed for AMPs [218, 252, 259, 207]. Here we see that these metaphilic peptides give us a valuable perspective: It is not possible to vary hydrophobicity and charge of many AMPs and CPPs over a large range due to solubility and stability issues. However, the adaptable architecture of metaphilic peptides can accommodate greater cationic charge and hydrophobicity. As a result, these are ideal systems for testing how physicochemical properties impact membrane activity, as the above comparison shows. Further details on the molecular model can be found in Methods and Supporting Information in Appendix 7.5.

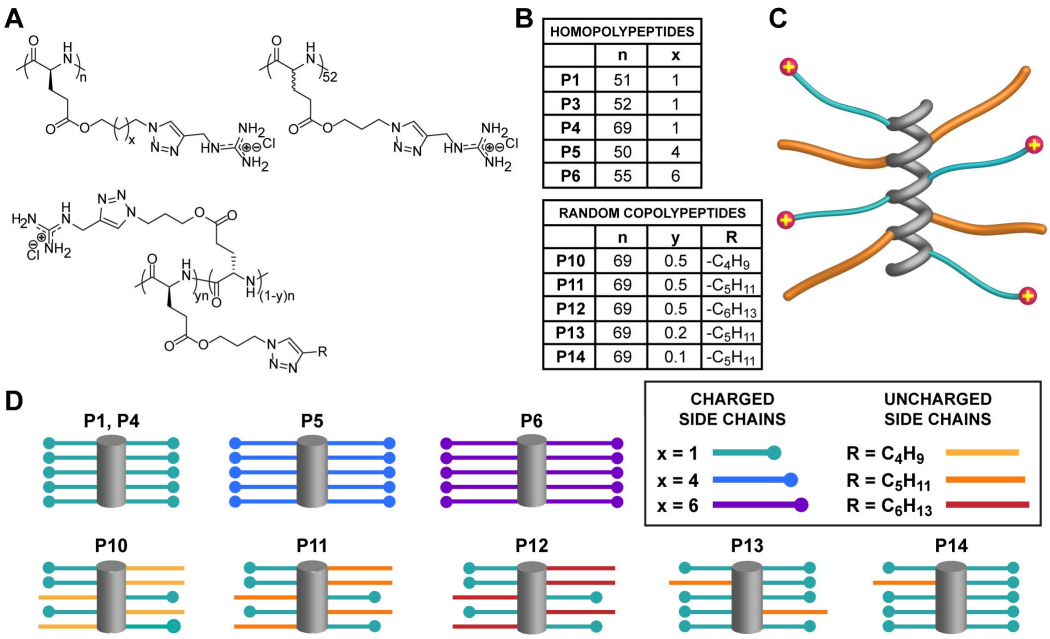

Figure 7.1. Design of metaphilic helical peptides. (A) Metaphilic helical peptides are poly(arginine) analogues characterized by long hydrophobic side chains (1318 σ-bonds in length) that have either a terminal guanidinium group or alkyl chain. Charged monomers having guanidinium groups were used to synthesize homopolypeptides (top left). A mixture of charged monomers and uncharged monomers, which feature terminal alkyl chains, were used to synthesize random copolypeptides (bottom). All prepared peptides adopt an -helical conformation except for P3 (top right), which was synthesized as a random coil from racemic monomers. (B) The structural peptide design parameters include the following: n (degree of polymerization), x (number of methylene groups), y (molar fraction of uncharged monomers), R (terminal alkyl chain), M_n (number-average molecular weight in kDa). (C) Metaphilic peptides featuring long side chains with terminal cationic and alkyl groups favor a stable α-helical conformation in aqueous solution. (D) Simplified cartoon depictions comparing the fractions of charged and uncharged side chains among the various metaphilic peptides.

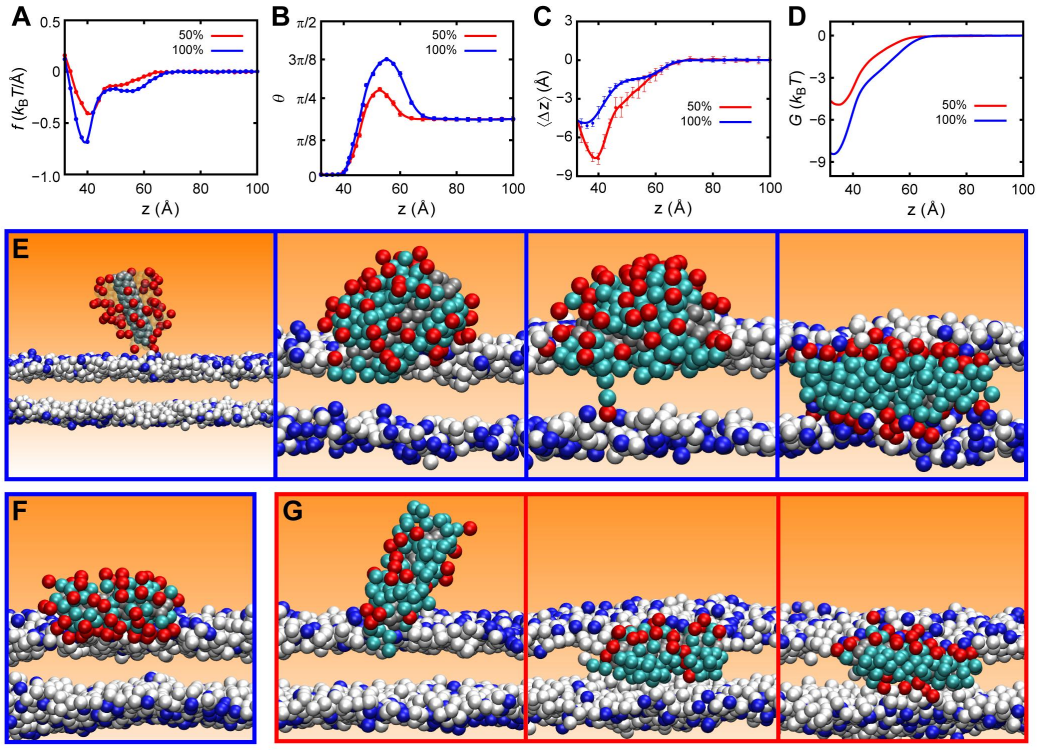

Figure 7.2. Landing and insertion processes of metaphilic peptides near a membrane. (A) Time-averaged force F exerted on the peptide upon landing. The force is evaluated as a function of the distance z between the center of mass of the peptide backbone and the head groups of the outer membrane leaflet. Two different cases are compared, in which 50% (red) and 100% (blue) of side chains are terminated by charged end groups. (B) Time-averaged tilt angle of the peptide backbone with respect to the membrane plane, as a function of peptide distance to the membrane. Note that tilt angle is zero when the peptide is parallel to the membrane and positive otherwise. (C) Averaged deviation Δ_z of the charged groups from the center of mass of the peptide backbone. (D) Free-energy profile G(z), obtained through integration of the force profile $F(z)$ shown in panel (A). (E) Sequence of simulation images demonstrating landing, initial anchoring (insertion of a side chain into the membrane), initial tunneling (a charged group of a side chain reaching the surface of the inner membrane leaflet), and full insertion in a membrane-spanning state, for a peptide with 4-bead long side chains, of which 100% have charged end groups. Lipid tails and surrounding ions are not shown here. The hydrophobic components of the side chains are colored in cyan, the peptide core is depicted in gray. The remaining beads are color coded based on their charges: red for $+1e$, white for uncharged, and blue for $1e$. (F) Final state of a peptide with 2-bead long side chains, of which 100

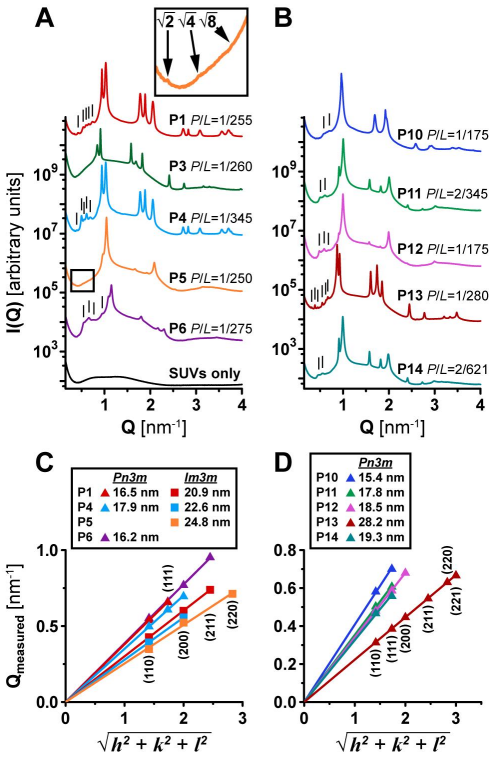

Figure 7.3. Metaphilic helical peptides generate NGC necessary for membrane permeation. SAXS spectra from DOPS/DOPE = 20/80 membranes incubated with homopolymer (A) and random copolymer (B) peptides at electroneutral P/L molar ratios. Correlation peaks corresponding to identified cubic phases are indicated (black lines). Inset in (A) provides an expanded view of the cubic reflections (boxed region) for P5. (C,D) Indexing of the peptide-induced Pn3m and Im3m cubic phases is shown by plotting the measured Q positions, Qmeasured, versus the assigned reflections in terms of Miller indices, $\sqrt{h^2+k^2+l^2}$. The slopes of the linear regressions were used to calculate their lattice parameters, which are listed in the legends.

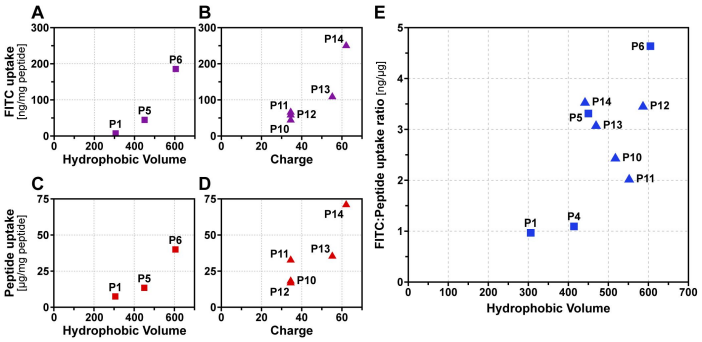

Figure 7.4. Relations of membrane permeation with hydrophobic volume and cationic charge. Membrane permeation, as measured by FITC and peptide uptake in cells, was found to correlate with the hydrophobic volumes and cationic charges of metaphilic helical peptides. A set of homopolypeptides (P1, P5, P6) with similar degree of polymerization and charge exhibited both FITC (A) and peptide (C) uptake levels that tracked well with their different hydrophobic volumes. Conversely, a set of random copolypeptides (P10P14) with identical degree of polymerization and comparable hydrophobic volumes showed that increasing cationic charge correlated with increased FITC (B) and peptide (D) uptake. (E) Among all nine metaphilic helical peptides tested, we also observed that the ratio of FITC uptake to peptide uptake generally increased with hydrophobic volume. Greater hydrophobic volumes promote more stable pores with longer lifetimes, which allow more efficient membrane permeation by free molecules of peptide and FITC. In contrast, lower hydrophobic volumes are expected to yield more transient pores with shorter lifetimes, and thus, facilitate rapid translocation of the peptide across a membrane.

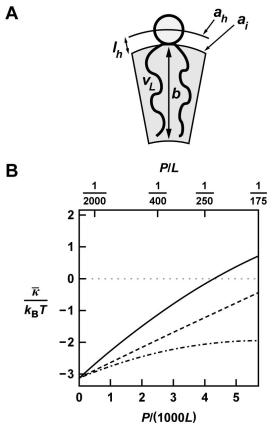

Figure 7.5. Membrane insertion of a metaphilic peptide results in a less negative Gaussian modulus. (A) We characterize a lipid molecule in terms of the cross-sectional area a_i at the hydrocarbon chain-headgroup interface, the cross-sectional headgroup area a_h (measured at a surface parallel to the hydrocarbon chain-headgroup interface at distance l_h away), and the effective thickness b of the hydrocarbon chain region. The volume v_L occupied by the lipid's two hydrocarbon chains is conserved. The polar headgroup is represented by a light-shaded circle. (B) The Gaussian modulus (measured in units of the thermal energy unit $k_B T$) as a function of the peptide-to-lipid ratio P/L. The full molecular model (solid line) accounts for both the increase in the hydrophobic volume of the membrane core upon peptide insertion and electrostatic interactions of the anionic lipid head groups with the cationic terminal groups of the metaphilic peptide side chains. This is contrasted with ignoring either the hydrophobic peptide volume ($v_P = 0$, dashed line) or electrostatic interactions (dash-dotted line).

7.4. Conclusions and Prospects

Membrane-permeating peptides such as AMPs and CPPs are usually composed of linear sequences of amino acids and have simple architectures. By using a class of peptides with a chemically adaptive metaphilic architecture, which have quasi- liquid surfaces and highly deformable shapes, we showed that it is possible to interact with the membrane in unexpected ways, and significantly enhance the membrane-permeating activity of linear arginine-based peptides. The root causes of this enhancement are explored using a combination of computer simulations, X-ray diffraction, and mean-field theory. Since the metaphilic architecture allows for permeation and translocation mechanisms not available for most peptides, these results here suggest that it may be possible to engineer nanoscopic molecular architectures optimized for applications such as antimicrobial agents for multidrug-resistant bacteria and drug delivery systems.

7.5. Methods

7.5.1. Synthesis of Polypeptides

All peptides (P1, P4P6, P10P14) were previously synthesized and characterized elsewhere[238]. The synthesis procedures are outlined in Scheme S1 of the Supporting Information. Typically, L-glutamic acid (1 equiv) was monoesterified using various chloroalkyl alcohols (1.5 - 2 equiv) under the catalysis of H2SO4. The resulting -chloroalkyl-L-glutamic acid was purified by recrystallization in deionized water/2-propanol (1:1, v/v) and lyophilized (yield 30- 70%). The lyophilized amino acid (1 equiv) was then reacted with phosgene (80% solution in toluene, 1.2 - 1.5 equiv) in anhydrous tetrahydrofuran (THF) at 50°C for 2 h to yield γ-chloroalkyl-L-glutamate based N-carboxyanhydrides (NCAs), which were further purified through recrystallization in THF/hexane (1:1, v/v, three times) (yield 60-70%). The dried NCA monomers were transferred into a glovebox and stored at -30° C. To obtain the target polypeptides, hexamethyld-isilazane was used to initiate the controlled ring-opening polymerization of NCAs in hydrous dimethyl-formamide (DMF)[236, 283, 284] where the degree of polymerization was predetermined by the feeding monomer-to-initiator ratio. After $> 99\%$ monomer conversion (monitored by Fourier transform infrared spectroscopy), an aliquot of the DMF solution was transferred to a new vial, diluted, and injected into gel permeation chromatography (GPC) for the determination of degree of polymerization and polydispersity

(polydispersity < 1.26 for all polymers). NaN3 was then added (10 equiv compared with side chain chloro groups) and the mixture was stirred at 60°C for 48 h. The resulting azide-functionalized polypeptide was purified through extraction with chloroform, and subsequent precipitation in hexane/diethyl ether (1:1, v/v) (yield 7085%). For the final copper-catalyzed click chemistry step, azide-functionalized polypeptide (1 equiv of azido groups) was mixed with propargyl guanidine (1.5 equiv), N,N,N,N,N-pentamethyldiethylenetriamine (0.10 equiv), and CuBr (0.01 equiv) in DMF in a glovebox. The mixture was stirred at room temperature for 24 h, and the final guanidine-functionalized metaphilic peptide was purified by dialysis against deionized water followed by lyophilization (yield 6070%). To incorporate additional hydrophobic moieties (P10P14), long chain alkynes were added together with propargyl guanidine for coconjugation. Azide-functionalized polypeptides were characterized by nuclear magnetic resonance (NMR) and GPC for their chemical structures and molecular weights. The polypeptides post click chemistry side chain modification were analyzed by NMR to verify the efficiency of side chain modifications and by circular dichroism to analyze their conformation[238].

7.6. Simulation Procedure

We performed molecular dynamics simulations using the Lammps package to investigate the landing and subsequent insertion process of prototypical metaphilic peptides on and into a membrane. In our coarse-grained model, all molecules were represented as assemblies of spherical beads (diameter $\sigma = 8.5\mathring{A}$[285] the size of a lipid headgroup). Specifically, the membrane was modeled as a bilayer of 4- bead long lipids and spanned an entire cross-section of the system. 20% of the lipids carried a 1e charge on their headgroup. The peptide possessed a helical core of 55 beads (corresponding to 55 amino acids), onto each of which was grafted a 4-bead long, flexible side chain. Either 50% or 100% of the side chains carried a terminal +1e charge. Both the membrane and the peptide were embedded in a 100mM salt solution mimicking physiological conditions. A relatively large system of size $60 \times 60 \times 60\sigma^3$ was chosen, giving rise to 7200 lipids and over 17 000 ions. Periodic boundary conditions were applied in all three dimensions.

The beads in the peptide core were grouped as a rigid body, whereas those in the side chains or in the lipids were stiffly bonded by a harmonic potential

$$U_{bond}(r) = k_{bond}(r - r_0)^2 \tag{7.1}$$

with equilibrium bond length $r_0 = \sigma$ and strength $k_{bond} = 300k_BT/\sigma^2$. For lipids, a strong angle potential was introduced between two adjacent bonds to maintain a linear structure,

$$U_{angle}(\theta) = k_{angle}(\theta - \theta_0)^2 \tag{7.2}$$

with $\theta_0 = 180^\circ$ and $k_{angle} = 10k_BT/rad^2$. All nonbonded beads were subject to excluded-volume effects and Coulomb interactions. The former were implemented via a shifted-truncated Lennard-Jones (LJ) potential with strength $\varepsilon = 0.8k_BT$ and cutoff $r_c = 21/6\sigma$, while the latter was treated via Ewald summation with a relative accuracy of 10^{-4}. Moreover, we employed a widely used generic model with implicit solvent to efficiently account for hydrophobicity[29]. Uncharged beads in the hydrophobic side chains and lipid tails experienced an effective attraction,

$$U_{cos}(r) = -\varepsilon\cos^2[\pi(r - r_c)/2w_c], \;\; r_c \le r \le r_c + w_c \tag{7.3}$$

with $w_c = 1.6\sigma$. Due to the soft attraction (strength $\varepsilon = 0.8k_BT$), side chains and lipids tended to display moderate aggregation, remaining in the liquid state rather than forming a solid.

When studying the landing process via steered molecular dynamics, we confined the lipid head groups of the outer leaflet of the membrane within the $x-y$ plane, and simultaneously fixed the center of mass of the peptide core but released all other degrees of freedom. By systematically varying the distance between the peptide and the membrane, we could measure the free-energy change upon landing. Here the system was examined in the NVT ensemble by applying a Langevin thermostat to introduce thermal fluctuations. In the subsequent investigation of the insertion process, to allow the reconfiguration of the membrane upon insertion, we also applied a Berendsen barostat and kept the system under constant pressure, equal to the osmotic pressure of a 100 mM salt solution. All simulations were performed for more than 107 time steps, with time step $dt = 0.002\tau$, where $\tau = (m\sigma^2/\varepsilon)^[1/2$ (m the bead mass) was the LJ time unit.

7.7. SAXS Experiments

SUVs were prepared from lyophilized phospholipids DOPS (1,2-dioleoyl-sn-glycero-3-phospho-L-serine (so- dium salt)) and DOPE (1,2-dioleoyl-sn-glycero-3-phosphoethanol- amine) purchased from Avanti Polar Lipids. Briefly, individual lipid stock solutions were prepared by dissolving DOPS and DOPE

in chloroform at 20 mg/mL. A model membrane composition was prepared from the lipid stock solutions as a mixture of DOPS/DOPE at a 20/80 molar ratio. The lipid mixture was evaporated under N2 and desiccated under vacuum overnight to form a lipid film, and then resuspended in aqueous 100 mM NaCl, 10 mM N-(2-hydroxyethyl)- piperazine-N-ethanesulfonic acid (HEPES) (pH 7.4) to a concen- tration of 20 mg/mL. The aqueous lipid suspension was incubated at 37°C overnight, sonicated until clear, and extruded through a 0.2 μm pore Nucleopore filter (Whatman) to obtain SUVs.

Metaphilic peptides were solubilized in aqueous 100 mM NaCl, 10 mM HEPES (pH 7.4) and mixed with SUVs at electroneutral P/L molar ratios, which are calculated based on 20 mol % of lipids having anionic charge. Samples were hermetically sealed into quartz capillaries (Hilgenberg GmbH, Mark-tubes) for SAXS experiments at the Stanford Synchrotron Radiation Lightsource (SSRL, beamline 4-2) using monochromatic X-rays with an energy of 9 keV. Scattered radiation was collected using a Rayonix MX255-HE detector (73.2 μm pixel size) and 2D SAXS powder patterns were integrated with Nika 1.50[286] package for Igor Pro 6.31 and FIT2D[287].

The integrated scattering intensity $I(Q)$ was plotted against Q using Origin Lab software. Phases present in each sample were identified by tabulating the measured peak positions, $Q_{measured}$, and comparing their ratios with those of the permitted reflections for different crystal phases. The lattice parameter of each identified phase was calculated from the slope of the linear regression through points corresponding to the peaks. For powder-averaged cubic and hexagonal phases, each point corresponding to a peak was defined by coordinates of the assigned reflection (in terms of Miller indices h,k,l) and $Q_{measured}$. For a cubic phase, $Q = (2\pi/a)\sqrt{h^2+k^2+l^2}$, and for a hexagonal phase, $Q = (4\pi/(a\sqrt{3}))\sqrt{h^2+hk+k^2}$, where a is the lattice parameter. Therefore, the slopes of the regressions of $Q_{measured}$ vs $\sqrt{h^2+k^2+l^2}$ and $Q_{measured}$ vs $\sqrt{h^2+hk+k^2}$ are $2\pi/a$ and $4\pi/(a\sqrt{3})$, respectively, which can be used to calculate a. For a lamellar phase, each point corresponding to a peak has coordinates of the order of the reflection, N, and $Q_{measured}$ with the relation $Q = 2/d$. The regression of $Q_{measured}$ vs N then has a slope of $2\pi/d$, which yields the periodic spacing d.

7.8. Cellular Uptake Experiments

Cellular Uptake Experiments. Cellular uptake data were sourced from experiments conducted previously elsewhere[238] to be compared with findings from this study. Briefly, HeLa cells were seeded into

96-well plates at a density of 1×10^4 cells/well and cultured for 24 h. The culture medium was then replaced with serum-free Dulbecco's modified Eagle's medium (DMEM). Endocytosis inhibitors chlorpro- mazine (10 μg/mL), genistein (200 μg/mL), methyl-β-cyclodextrin (50 μgM), and wortmannin (50 nM) were added to the cells 30 min before the addition of peptide. To investigate the membrane permeability, each peptide was labeled with rhodamine (RhB) and 2 μgg was added into each well containing HeLa cells. After incubating the RhB-peptide with the cells for 2 h at 37°C, the cells were washed with phosphate-buffered saline (PBS) containing 20 U/mL heparin and then lysed using radioimmunoprecipitation assay (RIPA) buffer at room temperature for 20 min. The intracellular content of the RhB- peptide in the cell lysate was quantified using spectrofluorimetry and the cellular protein level was quantified using a bicinchoninic acid (BCA) kit, such that the uptake level was expressed as the quantity (μg) of RhB-peptide per 1 mg of cellular protein. Peptide-induced pore formation in cell membranes was studied by measuring the cellular internalization of membrane-impermeable FITC. The procedures were the same as above, except 2 μg of peptide and 0.2 μg of FITC were added into each well containing HeLa cells. Cells that were treated with only FITC served as the control. FITC in the cell lysate was quantified using spectrofluorimetry and the uptake level was expressed as the quantity (μg) of FITC per 1 mg of cellular protein. The cellular uptake levels were compared against those of HIV-TAT and R9 that had been fluorescently labeled with carboxytetramethylrhodamine (TAMRA).

7.9. Calculation of Hydrophobic Volume for Metaphilic Peptide Comparisons

We defined the hydrophobic volume of a metaphilic peptide by the total number of methyl and/or methylene groups present among its side chains. For uncharged side chains, this includes: (a) R, conjugated alkyl chain with 4-6 hydrocarbons, (b) $x+2$, spacer between triazole and ester with 3, 6, or 8 methylene groups, (c) spacer between backbone and ester with 2 methylene groups. For charged side chains, this includes: (a) spacer between triazole and guanidine with 1 methylene group, (b) $x+2$, spacer between triazole and ester with 3, 6, or 8 methylene groups, (c) spacer between backbone and ester with 2 methylene groups. For example, for metaphilic peptide $P11 : (0.5)(69)(5+3+2)+(0.5)(69)(1+3+2) = 552$ total methyl and/or methylene groups.

7.10. Mean-Field Theory

We employ a molecular lipid model that was proposed and analyzed in previous work [281]. It describes the free energy per lipid

$$f(a_i, a_h, b) = \gamma a_i + \frac{B}{a_h} + \tau(b - l_c)^2 \tag{7.4}$$

in a lipid bilayer as a function of three molecular quantities, a_i, a_h, and b; see Fig. 5a. The first contribution to f corresponds to the interfacial energy of exposing the apolar hydrocarbon chains to the polar headgroup region; a_i is the cross-sectional area per lipid at this interface, and $\gamma \approx 12\, k_B T/\mathrm{nm}^2$ is the corresponding surface tension. The second term accounts for the repulsive interactions between lipid headgroups, here described in terms of a single headgroup interaction surface of cross-sectional area a_h per lipid, located a fixed distance l_h away from the hydrocarbon chain-headgroup interface. All headgroup interactions (steric, dipolar, hydration, etc) are lumped into a single parameter, B. Finally, the third term in Eq. 7.4 describes the stretching/compression energy of the hydrocarbon chain region, where b is the actual thickness and l_c the preferred thickness of the hydrocarbon core for each membrane leaflet. The prefactor τ and the preferred thickness l_c have been estimated previously using detailed molecular-level chain packing calculations [288], resulting in $\tau = 7.9\, k_B T/\mathrm{nm}^2$ and $l_c = 1.16\,\mathrm{nm}$ for lipids with two $-(\mathrm{CH_2})_{15} - \mathrm{CH_3}$ hydrocarbon chains. We also employ the assumption that the hydrophobic volume per lipid, $v_L = 0.918\,\mathrm{nm}^3$, is conserved for any given conformation a_i, a_h, and b. The bending free energy per unit area of an initially planar and symmetric lipid bilayer

$$\frac{\triangle f_E}{a_E} + \frac{\triangle f_I}{a_I} = \frac{\kappa}{2}(c_1 + c_2)^2 + \bar{\kappa} c_1 c_2 \tag{7.5}$$

can be expressed according to Helfrich [289] in terms of the two principal curvatures c_1 and c_2, measured at the midplane, with κ and $\bar{\kappa}$ denoting the bending stiffness and Gaussian modulus. The left-hand side of Eq. 7.5 separates the free energy into contributions from the external (E) and internal (I) leaflet of the lipid bilayer. We characterize the lipid conformation in the external leaflet by a_i^E, a_h^E, b_E and in the internal leaflet by a_i^I, a_h^I, b_I. Knowing these quantities allows us to calculate the bending-induced change in free energy per lipid, $\triangle f_E = f(a_i^E, a_h^E, b_E) - f(a_0, a_0, b_0)$ and $\triangle f_I = f(a_i^I, a_h^I, b_I) - f(a_0, a_0, b_0)$, in the external and internal leaflet, respectively, where a_0 is the equilibrium cross-sectional area per lipid of a planar membrane. Note

that the conservation of the hydrophobic volume per lipid, v_L, links $a_0 = v_L/b_0$ to the equilibrium chain extension in a planar membrane b_0. More generally, for non-vanishing membrane curvatures, conservation of v_L links the cross-sectional areas $a_E = v_L/\{b_E[1+(c_1+c_2)b_E/2+c_1c_2b_E^2/3]\}$ and $a_I = v_L/\{b_I[1-(c_1+c_2)b_I/2+c_1c_2b_I^2/3]\}$ of the lipids in the external and internal leaflets, measured at the bilayer midplane, to their respective chain lengths b_E and b_I. In fact, the molecular cross-sectional areas $a_i^E = a_E[1+(c_1+c_2)b_E+c_1c_2b_E^2]$, $a_i^I = a_I[1-(c_1+c_2)b_I+c_1c_2b_I^2]$, $a_h^E = a_E[1+(c_1+c_2)(b_E+l_h)+c_1c_2(b_E+l_h)^2]$, and $a_h^I = a_I[1-(c_1+c_2)(b_I+l_h)+c_1c_2(b_I+l_h)^2]$ can all be related to b_E and b_I through simple geometric relations. Yet, the hydrophobic thicknesses, $b_E = b_0[1+\eta(c_1+c_2)]$ and $b_I = b_0[1-\eta(c_1+c_2)]$, of the external and internal leaflets, respectively, may themselves be curvature-dependent. We account for the curvature-induced adjustment of leaflet thickness through a yet unknown relaxation parameter η. The free energy in Eq. 7.5 will adopt its minimum with respect to η. Force equilibrium of a planar membrane yields the condition

$$B = \frac{\gamma v_L^2}{b_0^2} - 2\tau v_L(b_0 - l_c). \tag{7.6}$$

for the equilibrium thickness b_0. Typical values for the equilibrium cross-sectional area per lipid of a planar membrane, $a_0 \approx 0.70\,\mathrm{nm}^2$, are well known from both experiments [290] and MD simulations [291]. Hence, we use $b_0 = v_L/a_0 = 1.31\,\mathrm{nm}$ as input in Eq. 7.6 to determine the headgroup repulsion parameter B.

Series expansion of the left-hand side of Eq. 7.5, minimization with respect to η, and comparison with the right-hand side of that equation allows us to calculate the Gaussian modulus $\bar{\kappa}$, the relaxation parameter η, and the bending stiffness κ. It is convenient to express the results in terms of the dimensionless quantities $\bar{B} = Bb_0^2/(\gamma v_L^2)$, $\bar{\tau} = b_0^3\tau/(\gamma v_L)$, $\bar{l}_c = l_c/b_0$ and $\bar{l}_h = l_h/b_0$. Eq. 7.6 is then equivalent to $\bar{B} = 1-2\bar{\tau}(1-\bar{l}_c)$. With that, our final results are

$$\begin{aligned}
\bar{\kappa} &= \frac{2}{3}b_0^2\gamma\left\{2(1-\bar{l}_c)[2+3\bar{l}_h(2+\bar{l}_h)]\bar{\tau} - 3\bar{l}_h(2+\bar{l}_h)\right\}. \\
\eta &= \frac{b_0}{2}\frac{1+2\bar{l}_h-(1-\bar{l}_c)(3+4\bar{l}_h)\bar{\tau}}{1+\bar{\tau}}, \\
\kappa &= \gamma b_0^2\left\{(1+2\bar{l}_h)^2[1+2(\bar{l}_c-1)\bar{\tau}] - \frac{[1+2\bar{l}_h+(\bar{l}_c-1)(3+4\bar{l}_h)\bar{\tau}]^2}{1+\bar{\tau}}\right\}.
\end{aligned} \tag{7.7}$$

As introduced above, we use $\gamma = 12\,k_BT/\mathrm{nm}^2$, $\tau = 7.9\,k_BT/\mathrm{nm}^2$, $l_c = 1.16\,\mathrm{nm}$, $v_L = 0.918\,\mathrm{nm}^3$, $b_0 = 1.31\,\mathrm{nm}$. With that we obtain the following values for $\bar{\kappa}$, η, and κ as function of the distance l_h between the headgroup interaction surface and the polar-apolar interface

We note that a small headgroup, such as for $l_h = 0.1\,\mathrm{nm}$, entails a positive Gaussian modulus and thus instability with respect to negative Gaussian curvature. Growing headgroup size increases the bending stiffness and decreases the Gaussian modulus to more negative values. In the following we use $l_h = 0.3\,\mathrm{nm}$.

Metaphilic peptides insert into the hydrocarbon core of the host bilayer such that their hydrophobic residues are buried into the hydrocarbon core whereas the charged moieties extend toward the polar-apolar interface The burying of the peptide into the hydrocarbon core is described in our model by an effective increase in the lipid's hydrophobic volume $v_L \to v_L + v_P^{eff} P/L$, where P/L is the peptide-to-lipid ratio. Here, v_P^{eff} is the effective hydrophobic volume of the peptide. If the peptide's residues were all hydrophobic, $v_P^{eff} = v_P$ would correspond to the hydrophobic volume of the peptide, $v_L = 15\,\mathrm{nm}^3$ for P11. We expect the effective value v_P^{eff} to be somewhat smaller than v_P, depending on how much area the charged residues occupy at the polar-apolar interface and at the headgroup interaction surface. The electrostatic interactions of the cationic side chains with the anionic lipid headgroups can be described within Poisson-Boltzmann theory. As pointed out by Israelachvili [279], the inverse $1/a_h$-dependence of the headgroup repulsion free energy contribution is consistent with the linearized Poisson-Boltzmann model, which is applicable for membranes with mole fractions of up to 20% of charged lipids at physiological conditions[36]. This simply implies to replace the headgroup repulsion parameter in Eq. 7.4 by $B - k_B T 2\pi l_B l_D \left[\phi^2 - (\phi - z_c\alpha)^2\right]$, where $l_B = 0.7\,\mathrm{nm}$ is the Bjerrum length in water, $l_D = 1\,\mathrm{nm}$ is the Debye screening length at physiological conditions, and $z_c = 35$ is the number of cationic side chains of P11. We also recall $\phi = 0.2$ is the mole fraction of anionic lipids. Fig. 5b is then calculated for $v_L^{eff} = 10\,\mathrm{nm}^3$ and $z_c = 35$ (solid line), $v_L^{eff} = 10\,\mathrm{nm}^3$ and $z_c = 0$ (dashed line), and $v_L^{eff} = 0\,\mathrm{nm}^3$ and $z_c = 35$ (dash-dotted line). A more systematic description of the Gaussian modulus and the bending stiffness for variations of v_L^{eff} and z_c is presented in Fig. S1 of the Supporting Information, suggesting that insertion of metaphilic peptides into membranes generally tends to shift the Gaussian modulus towards more positive values but has little effect on the bending stiffness.

Table 7.1. Values of $\bar{\kappa}$, η, and κ calculated for specific l_h.

l_h/nm	$\bar{\kappa}/(k_BT)$	η/b_0	$\kappa/(k_BT)$
0.1	6.0	0.14	14.9
0.3	-3.1	0.18	23.3
0.5	-13.5	0.23	33.6

7.11. Associated Content

Supporting information: The supporting information is available free of charge on the ACS Publication website at DOI: 10.1021/acsnano.6b07981.

7.12. Acknowledgments

This work is supported by grants from the National Science Foundation (DMR-1411329 to M.W.L. and G.C.L.W.; DMR- 1610796 to M.H. and E.L.; DMR-1309525 to J.C.) and the National Institutes of Health (1R21AI117080 to J.C.). G.V.B. acknowledges a doctoral scholarship from CAPES Foundation/ Brazil Ministry of Education (Grant No. 9466/13-4). Use of the Stanford Synchrotron Radiation Lightsource, SLAC National Accelerator Laboratory, is supported by the U.S. Department of Energy, Office of Science, Office of Basic Energy Sciences under Contract No. DE-AC02-76SF00515. The SSRL Structural Molecular Biology Program is supported by the DOE Office of Biological and Environmental Research, and by the National Institutes of Health, National Institute of General Medical Sciences (including P41GM103393).

8. POISSON-BOLTZMANN MODEL OF ELECTROLYTES CONTAINING UNIFORMLY CHARGED SPHERICAL NANOPARTICLES *

8.1. Introduction

Electrostatic interactions in aqueous solutions are omnipresent in biological and biotechnological systems and are of fundamental importance for the stability of colloidal suspensions, association and adsorption equilibria, and macroion complex formation [8]. One of the most fascinating aspects of interacting macroions in electrolyte solutions is the possibility of attraction between like-charged particles. Attraction is not predicted by the classical mean-field Poisson-Boltzmann (PB) theory [292], which assumes point-like ions and neglects ion-ion correlations. However, attraction is frequently observed experimentally. For example, small divalent metal cations induce condensation of DNA [293, 294], aggregation of rod-like M13 viruses [295] and bacteriophages fd [296], and network formation in actin solutions [297]. Multivalent ions with charges that are spatially separated tend to exhibit a particulary pronounced tendency to induce aggregation of like-charged macroions. Among the most notable examples are polyelectrolytes that are able to coagulate colloidal suspensions [298, 299] or lipid vesicles [300, 301]. Virtually any sufficiently large macroion that has spatially separated charges can serve as condensing agent: cationic peptides are able to trigger aggregation of anionic vesicles [302, 303], charged colloids and cationic micelles condense DNA [304], DNA condenses cationic lipid membranes [305] or lipid vesicles [306], and proteins aggregate helical filaments [307]. These macroions should be contrasted with large multivalent ions, yet with all charge located at their center such as for example tungsten, which tightly adsorbs onto an oppositely charged surface via electrostatic interactions [308] but is not particulary potent in mediating the attraction between like-charged objects.

Efforts to model electrostatic correlations have focused on the limits of strong and weak electrostatic

*Reprinted from "K. Bohinc, G. V. Bossa, S. Gavryushov, S. May, Poisson-Boltzmann model of electrolytes containing uniformly charged spherical nanoparticles, J. Chem. Phys. 145 (23) (2016) 234901", with the permission of AIP Publishing. Copyright 2016 IP Publishing. This paper can be accessed online at http://aip.scitation.org/doi/abs/10.1063/1.4968210. The material in this chapter was co-authored by Klemen Bohinc, Guilherme V. Bossa, Sergei Gavryushov, and Sylvio May. G. V. Bossa contributed to the mean-field modeling, figures preparation, writing and discussion of the results.

coupling [309, 310, 311]. The former case, which becomes most relevant for multivalent ions, has been elucidated by Shklovskii [312], who proposed an approximate method to describe inter-ionic correlations through the formation of a Wigner crystal [313]. Models that target the weak correlation regime can typically be viewed as some kind of modification of the classical PB theory. Examples include integral-equation theories [314, 315], perturbative expansions around the classical PB model [316], modified PB theory [317], local density-functional theory [318], and field theoretic methods [319, 320].

Besides correlations between the charges on distinct small mobile ions there are a number of other mechanisms that can lead to the attraction of like-charged particles. Examples include surface charge fluctuations of the like-charged particles [321] or depletion-mediated attraction due to the addition of an inert co-solute to the colloidal system [322, 323]. When ions carry multiple charges that are spatially separated, intra-ionic charge-charge correlations will be present in addition to inter-ionic correlations. These intra-ionic correlations are manifested by and refer to the fixed mutual distances between all individual charges that belong to a given ion. Intra-ionic correlations have been incorporated into the PB formalism [324, 325, 326, 31, 327]; they too can give rise to attractive interactions between like-charged macroions.

In addition to intra- and inter-ionic correlations, the finite size of ions also contributes to the properties of the electric double layer. Consequently, PB theory has been modified in a number of approaches so as to account for the steric repulsion between ions [328, 329]. For example, a lattice gas entropy has been incorporated into the PB model [80, 330, 331], and spherical ion geometry was included based on the Carnahan-Starling equation of state [90, 81]. Also, a density functional approach was modified by taking into account finite ion sizes [332]. Finite-size effects are especially important close to charged surfaces. Stern [333] argued that the closest approach of an ion to an oppositely charged surface is limited by the ion's steric size and thus proposed to model the structure of an electric double layer by a diffuse ion cloud that is separated from the charged surface by a parallel-plate capacitor of molecular thickness. He showed that the properties of the capacitor are determined by the degree of specific ion adsorption and by its much lower dielectric constant as compared to bulk water. The molecular origin of the dielectric constant depends on the polarization of interfacial water and reflects the hydrophobicity of the surface [334].

We have recently addressed the problem of incorporating into mean-field electrostatics spherical nanoparticles with uniform surface charge density that are mobile and reside in a salt solution sandwiched between two planar charged surfaces [335]. However, this task was only accomplished so far in the linearized PB regime, which is valid for very small charge densities on both the extended planar surfaces and

on the surfaces of the spherical nanoparticles. It was demonstrated that attraction between like-charged surfaces arises above a critical nanoparticle size. An approximate analytic expression was derived for the critical size above which attraction between like-charged surfaces starts to emerge.

In this work, we formulate a non-linear PB model for uniformly charged spherical nanoparticles, sandwiched between two extended like-charged surfaces. Our model represents a mean-field approach in the sense that correlations between different nanoparticles are neglected. Yet, intra-ionic correlations (i.e., the connectivity of the charges within each spherical particle) are fully incorporated into the model. In addition, we take into account the excluded volume interactions of the spherical nanoparticles with the charged surfaces. Minimization of the free energy of the system through a variational procedure results in a modified Boltzmann distribution for the local nanoparticle concentration. Insertion of this distribution into Poisson's equation results in an integral-differential equation that we have solved numerically. Our predictions for the local charge density are compared to results from Monte Carlo simulations. We also calculate the pressure that acts on the planar surfaces. Based on non-linear PB theory we predict a regime where the force between like-charged surfaces is attractive. We demonstrate that increasing salt concentration weakens the attraction between like-charged surfaces and ultimately reverses the attraction into a repulsion.

Our results for uniformly charged nanoparticles are compared to those for nanoparticles with their entire charge located at the particle center. In order to assess what role the spatial separation of the charges on the nanoparticles plays, we compare our results for uniformly charged nanoparticles to those for nanoparticles with the entire charge located at the nanoparticle center. The latter (in contrast to the former) always mediate a repulsive force between like-charged surfaces. Hence, our present work highlights the importance of properly accounting for the charge distribution of spatially extended multivalent ions in electrolyte solutions.

8.2. Theory

The system we consider is schematically displayed in Fig. 8.1; it consists of two planar, like-charged surfaces (both positively charged) of area A immersed in an aqueous solution containing negatively charged spherical nanoparticles of radius R and valence z. The solution is in contact with a salt reservoir consisting of small (in our model point-like) monovalent positive and negative ions, each with bulk concentration n_0. Because the present work focuses on the method of incorporating the electrostatic properties of particles

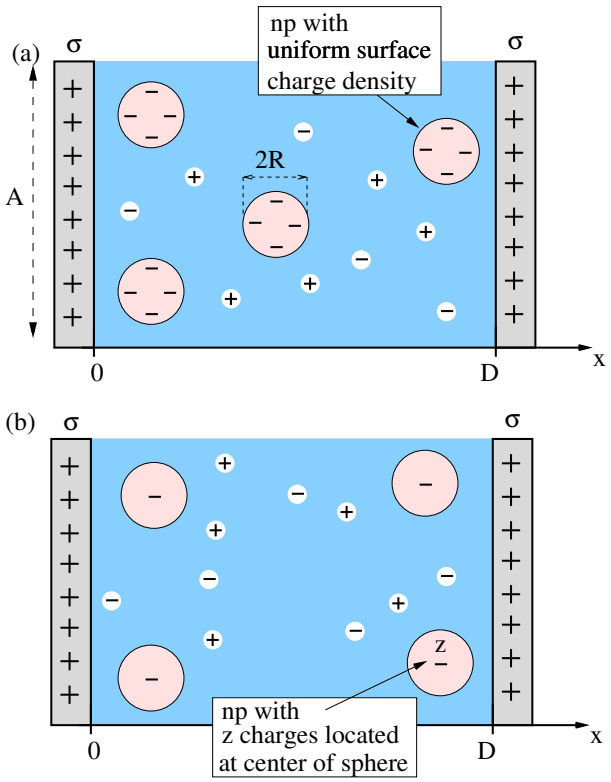

Figure 8.1. Schematic illustration of two like-charged planar surfaces (located at positions $x = 0$ and $x = D$, each of lateral area A and with surface charge density σ), embedded in a solution of negatively charged spherical nanoparticles (np). Each spherical nanoparticle has radius R and carries a uniform surface charge density $-z/(4\pi R^2)$ (a) or has all z charges located at the center of the sphere (b). The system is in contact with a reservoir of monovalent point-like positive and negative salt ions, each of concentration n_0.

with spatially extended charge distributions into the nonlinear PB formalism, it is convenient to demand all nanoparticles reside in between the two planar surfaces without being able to migrate into the bulk solution. This approximation becomes exact in the two limits of small n_0 or large z. We note that it is, of course, also possible to fix the chemical potential of the nanoparticles instead of their number when analyzing concrete applications. The two planar surfaces are parallel, and they are separated by a distance D (with $D > 2R$). Our choice of a planar geometry for the macroions was made in order to keep the system simple; it ensures that all average properties depend only on the normal direction x of the two surfaces. The two surfaces are located at positions $x = 0$ and $x = D$ of a Cartesian coordinate system; overall charge neutrality then requires

$$2\sigma + \int_0^D dx\, \rho(x) = 0\,, \tag{8.1}$$

where σ is the charge density at each of the two planar surfaces and $\rho(x)$ the local volume charge density in the aqueous solution. The surface charge density can be written as $\sigma = e/a$, where a is the surface area occupied by one elementary charge e.

The electrostatic mean-field free energy of the system, F, measured per unit area A and in units of the thermal energy k_BT (here k_B is Boltzmann's constant and T is the absolute temperature) can be expressed as

$$\begin{aligned}\frac{F}{k_BTA} &= \int_0^D dx \left[\frac{\Psi'^2}{8\pi l_B} + f_{mix}(m,m_0) + f_{mix}(n_+,n_0) \right. \\ &+ \left. f_{mix}(n_-,n_0) + Um \right] + \mu \int_0^D (m-m_0)\,dx\,. \end{aligned} \tag{8.2}$$

The first term on the right hand side of Eq. 8.2 corresponds to the energy stored in the electrostatic field, here expressed in terms of the commonly used dimensionless electrostatic potential $\Psi = e\Phi/k_BT$, instead of the electrostatic potential Φ, and in terms of the Bjerrum length $l_B = e^2/(4\pi\varepsilon\varepsilon_0 k_BT)$, instead of the dielectric constant ε of the aqueous solution (ε_0 is the permittivity of free space). At room temperature the Bjerrum length in the aqueous solution is 0.7 nm. We use a prime to denote the derivative with respect to x. The function $f_{mix}(m,m_0) = m\ln(m/m_0) - m + m_0$ in the second term describes the ideal mixing free energy of the nanoparticles, where $m(x)$ is the local concentration of the spherical nanoparticles (measured with respect to their center) and $m_0 = (1/D)\int_0^D m(x)dx$ is the corresponding average concentration.

We note that using an ideal mixing free energy for the nanoparticles requires us to work in the limit of small concentrations everywhere in the aqueous solution. One may go beyond this limit by adopting an appropriate non-ideal mixing entropy, for example that of a lattice gas [80] or that implied by the Carnahan-Starling [81] equation of state. However, these approaches are already well-established so that in the present work we may focus entirely on incorporating spatially extended charge distributions into the non-linear PB model, subject to an ideal mixing entropy.

The third and fourth term in Eq. 8.2, $f_{mix}(n_\pm,n_0) = n_\pm\ln(n_\pm/n_0) - n_\pm + n_0$, describe the ideal mixing free energy of the monovalent salt ions, where $n_-(x)$ is the local concentration of counterions (ions with their sign opposite to that of the charged surface) and $n_+(x)$ is the local concentration of coions (ions with their sign equal to that of the surface charges). The fifth term introduces an external potential $U(x)$ (measured in units of k_BT) that we choose below so as to account for the steric repulsion between the

spherical nanoparticles and the two planar surfaces. The last term in Eq. 8.2 ensures electroneutrality by demanding the number of nanoparticles to equal $m_0AD = 2\sigma A/(ze)$; the Lagrange multiplier μ must be determined accordingly. We consider two types of spherical nanoparticles. One type has its z charges uniformly distributed over the nanoparticle surface (Fig. 8.1a) whereas the second type has all z charges located at its center (Fig. 8.1b).

8.2.1. Spherical Nanoparticles with Uniform Surface Charge Density

The local volume charge density $\rho(x)$ at any point x between the two surfaces ($0 < x < D$) is composed of a contribution from the point-like salt cations and anions located at position x and another contribution from all nanoparticles residing in the region from $x-R$ to $x+R$,

$$\rho(x) = e\,[n_+(x) - n_-(x)] - \frac{ez}{2R}\int_{-R}^{R} ds\, m(x-s). \tag{8.3}$$

Note that it is the non-locality of last term on the right-hand side of Eq. 8.3 that accounts for the connectivity of the charges on the nanoparticle and thus for intra-ionic charge correlations.

In thermal equilibrium, the free energy $F = F(m, n_+, n_-)$ adopts a minimum with respect to the local concentrations of nanoparticles (m) and point-like salt ions (n_+ and n_-). Upon calculating the first variation $\delta F(m, n_+, n_-)$ and demanding it equals zero, we find the equilibrium concentration distributions for the spherical nanoparticles,

$$m(x) = m_0\, e^{-U(x) - \mu + \frac{z}{2R}\int_{-R}^{R} ds \Psi(x+s)}, \tag{8.4}$$

and for the monovalent point-like salt ions,

$$n_+(x) = n_0\, e^{-\Psi(x)}, \qquad n_-(x) = n_0\, e^{\Psi(x)}. \tag{8.5}$$

Inserting the equilibrium distributions $m(x)$, $n_+(x)$ and $n_-(x)$ into Poisson's equation $\Psi''(x) = -4\pi l_B\, \rho(x)/e$,

with $\rho(x)$ specified in Eq. 8.3, leads to a modified PB equation

$$\begin{aligned}\frac{\Psi''(x)}{4\pi l_B} &= n_0\, e^{-\Psi(x)} - n_0\, e^{\Psi(x)} \\ &+ m_0\, e^{-\mu}\, \frac{z}{2R} \int_{-R}^{R} d\bar{s}\, e^{-U(x-\bar{s})+\frac{z}{2R}\int_{-R}^{R} ds\Psi(x+\bar{s}-s)}.\end{aligned} \tag{8.6}$$

The Lagrange multiplier is calculated from the electroneutrality condition specified in Eq. 8.1,

$$e^{-\mu} = \frac{2}{z a m_0} \frac{1}{\int_0^D d\bar{x}\, \frac{1}{2R} \int_{-R}^{R} d\bar{s}\, e^{-U(\bar{x}-\bar{s})+\frac{z}{2R}\int_{-R}^{R} ds\,\Psi(\bar{x}+s-\bar{s})}}. \tag{8.7}$$

We specify the external potential so as to account for steric interactions between the nanoparticles and the two planar surfaces, $U(x)=0$ if $R<x<(D-R)$ and $U(x)\to\infty$ otherwise. Taking into account this external potential yields our final result, a non-linear PB equation for a mixture of uniformly charged spherical particles and monovalent point-like salt ions, which adopts the form of an integral-differential equation for the dimensionless electrostatic potential,

$$\Psi''(x) = \frac{1}{l_D^2}\sinh\Psi(x) + \frac{8\pi l_B}{a} \frac{\int_{-min(R,x-R)}^{min(R,D-R-x)} d\bar{s}\; e^{\frac{z}{2R}\int_{-R}^{R} ds\,\Psi(x+s-\bar{s})}}{\int_0^D d\bar{x} \int_{-min(R,\bar{x}-R)}^{min(R,D-R-\bar{x})} d\bar{s}\, e^{\frac{z}{2R}\int_{-R}^{R} ds\,\Psi(\bar{x}+s-\bar{s})}}. \tag{8.8}$$

Here, $l_D = 1/\sqrt{8\pi l_B n_0}$ is the Debye screening length due to the presence of salt. Eq. 8.8 has to be solved subject to the boundary conditions $\Psi'(0) = -\Psi'(D) = -4\pi l_B/a$. Note that the integrals in Eq. 8.8 render the differential equation non-local. This non-locality results from the connectivity of (or, equivalently, intra-ionic correlations between) the nanoparticle charges. We have computed solutions of the integral-differential equation 8.8 numerically based on employing a discretizaton scheme.

Once the potential in the region $0 \le x \le D$ is known, we can calculate the local concentration of the

nanoparticles in the interval $R < x < D - R$ through

$$m(x) = \frac{2}{az} \frac{e^{\frac{z}{2R}\int_{-R}^{R} ds\,\Psi(x+s)}}{\int_0^D d\bar{x} \int_{-min(R,\bar{x}-R)}^{min(R,D-R-\bar{x})} d\bar{s}\, e^{\frac{z}{2R}\int_{-R}^{R} ds\,\Psi(\bar{x}+s-\bar{s})}}, \tag{8.9}$$

where we have made use of inserting the Lagrange multiplier from Eq. 8.7 into Eq. 8.4.

We also derive an expression for the *pressure* that acts on each of the two charged surfaces. Eq. 8.2 can be re-expressed as

$$\begin{aligned} \frac{F}{k_B T A} &= \int_0^D dx \left[-\frac{\Psi'^2}{8\pi l_B} - \Psi \frac{z}{2R} \int_{-R}^{R} ds\, m(x-s) \right. \\ &+ f_{mix}(m, m_0) + \Psi n_+ - \Psi n_- \\ &+ \left. f_{mix}(n_+, n_0) + f_{mix}(n_-, n_0) \right]. \end{aligned} \tag{8.10}$$

Here, the local concentration $m(x)$ is non-vanishing only in the region $R < x < D - R$. Inserting the equilibrium distributions for m and $n_\pm$ into Eq. 8.10 yields a functional $F[\Psi(x)]$ whose variation δF vanishes. Hence, we obtain the pressure

$$P = -k_B T \frac{dF/(Ak_B T)}{dD} \tag{8.11}$$

that acts on the planar surfaces directly from the integrand of Eq. 8.10, namely

$$\begin{aligned} \frac{P}{k_B T} &= \frac{\Psi'^2}{8\pi l_B} + \Psi \frac{z}{2R} \int_{-R}^{R} ds\, m(x-s) - f_{mix}(m, m_0) \\ &- \Psi n_+ + \Psi n_- - f_{mix}(n_+, n_0) - f_{mix}(n_-, n_0). \end{aligned} \tag{8.12}$$

We conveniently evaluate Eq. 8.12 in the middle of the system at $x = D/2$. Due to the symmetry $\Psi(x) = \Psi(D-x)$, the first term in Eq. 8.12 equals zero at $x = D/2$. The relation $n_\pm f'_{mix}(n_\pm, n_0) - f_{mix}(n_\pm, n_0) = n_\pm - n_0$ simplifies Eq. 8.12 to

$$\begin{aligned} \frac{P}{k_B T} &= \Psi(D/2)\, \frac{z}{2R} \int_{-R}^{R} ds\, m(D/2-s) \\ &- f_{mix}[m(D/2), m_0] + n_+(D/2) + n_-(D/2). \end{aligned} \tag{8.13}$$

Note that for point-like ions ($R = 0$) the pressure becomes $P/k_BT = m(D/2) + n_+(D/2) + n_-(D/2) - 2n_0$.

8.2.2. Spherical Nanoparticles with Charge Located in the Center

Now we collect all charges from the nanoparticle surface and relocate them into the center of the nanoparticle. As a result of this process the integral $\int ds$ can be written as $\int ds\delta(s)$, where δ is the Dirac delta function. Eq. 8.8 then becomes

$$\Psi''(x) = \frac{1}{l_D^2}\sinh\Psi(x) + \frac{8\pi l_B}{a}\frac{e^{z\Psi(x)}h(x,R,D-R)}{\int_R^{D-R} d\bar{x}\, e^{z\Psi(\bar{x})}}, \tag{8.14}$$

where

$$h(x,x_1,x_2) = \begin{cases} 0 & x < x_1 \\ 1 & x_1 < x < x_2 \\ 0 & x > x_2\,. \end{cases} \tag{8.15}$$

Similarly, the nanoparticle concentration can be calculated from Eq. 8.9 through

$$m(x) = \frac{2}{az}\frac{e^{z\Psi(x)}h(x,R,D-R)}{\int_R^{D-R} d\bar{x}\, e^{z\Psi(\bar{x})}}. \tag{8.16}$$

Finally, the pressure between the two like charged surfaces is

$$\frac{P}{k_BT} = m(D/2) + n_+(D/2) + n_-(D/2) - 2n_0\,. \tag{8.17}$$

There is no influence of the nanoparticle size on the pressure because we have used an ideal mixing free energy $f_{mix}(m,m_0)$ in Eq. 8.2.

8.2.3. Monte Carlo Simulations

The Monte Carlo simulation model included hard spherical particles of diameter $2R$ bearing point charges on their surfaces. A homogeneous charge distribution was approximated by 30 point charges, distributed on the surface of the sphere such that each charge occupies roughly the same cross-sectional area.

All particles were contained inside a rectangular box of dimension $(L_{xy} \times L_{xy} \times D)\,\mathrm{nm}^3$. The value L_{xy} varied from 120 to 250 nm. Periodic boundary conditions along the x- and y-axis were applied. The external field created by the charges of the spherical particles outside the cut off radius (from 60 to 180 nm) was included according to a correction term. The temperature was T = 298 K throughout. The dielectric constant was $\varepsilon = 80$. For each system, the productive run simulations, involving $1000 \times M$ trial moves per particle, were performed after equilibration comprising 1000 trial moves. Typically, M was 10. All simulations were carried out employing the MOLSIM package [336]. Note that all our simulations model salt-free systems ($n_0 = 0$).

8.3. Results and Discussion

Our theoretical model yields the ion concentrations, charge density profiles, and the pressure between two like-charged surfaces that sandwich a solution of monovalent salt and charged nanoparticles, the latter either homogeneously charged or with all charges located at the nanoparticle centers. In the following, we analyze these properties based on numerical solutions of the nonlinear integral-differential equations 8.8 and 8.14. Some of the theoretical predictions are compared with results from Monte Carlo simulations.

8.3.1. Salt Free System

We first consider a system that does not contain monovalent salt ions ($n_0 = 0$). When a nanoparticle of given size carries a small number of charges, we expect a diffuse and spatially extended electric double layer near each of the two charged surfaces to form. In contrast, when the number of charges on each nanoparticle is large, they will tend to adsorb tightly onto the surfaces. To illustrate the former of these two limiting scenarios, we show in Fig. 8.2 the negative of the volume charge density, $-\rho(x)$, for nanoparticles with only one single charge ($z = 1$), distributed uniformly over the particle surface, and three different radii $R = 0.5\,\mathrm{nm}$ (green), $R = 1.0\,\mathrm{nm}$ (blue), and $R = 2.5\,\mathrm{nm}$ (red). The remaining parameters are $a = 60\,\mathrm{nm}^2$ and $D = 20\,\mathrm{nm}$. The inset of Fig. 8.2 displays the corresponding local particle concentrations $m(x)$ calculated according to Eq. 8.9. When moving away from either one of the two charged surfaces into the aqueous solution, the magnitude of $\rho(x)$ first increases, then passes through a maximum at $x = 2R$, and subsequently decreases. The maximum results from the steric restriction of the spherical nanoparticles close to the charged

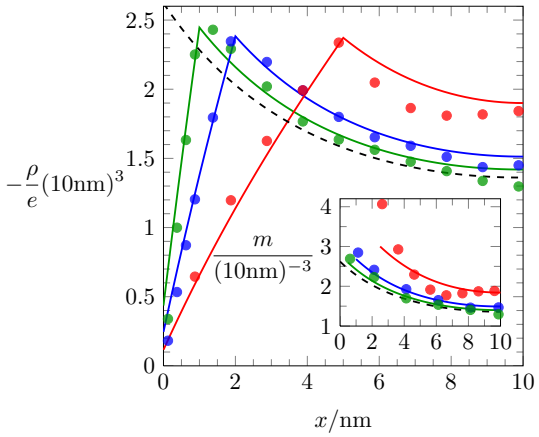

Figure 8.2. Local volume charge density $\rho(x)$ for homogeneously charged particles with $z = 1$, $a = 60\,\text{nm}^2$, $n_0 = 0$, and $D = 20\,\text{nm}$. Solid lines refer to our non-linear PB model (that is, solutions of Eqs. 8.8 and 8.9), and the bullets to the prediction from Monte Carlo simulations. Different colors refer to different particle radii: $R = 0.5\,\text{nm}$ (green), $R = 1.0\,\text{nm}$ (blue), and $R = 2.5\,\text{nm}$ (red). The inset shows the corresponding local particle concentration $m(x)$. The dashed black curve in the main figure and in the inset corresponds to the classical PB result for point-like ions.

wall. Comparison between Monte Carlo simulations (the bullets in Fig. 8.2 and its inset) and theory (the solid lines in Fig. 8.2 and its inset) reveals good agreement for the volume charge density $\rho(x)$ and particle concentration $m(x)$ produced by the smaller particles, where $R = 0.5\,\text{nm}$ (green) and $R = 1.0\,\text{nm}$ (blue). For the large particles, where $R = 2.5\,\text{nm}$ (red), packing effects become important, which our theoretical model ignores. We can rationalize the onset of packing effects by introducing the fractional surface coverage with the nanoparticles

$$\chi = \frac{\pi R^2}{za} \tag{8.18}$$

in the strong adsorption limit. Applicability of the ideal mixing assumption, see $f_{mix}(m, m_0)$ in Eq. 8.2, requires χ to be much smaller than the maximal value $\chi_{max} = \pi/\sqrt{12} \approx 0.907$ for dense packing in a hexagonal array. For the examples in Fig. 8.1 we obtain: $\chi = 0.013$ for $R = 0.5\,\text{nm}$ (green), $\chi = 0.052$ for $R = 1.0\,\text{nm}$ (blue), and $\chi = 0.33$ for $R = 2.5\,\text{nm}$ (red).

In the limit of infinitesimally small radius R, Eq. 8.8 recovers the familiar classical PB result for point-like ions

$$\Psi''(x) = \frac{8\pi l_B}{a} \frac{e^{z\Psi(x)}}{\int_0^D e^{z\Psi(\bar{x})} d\bar{x}}, \tag{8.19}$$

and Eq. 8.9 yields the local ion concentration

$$m(x) = \frac{2}{az} \frac{e^{z\Psi(x)}}{\int_0^D e^{z\Psi(\bar{x})} d\bar{x}}. \tag{8.20}$$

As is well known [337], the solution of Eq. 8.19 can be expressed as $\Psi(x) = -\ln\{\cos^2[\kappa(x-D/2)]\}/z$, where the constant κ must be determined from the transcendental equation $\kappa D = 2\arctan[(2\pi l_B z)/(a\kappa)]$. This indeed fulfills the boundary conditions $\Psi'(0) = -\Psi'(D) = -4\pi l_B/a$. In addition, the reference for the potential is chosen as $\Psi(D/2) = 0$. For the local counterion concentration we obtain from Eq. 8.20

$$m(x) = \frac{\kappa^2}{2\pi l_B z^2} \frac{1}{\cos^2\left[\kappa\left(x - \frac{D}{2}\right)\right]}. \tag{8.21}$$

With $a = 60\,\text{nm}^2$, $D = 20\,\text{nm}$, $l_B = 0.7\,\text{nm}$, and $z = 1$ we find $\kappa = 0.0764/\text{nm}$. Charge density $\rho(x)$ and concentration $m(x) = -\rho(x)/e$ according to this classical PB result for point-like ions are shown in Fig. 8.2 and its inset; see the dashed black curves.

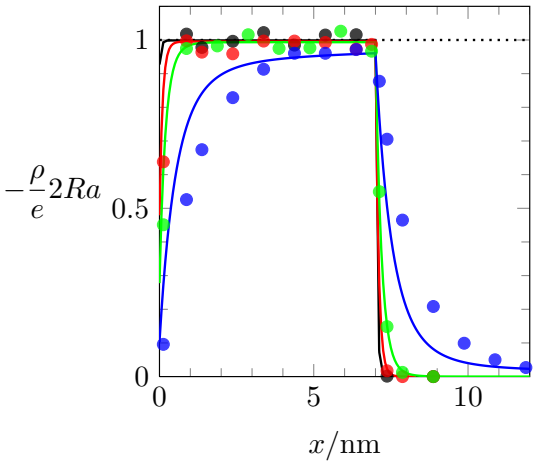

Figure 8.3. Normalized local volume charge density, $-2Ra\rho(x)/e$, for $R = 3.5\,\text{nm}$, $D = 50\,\text{nm}$, and $z = 24$. Solid lines and filled symbols are computed using PB theory and Monte Carlo simulations, respectively. Different colors correspond to different surface charge densities $\sigma = e/a$ with $a = 5\,\text{nm}^2$ (black), $a = 10\,\text{nm}^2$ (red), $a = 20\,\text{nm}^2$ (green), and $a = 60\,\text{nm}^2$ (blue).

To illustrate the other limiting scenario, that of a multivalent nanoparticle with $z >> 1$, Fig. 8.3 shows the normalized volume charge density $-2Ra\rho(x)/e$ for $z = 24$, $D = 50\,\text{nm}$, and $R = 3.5\,\text{nm}$. Solid lines and filled symbols are computed using PB theory and Monte Carlo simulations, respectively. Different

colors correspond to to different surface charge densities $\sigma = e/a$ with $a = 5\,\mathrm{nm}^2$ (black), $a = 10\,\mathrm{nm}^2$ (red), $a = 20\,\mathrm{nm}^2$ (green), and $a = 60\,\mathrm{nm}^2$ (blue). Nanoparticles that are all condensed to the charged surface imply a step function, $\rho(x) = -e/(2Ra)$ for $0 \le x \le 2R$ and $\rho(x) = 0$ for $x > 2R$, for their volume charge density. Fig. 8.3 reveals that with increasing $\sigma = e/a$ (or, equivalently, decreasing cross-sectional area a per elementary charge on the planar surface) $\rho(x)$ approaches the limit of complete nanoparticle adsorption. We point out that even for the highest surface charge density, $\sigma = e/(5\mathrm{nm}^2)$, the fractional surface coverage, $\chi = \pi R^2/(za) = \pi(3.5\mathrm{nm})^2/(24 \times 5\mathrm{nm}^2) = 0.032$, of the nanoparticles is so small that the ideal gas limit for the mixing entropy is appropriate.

The transition between the two limiting scenarios, weak and strong adsorption, can be captured by varying the nanoparticle valence from small to large values. To this end, Fig. 8.4 shows the volume charge density $\rho(x)$ for different valences $z = 3$ (blue), $z = 6$ (red), $z = 12$ (black), and $z = 24$ (green), all derived for fixed nanoparticle radius $R = 3.5\,\mathrm{nm}$, surface charge density $\sigma = e/(60\mathrm{nm}^2)$, and in the absence of added salt ($n_0 = 0$). Again, solid lines refer to PB theory and bullets to results from Monte Carlo simulations. The upper and lower diagram of Fig. 8.4 are computed for $D = 20\,\mathrm{nm}$ and $D = 50\,\mathrm{nm}$, respectively. The results in Fig. 8.4 demonstrate how increasing the valence z shifts the volume charge density $\rho(x)$ from that of weakly to strongly surface-associated nanoparticles. We have indicated the limiting cases of uniform particle distribution, where $-\rho(x)/e = x/[2Ra(D-2R)]$ for $0 \le x \le 2R$ and $-\rho(x)/e = 1/[a(D-2R)]$ for $2R \le x \le D/2$, and that of complete surface association, where $-\rho(x)/e = 1/(2Ra)$ for $0 \le x \le 2R$ and $-\rho(x)/e = 0$ for $2R \le x \le D/2$; see the dashed lines in Fig. 8.4. Indeed, the charge distributions approach these two limits if z becomes small or large.

8.3.2. Influence of Salt

In the following we consider the influence of added salt on the concentration profiles of nanoparticles. Fig. 8.5 shows concentration profiles $m(x)$ of nanoparticles for the two different radii $R = 1\,\mathrm{nm}$ (black curves) and $R = 3.5\,\mathrm{nm}$ (red curves). Two types of nanoparticles are compared, one (solid lines in Fig. 8.5) with uniformly distributed charge over the particle surface and another one (dashed lines in Fig. 8.5) with all charge localized in the particle center. In all cases, m decreases with increasing distance x from the nearest charged surface. Due to the excluded volume interaction with the wall, the concentration profile starts to adopt non-vanishing values at $x = R$, as marked by the dotted lines in Fig. 8.5. Close to the charged sur-

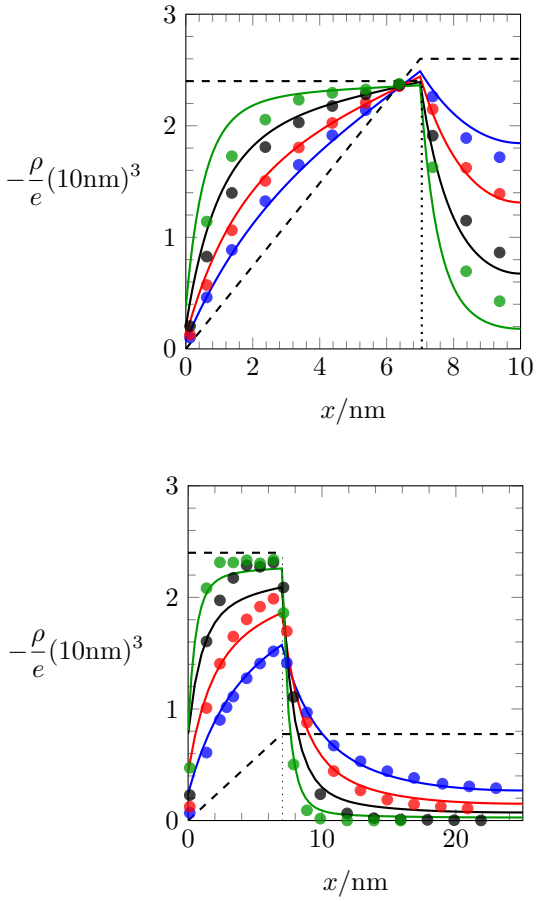

Figure 8.4. Local volume charge density $\rho(x)$ for homogeneously charged particles of radius $R = 3.5\,\text{nm}$ and surface charge density $\sigma = e/a$ with $a = 60\,\text{nm}^2$. Solid lines and filled symbols are computed using PB theory and Monte Carlo simulations, respectively. Different colors correspond to different particle valencies: $z = 3$ (blue), $z = 6$ (red), $z = 12$ (black) and $z = 24$ (green). Upper and lower diagram refer to $D = 20\,\text{nm}$ and $D = 50\,\text{nm}$, respectively. The two broken lines in each diagram indicate the two limiting cases of uniform particle distribution and complete surface adsorption. No salt is present ($n_0 = 0$).

faces the concentration of nanoparticles with uniform surface charge distribution is somewhat larger than the concentration of nanoparticles with all charge located in their center; compare the corresponding bullets in Fig. 8.5 which mark $m(R)$. The different behaviors of the two particle types might seem surprising because both produce the same potential distribution. However, their mutual interaction potential differs, predominantly due to the presence of a quadrupole moment of the uniformly charged nanoparticle which is absent for the particle with a central point charge. Specifically, when interacting with the non-homogeneous electric field produced by the diffuse ion cloud of an electric double layer, the additional quadrupole moment of the uniformly charged nanoparticles enhances the attraction with the oppositely charged surface and thus implies a larger surface concentration. This is indeed what we observe in Fig. 8.5. The reason is that the

non-homogeneous electric field produced by the diffuse cloud of mobile ions (consisting of both salt counterions and nanoparticles) favors spatially extended charge distributions along the x-axis in a similar manner as a quadrupole charge (as opposed to a monopole charge) is energetically biased along the direction of a changing electric field.

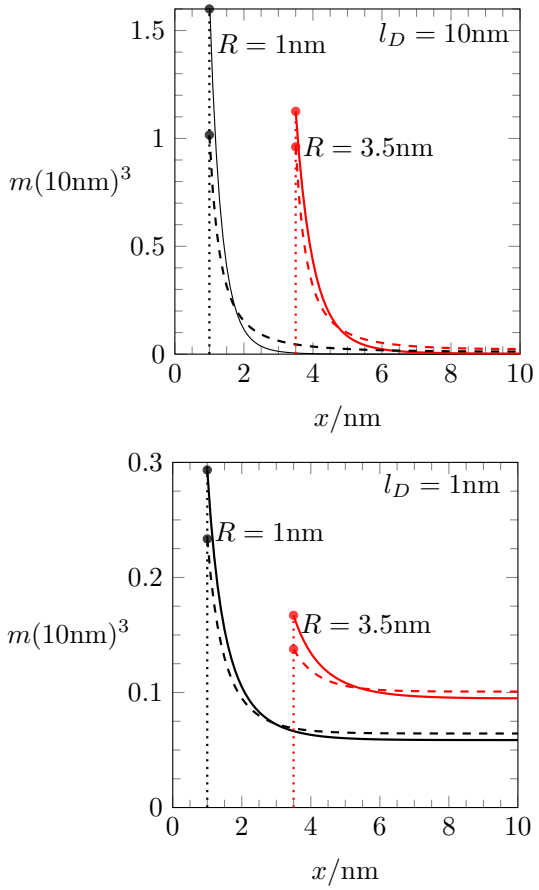

Figure 8.5. Nanoparticle concentration profiles $m(x)$ for different radii $R = 1$ nm (black curves) and $R = 3.5$ nm (red curves) as well as for uniform surface charge density (solid lines) and all charge being localized at the particle center (broken lines). The upper diagram refers to $l_D = 10$ nm, the lower to $l_D = 1.0$ nm. All calculations correspond to $l_B = 0.7$ nm, $D = 20$ nm, $a = 60\,\text{nm}^2$, and $z = 24$. The bullets mark the concentrations $m(R)$.

The upper and lower diagrams of Fig. 8.5 show the concentrations $m(x)$ for $l_D = 10$ nm and $l_D = 1$ nm, respectively. Smaller Debye lengths correspond to higher salt concentration and thus stronger electrostatic screening. As a result, magnitudes of surface potentials and concentrations are generally larger for larger l_D. Also, we observe larger variations of $m(x)$ along the x-axis for uniformly charged particles as

compared to particles with all charge at their center for both Debye lengths, $l_D = 10\,\mathrm{nm}$ and $l_D = 1\,\mathrm{nm}$. In order to verify that this is the case for all Debye lengths, we define an inhomogeneity parameter

$$\eta = \frac{\int_0^D dx \left(\frac{m(x)}{m_0} - 1\right)^2}{\left[\int_0^D dx \left(\frac{m(x)}{m_0} - 1\right)^2\right]_{l_D \to \infty}}, \tag{8.22}$$

which characterizes the overall degree of nonuniformity of $m(x)$, scaled by its value in the absence of salt (where $n_0 = 0$ or, equivalently, $l_D \to \infty$). Clearly, $\eta \to 1$ for large Debye lengths. Also, because the addition of salt results generally in more uniform ion distributions along the x-axis, we expect the function $\eta(l_D)$ to start from $\eta(l_D = 0) = 0$ and increase monotonously. This is indeed the case, as Fig. 8.6 exemplifies for $D = 20\,\mathrm{nm}$, $a = 60\,\mathrm{nm}^2$, and $z = 24$, $R = 3.5\,\mathrm{nm}$. Here, and similarly for other parameter choices, $\eta(l_D)$ is always larger for uniformly charged particles as compared to particles with all charge localized at the particle center.

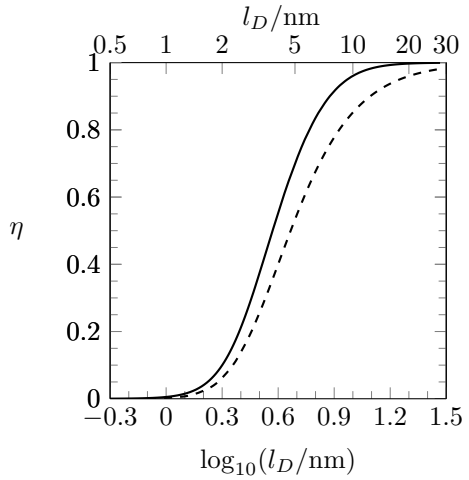

Figure 8.6. Inhomogeneity parameter η as function of l_D for fixed $D = 20\,\mathrm{nm}$, $a = 60\,\mathrm{nm}^2$, and $z = 24$, $R = 3.5\,\mathrm{nm}$. Solid line: uniform surface charge density. Dashed line: all z charges are located in the particle center.

One of our central conclusions of this work is that the spatial separation of the charges on the surface of nanoparticles leads to stronger surface adsorption and, generally, to a more non-uniform particle distribution. A second, and perhaps more important, consequence is related to the nature of the interaction between two like-charged surfaces: uniformly charged nanoparticles, but not nanoparticles with all the charge lo-

calized in their center, are able to induce an attractive interaction between two like-charged surfaces. We demonstrate this by plotting the pressure P as a function of the surface-to-surface separation D; see Fig. 8.7, which is calculated for $R = 3.5\,\text{nm}$, $z = 24$, $a = 60\,\text{nm}^2$, and different amounts of salt as indicated by the differently colored curves.

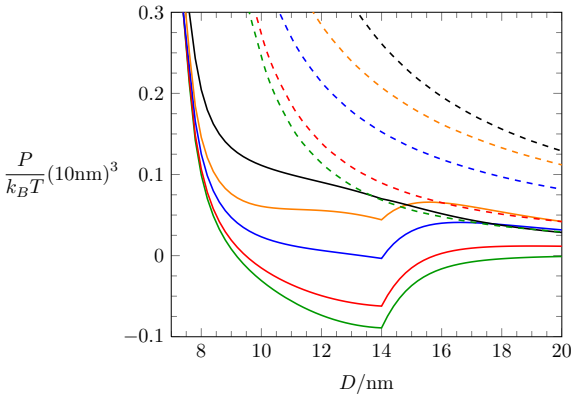

Figure 8.7. Pressure P as function of the separation D between two like-charged surfaces for nanoparticles with uniform surface charge density (solid lines) and for nanoparticles with all the charge localized in their center (broken lines). Different colors correspond to different salt content: $l_D = 1\,\text{nm}$ (black), $l_D = 3.5\,\text{nm}$ (orange) $l_D = 5\,\text{nm}$ (blue) and $l_D = 10\,\text{nm}$ (red), and $l_D \to \infty$ (no salt – green curve). All calculations correspond to fixed $R = 3.5\,\text{nm}$, $z = 24$, and $a = 60\,\text{nm}^2$.

If we locate the charge in the center of the nanoparticles then the interaction between the like-charged surfaces is repulsive (Fig. 8.7, dashed line). The pressure decreases with increasing surface separations. The strict repulsiveness of the interaction is the result of the neglect of intra-ionic correlations. The removal of salt generally tends to decrease the pressure P, which however remains always repulsive irrespective of the salt content. Note that in the limiting case of $l_D \to 0$ all electrostatic interactions are screened. The nanoparticles then behave as an ideal gas with a corresponding pressure $P/k_BT = 2/[(D-2R)az]$. For example, at D=20 nm, $P/k_BT = 0.1068/(10\,\text{nm})^3$.

If we relocate the nanoparticle charges from the center to the surface, the interaction between the two like-charged surfaces may become attractive. The negative pressure is entirely the result of intra-ionic correlations. Increasing the salt concentration (decreasing Debye length) diminishes the range of attraction. For sufficiently large salt concentration the attraction is lost. For nanoparticles with radius 3.5 nm, valence $z = 24$, and surface area $a = 60\,\text{nm}^2$, the transition between attraction and repulsion takes place at a Debye length of about $l_D = 5\,\text{nm}$. Attractive interactions between like-charged surfaces emerge at separations of

about the nanoparticle size (see Fig. 8.7). The charges on the nanoparticle surface link the two surfaces together. This "bridging" [338, 123, 325, 78] interaction is lost when we relocate the charges from the nanoparticle surface to its center.

8.4. Conclusions

In this work, we have presented a modified PB theory for an electrolyte that contains besides point-like monovalent ions also uniformly charged spherical nanoparticles, sandwiched between two parallel like-charged surfaces. We performed Monte Carlo simulations for these systems in order to validate the predictions of the theory and found that for sufficiently small nanoparticle density there was good agreement between both regarding ion concentration profiles. Our prediction of attractive interactions between like-charged surfaces corroborates the possibility of macroion condensation induced by particles/molecules with spatially distributed charges [339, 340, 341]. The attractiveness of the interaction is the result of intra-ionic correlations introduced through the uniform surface charge density of the spherical nanoparticles. Inter-ionic correlations will further enhance the degree of attraction, but they are not needed to explain its origin.

8.5. Acknowledgments

GVB acknowledges a doctoral scholarship from CAPES Foundation/Brazil Ministry of Education (Grant No. 9466/13- 4). KB thanks the Research Agency through program P3-0388.

9. SURFACE TENSION OF A YUKAWA FLUID ACCORDING TO MEAN-FIELD THEORY *

9.1. Introduction

Introduced originally as a nuclear potential [342], the Yukawa interaction emerges in a variety of additional physical subdisciplines such as plasma physics, condensed matter physics, and statistical physics. In the physics of simple and complex fluids the Yukawa potential can appear as the result of effective interactions. Examples include the screened electrostatic potential in ionic systems [343, 344, 345, 46, 346], ion-specific hydration effects [65, 31], solvation forces [347, 348], and the stability of colloidal dispersions [349, 350, 351, 352]. Systems with weakly changing scalar or vectorial order parameters also exhibit Yukawa-like interactions between their constituents [353, 354]. Moreover, due to its simplicity, the Yukawa potential is often combined with other interaction potentials. Obviously, it may act in addition to the steric repulsion between particles [355, 356, 348, 357, 358, 359, 360]. Another scenario that has received some attention is the addition of the Yukawa potential to a Coulomb interaction [361, 74, 362, 31, 222, 363] to model hydration effects of ionic fluids.

When a Yukawa fluid is confined inside a container, the presence of the impenetrable container walls affects the particle distribution and thus creates a surface tension – an excess free energy (per unit area) with respect to the bulk of the fluid [357, 360]. A surface tension also emerges at the boundary between the two coexisting phases (liquid and vapor) of a Yukawa fluid. A multitude of studies have addressed the thermodynamic stability of Yukawa fluids [364, 365, 366, 367] using methods such as density functional theory [368, 369, 4], perturbation approaches [370], and a field theoretic description [357, 359]. Density functional theories [371, 372, 373, 6] and virial expansions [5] have also been employed to predict the surface tension between the coexisting phases of attractive Yukawa fluids with added excluded volume repulsion. However, most of the available results for the surface tension are derived from Monte Carlo

*Reprinted from "G. V. Bossa, J. Norris, S. May, Surface tension of a Yukawa fluid according to mean-field theory, J. Chem Phys. 146 (13) (2017) 134701", with the permission of AIP Publishing. Copyright 2017 AIP Publishing. This paper can be accessed online at `http://aip.scitation.org/doi/abs/10.1063/1.4979203`. The material in this chapter was co-authored by Guilherme V. Bossa, Joseph Norris, and Sylvio May. G. V. Bossa contributed to the project design and manuscript writing. G.V.B. was responsible for the mathematical development, numerical and analytical solution of the equations, figures preparation, and discussion of the results.

simulations [374, 375, 376, 3, 377, 367, 378]. These simulations typically focus on the regime of a small (as compared to the particle size) screening length and, depending on the simulation method, often differ notably in their predictions of the surface tension [365, 379]. We note that the other limit, that of large screening length, is also interesting as a model for hydration-mediated interactions between small ions in an aqueous solution [361, 65, 74], but has not been studied in the past.

Mean-field theories often result as lowest order approximations of perturbation approaches; their range of applicability is limited, but their simplicity and transparency still renders them valuable [380]. One example is the field theoretic approach by di Caprio, Holovko, and coworkers, who have investigated Yukawa [357] and closely related [359, 360] fluids near system boundaries (the walls of the container in which the Yukawa fluid resides). The mean-field limit of their theory applies only to point-like particles, but it is non-local and, hence, does not assume that spatial changes in particle density are small. This, in fact, is the basis to investigate the step-like particle densities at system boundaries. Another example is the virial expansion from Weiss and Schröer [5], which models the fluid on the level of the second virial coefficient and calculates the surface tension of coexisting phases using the square gradient theory. This mean-field approach does not rely on assumptions about particle size and interaction range of the Yukawa potential, but it assumes that changes in particle density are small. Hence, the model is suitable to predict the surface tension of coexisting phases but cannot be applied to calculate the excess energy of a fluid near a system boundary. The present work represents an attempt to include into the field-based description of a Yukawa fluid [357] a non-vanishing particle size. To this end, we employ a field variable to describe the Yukawa-interactions between all particles, which renders our model non-local and allows us to investigate any type of interface, like those between coexisting phases as well as boundary walls. Including the particle size recovers the virial expansion approach [5] only in the limit of high temperature and large interaction range, yet goes beyond the square gradient theory by not assuming small changes of the particle density.

We calculate the surface tension γ of a Yukawa fluid on the mean-field level for particles that exhibit Yukawa and excluded-volume interactions. The Yukawa interaction can be repulsive or attractive. In the former case, the fluid is thermodynamically stable, and a surface tension will be associated with the presence of a system boundary (that is, a container wall). In the latter case, an attractive Yukawa fluid, macroscopic phase separation may occur. We calculate the corresponding surface tension associated with the phase boundary. Non-vanishing particle size is incorporated into our mean-field model by a nonideal contribution to the free energy, in addition to the Yukawa interaction energy between all particles and the free energy of

an ideal gas. We exemplify this nonideal contribution using two different models based on either a lattice gas or the Carnahan-Starling equation of state. The mean-field character in both cases implies the pair correlation function is $g_c \equiv 1$. The main result of this work is the prediction of γ on the mean-field level, completely in terms of two (or even one, in case of a phase boundary) appropriately defined parameters. Besides numerical results we derive a number of simple analytic expressions for the surface tension, valid for any choice of the additional nonideal free energy contribution and in the limit of either small particle density or close to the critical point for a phase-separating Yukawa fluid.

9.2. Mean-Field Model

We consider an ensemble of spherical particles, in which any given two particles that are separated by a center-to-center distance r interact though the Yukawa potential

$$u(r) = \frac{l}{r} e^{-\kappa r}. \tag{9.1}$$

Here, $1/\kappa$ is a characteristic decay length and l the interaction strength. The sign of l determines whether the interaction is repulsive (for $l > 0$) or attractive (for $l < 0$). Note that in Eq. 9.1 and everywhere else in this work we express energies in units of the thermal energy unit $k_B T$, where k_B is the Boltzmann constant and T the absolute temperature. It is convenient to define a dimensionless potential

$$\Psi(\mathbf{r}) = l \int d^3\bar{\mathbf{r}}\, \frac{e^{-\kappa|\mathbf{r}-\bar{\mathbf{r}}|}}{|\mathbf{r}-\bar{\mathbf{r}}|} n(\bar{\mathbf{r}}) \tag{9.2}$$

at any location $\mathbf{r}$, where the integration runs over all space. The potential $\Psi(\mathbf{r})$ is produced by all particles, which are present with local concentration (or, equivalently, number density) $n(\bar{\mathbf{r}})$ at a point $\bar{\mathbf{r}}$. We can express Eq. 12.3 as a local differential equation using the Green's function $G(\mathbf{r}) = -e^{-\kappa|\mathbf{r}|}/(4\pi|\mathbf{r}|)$ that corresponds to the operator $\mathscr{A} = \nabla^2 - \kappa^2$ (where ∇^2 denotes the Laplacian) and thus fulfills the relation $\mathscr{A}G(\mathbf{r}) = \delta(\mathbf{r})$. The result is a Helmholtz equation with a source term and complex wave number $i\kappa$,

$$\nabla^2\Psi(\mathbf{r}) - \kappa^2\Psi(\mathbf{r}) = -4\pi l\, n(\mathbf{r}). \tag{9.3}$$

The potential $\Psi(\mathbf{r})$ allows us to readily calculate the total interaction energy of all particles through

$$U = \frac{1}{2}\int d^3\mathbf{r}\,\Psi(\mathbf{r})n(\mathbf{r}) = \int d^3\mathbf{r}\,\frac{[\nabla\Psi(\mathbf{r})]^2 + \kappa^2\Psi^2}{8\pi l}, \tag{9.4}$$

where ∇ denotes the gradient.

In this work we study a Yukawa fluid that forms a planar interface, which either arises due to the presence of a container that confines the fluid or as the result of a phase separation. The properties of the Yukawa fluid depend in both cases only on the distance to the interface, which we measure along the x-axis of a Cartesian coordinate system. Hence, we conveniently use the x-coordinate instead of the position vector $\mathbf{r}$ as argument in all spatially varying functions; i.e., $\Psi(\mathbf{r}) \to \Psi(x)$ and $n(\mathbf{r}) \to n(x)$. For example, the Helmholtz equation now reads $\Psi''(x) - \kappa^2\Psi(x) = -4\pi l\, n(x)$ (where here and below a prime denotes the derivative with respect to the argument; i.e., $\Psi' = d\Psi/dx$) or, without an explicit account of the arguments,

$$\Psi'' - \kappa^2\Psi = -4\pi l\, n. \tag{9.5}$$

We express the entropic contribution $-TS$ to the mean-field Landau free energy $F = U - TS - \mu N$ of the Yukawa fluid in terms of the local volume fraction $\phi(x) = vn(x)$ of the particles, where $v = 4\pi R^3/3$ is the volume per particle. (We assume the spherical particles all have the same radius R, and we also note that in liquid-state theory the term "packing fraction" is often used instead of "volume fraction".) Specifically, we write

$$\frac{F}{A} = \int_{-\infty}^{\infty} dx \left[\frac{\Psi'^2 + \kappa^2\Psi^2}{8\pi l} + \frac{\phi\ln\phi - \phi + g(\phi) - \mu\phi}{v}\right], \tag{9.6}$$

where A is the (sufficiently large) lateral area of the interface. Evidently, the first two contributions to the integral express the interaction energy U specified in Eq. 9.4. We identify the next two contributions in Eq. 9.6, those involving the terms $\phi\ln\phi - \phi$, as the free energy of an ideal gas. The following term, that containing $g(\phi)$, introduces an additional nonideal contribution, which appears in the thermal equation of state of a homogeneous fluid (liquid or gas) with N particles confined in a volume V at pressure P and temperature T as $PV/(Nk_BT) = 1 + g'(\phi) - g(\phi)/\phi$, where $g'(\phi)$ denotes the derivative with respect to the volume fraction $\phi = vN/V$. Finally, μ, which appears in the last contribution to the integral in Eq. 9.6, is a chemical potential that can be used to constrain the concentration of the particles. In the most general case of accounting for an x-dependent constraint, $\mu = \mu(x)$.

We will focus in this work on three specific equations of state. The first is that characterized by $g(\phi) = 0$, which corresponds to a Yukawa fluid with an ideal gas entropy contribution to the free energy. We refer to this case as *ideal Yukawa fluid*. The second is the lattice gas equation of state, for which we introduce

$$g(\phi) = \phi \left(1 + \ln\frac{6}{\pi}\right) + \left(\frac{\pi}{6} - \phi\right) \ln\left(1 - \frac{6}{\pi}\phi\right). \tag{9.7}$$

Eq. 9.7 describes a lattice gas, where each particle occupies a fraction $(4/3)\pi R^3/(2R)^3 = \pi/6$ of a lattice site. We refer to a Yukawa fluid with a nonideal contribution to the free energy according to Eq. 9.7 as *lattice Yukawa fluid*. The third is the Carnahan-Starling equation of state [81] for which we define

$$g(\phi) = \frac{\phi^2(4-3\phi)}{(1-\phi)^2}. \tag{9.8}$$

We refer to the corresponding Yukawa fluid as *Carnahan-Starling Yukawa fluid*.

Note that Eqs. 9.7 and 9.8 indeed give rise to the familiar lattice gas equation of state, $PV/(Nk_BT) = -[\pi/(6\phi)]\ln(1-6\phi/\pi)$, and the Carnahan-Starling equation of state $PV/(Nk_BT) = (1+\phi+\phi^2-\phi^3)/(1-\phi)^3$, respectively. For later use we recall the expansion $PV/(Nk_BT) = 1 + B_2 N/V$ up to linear terms in N/V. The second virial coefficient $B_2 = vg''(0)/2$ is $B_2 = 3v/\pi$ for the lattice gas equation of state and $B_2 = 4v$ for the Carnahan-Starling equation of state.

In thermal equilibrium, the free energy F becomes minimal with respect to Ψ and ϕ, subject to these two quantities satisfying the Helmholtz equation $\Psi'' - \kappa^2\Psi = -(4\pi l/v)\phi$. This implies the variation of Eq. 9.6,

$$\frac{\delta F}{A} = \frac{\Psi\delta\Psi'}{4\pi l}\bigg|_{-\infty}^{\infty} + \frac{1}{v}\int_{-\infty}^{\infty} dx\, \delta\phi \, \left[\Psi + \ln\phi + g'(\phi) - \mu\right], \tag{9.9}$$

will vanish. The first term on the right-hand side of Eq. 9.9 is zero if we demand the system to adopt bulk properties far away from the interface, entailing a constant (possibly vanishing) potential $\Psi(x \to \pm\infty)$ and thus $\delta\Psi'(x \to \pm\infty) = 0$. From the requirement that also the second term in Eq. 9.9 vanishes, we obtain the equilibrium distribution

$$\phi = e^{-\Psi - g'(\phi) + \mu} \tag{9.10}$$

that specifies the local particle volume fraction $\phi(x)$ as function of the potential $\Psi(x)$ at any given point x in the region $-\infty < x < \infty$. Generally, Eq. 9.10 constitutes a transcendental relation.

In a bulk system (say, for $x \to +\infty$), where the potential $\Psi = \Psi_b$ is constant, the volume fraction of the particles adopts the constant value $\phi = \phi_b$, which is based on the choice $\mu = \Psi_b + g'(\phi_b) + \ln \phi_b$. The Helmholtz equation, when applied to a bulk system, implies the relation

$$\Psi_b = -2\chi\phi_b, \quad \text{with} \quad \chi = -\frac{2\pi l}{v\kappa^2}. \tag{9.11}$$

Note that an attractive Yukawa potential ($l < 0$) entails $\chi > 0$. Conversely, $\chi < 0$ for a repulsive Yukawa potential ($l > 0$). The Helmholtz free energy per particle $f = F/N + \mu$ in a bulk system is then $f(\phi_b) = -\chi\phi_b^2 + \phi_b \ln \phi_b - \phi_b + g(\phi_b)$, giving rise to the thermal equation of state $PV/(Nk_BT) = 1 + g'(\phi_b) - g(\phi_b)/\phi_b - \chi\phi_b$. Obviously, the Yukawa potential enters only through the parameter χ in the last term, and positive χ decreases the pressure. The second virial coefficient predicted by our free energy in Eq. 9.6 is $B_2 = vg''(0)/2 + 2\pi l/\kappa^2$. This is the large temperature ($u(r) \ll k_BT$) and large screening length ($\kappa R \ll 1$) limit of the virial coefficient $B_2 = vg''(0)/2 - 2\pi \int_{2R}^{\infty} dr r^2 (e^{-u(r)/k_BT} - 1)$. We note that the general expression for B_2, valid for any temperature and screening length, has been used by Weiss and Schröer [5] in conjunction with a small gradient approximation to predict the surface tension between two coexisting phases. Our present approach uses the simple $B_2 = vg''(0)/2 + 2\pi l/\kappa^2$ but is non-local and hence operates without assuming small gradients of the particle density.

Using the bulk free energy $f(\phi_b)$, we can investigate the thermodynamic stability of a Yukawa fluid through the familiar common-tangent construction (binodal) and determination of the inflection points (spinodal). This also yields the critical point, $\chi = \chi_c$ at $\phi_b = \phi_c$, from the two equations

$$\phi_c^2\, g'''(\phi_c) = 1, \qquad \chi_c = \frac{1}{2}\left[\frac{1}{\phi_c} + g''(\phi_c)\right]. \tag{9.12}$$

The results are displayed in Fig. 9.1 for the lattice Yukawa fluid (red lines) and for the Carnahan-Starling Yukawa fluid (blue lines). Note, first, that for the lattice Yukawa fluid the predicted phase behavior is described by the familiar Bragg-Williams approximation of a lattice gas with attractive interactions [63]. Second, the two models give rise to critical points $\chi_c = 12/\pi$ and $\phi_c = \pi/12$ for the lattice Yukawa fluid as well as $\chi_c = 10.60$ and $\phi_c = 0.130$ for the Carnahan-Starling Yukawa fluid [365]. Third, above volume fractions close to $\phi_b = 0.5$, a fluid-solid transition sets in [381]; this transition is outside the scope of the present work.

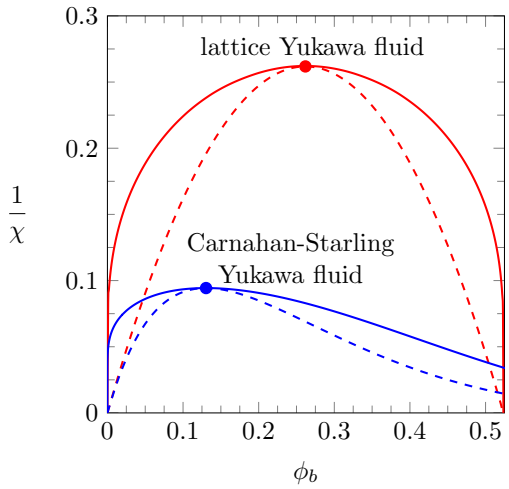

Figure 9.1. Binodal (solid lines) and spinodal (dashed lines) as function of the bulk volume fraction, ϕ_b, of the spherical particles. The red and blue pairs of curves apply to the lattice Yukawa fluid and the Carnahan-Starling Yukawa fluid, respectively. The critical points $\chi = \chi_c$ at $\phi_b = \phi_c$ are $\chi_c = 12/\pi \approx 3.82$ at $\phi_c = \pi/12 \approx 0.262$ for the lattice Yukawa fluid (marked by a red bullet), as well as $\chi_c = 10.60$ at $\phi_c = 0.130$ for the Carnahan-Starling Yukawa fluid (marked by a blue bullet).

9.3. Stable Yukawa fluid in a container

In this section we consider a homogeneous Yukawa fluid that is thermodynamically stable and confined to reside in the region $x > 0$ due to the presence of a planar rigid wall at $x = 0$. This, together with the qualitative behavior of the local particle concentration $n(x)$ and corresponding potential $\Psi(x)$, is schematically illustrated in Fig 9.2. Our goal is to calculate the boundary-induced surface tension γ.

The absence of particles for $x < 0$ can be enforced by setting the chemical potential μ to $-\infty$ in that region. Eq. 9.10 then reads $\phi(x) = 0$ for $x < 0$, and the resulting Helmholtz equation $\Psi'' - \kappa^2\Psi = 0$ implies the potential $\Psi(x) = \Psi(0)\, e^{\kappa x}$. At the specific position $x = 0$, the potential and its slope are thus related according to

$$\frac{1}{\kappa}\Psi'(0) = \Psi(0). \tag{9.13}$$

Consider now the region $x > 0$ and recall that the Yukawa fluid has a bulk volume fraction ϕ_b and a bulk potential $\Psi_b = -2\chi\phi_b$. With our choice $\mu = \Psi_b + g'(\phi_b) + \ln\phi_b$ for the chemical potential we can express

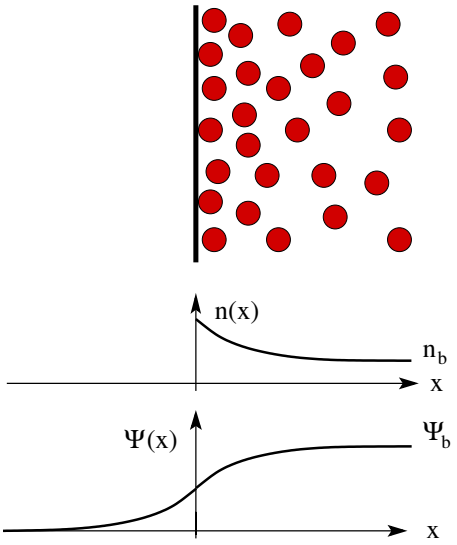

Figure 9.2. Schematic illustration of a Yukawa fluid confined to the region $x > 0$ due to the presence of a planar rigid wall at $x = 0$. The concentration profile $n(x)$ (with bulk value n_b) and corresponding potential $\Psi(x)$ (with bulk value Ψ_b) along the x-axis are plotted qualitatively for the case $l > 0$ (thus implying $\chi < 0$).

the local volume fraction of the particles, Eq. 9.10, and the Helmholtz equation, Eq. 9.5, as

$$\begin{aligned} \frac{\phi}{\phi_b} &= e^{-\Psi+\Psi_b-g'(\phi)+g'(\phi_b)}, \\ -\Psi_b\frac{\phi}{\phi_b} &= \frac{1}{\kappa^2}\Psi'' - \Psi. \end{aligned} \tag{9.14}$$

The second equation (the Helmholtz equation) is an ordinary second-order differential equation that must be solved based on the relation between ϕ as function of Ψ, as defined by the first equation. Solutions are needed for $x > 0$ subject to the boundary conditions $\Psi(x \to \infty) = \Psi_b$ and $\Psi'(0) = \kappa\Psi(0)$; see Eq. 9.13. Analytic solutions will generally not exist, but we may nevertheless formally express the solution of the first equation by defining a function

$$h(\phi) = \phi\, e^{g'(\phi)}. \tag{9.15}$$

We then isolate ϕ using the inverse function $\phi = h^{-1}(\phi\, e^{g'(\phi)})$ and Eq. 9.14 (the first equation), resulting in

$$\phi = \phi(h) = h^{-1}(\phi_b\, e^{-\Psi+\Psi_b+g'(\phi_b)}). \tag{9.16}$$

Depending on the nature of $g(\phi)$, we compute the inverse h^{-1} of the function h either analytically, numerically, or through a series expansion. More specifically, the lattice Yukawa fluid leads to a closed form

expression for h^{-1} whereas a numerical representation will be employed for the Carnahan-Starling Yukawa fluid. As further outlined below, series expansions of h^{-1} can be found without specifying $g(\phi)$.

We can carry out the first integration of the Helmholtz equation in Eq. 9.14, subject to the condition $\Psi = \Psi_b$ when $\Psi' = 0$, immediately. The result is

$$\frac{1}{\kappa}\Psi' = \sqrt{\Psi^2 - \Psi_b^2 - 2\frac{\Psi_b}{\phi_b}\int_{\Psi_b}^{\Psi} d\bar{\Psi}\, h^{-1}(\phi_b\, e^{-\bar{\Psi}+\Psi_b+g'(\phi_b)})}. \tag{9.17}$$

The second integration must satisfy the boundary condition in Eq. 9.13. Alternatively, we can integrate Eq. 9.17 for fixed surface potential $\Psi(0)$. The surface potential follows from combining Eq. 9.13 and Eq. 9.17 at $x = 0$, yielding the relation

$$\Psi_b = -\frac{2}{\phi_b}\int_{\Psi_b}^{\Psi(0)} d\Psi\, h^{-1}(\phi_b\, e^{-\Psi+\Psi_b+g'(\phi_b)}). \tag{9.18}$$

Eq. 9.18 constitutes an algebraic relation that can be solved for $\Psi(0)$.

Our next step is to calculate the free energy per unit area, F/A, in Eq. 9.6. Using the equilibrium distribution of the local volume fraction, ϕ, and the Helmholtz equation (as well as the chemical potential $\mu = \Psi_b + g'(\phi_b) + \ln\phi_b$ and the definition of the bulk potential $\Psi_b = -2\chi\phi_b$) allows us to re-express the free energy as

$$\frac{F}{A} = -\frac{1}{v}\int_0^{\infty} dx \left[\left(\frac{\Psi}{2}+1\right)\phi - g(\phi) + \phi g'(\phi)\right]. \tag{9.19}$$

The same free energy,

$$\frac{F_b}{A} = -\frac{1}{v}\int_0^{\infty} dx \left[\left(\frac{\Psi_b}{2}+1\right)\phi_b - g(\phi_b) + \phi_b g'(\phi_b)\right], \tag{9.20}$$

calculated for bulk conditions, $\phi = \phi_b$ and $\Psi = \Psi_b$, serves as a reference to calculate the surface tension of the Yukawa fluid

$$\gamma = \frac{F - F_b}{A}. \tag{9.21}$$

Hence, the surface tension is the interface-induced excess free energy per unit area. We can calculate γ even without explicit knowledge of the functions $\Psi(x)$ and $\phi(x)$. To this end, we change the integration variable

in Eqs. 9.19 and 9.20 from x to Ψ using $dx = d\Psi/\Psi'$. Eqs. 9.19 and 9.20 then read

$$\frac{F}{A} = -\frac{1}{v\kappa}\int_{\Psi(0)}^{\Psi_b} d\Psi\, \frac{\left(\frac{\Psi}{2}+1\right)\phi - g(\phi) + \phi g'(\phi)}{\frac{1}{\kappa}\Psi'} \tag{9.22}$$

and

$$\frac{F_b}{A} = -\frac{1}{v\kappa}\int_{\Psi(0)}^{\Psi_b} d\Psi\, \frac{\left(\frac{\Psi_b}{2}+1\right)\phi_b - g(\phi_b) + \phi_b g'(\phi_b)}{\frac{1}{\kappa}\Psi'}, \tag{9.23}$$

where ϕ and Ψ'/κ are replaced by the expressions in Eqs. 9.16 and 9.17 and where the surface potential $\Psi(0)$ follows from Eq. 9.18. Given the function $g(\phi)$ is known, we can thus use Eqs. 9.22 and 9.23 to numerically calculate the surface tension γ in Eq. 9.21.

In the limit of a small bulk volume fraction $\phi_b \ll 1$ we can calculate the surface tension analytically. To this end, we expand the inverse of the function $h(\phi)$ (see Eq. 9.15) in terms of h at position $h = 0$ up to fourth order, yielding $\phi = \phi(h) = \sum_{i=1}^{\infty} b_i h^i$ with $b_1 = e^{-g'(0)}$, $b_2 = -g''(0)e^{-2g'(0)}$, $b_3 = [3g''(0)^2 - g'''(0)]\, e^{-3g'(0)}/2$, and $b_4 = [12g''(0)g'''(0) - 16g''(0)^3 - g''''(0)]\, e^{-4g'(0)}/6$. That allows us to also expand the surface potential $\Psi(0)$ in terms of ϕ_b at $\phi_b = 0$; up to third order we find $\Psi(0) = -\chi\phi_b + \chi^2\phi_b^2/2 + \chi^2[2\chi - 3g''(0)]\phi_b^3/6$. With this we obtain our final result (correct up to fourth order in ϕ_b) for the scaled surface tension,

$$\gamma v\kappa = \frac{1}{2}\chi\phi_b^2 - \frac{1}{4}\chi^2\phi_b^3 - \frac{7}{36}\chi^3\phi_b^4 + \frac{1}{4}\chi^2 g''(0)\phi_b^4. \tag{9.24}$$

Note that the additional nonideal free energy contribution $g(\phi)$ in Eq. 9.6 (and hence, the particle size) enters only through the final term. In fact, $g''(0) = 2B_2/v$ is related to the second virial coefficient B_2 of a bare hard sphere fluid. The first three terms in Eq. 9.24 represent an ideal Yukawa fluid, which we discuss in the following.

9.3.1. Ideal Yukawa Fluid

We apply our formalism of calculating γ to the most simple case, the ideal Yukawa fluid, where $g(\phi) = 0$ in Eq. 9.6. Note that ideality assumes point-like particles. Hence, we expect none of the physical quantities, including the surface tension γ, to depend on the particle volume v.

For an ideal Yukawa fluid, $h(\phi) = \phi$ (see Eq. 9.15) and thus $\phi(h) = h$, implying that the particles are

Boltzmann-distributed, $\phi = \phi_b e^{-\Psi+\Psi_b}$. With this, the Helmholtz equation in Eq. 9.14 becomes a differential equation, $\Psi''/\kappa^2 - \Psi = -\Psi_b e^{-\Psi+\Psi_b}$, that we refer to as Helmholtz-Boltzmann equation. Its first integration, see Eq. 9.17, reads

$$\frac{1}{\kappa}\Psi' = \sqrt{\Psi^2 - \Psi_b^2 + 2\Psi_b\,(e^{-\Psi+\Psi_b} - 1)}. \tag{9.25}$$

This equation must be solved numerically in the region $x > 0$, subject to fixed surface potential

$$\Psi(0) = \Psi_b - \ln\left(\frac{\Psi_b}{2} + 1\right), \tag{9.26}$$

which follows from Eq. 9.18. Based on Eqs. 9.21-9.23 and Eqs. 9.25-9.26, we can compute the scaled surface tension through

$$\frac{\gamma\kappa}{n_b} = -\int\limits_{\Psi(0)}^{\Psi_b} d\Psi\, \frac{\left(\frac{\Psi}{2}+1\right) e^{-\Psi+\Psi_b} - \left(\frac{\Psi_b}{2}+1\right)}{\sqrt{\Psi^2 - \Psi_b^2 + 2\Psi_b(e^{-\Psi+\Psi_b} - 1)}}, \tag{9.27}$$

where we recall that $n_b = \phi_b/v$ is the particle bulk concentration. Eq. 9.27 specifies a relation $\gamma\kappa/n_b$ as function of $\Psi_b = (4\pi l/\kappa^2)n_b$, which completely defines the surface tension $\gamma = \gamma(l,\kappa,n_b)$ of an ideal Yukawa fluid and, as expected, does not involve the particle volume v. The integration in Eq. 9.27 can be carried out numerically; the result is shown by the solid line in Fig. 9.3.

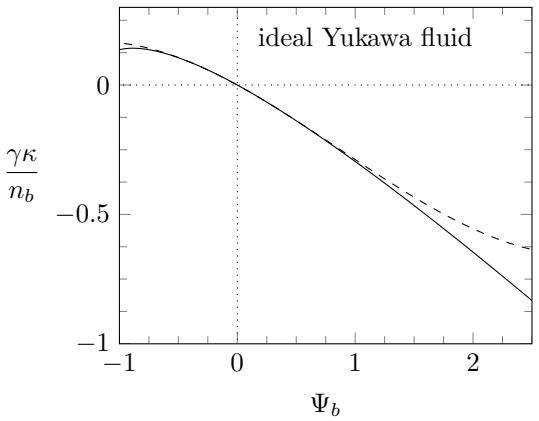

Figure 9.3. Scaled surface tension $\gamma\kappa/n_b$ versus bulk potential $\Psi_b = (4\pi l/\kappa^2)n_b$ for an ideal Yukawa fluid calculated on the level of mean-field theory. The solid curve shows the result according to a numerical integration of Eq. 9.27. The dashed curve corresponds to a series expansion, $\gamma\kappa/n_b = -\Psi_b/4 - \Psi_b^2/16 + 7\Psi_b^3/288$, valid up to third order in Ψ_b. The fluid is locally unstable for $\Psi_b < -1$.

We complete our analysis of the ideal Yukawa fluid by four comments:

First, the surface tension γ is negative for $l > 0$ and positive for $l < 0$. Indeed, particles in a repulsive Yukawa fluid ($l > 0$) exhibit more favorable interactions close to an interface as compared to the bulk. Hence, the particle concentration increases close to the interface until the chemical potential adopts a uniform value across the fluid. The adjustment in concentration can be studied conveniently in the limit $|\Psi_b| \ll 1$, where the linearized Helmholtz-Boltzmann equation, $\Psi''/\kappa^2 - \Psi = -\Psi_b$, subject to the boundary conditions $\Psi(0) = \Psi_b/2$ (see Eq. 9.26 in the limit $|\Psi_b| \ll 1$) and $\Psi(x \to \infty) = \Psi_b$, is solved by $\Psi(x) = \Psi_b(1 - e^{-\kappa x}/2)$. A positive sign of l renders $\Psi_b = (4\pi l/\kappa^2)n_b$ positive, implying $\Psi(x) \leq \Psi_b$ and thus an increased particle concentration $n = n_0 e^{-\Psi+\Psi_b} > n_0$ close to the container wall. This is schematically illustrated in Fig. 9.2.

Second, an attractive Yukawa fluid (for which $l < 0$ and thus $\Psi_b < 0$) may or may not be unstable with respect to phase separation. The onset of a *local* (that is, spinodal) instability imposes the restriction $\Psi_b > -1$ on the bulk potential. This limit follows from the presence of a point of inflection at $\phi_b = 1/(2\chi)$ in the Helmholtz free energy per particle $f(\phi_b) = -\chi\phi_b^2 + \phi_b \ln \phi_b - \phi_b$. Without information about the free energy of the high density phase we cannot determine the binodal line. Hence, metastability of the fluid may start anywhere in the region $-1 < \Psi_b < 0$.

Third, for a sufficiently small bulk concentration of the particles, $|\Psi_b| = |(4\pi l/\kappa^2)n_b|$ becomes small, and so do $|\Psi(0)|$ and $|\Psi|$. The integral in Eq. 9.27 can then be carried out in powers of Ψ_b. Up to third order we find $\gamma\kappa/n_b = -\Psi_b/4 - \Psi_b^2/16 + 7\Psi_b^3/288$, which is displayed in Fig. 9.1 as a dashed curve and indeed recovers Eq. 9.24 with $g''(\phi_b) = 0$. In the limit of very small particle concentration n_b, the first nonvanishing term of Eq. 9.24 is

$$\gamma = -\frac{\pi l}{4\kappa^3} n_b^2. \tag{9.28}$$

This is the low-density limit of the surface tension of a Yukawa fluid induced by a system boundary. Let us rationalize Eq. 9.28. Linearity of the Yukawa interaction implies $\gamma \sim l$, and symmetry demands $\gamma \sim n_b^2$. The surface tension must therefore scale as $\gamma \sim l\, n_b^2/\kappa^3$. Our analysis, leading to Eq. 9.28, adds to that the numerical prefactor $-\pi/4$.

Finally, note that γ diverges as κ approaches zero. Indeed, for $l > 0$ the limit $\kappa \to 0$ turns the Yukawa potential into a Coulomb repulsion, thus inducing *all* particles to migrate to the system boundary (as for mobile excess charge carriers in a conducting material) and decreasing γ to a negative value of infinite magnitude.

9.3.2. Lattice Yukawa Fluid

Using a lattice model is perhaps the most simple approach to account for finite particle volume. Recall that the nonideality of the lattice gas is expressed by $g(\phi)$ according to Eq. 9.7. Each lattice site can host one or no particle. Fitting one spherical particle of radius R into a single cubic lattice site of volume $(2R)^3$ limits the maximal volume fraction of the particles to $\pi/6 \approx 0.52$. Because particles are tagged to lattice positions, the number of available states is vastly underestimated, which leads to a smaller pressure as compared to more accurate approaches. Its simplicity still renders the lattice model a widely used and instructive approach, for example, in the mean-field modeling of ionic fluids [382].

Using $g(\phi)$ according to Eq. 9.7 yields $h(\phi) = \phi/[(\pi/6) - \phi]$ for the function $h(\phi)$ defined in Eq. 9.15. The inverse function is thus $\phi(h) = (\pi/6)\, h/(1+h)$. With our identification $h^{-1} \to \phi$ and $h \to \phi_b\, e^{-\Psi+\Psi_b+g'(\phi_b)}$ we obtain for the equilibrium distribution function (Eqs. 9.14, the first equation)

$$\phi = \frac{\phi_b}{\frac{6}{\pi}\phi_b + \left(1 - \frac{6}{\pi}\phi_b\right) e^{\Psi-\Psi_b}}. \tag{9.29}$$

Note that this Fermi-Dirac distribution enforces the condition $0 \le \phi \le \pi/6$. For sufficiently small ϕ, we recover the Boltzmann distribution, $\phi = \phi_b e^{-\Psi+\Psi_b}$, of the ideal Yukawa fluid.

Inserting $\phi = \phi(\Psi)$ from Eq. 9.29 into the Helmholtz equation (Eqs. 9.14, the second equation) yields a Helmholtz-Fermi-Dirac equation

$$\frac{1}{\kappa^2}\Psi'' - \Psi = -\frac{\Psi_b}{\frac{6}{\pi}\phi_b + \left(1 - \frac{6}{\pi}\phi_b\right) e^{\Psi-\Psi_b}}. \tag{9.30}$$

From its first integration

$$\frac{1}{\kappa}\Psi' = \sqrt{\Psi^2 - \Psi_b^2 + \frac{\pi}{3}\frac{\Psi_b}{\phi_b}\ln\left[1 + \frac{6\phi_b}{\pi}\,\left(e^{-\Psi+\Psi_b} - 1\right)\right]}, \tag{9.31}$$

taken at position $x = 0$, and the boundary condition $\Psi'(0) = \kappa\Psi(0)$ (see Eq. 9.13) we can calculate an explicit expression for the surface potential

$$\Psi(0) = \Psi_b - \ln\left[1 + \frac{\pi}{6\phi_b}\left(e^{\frac{3}{\pi}\phi_b\Psi_b} - 1\right)\right]. \tag{9.32}$$

This result can also be obtained directly from Eq. 9.18. Again, this serves as the lower integration limit for our calculation of γ according to Eqs. 9.21-9.23. The final expression for the scaled surface tension can be written as

$$\gamma v\kappa = -\int_{\Psi(0)}^{\Psi_b} \frac{d\Psi \left[\frac{1}{2}(\Psi\phi - \Psi_b\phi_b) - \frac{\pi}{6}\ln\left(\frac{\pi-6\phi}{\pi-6\phi_b}\right)\right]}{\sqrt{\Psi^2 - \Psi_b^2 + \frac{\pi}{3}\frac{\Psi_b}{\phi_b}\ln[1+\frac{6\phi_b}{\pi}(e^{-\Psi+\Psi_b}-1)]}}, \tag{9.33}$$

where ϕ is specified in Eq. 9.29 and $\Psi(0)$ in Eq. 9.32. Note that $\gamma v\kappa$ depends on two parameters, Ψ_b and ϕ_b. Because of $\Psi_b = -2\chi\phi_b$ we can consider $\gamma v\kappa$ to be a function of ϕ_b for any fixed $\chi = -2\pi l/(v\kappa^2)$. Fig. 9.4 shows numerical results (solid red lines) for $\gamma v\kappa$ according to Eq. 9.33 as function of ϕ_b for four different choices of χ. We also display in Fig. 9.4 (dashed red lines) the prediction of Eq. 9.24, with $g''(0) = 6/\pi$ according to Eq. 9.7. In order to observe the influence of the finite particle size, we have also added the predictions for the ideal Yukawa fluid according to Eq. 9.27 (solid black lines) and the corresponding fourth-order expansion (see Eq. 9.24 with $g''(0) = 0$; dashed black lines) to Fig. 9.4. Note that, as expected on thermodynamic grounds, the finite particle volume always increases the surface tension as compared to treating the entropy contribution to the free energy in Eq. 9.6 on the level of an ideal gas.

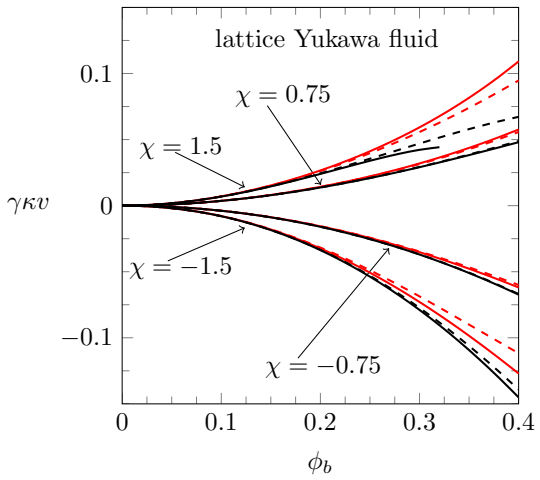

Figure 9.4. Scaled surface tension $\gamma v\kappa$ versus bulk volume fraction ϕ_b for a lattice Yukawa fluid (red lines) with different choices of $\chi = -2\pi l/(v\kappa^2)$ as marked. The solid red lines correspond to numerical solutions of Eq. 9.33. The dashed red lines represent the fourth-order expansion according to Eq. 9.24 with $g''(0) = 6/\pi$. We compare these results with our findings for the ideal Yukawa fluid: the numerical prediction according to Eq. 9.27 (solid black lines) and the fourth-order expansion (Eq. 9.24 with $g''(0) = 0$; dashed black lines).

9.3.3. Carnahan-Starling Yukawa Fluid

The Carnahan-Starling equation of state [81, 83, 90, 82], which is characterized by $g(\phi) = \phi^2(4-3\phi)/(1-\phi)^2$, see Eq. 9.8, provides a more realistic description of a hard sphere fluid than the lattice model. However, there is no analytic expression for the inverse $\phi(h)$ of the function $h(\phi) = \phi e^{g'(\phi)}$ defined in Eq. 9.15. We therefore have represented that function numerically and used it in Eqs. 9.16-9.18 (with the identification $h^{-1} \to \phi$) to compute the surface tension according to Eqs. 9.21-9.23. The results for $\gamma\kappa v$ are shown in Fig. 9.5 (solid blue lines) as function of ϕ_b for different values of χ as marked. We also show in Fig. 9.5 (dashed blue lines) the fourth-order series expansion result for $\gamma v\kappa$ according to Eq. 9.24, with $g''(0) = 8$ for the Carnahan-Starling Yukawa fluid. As already in Fig. 9.4, we re-display the results for the ideal Yukawa fluid (solid black lines for the prediction of Eq. 9.27 and dashed black lines for Eq. 9.24 with $g''(0) = 0$).

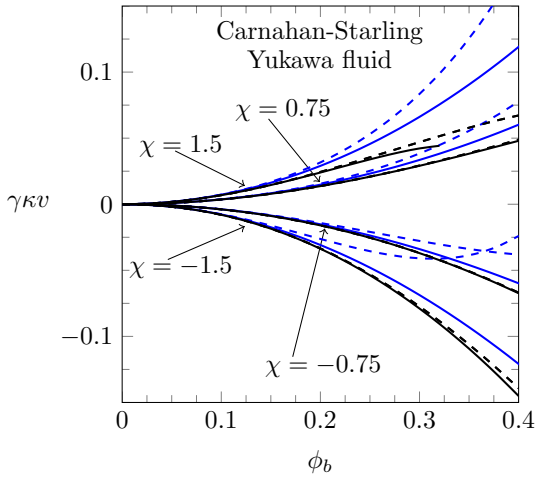

Figure 9.5. Scaled surface tension $\gamma v\kappa$ versus bulk volume fraction ϕ_b for a Carnahan-Starling Yukawa fluid (blue lines) with different choices of $\chi = -2\pi l/(v\kappa^2)$ as marked. The solid blue lines correspond to numerical solutions of Eqs. 9.21-9.23. The dashed blue lines represent the fourth-order expansion according to Eq. 9.24 with $g''(0) = 8$. We compare these results with our findings for the ideal Yukawa fluid: the numerical prediction according to Eq. 9.27 (solid black lines) and the fourth-order expansion (Eq. 9.24 with $g''(0) = 0$; dashed black lines).

The larger value of the second virial coefficient B_2 for the Carnahan-Starling equation of state ($B_2 = 4v$) as compared to the lattice gas equation of state ($B_2 = 3v/\pi$), together with the fourth-order expansion of $\gamma v\kappa$ according to Eq. 9.24, already suggest that the surface tension is generally larger in the former case.

From Figs. 9.4 and 9.5 we observe that this is indeed the case for all bulk volume fractions ϕ_b (compare the corresponding red and blue solid curves).

9.4. Phase-Separated Yukawa Fluid

In this section we consider an attractive Yukawa fluid that is thermodynamically unstable ($\chi > \chi_c$) and thus has undergone phase separation into a low-density (vapor, indexed "1") and a high-density (liquid, indexed "2") phase. Let us denote the particle concentrations in the bulk of each phase by $n_{b,1}$ and $n_{b,2}$ and the corresponding bulk potentials by $\Psi_{b,1}$ and $\Psi_{b,2}$. Given the interface between the two phases is planar, we place the origin of the x-axis (which points normal to the interface) somewhere inside the transition region. We refer to the position $x = 0$ as dividing surface. Fig. 9.6 illustrates the two coexisting phases as well as the concentration profile $n(x)$ and potential $\Psi(x)$. Our goal is to calculate the surface tension γ due to the presence of the interfacial region between the two phases. Recall that the mean-field properties of a Yukawa fluid are expressed by the parameter $\chi = -2\pi l/(v\kappa^2)$. For any given $\chi > \chi_c$ we can numerically extract from the binodal line the particles' bulk volume fractions $\phi_{b,1} = vn_{b,1}$ and $\phi_{b,2} = vn_{b,2}$ of the two coexisting phases in thermal equilibrium. As a result, the scaled surface tension $\gamma v\kappa$ is a function of only χ (and not a function of both χ and ϕ_b as in Section III).

It is straightforward to apply the general formalism introduced in Section III to the case of an interfacial region that separates two coexisting phases. We simply apply that formalism individually to the two regions of the Yukawa fluid located at $x < 0$ and $x > 0$. We point out, however, that the position of the dividing surface, $x = 0$, is arbitrary and, thus, will not affect the surface tension γ. Based on Eqs. 9.21-9.23, we can thus calculate the scaled surface tension directly from

$$\begin{aligned} \gamma v\kappa &= -\int_{\Psi_{b,1}}^{\Psi_{b,2}} d\Psi \, \frac{\left(\frac{\Psi}{2}+1\right)\phi - g(\phi) + \phi g'(\phi)}{\frac{1}{\kappa}\Psi'} \\ &+ \int_{\Psi_{b,1}}^{\Psi_{b,2}} d\Psi \, \frac{\left(\frac{\Psi_b}{2}+1\right)\phi_b - g(\phi_b) + \phi_b g'(\phi_b)}{\frac{1}{\kappa}\Psi'} \end{aligned} \tag{9.34}$$

with $\phi = h^{-1}(\phi_b\, e^{-\Psi+\Psi_b+g'(\phi_b)})$ and

$$\frac{1}{\kappa}\Psi' = \sqrt{\Psi^2 - \Psi_b^2 - 2\frac{\Psi_b}{\phi_b}\int_{\Psi_b}^{\Psi} d\bar{\Psi}\, h^{-1}(\phi_b\, e^{-\bar{\Psi}+\Psi_b+g'(\phi_b)})}. \tag{9.35}$$

The bulk volume fraction ϕ_b and corresponding bulk potential $\Psi_b = -2\chi\phi_b$ in Eqs. 9.34-9.35 can be chosen according to $\phi_b = \phi_{b,1}$ and $\Psi_b = \Psi_{b,1}$ for $\Psi_{b,1} > \Psi > \Psi(0)$, as well as $\phi_b = \phi_{b,2}$ and $\Psi_b = \Psi_{b,2}$ for $\Psi(0) > \Psi > \Psi_{b,2}$, where $\Psi(0)$ is an arbitrary potential with $\Psi_{b,1} > \Psi(0) > \Psi_{b,2}$.

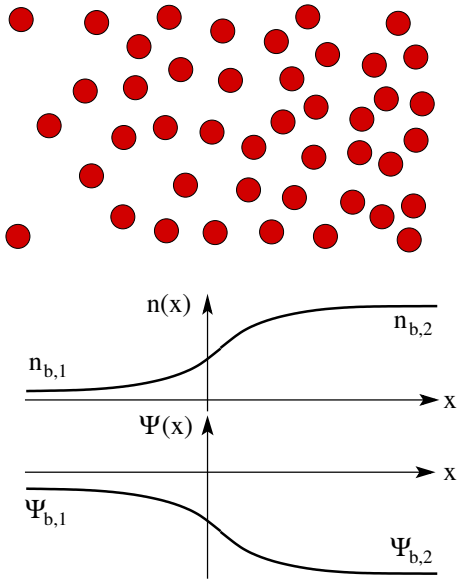

Figure 9.6. Schematic illustration of an attractive Yukawa fluid (with $l < 0$ and thus $\chi > 0$) that phase separates into two macroscopic phases with bulk concentrations $n_{b,1}$ and $n_{b,2}$ and corresponding bulk potentials $\Psi_{b,1}$ and $\Psi_{b,2}$. The concentration profile $n(x)$ and corresponding potential $\Psi(x)$ along the x-axis are both plotted qualitatively.

The fact that $\Psi(0)$ is arbitrary follows from the freedom to choose the position of the dividing surface (that is, the origin $x = 0$) anywhere along x-axis. Specifically, at the position of the dividing surface, the potential $\Psi(x)$ must be continuous and smooth. Using Eq. 9.17 we can extract from those two conditions an equation for the potential $\Psi(0)$

$$\Psi_{b,1}^2 - 4\chi\int_{\Psi_{b,1}}^{\Psi(0)} d\bar{\Psi}\, h^{-1}(\phi_{b,1}\, e^{-\bar{\Psi}+\Psi_{b,1}+g'(\phi_{b,1})}) = \Psi_{b,2}^2 - 4\chi\int_{\Psi_{b,2}}^{\Psi(0)} d\bar{\Psi}\, h^{-1}(\phi_{b,2}\, e^{-\bar{\Psi}+\Psi_{b,2}+g'(\phi_{b,2})}). \tag{9.36}$$

It is straightforward to demonstrate that a choice of $\Psi(0)$ anywhere between the two bulk potentials satisfies Eq. 9.36.

As in the previous section we exemplify our general result for the surface tension using the lattice Yukawa fluid and the Carnahan-Starling Yukawa fluid. In Fig. 9.7A we display the mean-field prediction for the scaled surface tension $\gamma v\kappa$ as function of χ for the lattice Yukawa fluid (solid red line) and for the Carnahan-Starling Yukawa fluid (solid blue line). Both curves are calculated numerically based in Eq. 9.34, with the corresponding choice for $g(\phi)$ for each model. Note that at the critical point, for $\chi = \chi_c$, the surface tension vanishes.

As discussed above, the mean-field result for $\gamma v\kappa$ is completely determined by the choice of $\chi = -2\pi l/(v\kappa^2)$; there is no additional parameter to be specified. The binodal line maps any value of χ (with $\chi > \chi_c$) to the two coexisting bulk volume fractions $\phi_{b,1}$ and $\phi_{b,2}$. Fig. 9.7B shows $\gamma v\kappa$ also as a function of half the difference of the bulk volume fractions, $\triangle\phi = (\phi_{b,2} - \phi_{b,1})/2$; the solid red and solid blue lines correspond to the lattice Yukawa and Carnahan-Starling Yukawa fluids, respectively. While Eq. 9.34 yields numerical values for the surface tension, we can also extract from that equation an analytic expression for $\gamma v\kappa$ close to the critical point. To this end, we express all quantities that enter into Eq. 9.34 in terms of $\triangle\phi = (\phi_{b,2} - \phi_{b,1})/2$ and then expand $\gamma v\kappa$ up to third order in $\triangle\phi$. Using Eq. 9.12, $\chi = \chi_c + (\triangle\phi)^2[2/\phi_c^3 + g''''(\phi_c)]/12$, $\Psi_{b,1} = -2\chi\phi_{b,1}$, $\Psi_{b,2} = -2\chi\phi_{b,2}$, $\phi_{b,1} = \phi_c - \triangle\phi$, and $\phi_{b,2} = \phi_c + \triangle\phi$, we find after some algebra

$$\begin{aligned} \gamma v\kappa &= \frac{1}{15\sqrt{3}} \frac{(\triangle\phi)^3}{\phi_c^3} \sqrt{\frac{1/\phi_c + g''(\phi_c)}{2/\phi_c^3 + g''''(\phi_c)}} \\ &\times \left[2 + 10\phi_c^3 g''''(\phi_c) + 3\phi_c^4 g'''''(\phi_c)\right], \end{aligned} \tag{9.37}$$

or, equivalently, when expressed as function of χ,

$$\begin{aligned} \gamma v\kappa &= \frac{2\sqrt{2}}{5\,\phi_c^3} \left(\frac{\chi - \chi_c}{\chi_c}\right)^{3/2} \left(\frac{1/\phi_c + g''(\phi_c)}{2/\phi_c^3 + g''''(\phi_c)}\right)^2 \\ &\times \left[2 + 10\phi_c^3 g''''(\phi_c) + 3\phi_c^4 g'''''(\phi_c)\right]. \end{aligned} \tag{9.38}$$

The expressions in Eqs. 9.37 and 9.38 apply to *any* choice of the function $g(\phi)$ as defined in Eq. 9.6. Recall that the critical volume fraction ϕ_c represents the solution of the algebraic equation $\phi_c^2\, g'''(\phi_c) = 1$, and with that $\chi_c = [1/\phi_c + g''(\phi_c)]/2$ follows; see Eq. 9.12. Note that the mean-field scaling in Eq. 9.38,

$\gamma \sim (\chi - \chi_c)^{3/2}$, is consistent with the prediction $\gamma \sim (T_c - T)^{3/2}$ from Landau-Ginzburg theory [383] where $T \sim 1/\chi$ is the temperature and $T_c \sim 1/\chi_c$ its critical value.

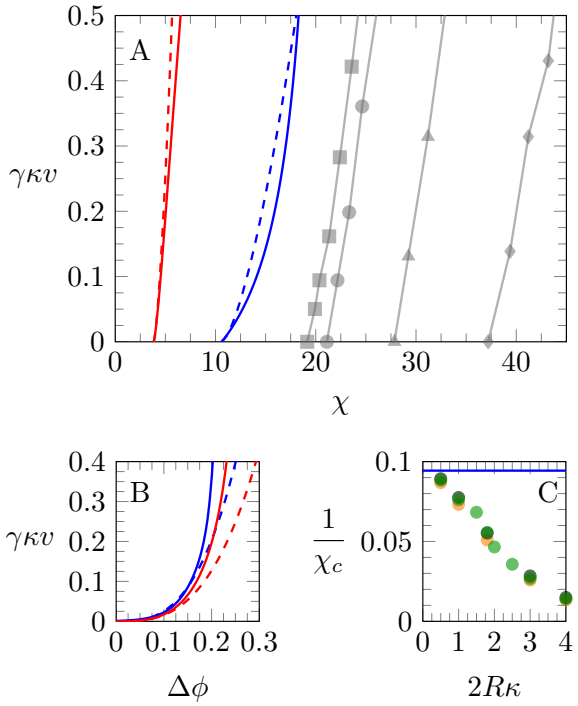

Figure 9.7. Scaled surfaced tension $\gamma v \kappa$ as function of χ (diagram A) and as function of $\triangle\phi = (\phi_{b,2} - \phi_{b,1})/2$ (diagram B). Red (for the lattice Yukawa fluid) and blue (for the Carnahan-Starling Yukawa fluid) solid lines correspond to numerical solutions of Eq. 9.34; the dashed lines display $\gamma v \kappa$ according to Eq. 9.39 (red) and Eq. 9.40 (blue). The gray symbols in diagram A re-display Monte Carlo results reported by Galicia-Pimentel *et al* [3] for $2R\kappa = 3.0$ (gray diamonds), $2R\kappa = 2.5$ (gray triangles), $2R\kappa = 2.0$ (gray bullets), and $2R\kappa = 1.8$ (gray squares). Diagram C: Critical value χ_c as function of $2R\kappa$ reported by El Mendoub *et al* [4] (green), Weiss and Schröer [5] (orange), and Duh and Mier-y-Terán [6] (black symbols). The horizontal solid blue line shows the mean-field prediction for the Carnahan-Starling Yukawa fluid, which is independent of $R\kappa$.

If we specify $g(\phi)$ according to lattice Yukawa fluid, we obtain from Eqs. 9.37 and 9.38

$$\gamma v \kappa = \frac{64}{\pi^2}\sqrt{6}\,(\triangle\phi)^3 = \frac{\sqrt{2}}{3}\pi\left(\frac{\chi - \chi_c}{\chi_c}\right)^{3/2}, \tag{9.39}$$

and for the Carnahan-Starling Yukawa fluid we find

$$\gamma v \kappa = 25.39\,(\triangle\phi)^3 = 0.848\left(\frac{\chi - \chi_c}{\chi_c}\right)^{3/2}. \tag{9.40}$$

The results in Eqs. 9.39 and 9.40 are displayed in Fig.9.7A and 9.7B as dashed lines (red for the lattice Yukawa fluid and blue for the Carnahan-Starling Yukawa fluid). As expected, they approximate the general mean-field results close to the critical points.

Our prediction of the surface tension γ of a phase boundary is subject to the mean-field approximation. We cannot expect such a model to quantitatively predict correct values for the surface tension. But we do expect good agreement of the Carnahan-Starling Yukawa fluid (which is based on a reasonably accurate equation of state for a hard-sphere fluid) in the limit of small κ, where each particle interacts with many other particles. To support this assertion we re-display in Fig. 9.7A (gray lines) predictions from Monte Carlo simulations reported by Galicia-Pimentel *et al* [3] for $2R\kappa = 3.0$ (gray diamonds), $2R\kappa = 2.5$ (gray triangles), $2R\kappa = 2.0$ (gray bullets), and $2R\kappa = 1.8$ (gray squares). Unfortunately, we are not aware of simulation results for smaller κ; yet, we expect good agreement in the limit $R\kappa \ll 1$. Note that the critical point χ_c (that is, the value of χ at which $\gamma \to 0$ in Fig. 9.7A), is predicted in simulation studies and in density functional theory to explicitly depend on $R\kappa$ whereas in the present mean-field theory it is invariant. We display this dependence in Fig. 9.7C, which shows how the critical point χ_c depends on $2R\kappa$ according to results from density functional theory [4, 5, 6]. For example, at $2R\kappa = 1.8$ density functional theory predicts $\chi_c \approx 20$, which indeed agrees with the Monte Carlo simulation results [3] in Fig. 9.7A. Our mean-field model appears to reproduce the critical point in the limit $R\kappa \ll 1$; see Fig. 9.7C. It will thus be interesting in future work to produce simulation results in this limit.

9.5. Conclusions

Mean-field results for the surface tension γ of fluids can serve as useful references for more advanced theoretical models and for simulation results. Yet, to the best of our knowledge, no mean-field predictions for γ of a Yukawa fluid *based on a non-local field-based representation* were available so far. Our present work demonstrates how to compute γ for a wide range of nonideal contributions to the free energy. Simple analytic predictions for γ are calculated for small particle density and close to the critical point of a phase-separating Yukawa fluid.

Two specific cases, the lattice Yukawa fluid and the Carnahan-Starling Yukawa fluid, are analyzed in some detail. The former is particularly simple while the latter provides a more realistic description of the underlying hard sphere fluid. Of course, other models can be used. For example, the van der Waals fluid

has a nonideality contribution $g(\phi) = \phi[1 - \ln(1-\phi)]$, implying a critical point $\chi_c = 27/8$ at $\phi_c = 1/3$ and according to Eq. 9.38 a scaled surface tension $\gamma v\kappa = (7/5)\sqrt{2}[(\chi - \chi_c)/\chi_c]^{3/2}$ of a phase boundary.

Besides a comprehensive set of numerical results for γ, our work also presents the limiting expression $\gamma = -\pi l n_b^2/(4\kappa^3)$ for small particle concentrations n_b of a homogeneous Yukawa fluid near a system boundary. In addition, we argue that our mean-field prediction for the surface tension of a phase boundary works best in the limit of a large screening length $1/\kappa \gg R$, when the function $g(\phi)$ is accounted for on the basis of the Carnahan-Starling equation of state. In this case, the second virial coefficient of our underlying free energy is $B_2 = 4v + 2\pi l/\kappa^2$. Weiss and Schröer [5] have used the full expression of the second virial coefficient $B_2 = 4v - 2\pi \int_{2R}^{\infty} dr r^2 (e^{-u(r)/k_BT} - 1)$ to predict the surface tension γ of two coexisting phases using a small gradient approximation. It is interesting to ask if a non-local mean-field model can be constructed that is based on the general expression for B_2 instead of $B_2 = 4v + 2\pi l/\kappa^2$. One method would be to use a function $g(\phi)$ in Eq. 9.6 that has the property

$$g''(0) = 8 - \frac{4\pi}{v}\left[\frac{l}{\kappa^2} + \int_{2R}^{\infty} dr r^2 \left(e^{-u(r)/k_BT} - 1\right)\right]. \tag{9.41}$$

The second virial coefficient of the homogeneous Yukawa fluid $B_2 = vg''(0)/2 + 2\pi l/\kappa^2$ is then accurate, whereas interactions are still accounted for on a non-local level and without assuming small gradients of the particle density. Working this out could be the subject of a future study.

9.6. Acknowledgments

SM and GVB thank Jacob Sockness for discussions. GVB acknowledges a doctoral schol- arship from CAPES Foundation/Brazil Ministry of Education (Grant No. 9466/13-4).

10. EMERGENCE OF A STERN LAYER FROM THE INCORPORATION OF HYDRATION INTERACTIONS INTO THE GOUY-CHAPMAN MODEL OF THE ELECTRICAL DOUBLE LAYER*

10.1. Introduction

It is generally accepted that the specific nature of the electrolyte ions in aqueous solutions plays a vital role in dictating the electrical properties of charged interfaces. Both the surface charge densities [384, 385] and the electrical potentials [386, 387] regularly depend on the identity of the co- and counterions in the electrolyte solution. These general observations are often termed specific ion effects [388, 66] and their ramifications are, for example, evident in colloidal [389] and biological [390] settings. The microscopic origins of specific ion effects are, however, complex and poorly understood and therefore continue to fascinate the experimental and theoretical communities alike.

There exist several different models for the structure of the electrical double layer (EDL) but the Gouy-Chapman-Stern (GCS) model [333] has proved most successful in fitting experimental results for a variety of different solid-electrolyte interfaces [391, 392]. The GCS model is an elementary extension of the Gouy-Chapman (GC) model that inserts a Helmholtz capacitor of thickness d_{Stern}, termed the Stern layer, between the charged surface and the diffuse ion cloud [393]. Because no electrolyte ions reside within d_{Stern} the potential drop to the surface is like that of a capacitor (a linear function in the case of a smooth planar surface). Outside the Stern layer the potential profile and ion distributions of the GCS model are given by the solution of the classical Poisson-Boltzmann equation. The combination of capacitor and diffuse layer regions in the GCS model results in an (often substantial) increase of the predicted magnitude of the surface potential relative to models that have only one or the other.

*Reproduced with permission from "M. A. Brown, G. V. Bossa, S. May, Emergence of a Stern layer from the incorporation of hydration interactions into the Gouy–Chapman model of the electrical double layer, Langmuir 31 (42) (2015) 11477–11483". Copyright 2015 American Chemical Society. This paper can be accessed online at `http://pubs.acs.org/doi/abs/10.1021/acs.langmuir.5b02389`. The material in this chapter was co-authored by Matthew A. Brown, Guilherme V. and Sylvio May. G.V.B. was responsible for the mathematical development, numerical solution of the equations, figures preparation, and discussion of the results.

From a theoretical standpoint the Stern layer does not emerge naturally from the solution of the classical Poisson-Boltzmann equation, but appears after accounting for the finite sizes of the ions in the electrolyte through excluded volume interactions [90, 91, 394, 395, 396]. This places the charge of each ion at the center of a sphere of well defined radius, typically chosen to match the hydrated ion size. The finite-size modification limits the concentration of counterions near the surface, an obvious improvement over the solution of the classical Poisson-Boltzmann equation, while at the same time creating a thin, charge-depleted region close to the surface. The width of this uncharged region is set by the imposed excluded volume potential and is equal to d_{Stern}. Computer simulations suggest, however, that the non-electrostatic contributions to the ion-ion interaction potentials in aqueous solutions are *soft* and decay over the length scale of a few water molecules [65], and are therefore not best modeled by the hard-core potential of the excluded volume interaction. A few attempts have been made to incorporate additional soft interaction potentials into the Gouy-Chapman model [397, 73, 398, 78], but the predictions were not analyzed in terms of Stern layer formation.

In the approach put forward here the non-electrostatic interactions of the counterions with the charged surface, and that between the counterions themselves, are modeled as soft interactions, namely repulsive Yukawa potentials that mimic the structural forces due to ion- and surface-induced hydration effects [353]. We describe these hydration-mediated interactions on the same level as the electrostatic interactions by introducing a hydration potential in addition to the electrostatic potential. Our approach, which retains the conceptual simplicity of the GC model, yields properties reminiscent of the Stern layer, with a charge-depleted region and corresponding linear behavior of the electrostatic potential. In addition, the inter-ionic hydration repulsion limits the counterion concentration close to the surface. The maximal value of the counterion concentration close to the surface reflects the packing of the counterions including their hydration shells: it decreases with the effective counterion size but remains largely independent of the bulk salt concentration.

10.2. Theory

Consider a planar solid surface with a fixed, uniform and sufficiently high negative surface charge density σ_e. The surface is in contact with an aqueous solution containing a symmetric 1:1 electrolyte of bulk concentration n_0. The electrostatic potential in the aqueous solution, $\Phi(x)$, at distance x away from

the surface fulfills the Poisson equation $\varepsilon_W \varepsilon_0 \Phi''(x) = -\rho(x)$, where a prime denotes the derivative with respect to the argument; $\varepsilon_0 = 8.85 \times 10^{-12}$ F/m is the permittivity of free space and $\varepsilon_W = 78$ the dielectric constant of water. The local volume charge density within the electrolyte $\rho(x) = e[n_+(x) - n_-(x)]$ reflects the difference of concentrations between mobile electrolyte cations (n_+) and anions (n_-); the elementary charge is $e = 1.6 \times 10^{-19}$ C. It is common to re-express the Poisson equation

$$\Psi''(x) = -4\pi l_e [n_+(x) - n_-(x)] \tag{10.1}$$

in terms of the dimensionless electrostatic potential $\Psi = e\Phi/k_BT = \Phi/(25\text{mV})$ and the Bjerrum length in water $l_e = e^2/(4\pi\varepsilon_W\varepsilon_0 k_B T) = 0.7$ nm, where k_B is the Boltzmann constant and $T = 300$ K the absolute temperature. The classical GC model combines the Poisson equation with Boltzmann distributions for the local ion concentrations, $n_+ = n_0 e^{-\Psi}$ and $n_- = n_0 e^{\Psi}$, yielding the classical Poisson-Boltzmann equation $\Psi''(x) = \kappa_e^2 \sinh[\Psi(x)]$ with

$$\kappa_e^2 = 8\pi l_e n_0. \tag{10.2}$$

The length $1/\kappa_e$ is known as the Debye screening length [130]. We point out that the Poisson equation expresses interactions through the Coulomb potential with electrostatic energies $U_e/k_BT = l_e/r$ and $U_e/k_BT = -l_e/r$ between elementary charges of the same and different signs, respectively, that are separated by a distance r. Consequently, the classical GC model accounts only for purely electrostatic ion-ion and ion-surface interactions.

Ions and surfaces induce water molecules to form hydration shells, which mediate hydration interactions [399, 400, 401]. A negatively charged surface attracts mobile cations (the counterions) that reside in close proximity at elevated concentrations as compared to the bulk, whereas the mobile anions (the coions) are depleted from the surface. Hence, close to a highly negatively charged surface we expect hydration interactions to be relevant for the mobile cations and negligible the mobile anions. To model these interactions we assume cations to produce not only an electrostatic but also an additional hydration interaction that we model as a Yukawa potential $U_h/k_BT = e^{\kappa(l_h - r)}\, l_h/r$, where $1/\kappa = 0.3$ nm is the decay length of the ordered water layers [399] and r the distance between two cations. The length l_h denotes the ion-to-ion separation at which the hydration interaction is equal to the thermal energy unit k_BT. Hence, we expect l_h reflects the effective ion size, namely the crystallographic size plus the thickness of a soft hydration shell [402].

The choice of a Yukawa-like interaction $\sim e^{-\kappa r}/r$ is motivated by a phenomenological model of hydration forces due to Marcelja and Radic [353] and ensures the cations remain fully hydrated near the charged surface. Detailed Molecular Dynamics (MD) simulations [67, 403, 270] and continuum solvation models [404] predict a similar decay, yet with an additional oscillatory component that under specific conditions would allow cations near the charged surface to get trapped in a local minimum state that may involve (partial) dehydration and the formation of an inner-sphere complex. The inclusion of an oscillatory component into the present model is possible but mathematically more involved. For this reason we have omitted its inclusion in the present work. Hence, the total cation-cation interaction energy in our model is

$$\frac{U_{tot}}{k_B T} = \frac{U_e}{k_B T} + \frac{U_h}{k_B T} = \frac{l_e}{r} + \frac{l_h}{r}\, e^{\kappa(l_h - r)}, \tag{10.3}$$

whereas cation-anion and anion-anion interactions remain purely Coulombic ($U_{tot}/k_B T = l_e/r$ for the anion-anion interaction and $U_{tot}/k_B T = -l_e/r$ for the cation-anion interaction). Here we note again that there is no need to include hydration interactions involving the anions as long as their local concentration is sufficiently small everywhere in the aqueous solution. Fig. 10.1 shows the cation-cation interaction energy $U_{tot}(r)/k_B T$ for $l_h = 0.2$ nm (black solid line), $l_h = 0.4$ nm (blue line), $l_h = 0.6$ nm (red line), and $l_h = 0.8$ nm (green line). These are the values on which our analysis in the Results and Discussion section will focus. The first three of these effective cation sizes are representative of the hydrated alkali metal cations [402] ($Cs^+_{hyd} \sim 0.2$ nm, $Na^+_{hyd} \sim 0.4$ nm, and $Li^+_{hyd} \sim 0.6$ nm).

Similarly to translating the Coulomb interaction $U_e/k_B T = \pm l_e/r$ between two ions to the Poisson equation for the associated dimensionless electrostatic potential Ψ in Eq. 10.1, we can also translate the hydration interaction $U_h/k_B T = e^{\kappa(l_h - r)} l_h/r$ to a local differential equation for an associated (dimensionless) hydration potential $\Psi_h(x)$. The result is the inhomogeneous Helmholtz equation [78]

$$\Psi_h''(x) - \kappa^2 \Psi_h(x) = -4\pi l_h\, e^{\kappa l_h} [n_+(x) - n_0]. \tag{10.4}$$

Eq. 10.4 does not contain n_-; this is a consequence of focusing exclusively on hydration interactions between cations (counterions) in the aqueous solution. The local cation and anion concentrations fulfill Boltzmann distributions

$$n_+(x) = n_0 e^{-\Psi(x) - \Psi_h(x)}, \quad n_-(x) = n_0 e^{\Psi(x)}, \tag{10.5}$$

where, again, the hydration potential $\Psi_h(x)$ is only associated with the mobile cations. The Boltzmann distributions in Eq. 10.5 can be derived rigorously by minimizing an appropriate mean-field free energy functional [78].

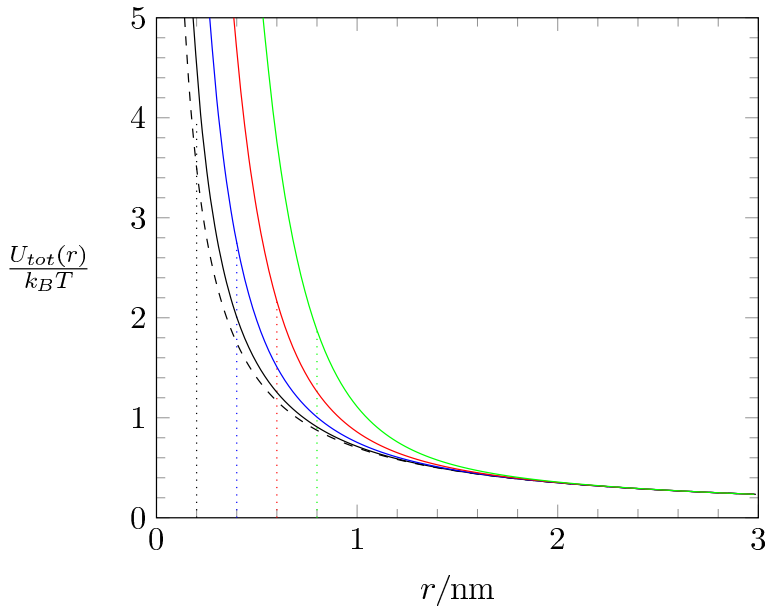

Figure 10.1. Total cation-cation interaction energy $U_{tot}(r)$ according to Eq. 10.3 with $l_e = 0.7$ nm and $\kappa^{-1} = 0.3$ nm. The different solid lines correspond to $l_h = 0.2$ nm (black), $l_h = 0.4$ nm (blue), $l_h = 0.6$ nm (red), and $l_h = 0.8$ nm (green). At these values for l_h (marked by dotted vertical lines) the hydration interaction energy $U_h(r = l_h)$ equals the thermal energy k_BT. The dashed line shows the electrostatic contribution $U_e/k_BT = l_e/r$.

Inserting the Boltzmann distributions into Eqs. 10.1 and 10.4 yields two second-order, coupled differential equations for the two fields $\Psi(x)$ and $\Psi_h(x)$,

$$\begin{aligned} \Psi''(x) &= \frac{\kappa_e^2}{2}\left[e^{\Psi(x)} - e^{-\Psi(x)-\Psi_h(x)}\right], \\ \Psi_h''(x) - \kappa^2\Psi_h(x) &= \frac{\kappa_h^2}{2}\left[1 - e^{-\Psi(x)-\Psi_h(x)}\right], \end{aligned} \tag{10.6}$$

where κ_e (the inverse of the Debye screening length) is defined in Eq. 10.2 and

$$\kappa_h^2 = 8\pi l_h e^{\kappa l_h} n_0. \tag{10.7}$$

In the absence of the hydration potential we identify the first line in Eqs. 10.6 as the classical Poisson-

Boltzmann equation. Prior to solving the coupled system in Eqs. 10.6 we need to specify four boundary conditions. Two of them,

$$\Psi'(0) = -4\pi l_e \frac{\sigma_e}{e}, \qquad \Psi_h'(0) = -4\pi l_h e^{\kappa l_h} \sigma_h, \tag{10.8}$$

reflect the surface charge density σ_e and the density of sources for the hydration interaction of the cations with the surface, respectively. Regarding the latter, each ordered water molecule on the surface can be expected to act as a source; a reasonable choice is therefore the surface density of water molecules $\sigma_h = 5/\mathrm{nm}^2$. The remaining two boundary conditions, $\Psi(x \to \infty) = 0$ and $\Psi_h(x \to \infty) = 0$, render the surface to be isolated. We treat the two parameters $\kappa^{-1} = 0.3$ nm and $\sigma_h = 5/\mathrm{nm}^2$ as fixed constants throughout this work. (However, this does not exclude them from being adjusted in order to fit experimental data.)

The two coupled second-order differential equations for $\Psi(x)$ and $\Psi_h(x)$, specified in Eqs. 10.6, can be solved numerically by employing a Newton Raphson iteration procedure. To this end, the two nonlinear equations are re-expressed as a two linear second-order differential equations,

$$\begin{aligned} \frac{2}{\kappa_e^2}\Psi'' &= \left(e^{\tilde{\Psi}_e} + e^{-\tilde{\Psi}_e - \tilde{\Psi}_h}\right)(\Psi - \tilde{\Psi}_e) \\ &+ e^{-\tilde{\Psi}_e - \tilde{\Psi}_h}(\Psi_h - \tilde{\Psi}_h) + e^{\tilde{\Psi}_e} - e^{-\tilde{\Psi}_e - \tilde{\Psi}_h}, \\ \frac{2}{\kappa_h^2}(\Psi_h'' - \kappa^2 \Psi_h) &= e^{-\tilde{\Psi}_e - \tilde{\Psi}_h}(\Psi - \tilde{\Psi}_e + \Psi_h - \tilde{\Psi}_h) \\ &+ 1 - e^{-\tilde{\Psi}_e - \tilde{\Psi}_h}, \end{aligned} \tag{10.9}$$

whose solutions $\Psi(x)$ and $\Psi_h(x)$ are used as input $\tilde{\Psi}_e$ and $\tilde{\Psi}_h$ for the next iteration. Convenient starting functions are $\tilde{\Psi}_e = \tilde{\Psi}_h = 0$. Once the solutions have become stationary, $\Psi(x) = \tilde{\Psi}_e(x)$ and $\Psi_h(x) = \tilde{\Psi}_h(x)$, the nonlinear system is solved. The computational effort to solve Eqs. 10.9 is marginal and, in fact, comparable to numerically solving the classical Poisson-Boltzmann equation.

10.3. Results and Discussion

The combination of electrostatic and hydration-mediated interactions in the EDL can lead to structural properties similar to the Stern layer extension of the GC model. We illustrate this behavior by presenting in Fig. 10.2 the potentials $\Psi(x)$ and $\Psi_h(x)$ (upper diagram) as well as $n_+(x)$ and $n_-(x)$ (lower diagram),

derived for $\kappa^{-1} = 0.3\,\text{nm}$, $\sigma_e/e = -1/\text{nm}^2$, $\sigma_n = 5/\text{nm}^2$, and $\kappa_e^{-1} = 1\,\text{nm}$. The four solid lines in each diagram (and the insets) correspond to $l_h = 0.2$ nm (black), $l_h = 0.4$ nm (blue), $l_h = 0.6$ nm (red), and $l_h = 0.8$ nm (green).

Fig. 10.2 is a manifestation of Stern-like EDL properties: Each electrostatic potential $\Phi(x) = \Psi(x) \times 0.025$ V (solid lines in the upper diagram) exhibits linear behavior within a region $0 \leq x \lesssim d_{Stern}$ of the charged surface, prior to decaying to zero. Both the magnitude of the surface potential $\Phi(0)$ and the width d_{Stern} of the linear region grow with the effective counterion size l_h. (Recall that l_h is the distance at which the hydration repulsion equals the thermal energy $k_B T$.) The linearity of $\Phi(x)$ suggests to identify the region from the surface to d_{Stern} as a Stern layer. Consistent with this notion, the counterion concentrations (lower diagram in Fig. 10.2) adopt their maximum value $n_+(d_{Stern})$ at the Stern plane $x = d_{Stern}$, whereas counterions (and coions, see inset) are depleted from within the Stern layer, $x \lesssim d_{Stern}$. The locations d_{Stern} and $n_+(d_{Stern})$ are marked by a filled circle in the lower diagram of Fig. 10.2. We also note that unlike the classical Gouy-Chapman model for point-like ions, the addition of a hydration repulsion confines the maximal counterion concentrations $n_+(d_{Stern})$ to physically reasonable values. For a surface charge density $\sigma_e/e = -1/\text{nm}^2$ and a 0.1 M bulk salt concentration (which implies a Debye screening length $\kappa_e^{-1} = 1\,\text{nm}$) the classical Gouy-Chapman model (see the dash-dotted lines in Fig. 10.2) predicts a surface potential of $\Phi_e(0) = -110$ mV and a corresponding counterion concentration of 8 M at the surface. In contrast, with the hydration repulsion included we find maximal counterion concentrations $n_+(d_{Stern})$ in the range of 1 to 2 M. We also make the physically reasonable observation that a larger effective ion size (growing l_h) results in decreasing $n_+(d_{Stern})$, If we again reference the hydrated alkali metal cations, to which our values of l_n are most directly compared [402], this result is directly supported by experiment [386].

To obtain a better physical understanding of how hydration interactions affect EDL properties, we switch off the mutual hydration repulsion between cations while retaining the hydration repulsion of the cations with the surface. Mathematically this is accomplished by setting the right-hand side of the second equation of Eqs. 10.6 to zero, yielding $\Psi_h''(x) - \kappa^2 \Psi_h(x) = 0$, while keeping the boundary condition for the hydration potential Ψ_h in Eq. 10.8. We obtain the simple exponential decay

$$\Psi_h(x) = \frac{4\pi l_h \sigma_h}{\kappa}\, e^{\kappa(l_h - x)}, \tag{10.10}$$

which enters the Boltzmann distribution of the counterions $n_+(x)$ in Eq. 10.4 as a fixed potential. Hence,

counterions interact with the charged surface not only electrostatically but also via the external, surface-generated hydration potential in Eq. 10.10. A related approach of incorporating ion-surface hydration forces, mediated through dielectric saturation, was developed by Gur *et al* [405]. The predictions of the model based on Eq. 10.10 are shown in Fig. 10.2 as dashed lines. Solid and dashed lines of the same color correspond to, respectively, including and ignoring cation-cation hydration repulsion for fixed effective cation size (fixed l_h). The dashed lines in the inset of the upper diagram in Fig. 10.2 correspond to $\Psi_h(x)$ according to Eq. 10.10. Recall that a more positive hydration potential $\Psi_h(x)$ reduces the local counterion concentration $n_+ = n_0 e^{-\Psi-\Psi_h}$. Indeed, close to the surface $\Psi_h(x)$ adopts large positive values. Without accounting for cation-cation hydration repulsion, $\Psi_h(x)$ originates only from the surface and decays exponentially. With cation-cation hydration repulsion being present, $\Psi_h(x)$ develops an additional tail that extends further into the EDL (solid lines in the inset of the upper diagram) and thus decreases the counterion concentration even more. This decrease is more pronounced for larger effective cation sizes l_h. We contrast this to the absence of cation-cation hydration repulsion, where a Stern layer still forms but the maximal counterion concentration $n_+(d_{Stern})$ remains unaffected by the counterion size, a finding that is physically unreasonable. This highlights the importance of accounting for hydration interactions of counterions not only with the surface but also among each other.

Varying the salt concentration in the bulk of the aqueous solution affects the Debye screening length and thus the diffuse part of the EDL but has virtually no effect on the counterion concentration profile close to the Stern layer. This is illustrated in Fig. 10.3 for fixed $\kappa^{-1} = 0.3\,\text{nm}$, $\sigma_e/e = -1/\text{nm}^2$, $\sigma_n = 5/\text{nm}^2$, and $l_h = 0.4\,\text{nm}$. Different curves correspond to different salt concentrations in the bulk: 1 mM (red), 4 mM (green), 100 mM (blue), and 400 mM (black).

Saturation of the counterion concentration due to steric (that is, excluded volume) repulsion is predicted by various recent models [80, 406, 396, 407]. One prominent example is to replace the ideal gas that forms the basis of the classical GC model by a lattice gas with a cell volume a^3 that represents the effective (including a hydration shell of fixed extension) ion size. This simple modification does not only enforce counterion saturation, it also leads to a non-monotonic dependence of the differential capacitance on the surface potential [408]. Fedorov and Kornyshev [406] have pointed out that the approach has been introduced independently by multiple authors starting already in 1942 [79]; it leads to the modified Poisson-Boltzmann

equation [80]

$$\Psi'' = \kappa_e^2 \frac{\sinh\Psi}{1-\phi_0(1-\cosh\Psi)}, \tag{10.11}$$

where $\phi_0 = 2a^3 n_0$ is the volume fraction of the salt ions in the bulk. The inset of Fig. 10.3 shows the local counterion volume fraction $a^3 n_+ \sim 1/(1+2e^{\Psi}(1-\phi_0)/\phi_0)$ calculated from the solution of Eq. 10.11 with the boundary conditions $\Psi'(0) = -4\pi l_e \sigma_e/e$ and $\Psi(x\to\infty) = 0$. The two sets of curves in the inset correspond to the two surface charge densities $\sigma_e/e = -1/\text{nm}^2$ (solid lines) and $\sigma_e/e = -2/\text{nm}^2$ (dashed lines). Similar to our present model, the lattice gas GC model predicts counterion saturation that is largely independent of the bulk salt concentration. However, the model does not produce a Stern layer with its ion depletion zone, large magnitude of the surface potential $\Psi(0)$, and capacitor-like properties close to the surface.

The GCS model of the EDL places a Stern adsorption plane at distance d_{Stern} away from the charged surface. In addition to the fixed charge density σ_e at the surface, the Stern adsorption plane is assumed to carry a surface charge density σ_{Stern} that originates from ion adsorption. The GCS model does not specify the origin of the ion adsorption; it may reflect exclusively electrostatic attraction or a combination of electrostatic interactions and non-electrostatic binding [401]. It is also common to assume a uniform dielectric constant ε_{Stern} within the Stern layer (that is in the region $0 \le x \le d_{Stern}$), which may be significantly smaller than the dielectric constant of bulk water, ε_W. Mathematically, the dimensionless electrostatic potential according to the GCS model is

$$\Psi(x) = \begin{cases} \Psi(d_{Stern}) - \frac{4\pi l_e}{\varepsilon_{rel}} \frac{\sigma_e}{e}(x - d_{Stern}) \\ 2\ln\left[1 - \frac{2}{1+e^{\kappa_e(x-d_{Stern})}\coth\frac{\Psi(d_{Stern})}{4}}\right], \end{cases} \tag{10.12}$$

where the upper line describes the parallel-plate capacitor in the region $0 \le x \le d_{Stern}$ and the lower line the diffuse ion layer for $x \ge d_{Stern}$. Also, $\varepsilon_{rel} = \varepsilon_{Stern}/\varepsilon_W$ is the relative dielectric constant within the Stern layer, and

$$\Psi(d_{Stern}) = 2\,\text{arsinh}\left[\frac{2\pi l_e}{\kappa_e e}(\sigma_e + \sigma_{Stern})\right] \tag{10.13}$$

is the dimensionless electrostatic potential at the Stern adsorption surface. Note that σ_{Stern} is a phenomenological parameter that can in principle take on any value, but the two limiting cases of significance are $\sigma_{Stern} = -\sigma_e$ and $\sigma_{Stern} = 0$. The former reduces the problem to that of a simple parallel-plate capacitor–the

Helmholtz model, while the latter implies no specific ion adsorption at the Stern plane. In Fig. 10.4 we compare the prediction of the present GC model with hydration repulsion to the GCS model of the EDL. The blue solid and dashed lines show $\Psi(x)$ for $l_h = 0.4\,\mathrm{nm}$ with and without cation-cation hydration repulsion included (these are the same blue curves as already shown and discussed in the upper diagram of Fig. 10.2). Recall that we identify the position $x = d_{Stern}$ of the counterion concentration maximum $n_+(d_{Stern})$ with the position of the Stern layer; $x = d_{Stern} = 0.77\,\mathrm{nm}$ for the case displayed in Fig. 10.4 (marked by the dashed vertical line). To compare our present model with the GCS model of the EDL, we also plot in Fig. 10.4 the potential $\Psi(x)$ according to Eq. 10.12, derived for $\sigma_e/e = -1\,\mathrm{nm}^2$, $\kappa_e^{-1} = 1\,\mathrm{nm}$, and $\varepsilon_{rel} = 1$. The five different solid lines correspond to different values of the surface charge density σ_{Stern} at the Stern plane: $\sigma_{Stern} = -\sigma_e$, $\sigma_{Stern} = -0.75\sigma_e$, $\sigma_{Stern} = -0.5\sigma_e$, $\sigma_{Stern} = -0.25\sigma_e$, and $\sigma_{Stern} = 0$ (from top to bottom). Note there is a discontinuous change in slope for $\Psi(x)$ at $x = d_{Stern}$ for all $\sigma_{Stern} \neq 0$. When $\sigma_{Stern} = -\sigma_e = 1\,e/\mathrm{nm}^2$ the potential profile $\Psi(x)$ corresponds to that of a parallel-plate capacitor. The surface potential $\Phi(0) = \Psi(0) \times 0.025$ V (plotted as function of σ_{Stern} in the inset of Fig. 10.4) is -0.15 V, and the potential outside the Stern layer (that is, for $x > d_{Stern}$) is zero. When $\sigma_{Stern} = 0$ the surface potential is significantly more negative (-0.26 V) than in the Helmholtz model, but remains less negative than the prediction of our present GC model with hydration repulsion (-0.31 V). The origin of this behavior is that the additional repulsive hydration interactions between cations tend to widen the width of the EDL. This renders the surface potential more negative as compared to the GCS model. We note that the similarity of our present model and the GCS model of the EDL also leads to similar values of the differential capacitance $C = d\sigma_e/d\Phi(0)$. For the parameters used in Fig. 10.4 (namely, $\sigma_e/e = -1\,\mathrm{nm}^2$, $\kappa_e^{-1} = 1\,\mathrm{nm}$, $\varepsilon_{Stern} = 78$, $d_{Stern} = 0.77\,\mathrm{nm}$, and $\sigma_{Stern} = 0$, which corresponds to the bottom solid black line in Fig. 10.4) we obtain $C = C_{Stern}C_{GC}/(C_{Stern}+C_{GC}) = 0.70\,\mathrm{F/m}^2$, where $C_{Stern} = \varepsilon_{Stern}\varepsilon_0/d_{stern} = 0.90\,\mathrm{F/m}^2$ is the capacitance of a parallel-plate capacitor and $C_{GC} = \varepsilon_W\varepsilon_0\kappa_e\cosh[\Psi(d_{stern})/2] = 3.11\,\mathrm{F/m}^2$ the differential capacitance of the EDL according to the classical GC model. This compares well with our present GC model with hydration repulsion (the solid blue line in Fig. 10.4), for which we obtain $C = 0.72\,\mathrm{F/m}^2$.

Our final discussion addresses the dielectric constant. The model put forward in the Theory section assumes a uniform dielectric constant throughout the aqueous phase. A more elaborate model could attempt to couple the dielectric constant to the hydration potential or could include dielectric saturation effects [409, 410], but this is beyond the scope of the present work. Instead, we investigate the influence of a fixed drop in the local dielectric constant $\varepsilon(x)$ as the distance x to the solid surface decreases. This modification

is straightforward to implement in our model by replacing the left-hand side, $\Psi''(x)$, of the first equation in Eqs. 10.6 by $(\varepsilon_{rel}(x)\Psi'(x))'$, where $\varepsilon_{rel}(x) = \varepsilon(x)/\varepsilon_W$ is the local relative dielectric constant with respect to water. Using MD simulations Wander and Clark [411] have recently predicted a drop in $\varepsilon(0)$ to about 50% of its bulk value $\varepsilon(x \to \infty) = \varepsilon_W = 78$ at a charged oxide-electrolyte interface; see Figure 5 in Ref. wander08. An exponential decay with a characteristic length $\kappa^{-1} = 0.3$ nm appears to be a reasonable approximation to these simulation results. A similar exponential decay of $\varepsilon(x)$ was also predicted by Podgornik *et al* [412] using nonlocal dielectric response theory. We therefore use the function $\varepsilon_{rel}(x) = \varepsilon_{rel}(0) + (1 - e^{-\kappa x})[1 - \varepsilon_{rel}(0)]$ with $\varepsilon_{rel}(0) = 0.5$. Fig. 10.5 shows the influence of modifying the dielectric constant close to the surface. The solid lines in Fig. 10.5, which apply to a uniform dielectric constant ($\varepsilon_{rel}(x) \equiv 1$), replot results from the upper diagram of Fig. 10.2 (which were calculated for $\sigma_e/e = -1/\text{nm}^2$). The corresponding results with $\varepsilon_{rel}(0) = 0.5$ are shown as dashed lines. As expected, the surface potential $\Psi(0)$ becomes more negative for the lower dielectric constant near the surface, but the differences between the two models (for $\varepsilon_{rel}(0) = 1$ and $\varepsilon_{rel}(0) = 0.5$) are minor and do not invalidate the findings of this work. This conclusion remains valid if the surface charge density σ_e is varied; see the inset of Fig. 10.5, which shows the relation between the dimensionless surface potential $\Psi(0)$ and surface charge density σ_e both for uniform ($\varepsilon_{rel}(0) = 1$, solid lines) and exponentially decaying ($\varepsilon_{rel}(0) = 0.5$, dashed lines) dielectric constants. The corresponding relation according to the classical GC model, $\Psi(0) = 2\,\text{arsinh}(2\pi l_e \kappa_e^{-1} \sigma_e/e)$, is known as the Grahame equation. The inset of Fig. 10.5 suggests that the relation between $\Psi(0)$ and σ_e is strongly influenced by the inter-ionic and ion-surface hydration interactions. For surfaces of equal surface charge density our model predicts the surface potential becomes more negative as the size of the hydrated cation (l_n) increases. This result is qualitatively supported by electrophoretic mobility experiments (colloidal silica in aqueous solutions of LiCl, NaCl and CsCl) that report on the potential at the start of the diffuse layer (zeta-potentials) [386], but direct comparison with experimentally determined surface potentials is not, at present, possible because of a lack of data.

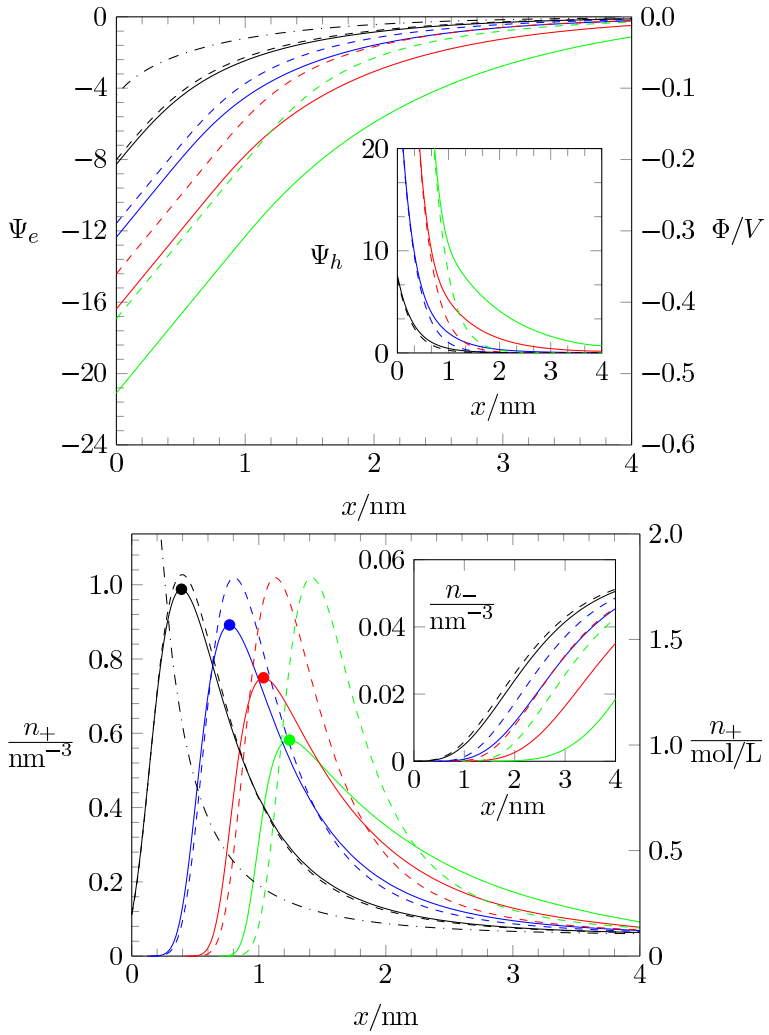

Figure 10.2. $\Psi(x)$ and $\Psi_h(x)$ (upper diagram), and $n_+(x)$ and $n_-(x)$ (lower diagram). Different curves correspond to different hydration repulsion strengths: $l_h = 0.2\,\mathrm{nm}$ (black), $l_h = 0.4\,\mathrm{nm}$ (blue), $l_h = 0.6\,\mathrm{nm}$ (red), $l_h = 0.8\,\mathrm{nm}$ (green). The solid lines account for cation-cation hydration repulsion whereas the dashed lines ignore it. The dashed lines in the inset of the upper diagram follow Eq. 10.10. The filled circles in the lower diagram mark the maximum counterion concentration $n_+(d_{Stern})$ at position d_{Stern}. The black dash-dotted line corresponds to the electrostatic potential (upper diagram) and counterion concentration (lower diagram) according to the classical GC model. All results are derived for fixed $\kappa^{-1} = 0.3\,\mathrm{nm}$, $\sigma_e/e = -1/\mathrm{nm}^2$, $\sigma_n = 5/\mathrm{nm}^2$, and $\kappa_e^{-1} = 1\,\mathrm{nm}$. The Debye screening length $\kappa_e^{-1} = 1\,\mathrm{nm}$ corresponds to a bulk salt concentration of $n_0 = 0.057/\mathrm{nm}^3$; for large x all curves in the lower diagram (including the inset) converge to this value.

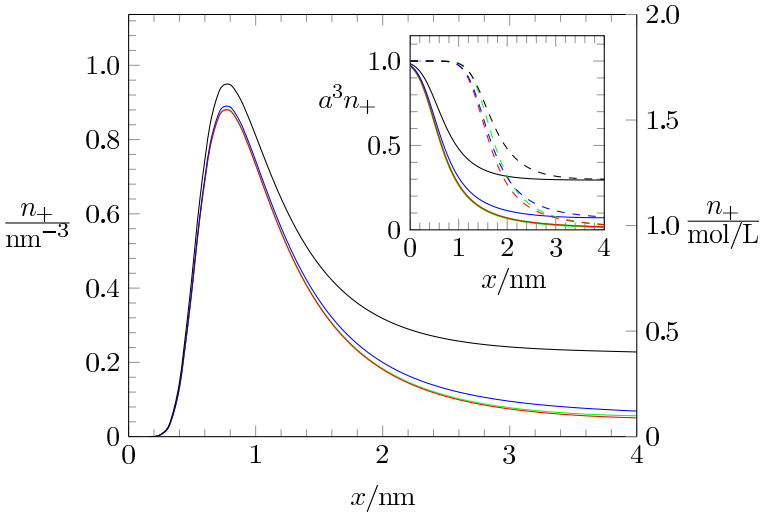

Figure 10.3. Counterion concentration profile $n_+(x)$ for $\kappa^{-1} = 0.3\,\mathrm{nm}$, $\sigma_e/e = -1/\mathrm{nm}^2$, $\sigma_n = 5/\mathrm{nm}^2$, and $l_h = 0.4\,\mathrm{nm}$. Different curves correspond to different salt concentrations in the bulk: n_0 =1 mM (red), 4 mM (green), 100 mM (blue), and 400 mM (black). The inset shows predictions of the lattice gas GC model with a cell size of $a = 2l_h = 0.8\,\mathrm{nm}$ according to Eq. 10.11 for the same set of salt concentrations as in the main diagram. Solid and dashed lines in the inset correspond to $\sigma_e/e = -1/\mathrm{nm}^2$ and $\sigma_e/e = -2/\mathrm{nm}^2$, respectively.

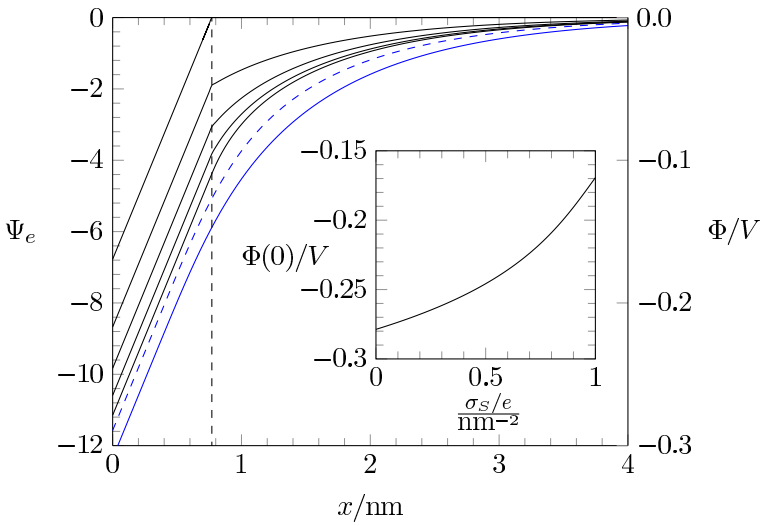

Figure 10.4. The two blue lines (one solid and one dashed) replot the potential profiles from the upper diagram in Fig. 10.2 for $l_h = 0.4$ nm. The vertical dashed line marks the position $x = d_{Stern} = 0.77\,\mathrm{nm}$ of the Stern plane (see the blue bullet in the lower diagram of Fig. 10.2). The five black solid lines show $\Psi(x)$ according to Eq. 10.12 (the GCS model) for $\sigma_e/e = -1\,\mathrm{nm}^2$, $\kappa_e^{-1} = 1\,\mathrm{nm}$, $\varepsilon_{rel} = 1$, and different values of the surface charge density σ_{Stern} at the Stern layer: $\sigma_{Stern} = -\sigma_e$, $\sigma_{Stern} = -0.75\sigma_e$, $\sigma_{Stern} = -0.5\sigma_e$, $\sigma_{Stern} = -0.25\sigma_e$, and $\sigma_{Stern} = 0$ (from top to bottom). The surface potential $\Phi(0)$ is plotted in the inset as function of σ_{Stern}.

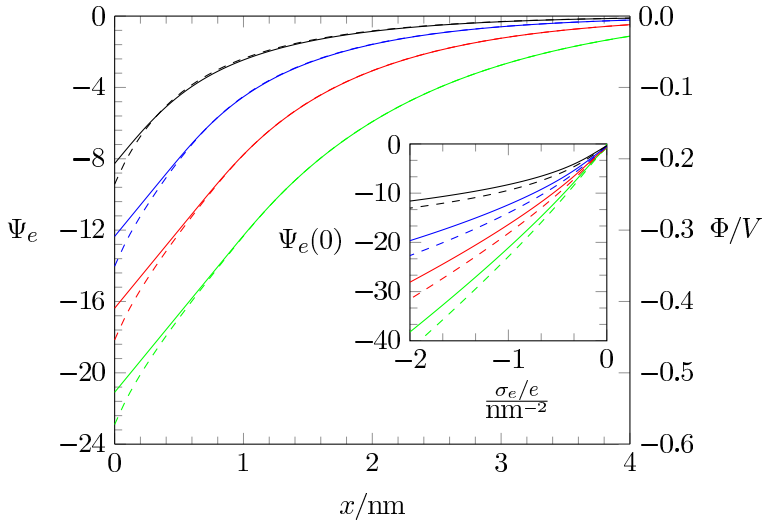

Figure 10.5. The dimensionless electrostatic potential $\Psi(x)$ for $\sigma_e/e = -1/\mathrm{nm}^2$. The solid lines replot the results for uniform dielectric constant, $\varepsilon_{rel}(x) \equiv 1$, from the upper diagram in Fig. 10.2, where $l_h = 0.2\,\mathrm{nm}$ (black), $l_h = 0.4\,\mathrm{nm}$ (blue), $l_h = 0.6\,\mathrm{nm}$ (red), $l_h = 0.8\,\mathrm{nm}$ (green). The dashed lines show the corresponding results for an exponentially decaying dielectric constant with a relative surface value $\varepsilon_{rel}(0) = 0.5$. The inset shows the relation between the dimensionless surface potential $\Psi(0)$ and the surface charge density σ_e for uniform (solid lines) and exponentially decaying (dashed lines) dielectric constants, the latter with $\varepsilon_{rel}(0) = 0.5$.

10.4. Conclusions

By simply adding a non-electrostatic hydration repulsion in the form of a Yukawa potential to the electrostatic interaction inherent in classical Gouy-Chapman theory (the solution of the Poisson-Boltzmann equation) a picture of the EDL that resembles very closely the GCS model emerges naturally. A thin counterion-free region develops at the charged surface whose thickness increases with the effective size of the counterion (crystallographic size plus the thickness of a soft hydration shell). We bound the Stern-like layer by the maximum in counterion concentration, which our model predicts to be physically reasonable, and furthermore, to decrease as the size of the counterion increases. Within the Stern-like region the potential drop to the charged surface is (nearly) linear, again in resemblance to the GCS model of the EDL. We make a direct comparison to the GCS model and conclude that the two models predict effectively the same surface potential only when σ_{Stern} is assumed 0. Finally, we note that the simplicity of our model (both conceptually and mathematically) makes it a convenient tool to fit experimental data or to use it as starting point in further refinements of modeling the EDL. Possible examples regarding the latter include (1) the incorporation of hydration-mediated interactions involving coions (instead of only counterions), (2) the addition of oscillations to the hydration potential between mobile ions (which then can capture different ionic hydration states), and (3) the application of the model to different geometries (where a Laplacian replaces the second derivatives in Eq. 10.6).

10.5. Acknowledgments

M.A.B. acknowledges the Swiss National Science Foundation for an International Short Visit travel grant to North Dakota State University. G.V.B. acknowledges a doctoral scholarship from CAPES Foundation/Brazil Ministry of Education (Grant No. 9466/13-4).

11. ROLE OF ION HYDRATION FOR THE DIFFERENTIAL CAPACITANCE OF AN ELECTRIC DOUBLE LAYER *

11.1. Introduction

The presence of an electrode in an electrolyte solution changes the way ions are distributed. Mobile ions rearrange so as to screen the charge at the electrode surface, thus forming an electrical double layer (EDL) in this process. The EDL has great importance in biological, colloidal and polyelectrolyte sciences [413, 414, 415, 416, 417], surface conductivity [418], renewable energy systems [419, 420], new methods for oil recovery [421], and in electrical double layer capacitors, a device that stores electrochemical energy through the EDL [422, 423]. The electrode is often approximately described by a perfectly planar charged surface, but other geometries have also been taken into account [424]. The most simple model of an EDL is a parallel-plate capacitor, where one plate corresponds to the charged surface while the other plate represents the diffuse ion cloud formed by the mobile counter- and co-ions. Based on this, an EDL can be characterized by three quantities: the electrostatic potential at the surface $\Phi(0)$, the surface charge density σ_e, and the differential capacitance $C^{diff} = d\sigma_e/d\Phi(0)$, which embodies the relationship between σ_e and $\Phi(0)$.

The differential capacitance C^{diff} is often observed to initially increase and then pass through a maximum as $|\sigma_e|$ increases. Yet, no maximum is predicted by the most simple and widely used theoretical model, which is based on the classical Poisson-Boltzmann (PB) theory [425, 426]. This discrepancy, which has motivated the advancement of theoretical models and the application of computer simulations, appears to be related to two approximations that are inherent in the classical PB theory [427, 428, 429, 430]: First, it treats the mobile ions as being point-like instead of accounting for their non-vanishing sizes and, second, it ignores the structure of the solvent by assuming a structureless medium of uniform dielectric constant [431].

The most simple yet widely used approach to account for the finite size of the mobile ions goes

*Reprinted from " D. L. Z. Caetano, G. V. Bossa, V. M. de Oliveira, M. A. Brown, S. J. de Carvalho, S. May, Role of ion hydration for the differential capacitance of an electric double layer, Phys. Chem. Chem. Phys. 18 (40) (2016) 27796–27807". Reproduced by permission of The Royal Society of Chemistry. Copyright 2016 The Royal Society of Chemistry. This paper can be accessed online at `http://pubs.rsc.org/-/content/articlehtml/2016/cp/c6cp04199j`. The material in this chapter was co-authored by Daniel L. Z. Caetano, Guilherme V. Bossa, Vinicius M. de Oliveira, Matthew A. Brown, Sidney J. de Carvalho, and Sylvio May. G. V. Bossa contributed to the project design and manuscript writing. G.V.B. was responsible for the mathematical development, numerical and analytical solution of the equations, mathematical processing of simulation data, figures preparation, and discussion of the results.

back to Stern [333], who assumed that some of the mobile counterions adsorb onto the flat surface, thus creating a region that separates the charged surface from the diffuse part of the EDL. Stern proposed to treat that region as a planar capacitor with a constant thickness equal to the effective ion radius. The incorporation of steric effects directly into the diffuse ion layer on the basis of a lattice gas model dates back to Bikerman [79]. Since then, several other approaches have been developed to include steric effects, such as different modified Poisson-Boltzmann equations [432, 433, 408], lattice-based models [434, 382, 435], integral equations theories [436, 437, 438], equations of state based on liquid-state theory for hard spheres mixtures [82, 83, 90, 439] and Monte Carlo simulations [440, 441, 442, 443].

Steric effects render the structure of the EDL ion-specific. However, ion specificity is also manifested by the formation of a hydration shell consisting of ordered water molecules in the vicinity of the mobile ions [66]. Previous experimental [413, 280] and simulation studies [65, 67] have demonstrated that hydration-mediated ion-ion and ion-surface interactions are soft with a characteristic decay length corresponding to the size of a water molecule and can exhibit oscillatory behavior [92, 93]. For example, Baimpos et al. [94] have observed that, depending on the type of salt and its concentration, the measured force between two mica surfaces becomes oscillatory when the plates approach each other.

Reducing the non-electrostatic ion-ion and ion-surface interaction in an EDL to steric repulsions between hard spheres can therefore not be expected to capture the full scope of ion specificity [444, 445]. In line with this, some efforts have been made recently to incorporate soft potentials as models for hydration-mediated ion-ion interactions into PB theory [446, 397, 73]. One approach employs a Yukawa potential [31, 78], which represents not only the most simple approximation to the soft ion-ion potentials extracted from recent simulations [65, 67] but is also consistent with the measured exponential decay of the hydration force between two planar surfaces as demonstrated by Israelachvili and Sornette [447]. The Yukawa potential also emerges from the phenomenological hydration model of Marcelja and Radic [353]. Based on this it was shown that a thin charge-depleted region similar to that proposed originally by Stern emerges naturally from the presence of a repulsive Yukawa potential between the surface and counterions [8].

The present study pursues two objectives. First, we present a theoretical approach of incorporating hydration-mediated ion-ion interaction potentials into the PB formalism. We extend previous works [31, 78] by adding independent hydration-mediated cation-cation, cation-anion, and anion-anion potentials to the electrostatic Coulomb interactions. Moreover, we incorporate into our theoretical approach two frequently used methods of accounting for excluded volume interaction between ions. One is based on the

Carnahan-Starling equation of state [81], and the other on the above-mentioned lattice gas model [79, 382]. Our second objective is to investigate how hydration-mediated interactions and their interplay with finite ion size effects affect the differential capacitance C^{diff}. To this end, we have performed Monte Carlo simulations for different combinations of hydration-mediated and excluded volume interactions and compared their predictions with the corresponding mean-field approaches. We find our simulations and mean-field predictions to agree remarkably well when both include soft, hydration-mediated ion-ion interactions (but not in their absence), which suggests the importance of ion-ion correlations to be diminished by the additional soft hydration potential. Specifically, for low surface charge densities $|\sigma_e|$ the agreement is best if excluded volume effects are modeled based on the Carnahan-Starling equation of state. For large $|\sigma|$, however, better agreement is obtained when accounting for excluded volume effects using the lattice gas model.

We point out that the present study focuses on symmetric hydration-mediated interactions, where $C^{diff}(\sigma) = C^{diff}(-\sigma)$, leaving the analysis of asymmetric cases to a forthcoming study. In addition, while we include hydration-mediated interactions in the form of non-electrostatic potentials, we ignore changes in the dielectric constant through dielectric saturation [431] and polarization effects [448].

11.2. Theory

We consider an extended planar surface with surface charge density σ_e in contact with a symmetric $1:1$ electrolyte of bulk cation and anion concentrations n_0 and dielectric constant $\varepsilon_W \approx 80$. The planar surface, which represents a flat electrode, is located at position $x = 0$ of a Cartesian coordinate system that has its x-axis point into the electrolyte; see Fig. 11.1 for a schematic illustration. Mobile ions interact with each other through their excluded volume and through a combination of electrostatic and hydration-mediated interactions. Hydration interactions reflect the formation of hydration shells around ions and water structuring in the vicinity of charged surfaces. Inspired by a phenomenological approach developed by Marcelja and Radic [353], Molecular Dynamics simulations [67, 270], and previous mean-field models [31], we represent hydration-mediated interactions by a Yukawa potential. Specifically, we use for the combined Coulomb and Yukawa pair potentials the expressions $U_{aa} = k_B T(l_B + ae^{-\kappa(r-a)})/r$ (for the anion-anion interaction), $U_{ac} = k_B T(-l_B + be^{-\kappa(r-b)})/r$ (for the anion-cation interaction), and $U_{cc} = k_B T(l_B + ce^{-\kappa(r-c)})/r$ (for the cation-cation interaction). Here r denotes the center-to-center distance between two ions, k_B the Boltzmann constant, T the absolute temperature, and $1/\kappa$ a characteristic length associated with

the hydration interaction potential. The Bjerrum length $l_B = e^2/(4\pi\varepsilon_W\varepsilon_0 k_B T)$ corresponds to the separation at which the electrostatic interaction energy between two water-immersed elementary charges e equals the thermal energy $k_B T$ (ε_0 is the permittivity of free space). Analogously, the hydration interaction strength equals $k_B T$ at distance a between two anions, at distance b between an anion and a cation, and at distance c between two cations. In the following, we develop a mean-field formalism that consistently incorporates U_{aa}, U_{ac}, and U_{cc}.

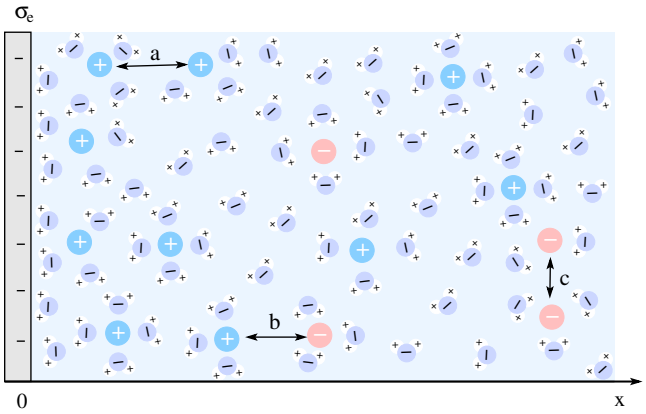

Figure 11.1. Schematic illustration of a planar surface with surface charge density σ_e in contact with an aqueous solution containing monovalent ions of bulk cation and anion concentrations n_0 and dielectric constant $\varepsilon_W \approx 80$. Mobile ions interact with each other through their excluded volume, through a Coulomb potential, and through a Yukawa potential. The latter two account for electrostatic and hydration-mediated interactions, respectively. They are specified by the relationships $U_{aa}(r)$, $U_{ac}(r)$, and $U_{cc}(r)$ for anion-anion, anion-cation, and cation-cation interactions, respectively, where r is the ion-to-ion distance; see the text for details. The strength of the electrostatic interaction equals $k_B T$ if two ions are separated by a distance l_B. Similarly, the strength of the hydration interaction equals $k_B T$ for an anion-anion pair at distance a, for an anion-cation pair at distance b, and for a cation-cation pair at distance c away from each other.

11.2.1. Mean-Field Theory

Our model starts with the total free energy,

$$F_{tot} = U_{el} + U_{hyd} + F_{mix}, \tag{11.1}$$

that accounts for electrostatic interactions (U_{el}), for hydration interactions (U_{hyd}) and for an ideal or non-ideal mixing entropy contribution (F_{mix}) of the ions in solution. We discuss each term individually.

The electrostatic energy (in units of k_BT) of the electrolyte can be expressed as

$$\frac{U_{el}}{k_BT} = \frac{1}{2}\int_V d^3\mathbf{r}\int_V d^3\mathbf{r}'\,\frac{1}{|\mathbf{r}-\mathbf{r}'|}\begin{pmatrix} n_+(\mathbf{r})-n_0 \\ n_-(\mathbf{r})-n_0\end{pmatrix}^T \mathscr{M}_e \begin{pmatrix} n_+(\mathbf{r}')-n_0 \\ n_-(\mathbf{r}')-n_0\end{pmatrix}, \tag{11.2}$$

where $n_+(\mathbf{r})$ and $n_-(\mathbf{r})$ are the local concentrations of cations and anions, respectively, as function of the position vector $\mathbf{r}$. The two integrations are carried out over the volume V that contains the ions. The electrostatic interaction matrix in Eq. 11.2,

$$\mathscr{M}_e = l_B\begin{pmatrix} 1 & -1 \\ -1 & 1\end{pmatrix}, \tag{11.3}$$

specifies the prefactors for the $1/r$-Coulomb potential between two cations and two anions (the diagonal elements), and between an anion and a cation (the non-diagonal elements). Recall that both ions are monovalent. The Bjerrum length is $l_B = 0.7\,\text{nm}$ for an aqueous medium ($\varepsilon_W \approx 80$) at room temperature. From Eq. 11.2 we define a dimensionless electrostatic potential Ψ through

$$\begin{pmatrix} \Psi(\mathbf{r}) \\ -\Psi(\mathbf{r})\end{pmatrix} = \int_V d^3\mathbf{r}'\,\frac{1}{|\mathbf{r}-\mathbf{r}'|}\,\mathscr{M}_e\begin{pmatrix} n_+(\mathbf{r}')-n_0 \\ n_-(\mathbf{r}')-n_0\end{pmatrix}. \tag{11.4}$$

The reason why only one single electrostatic potential appears in Eq. 11.4 is the vanishing determinant of $\mathscr{M}_e$. We note the relation $\Psi = e\Phi/k_BT$ between the dimensionless electrostatic potential Ψ and the electrostatic potential Φ. As is well known, applying the Laplace operator ∇^2 to Eq. 11.4 and using Green's function $G(\mathbf{r}) = -1/(4\pi|\mathbf{r}|)$ yields the Poisson equation

$$\nabla^2\Psi(\mathbf{r}) = -4\pi l_B[n_+(\mathbf{r}) - n_-(\mathbf{r})]. \tag{11.5}$$

When expressed in terms of the dimensionless electrostatic potential, the electrostatic interaction energy reduces to the familiar expression

$$\frac{U_{el}}{k_BT} = \int d^3\mathbf{r}\frac{(\nabla\Psi)^2}{8\pi l_B}, \tag{11.6}$$

where the integration runs over all space. The energy due to Yukawa-like interaction potentials can be

expressed in analogy to Eq. 11.2 by

$$\frac{U_{hyd}}{k_B T} = \frac{1}{2} \int\limits_V d^3\mathbf{r} \int\limits_V d^3\mathbf{r}' \, \frac{e^{-\kappa|\mathbf{r}-\mathbf{r}'|}}{|\mathbf{r}-\mathbf{r}'|} \begin{pmatrix} n_-(\mathbf{r}) - n_0 \\ n_+(\mathbf{r}) - n_0 \end{pmatrix}^T \mathscr{M}_h \begin{pmatrix} n_-(\mathbf{r}') - n_0 \\ n_+(\mathbf{r}') - n_0 \end{pmatrix} \tag{11.7}$$

with a hydration interaction matrix

$$\mathscr{M}_h = \begin{pmatrix} ae^{\kappa a} & be^{\kappa b} \\ be^{\kappa b} & ce^{\kappa c} \end{pmatrix}. \tag{11.8}$$

Recall that the constants a, b, and c represent the distances where the interaction between an anion-anion, anion-cation, and cation-cation pair, respectively, equals $k_B T$. The values for a, b, and c embody the specificity of the ion-ion interaction. In our present work we do not attempt to determine these parameters. Instead, we simply assume $a = b = c$, thus leaving the analysis of asymmetric interactions and the identification with specific ions to be worked out in future studies. We also note that the parameter $1/\kappa = 0.3\,\text{nm}$ accounts for the characteristic decay length of ordered water layers [413]. Based on Eq. 11.7, we define two non-electrostatic (hydration) potentials Ψ_a and Ψ_c via

$$\begin{pmatrix} \Psi_a(\mathbf{r}) \\ \Psi_c(\mathbf{r}) \end{pmatrix} = \int\limits_V d^3\mathbf{r}' \, \frac{e^{-\kappa|\mathbf{r}-\mathbf{r}'|}}{|\mathbf{r}-\mathbf{r}'|} \mathscr{M}_h \begin{pmatrix} n_-(\mathbf{r}') - n_0 \\ n_+(\mathbf{r}') - n_0 \end{pmatrix}. \tag{11.9}$$

Generally, there are indeed two independent hydration potentials because the determinant of the hydration interaction matrix, $\det(\mathscr{M}_h)$, may be non-vanishing. Special cases with $\det(\mathscr{M}_h) = 0$ have been introduced and discussed in previous works. Specifically, Bohinc *et al* [78] have used $\mathscr{M}_h = l_n e^{\kappa l_n} \{\{(1-\alpha)^2, -(1-\alpha^2)\}, \{-(1-\alpha^2), (1+\alpha)^2\}\}$ with fixed constants l_n and α. Brown *et al* [8] have used $\mathscr{M}_h = l_h e^{\kappa l_n} \{\{0,0\}, \{0,1\}\}$ with a single fixed constant l_h. As already exercised for the electrostatic interaction, see the transition from Eq. 11.4 to Eq. 11.5, we can find an operator that produces a Yukawa-like Green's function. The operator is $\nabla^2 - \kappa^2$ and the corresponding Green's function $G(\mathbf{r}) = -e^{-\kappa|\mathbf{r}|}/(4\pi|\mathbf{r}|)$. With that we can cast Eq. 12.3 into the local form

$$\begin{pmatrix} (\nabla^2 - \kappa^2)\,\Psi_a(\mathbf{r}) \\ (\nabla^2 - \kappa^2)\,\Psi_c(\mathbf{r}) \end{pmatrix} = -4\pi \mathscr{M}_h \begin{pmatrix} n_-(\mathbf{r}) - n_0 \\ n_+(\mathbf{r}) - n_0 \end{pmatrix}. \tag{11.10}$$

We refer to Eqs. 11.10 as Helmholtz equations (with complex wavenumber and a source term). When

expressed in terms of the potentials Ψ_a and Ψ_c, the energy associated with hydration-mediated interactions becomes

$$\frac{U_{hyd}}{k_B T} = \frac{1}{8\pi} \int d^3\mathbf{r} \left[\begin{pmatrix} \nabla\Psi_a \\ \nabla\Psi_c \end{pmatrix}^T \mathscr{A}_h^{-1} \begin{pmatrix} \nabla\Psi_a \\ \nabla\Psi_c \end{pmatrix} + \kappa^2 \begin{pmatrix} \Psi_a \\ \Psi_c \end{pmatrix}^T \mathscr{A}_h^{-1} \begin{pmatrix} \Psi_a \\ \Psi_c \end{pmatrix} \right], \tag{11.11}$$

where the integration runs over all space and where $\mathscr{A}_h^{-1}$ is the inverse of $\mathscr{A}_h$.

Consider finally the mixing entropy contribution F_{mix} in Eq. 11.1. We express F_{mix} as the sum of an ideal mixing contribution of the mobile anions and cations and a non-ideal contribution that depends only on the total concentration $n_- + n_+$ but is otherwise general

$$\begin{aligned} \frac{F_{mix}}{k_B T} &= \int_V d^3\mathbf{r} \left[n_- \ln\left(\frac{n_-}{n_0}\right) - n_- + n_+ \ln\left(\frac{n_+}{n_0}\right) - n_+ \right. \\ &+ \left. g(n_- + n_+) - (n_- + n_+) g'(2n_0) \right]. \end{aligned} \tag{11.12}$$

The function $g(n)$ appears in the thermal equation of state $pV/(Nk_BT) = 1 - (V/N)g(N/V) + g'(N/V)$ of a gas that exerts a pressure p at fixed particle number N, volume V, and temperature T. The choice $g(n) = 0$ leads to an ideal gas. Note that a prime denotes the first derivative; for example $g'(n_0) = [dg(n)/dn]_{n=n_0}$. The function $g(n)$ can be used to account for finite ion sizes. We consider two different choices, $g = g^{CS}(n)$ and $g = g^{LG}(n)$. The first one,

$$g^{CS}(n) = \frac{g_0^{CS} n^2 (4 - 3 g_0^{CS} n)}{(1 - g_0^{CS} n)^2}, \tag{11.13}$$

employs the Carnahan-Starling (CS) equation of state [81, 82, 90], which treats all mobile ions as identical spherical particles of radius R and corresponding volume $g_0^{CS} = 4\pi R^3/3$. The second one,

$$g^{LG}(n) = \frac{g_0^{LG} n + (1 - g_0^{LG} n) \ln(1 - g_0^{LG} n)}{g_0^{LG} n}, \tag{11.14}$$

has been introduced by Bikerman and others [79, 382]; it embodies a lattice gas model in which each cell occupies a volume $g_0^{LG} = (2R)^3$ that hosts no more than one single ion of spatial extension $2R$.

With all three contributions to the free energy in Eq. 11.1 being specified (see Eqs. 11.6, 11.11, and 11.12), we can carry out the first variation $\delta F_{tot}[\Psi(n_-, n_+), \Psi_a(n_-, n_+), \Psi_c(n_-, n_+), n_-, n_+]$, subject to the

potentials Ψ, Ψ_a, Ψ_c being related to the ion concentrations through Eqs. 11.5 and 11.10. This results in

$$\begin{aligned}\frac{\delta F_{tot}}{k_B T} &= \int_V d^3\mathbf{r}\Bigg\{\delta n_-\left[-\Psi+\Psi_a+\ln\frac{n_-}{n_0}+g'(n_-+n_+)-g'(2n_0)\right]\\ &+ \delta n_+\left[\Psi+\Psi_c+\ln\frac{n_+}{n_0}+g'(n_-+n_+)-g'(2n_0)\right]\Bigg\}. \end{aligned} \tag{11.15}$$

Thermal equilibrium demands $\delta F_{tot}=0$, which can only be fulfilled if each of the two expressions enclosed by square brackets in Eq. 11.15 vanishes identically,

$$\begin{aligned}-\Psi+\Psi_a+\ln\frac{n_-}{n_0}+g'(n_-+n_+)-g'(2n_0)=0,\\ \Psi+\Psi_c+\ln\frac{n_+}{n_0}+g'(n_-+n_+)-g'(2n_0)=0.\end{aligned} \tag{11.16}$$

These two, generally transcendental, equations define the two relations $n_-=n_-[\Psi(\mathbf{r}),\Psi_a(\mathbf{r}),\Psi_c(\mathbf{r})]$ and $n_+=n_+[\Psi(\mathbf{r}),\Psi_a(\mathbf{r}),\Psi_c(\mathbf{r})]$ which upon insertion into the Poisson and Helmholtz equations, Eqs. 11.5 and 11.10, yield a system of three differential equations that define the mean-field potentials $\Psi(\mathbf{r})$, $\Psi_a(\mathbf{r})$, and $\Psi_c(\mathbf{r})$.

Previous models that include hydration-mediated interactions [78] have focused on an ideal mixing free energy, F_{mix}, which results from setting $g(n)=0$ in Eq. 11.12. This implies the Boltzmann distributions $n_-(\mathbf{r})=n_0e^{\Psi(\mathbf{r})-\Psi_a(\mathbf{r})}$ and $n_+(\mathbf{r})=n_0e^{-\Psi(\mathbf{r})-\Psi_c(\mathbf{r})}$. We refer to this specific case as the Poisson-Helmholtz-Boltzmann (PHB) approach [31]. The corresponding PHB equations result from inserting the Boltzmann distributions into the Poisson and Helmholtz equations.

Because for our geometry (see Fig. 11.1) all system properties depend only on the x-coordinate, we replace the argument $\mathbf{r}$ by x. That is, $\Psi_{e/a/c}(\mathbf{r})\to\Psi_{e/a/c}(x)$, and $n_\pm(\mathbf{r})\to n_\pm(x)$. Eqs. 11.16 then define the relations $n_-=n_-[\Psi(x),\Psi_a(x),\Psi_c(x)]$ and $n_+=n_+[\Psi(x),\Psi_a(x),\Psi_c(x)]$ that enter the Poisson and Helmholtz equations

$$\begin{aligned}\Psi''(x) &= -4\pi l_B(n_+-n_-),\\ \begin{pmatrix}\Psi_a''(x)-\kappa^2\Psi_a(x)\\ \Psi_c''(x)-\kappa^2\Psi_c(x)\end{pmatrix} &= -4\pi\mathscr{M}_h\begin{pmatrix}n_--n_0\\ n_+-n_0\end{pmatrix}.\end{aligned} \tag{11.17}$$

where a prime denotes the derivative with respect to x. These three second-order differential equations

must be solved subject to appropriate boundary conditions, which follow from applying the Poisson and Helmholtz equations to an infinitely small region in the vicinity of $x = 0$. The boundary conditions for solving Poisson's equation are $\Psi'(x)|_{x=0} = -4\pi l_B \sigma_e / e$ and $\Psi'(x)|_{x\to\infty} = 0$, and those for solving the Helmholtz equations are

$$-\kappa \begin{pmatrix} \Psi_a(0) \\ \Psi_c(0) \end{pmatrix} + \begin{pmatrix} \Psi_a'(x) \\ \Psi_c'(x) \end{pmatrix}_{x=0} = -4\pi \mathscr{M}_h \begin{pmatrix} \sigma_- \\ \sigma_+ \end{pmatrix} \tag{11.18}$$

and $\Psi_a'(x)|_{x\to\infty} = \Psi_c'(x)|_{x\to\infty} = 0$. The quantities σ_+ and σ_- represent the surface densities of the sources responsible for the hydration-mediated interaction with mobile cations and anions, respectively. In our present work we identify the sum $\sigma_- + \sigma_+$ with the density of ordered water molecules in immediate contact to the electrode. Because the hydration-mediated ion-surface interaction is of non-electrostatic origin, it may be viewed as one contribution (among others, such as dispersion forces) to specific ion adsorption. We note the presence of the first term on the left-hand side of Eq. 11.18. It originates in the absence of mobile ions for $x < 0$, which implies the exponential functions $\Psi_a(x) = \Psi_a(0)e^{\kappa x}$ and $\Psi_c(x) = \Psi_c(0)e^{\kappa x}$ in this region.

Once the potentials $\Psi(x)$, $\Psi_a(x)$, and $\Psi_c(x)$ are known, we can compute the relation between the surface charge density σ_e and the surface potential $\Phi(0) = k_B T \Psi(0)/e$, and from that, the differential capacitance

$$C^{diff} \equiv \frac{d\sigma_e}{d\Phi(0)}. \tag{11.19}$$

Recall that studying the influence of hydration-mediated interactions on C^{diff} is one of the main objectives of the present work. Below we discuss C^{diff} based on seven different mean-field models that emerge as special cases from the formalism presented so far. Based on the identification P-Poisson, B-Boltzmann, H-Helmholtz, CS-Carnahan-Starling, and LG-lattice gas, we refer to these models as: classical PB, PB-Stern, PCS-Stern, PLG-Stern, PHB, PHCS, and PHLG. The first four models all ignore the presence of hydration-mediated interactions. The most simple case, the *classical PB model*, emerges upon assuming $g(n) = 0$ in Eq. 11.12. The ensuing differential capacitance is

$$C_{PB}^{diff} = \frac{\varepsilon_W \varepsilon_0}{l_D} \sqrt{1 + p_0^2}, \tag{11.20}$$

where we have introduced the definition $p_0 = 2\pi l_B l_D \sigma_e / e$. Here, $l_D = (8\pi l_B n_0)^{-1/2}$ is the Debye screening length of the electrolyte. Adding a Stern layer (that is, a planar capacitor of capacitance $C_{Stern} = \varepsilon_W \varepsilon_0 / d_{Stern}$,

where the Stern layer thickness $d_{Stern} = R$ equals the ion radius R) to the classical PB model produces a differential capacitance $C_{PB}^{diff} C_{Stern}/(C_{PB}^{diff} + C_{Stern})$. We refer to this as the *PB-Stern model*. Adding a Stern layer to the Carnahan-Starling model (that is, $g(n) = g^{CS}(n)$ in Eq. 11.12) yields a differential capacitance $C_{CS}^{diff} C_{Stern}/(C_{CS}^{diff} + C_{Stern})$. We refer to this as the *PCS-Stern model*. Note that no closed-form expression for C_{CS}^{diff} is available. Adding a Stern layer to the lattice gas model (that is, $g(n) = g^{LG}(n)$ in Eq. 11.12) yields a differential capacitance $C_{LG}^{diff} C_{Stern}/(C_{LG}^{diff} + C_{Stern})$. We refer to this as the *PLG-Stern model*. Here, a closed-form expression for the differential capacitance in the absence of a Stern layer is available [382, 431],

$$C_{LG}^{diff} = \frac{\varepsilon_W \varepsilon_0}{l_D} \frac{\sqrt{\left(e^{2g_0^{LG} n_0 p_0^2} - 1\right)\left(e^{2g_0^{LG} n_0 p_0^2} - 1 + 2g_0^{LG} n_0\right)}}{2g_0^{LG} n_0 p_0 \, e^{2g_0^{LG} n_0 p_0^2}}, \tag{11.21}$$

where we recall $g_0^{LG} = (2R)^3$ and $p_0 = 2\pi l_B l_D \sigma_e / e$. The final three models all include the presence of hydration-mediated interactions but they differ in the expressions for F_{mix}. Using $g(n) = 0$ (that is, ideal mixing for F_{mix}) gives rise to the *PHB model*. Similarly, the choices $g(n) = g^{CS}(n)$ and $g(n) = g^{LG}(n)$ are referred to as the *PHCS* and *PHLG models*, respectively. Note that the inclusion of hydration-mediated interactions removes the need to explicitly add a Stern layer [8].

11.2.2. Monte Carlo Simulations

We have also carried out Metropolis Monte Carlo simulations in the canonical ensemble for a 1 : 1 electrolyte of bulk concentration n_0 confined between two perfectly smooth and impenetrable walls placed at $x = 0$ and $x = H$. In order to describe the same system as in our mean-field approach, the surface located at $x = 0$ carries uniform surface densities of electric charges, σ_e, and of sources for the hydration-mediated interaction, σ_+ and σ_-. All simulations were performed in a rectangular simulation cell of dimensions $H \times L \times L$, with $H = 30\,\text{nm}$ and $L = 10\,\text{nm}$. Periodic boundary conditions are applied in the L directions, and overall electroneutrality is ensured by the addition of neutralizing counterions. The electrolyte solution is modeled within the framework of the primitive model [449], where all ions are treated as charged hard spheres of radius R immersed in a continuum medium of uniform dielectric constant ε_W. Hence, the electrostatic interaction energy between two distinct ions i and j is given by

$$\frac{U_{el}(r_{ij})}{k_B T} = z_i z_j \frac{l_B}{r_{ij}} \tag{11.22}$$

if $r_{ij} \geq 2R$ and $U_{el}(r_{ij}) \to \infty$ otherwise. Here, z_i and z_j are the respective valencies and r_{ij} is the nearest-image distance between ions i and j. The electrostatic interaction energy of a given ion i at distance x_i away from the charged surface is

$$\frac{U_{el}(x_i)}{k_B T} = z_i l_B \sigma_e L \left[2 \ln \left(\frac{d_i + L}{d_i - L} \right) - \frac{4x_i}{L} \arctan \left(\frac{L^2}{2x_i d_i} \right) \right] \tag{11.23}$$

if $x_i \geq R$ and $U_{el}(x_i) \to \infty$ for $x_i < R$. In Eq. 11.23 we have defined $d_i \equiv \sqrt{2L^2 + 4x_i^2}$.

Due to the long-range nature of the Coulomb potential, the total electrostatic energy of our system is not only given by the sum of $U_{el}(r_{ij})$ in Eq. 11.22 over interactions of ions in the central cell with each other, but also with ions in the image cells. The same argument applies to the interaction of an ion with the fixed charges on the surface; see Eq. 11.23. In order to include these contributions, we used the so-called External Potential Method (EPM) developed by Torrie and Vallue [440]. According to this method, each ion in the central cell interacts with the image cells by means of the usual minimum image convention and with an external electrostatic potential given by the average ionic distributions in the image cells, including the charges located at the surface (we assume that the ionic distributions in the image cells are identical to those evaluated in the central cell) [440, 450, 438, 443].

To incorporate hydration-mediated interactions into our simulations, we added the Yukawa-like interaction energies $U_{hyd}(r_{ij})/k_B T = a e^{-\kappa(r_{ij}-a)}/r_{ij}$ for an anion-anion pair, $U_{hyd}(r_{ij})/k_B T = b e^{-\kappa(r_{ij}-b)}/r_{ij}$ for an anion-cation pair, and $U_{hyd}(r_{ij})/k_B T = c e^{-\kappa(r_{ij}-c)}/r_{ij}$ for a cation-cation pair. Similarly, for an anion interacting with the charged surface at distance x_i away, we added the hydration-mediated interaction energy

$$\begin{aligned} \frac{U_{hyd}(x_i)}{k_B T} &= 2\pi \left(a\sigma_- e^{\kappa a} + b\sigma_+ e^{\kappa b} \right) \int_0^\infty dr\, r \frac{e^{-\kappa\sqrt{r^2 + x_i^2}}}{\sqrt{r^2 + x_i^2}} \\ &= \frac{2\pi}{\kappa} \left(a\sigma_- e^{\kappa a} + b\sigma_+ e^{\kappa b} \right) e^{-\kappa x_i}. \end{aligned} \tag{11.24}$$

The expression for a cation that interacts with the surface is analogous, $U_{hyd}(x_i)/k_B T = 2\pi(b\sigma_- e^{\kappa b} + c\sigma_+ e^{\kappa c})\, e^{-\kappa x_i}/\kappa$. We point out that the total interaction potentials used in the Monte Carlo simulations between anion-anion, anion-cation, and cation-cation pairs are identical to the respective interactions U_{aa}, U_{ac}, and U_{cc} as introduced in Fig. 11.1, supplemented by an additional excluded volume repulsion.

For each value of σ_e, our simulations yield the ionic distributions, $n_-(x)$ and $n_+(x)$. We used

the corresponding charge density $e[-n_-(x)+n_+(x)]$ to numerically solve the Poisson equation and thus to obtain the electrostatic potential $\Psi(x)$. In order to compute the differential capacitance (C^{diff} as defined in Eq. 12.7), we first created a set of discrete points representing the surface charge density, σ_e, and the corresponding electrostatic surface potential, $\Psi(0)$ (see inset of Fig. 11.2). Then, the values of C^{diff} are determined using the algorithm developed by Lamperski and Zydor [443]. In Fig. 11.2, the results obtained from this algorithm and those predicted by obtaining the derivative simply through the slope of two neighboring data points (i.e., the two-point derivative) are shown as black bullets and blue-colored bar chart, respectively. We note that the Lamperski-Zydor algorithm is able to smoothen fluctuations resulting from the simulations and provides a reliable continuous derivative.

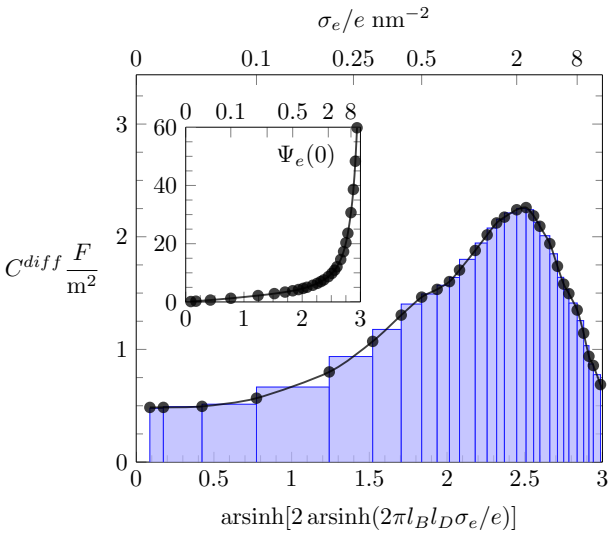

Figure 11.2. Monte Carlo simulation results for the differential capacitance $C^{diff} = d\sigma_e/d\Phi(0)$ as function of the surface charge density σ_e, obtained by two different methods: the Lamperski-Zydor algorithm (black bullets) and the two-point derivative (blue-colored bar-chart). The inset shows the variation of the dimensionless electrostatic surface potential, $\Psi(0) = e\Phi(0)/k_BT$, as function of σ_e. (Abscissa labels in the inset and main figure are identical.) The blue-colored bar-chart illustrates the intervals used for the two-point derivative. The displayed example is based on an ion radius of $R = 0.2$ nm and the absence of hydration interactions ($a = b = c = 0$).

11.2.3. Parameter Selection

The present work focuses on hydration interactions that are symmetric. That is, the distance at which the hydration interaction strength equals k_BT is the same for anion-anion, anion-cation, and anion-cation pairs, implying $a = b = c$ in Eq. 11.8. We also assume the ion-surface hydration interactions do not distinguish between anions and cations; this entails $\sigma_+ = \sigma_-$. The total source density $\sigma_- + \sigma_+ = 5.0/\mathrm{nm}^2$ reflects the area density of water molecules that are bound to a flat surface [8]. Throughout this work (with the exception of Fig. **??**) we consider a 0.1 M salt concentration; this corresponds to a bulk concentration of $n_0 = 0.057/\mathrm{nm}^3$ or, equivalently, to a Debye screening length of $l_D = 1.0\,\mathrm{nm}$. As already pointed out above, we fix the Bjerrum length $l_B = 0.7\,\mathrm{nm}$ and the characteristic decay length of the hydration potential $\kappa^{-1} = 0.3\mathrm{nm}$.

11.3. Results and Discussion

In the following, we present and discuss Monte Carlo simulation and mean-field results for the differential capacitance C^{diff} as function of the surface charge density σ_e, first in the absence and then in the presence of hydration interactions.

11.3.1. Absence of Hydration Interactions

We first investigate the joint presence of electrostatic and excluded volume interactions, yet in the absence of hydration interactions. Fig. 11.3 shows C^{diff} as function of the surface charge density σ_e for a fixed ion radius $R = 0.2\,\mathrm{nm}$. Monte Carlo simulation results are displayed by bullets in Fig. 11.3. We observe a characteristic camel-like shape, the origin of which has been discussed intensively in the past [427, 429, 428, 430, 431]. The initial growth of $C^{diff}(|\sigma_e|)$ as function of increasing magnitude of σ_e is captured by the classical PB model (see Eq. 11.20), which is shown by the dotted line in Fig. 11.3. Note that for $\sigma_e = 0$, Eq. 11.20 predicts $C^{diff} = \varepsilon_W\varepsilon_0/l_D = 0.71\,\mathrm{F/m}^2$. After passing through a maximum, $C^{diff}(|\sigma_e|)$ decreases roughly according to $C^{diff} \sim 1/|\sigma_e|$. The decrease results from packing of the counterions due to their finite size. We capture the $1/\sigma_e$-dependence by a simple model in which the counterions are forced to adopt a uniform density $1/(2R)^3$, leading for a surface with charge density σ_e to a counterion layer thickness

$d = (2R)^3\sigma_e/e$. This implies a differential capacitance $C^{diff} = 2\varepsilon_0\varepsilon_W/d = 2\varepsilon_0\varepsilon_W/[(2R)^3(\sigma_e/e)]$, which is shown in Fig. 11.3 by the gray solid lines in the large $|\sigma_e|$-region. The formation of counterion layers for large $|\sigma_e|$ is also demonstrated in the inset of Fig. 11.3, which displays Monte Carlo simulation results of $n_-(x)$ for the three specific values: $\sigma_e = 1.6\,e/\mathrm{nm}^2$ (blue curve), $\sigma_e = 3.2\,e/\mathrm{nm}^2$ (green), and $\sigma_e = 6.4\,e/\mathrm{nm}^2$ (red). A second layer of counterions in the latter case is visible at $x = 3R = 0.6\,\mathrm{nm}$.

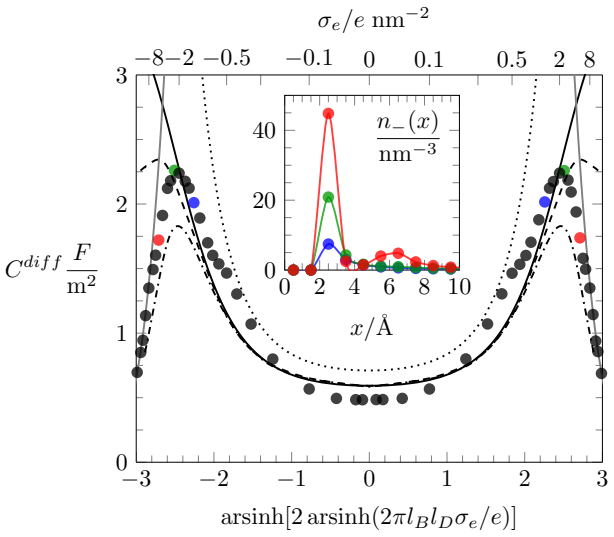

Figure 11.3. Differential capacitance C^{diff} as function of the surface charge density σ_e. Filled circles are results obtained by Monte Carlo simulations. The dotted, solid, dashed, and dash-dotted black lines correspond to the PB, PB-Stern, PCS-Stern, and PLG-Stern models, respectively. The thickness of the Stern layer, $d_{Stern} = R$, is equal to the ion radius $R = 0.2\,\mathrm{nm}$. The solid gray line is the result predicted by the approximation of dense ion packing, $C^{diff} = 2\varepsilon_0\varepsilon_W/[(2R)^3(\sigma_e/e)]$. The inset shows Monte Carlo simulation results of the counterion concentration profiles $n_-(x)$ for various charge densities: $\sigma_e = 6.4\,e/\mathrm{nm}^2$ (red), $\sigma_e = 3.2\,e/\mathrm{nm}^2$ (green), and $\sigma_e = 1.6\,e/\mathrm{nm}^2$ (blue). The same color scheme is used to mark the corresponding values of C^{diff} in the main plot.

One striking feature of Fig. 11.3 is the inability of the classical PB model (dotted line, calculated according to Eq. 11.20) to reproduce the simulation results of C^{diff} in the limit of small $|\sigma_e|$. Even upon the addition of a Stern layer of thickness $d_{Stern} = R$ (the PB-Stern model – indicated by the solid line in Fig. 11.3), the discrepancy between simulation and theoretical model persists. Combining the Stern layer with a modified Poisson-Boltzmann model – namely the PCS-Stern model (the dashed line in Fig. 11.3) or the PLG-Stern model (the dash-dotted line in Fig. 11.3) – does produce a maximum in C^{diff} for large $|\sigma_e|$ but does not alter the prediction for C^{diff} at small $|\sigma_e|$. The inability of the PB-Stern, PCS-Stern, and PLG-Stern models to reproduce C^{diff} for small $|\sigma_e|$ originates in the *ad hoc* assumption of adding a

Stern layer whose thickness does not adjust as function of σ_e. We demonstrate below that our approach of incorporating hydration-mediated interactions in a consistent manner into the ion-ion interaction potential removes the need to invoke a Stern layer and leads to excellent agreement of mean-field predictions with the Monte Carlo simulation results. In particular, unlike for the exclusive presence of Coulomb and excluded volume interactions, where density functional theory is an established method to predict the differential capacitance [448, 451], the additional presence of a soft hydration potential empowers mean-field models to successfully capture the behavior of C^{diff}.

While Fig. 11.3 applies to a fixed ion radius of $R = 0.2\,\mathrm{nm}$, in Fig. 11.4 we show $C^{diff}(\sigma_e)$ for the three different choices $R = 0.2\,\mathrm{nm}$ (black triangles), $R = 0.4\,\mathrm{nm}$ (red diamonds), and $R = 0.6\,\mathrm{nm}$ (green bullets), in each case together with a color-matching solid and dashed line that correspond to the PCS-Stern and PLG-Stern approaches, respectively. We first note that our simulations predict the maximum of $C^{diff}(|\sigma_e|)$ to move from a nonvanishing value of σ_e at low volume density density of the ions (small R) to $\sigma_e = 0$ for high volume density (large R). This transition from a "camel"-shape to a "bell"-shape [452] is consistent with predictions from theoretical modeling such as density functional theory [453, 452], modified Grahame equations [431], and Monte Carlo simulations performed by Lamperski and coworkers [454, 451, 448, 455].

For $|\sigma_e| \ll 1$ the two mean-field predictions coincide, and they are identical to the PB-Stern model. Due to the varying thickness $d_{Stern} = R$ of the Stern layer, the differential capacitance of the PB-Stern model varies with R according to $C^{diff} = \varepsilon_W \varepsilon_0/(R + l_D)$ for $\sigma_e = 0$. However, our simulation results suggest $C^{diff}(\sigma_e = 0) = 0.5\,\mathrm{F/m^2}$, virtually independent of R. Here again, as in Fig. 11.2, the Stern layer approach is not capable of reproducing the simulation results in the limit of small $|\sigma_e|$. To rationalize for why $C^{diff}(\sigma_e = 0) = 0.5\,\mathrm{F/m^2}$ remains independent of R we refer to our discussion in Fig. 11.7 below. From there it will become apparent that the predicted decrease of C^{diff} for growing R according to the Stern model is counteracted (and effectively compensated) by a compression of the EDL due to a larger osmotic pressure exerted by the larger ions. Only when hydration interactions are accounted for does mean-field modelling appear to capture this mechanism.

In the other limit, that of large $|\sigma_e|$, we observe smaller C^{diff} for larger ion radius R. In addition, while the PCS-Stern model qualitatively but not quantitatively agrees with the predictions of our simulations, the PLG-Stern model exhibits remarkably good agreement, and even better so with growing of ion radius R.

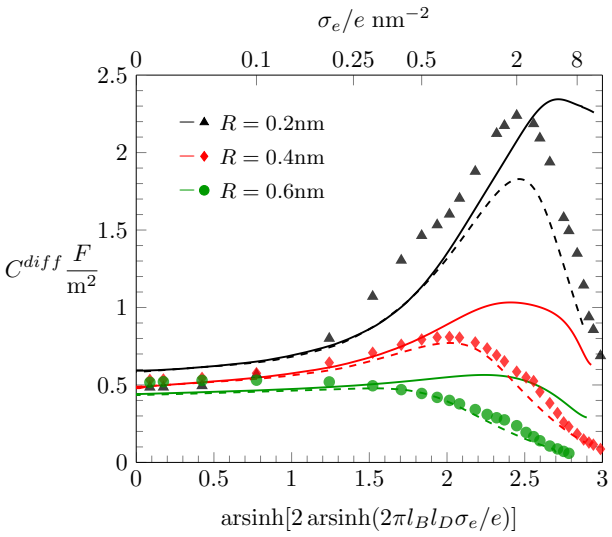

Figure 11.4. Differential capacitance C^{diff} as function of the surface charge density σ_e for various ion radii R when only electrostatics and finite ion size effects (but no hydration-mediated interaction, $a = b = c = 0$) are taken into account. Symbols mark results obtained from Monte Carlo simulations. Solid and dashed lines correspond to the PCS-Stern and PLG-Stern models, respectively. The Stern layer thickness is $d_{Stern} = R$. Different colors correspond to $R = 0.2\,\text{nm}$ (black), $R = 0.4\,\text{nm}$ (red), and $R = 0.6\,\text{nm}$ (green).

11.3.2. Presence of Hydration Interactions

In the following, we discuss the influence of including hydration-mediated interactions on the differential capacitance C^{diff}. Recall that we model hydration interactions as a soft, Yukawa-like, pair potential that is added to the Coulomb potential between any two mobile ions and between mobile ions and the surface. Fig. 11.5 displays C^{diff} as function of σ_e for fixed $R = 0.2\,\text{nm}$. The three differently colored sets of data points represent predictions from Monte Carlo simulations: $a = b = c = 0.2\,\text{nm}$ (black bullets), $a = b = c = 0.4\,\text{nm}$ (red diamonds), and $a = b = c = 0.6\,\text{nm}$ (green triangles). Clearly, growing hydration repulsion leads to larger ion-surface and ion-ion distances; this decreases C^{diff} irrespective of σ_e. In the limit of large $|\sigma_e|$, all simulation results approach the limiting behavior $C^{diff} \approx 2\varepsilon_0\varepsilon_W/[(2R)^3(\sigma_e/e)]$ (marked by the gray curve in Fig. 11.5), where hydration interactions become irrelevant because ions are densely packed. Note that the soft nature of the hydration interactions shifts the maximum of $C^{diff}(\sigma_e)$ to larger $|\sigma_e|$.

Fig. 11.5 also shows results derived from the PHB (color-matching solid lines), PHCS (dashed lines) and PHLG models (dash-dotted lines). For $|\sigma_e| \ll 1$, the different mean-field models (PHB, PHCS,

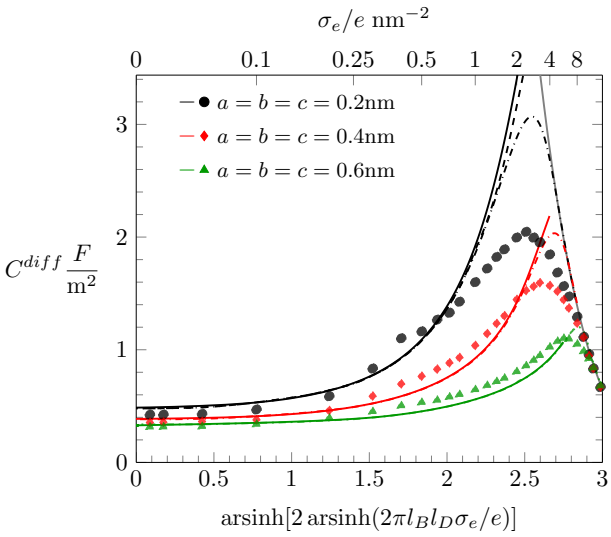

Figure 11.5. Differential capacitance C^{diff} as function of the surface charge density σ_e for $R = 0.2\,\mathrm{nm}$ and different values of $a = b = c = 0.2\,\mathrm{nm}$ (black bullets), $a = b = c = 0.4\,\mathrm{nm}$ (red diamonds), and $a = b = c = 0.6\,\mathrm{nm}$ (green triangles). Monte Carlo simulation results are marked by the different symbols as indicated. The color-matching solid, and dash-dotted lines correspond to the PHB and PHLG models, respectively. For $R = 0.2\,\mathrm{nm}$ we have also added a broken line (in black), which displays the prediction of the PHCS model. The solid gray line marks the limiting behavior $C^{diff} = 2\varepsilon_0\varepsilon_W/[(2R)^3(\sigma_e/e)]$.

and PHLG) coincide with each other and agree well with the Monte Carlo simulation results. We emphasize that no Stern layer is added. Instead, an ion depletion zone emerges naturally from the hydration-mediated repulsion between the ions and the surface [8]. The effective thickness of the ion depletion zone adjusts so as to minimize the total free energy. As a result, the PHB model reproduces the trends of the simulation results for $|\sigma_e| \ll 1$ quite accurately. For large $|\sigma_e|$, ion-ion correlations and ion packing effects become important. They can be described approximately by the PHLG model (the dash-dotted lines in Fig. 11.5), which predicts the function $C^{diff}(|\sigma_e|)$ to pass through a maximum. With growing $a = b = c$ the maximum shifts to larger surface charge density $|\sigma_e|$. In other words, for stronger hydration-mediated interactions, C^{diff} continues to grow up to higher $|\sigma_e|$. This indicates that the soft, hydration-mediated interactions render the diffuse counterion cloud more compressible, thus allowing its effective thickness to decrease as function of $|\sigma_e|$. However, for sufficiently large σ_e, C^{diff} becomes independent of our choices for $a = b = c$, thus evidencing the saturation of counterion packing near the surface. Fig. 11.5 also shows the prediction of the PHB model (solid lines) and for $R = 0.2\,\mathrm{nm}$ the prediction of the PHCS model (black dashed line).

In Fig. 11.6 we study how changing the ion radius R affects C^{diff} at fixed $a = b = c = 0.6\,\mathrm{nm}$. Here again, Monte Carlo simulation results are marked by symbols as indicated in the figure legend. The color-

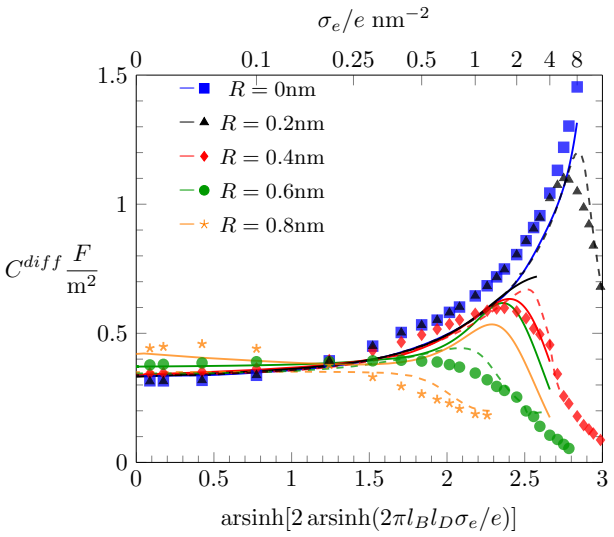

Figure 11.6. Differential capacitance C^{diff} as function of the surface charge density σ_e when hydration-mediated interactions are present with $a = b = c = 0.6\,\mathrm{nm}$. Different colors correspond to different ion size R according to $R \to 0\,\mathrm{nm}$ (blue), $R = 0.2\,\mathrm{nm}$ (black), $R = 0.4\,\mathrm{nm}$ (red), $R = 0.6\,\mathrm{nm}$ (green), and $R = 0.8\,\mathrm{nm}$ (orange). Monte Carlo simulation results are marked by the different symbols as indicated. The color-matching solid, and dashed lines correspond to the PHCS and PHLG models, respectively.

matching solid and dashed lines display C^{diff} according to the PHCS and PHLG models, respectively. It is notable that in the limit of small $|\sigma_e|$ our Monte Carlo simulations predict C^{diff} to *increase* with growing ion radius R. Based on the simple Stern layer model, one would expect $C^{diff} \sim 1/R$, which is in contrast of what is observed in the simulations. The PHLG model (dashed lines) predicts virtually no dependence of C^{diff} on R for small $|\sigma_e|$, again in contrast to the simulation results. However, the PHCS model correctly captures the increase of C^{diff} as function of R. The mechanism that explains why C^{diff} increases with R for small $|\sigma_e|$ originates in the increasing osmotic pressure of the ions in the bulk. The larger bulk pressure due to larger ion radius R tends to compactify the EDL and thus increases C^{diff}. This assertion is supported by the upper diagram of Fig. 11.7, which shows the local anion concentration distribution $n_-(x)$ for fixed $\sigma_e = 0$. The black symbols correspond to $R = 0.2\,\mathrm{nm}$ with $a = b = c = 0$ (filled circles) and $a = b = c = 0.6\,\mathrm{nm}$ (open circles). The green symbols correspond to $R = 0.6\,\mathrm{nm}$ with $a = b = c = 0$ (filled circles) and $a = b = c = 0.6\,\mathrm{nm}$ (open circles). Note that anion and cation profiles are identical for $\sigma_e = 0$; no excess charge is present in this case at any point in the electrolyte. Clearly, the larger ions tend to accumulate more near the wall. In the absence of hydration-mediated interactions, the enhanced concentration of the larger ions compensates with the larger distance of the ion center to the wall so that C^{diff} remains virtually unchanged (see Fig. 11.4). In the presence of soft, hydration-mediated interactions, the increase of the

concentration $n_-(x)$ near the surface for larger R causes C^{diff} to increase.

We address the question why for small and fixed $|\sigma_e|$ the PHCS model, but not the PHLG model, captures the increase of C^{diff} as function of R. The PHCS model is based on the Carnahan-Starling equation of state for a bulk fluid of spherical particles of radius R; it describes the bulk osmotic pressure of the finite-sized ions quite accurately. This is in contrast to the more restrictive PHLG model, which confines the number of states by introducing a lattice model where each cell can host exactly one or no particle. This results in a larger osmotic pressure of the particles in the PHCS model as compared to the PHLG model. More specifically, expanding the Carnahan-Starling equation of state [82, 83, 90] $pV/(Nk_BT) = (1+\eta+\eta^2-\eta^3)/(1-\eta)^3$, with $\eta = (4/3)\pi R^3 N/V$, in powers of the particle density N/V up to second order yields

$$\frac{pV}{Nk_BT} = 1 + \frac{16\pi}{3}\frac{N}{V}R^3. \tag{11.25}$$

The same expansion for the lattice gas equation of state $pV/k_BT = -(V/v)\ln(1-Nv/V)$, with $v = (2R)^3$, leads to

$$\frac{pV}{Nk_BT} = 1 + 4\frac{N}{V}R^3. \tag{11.26}$$

Hence the osmotic pressure exerted by the ions in the bulk is greater by roughly a factor of 4 when the PHCS model is compared to the PHLG model. This provides a rationale for the PHCS model being preferable over the PHLG model when predicting C^{diff} in the limit of small surface charge density $|\sigma_e|$. Indeed, the black (in the limit $R \to 0$) and green (for $R = 0.6\,\text{nm}$) dashed lines in the upper diagram of Fig. 11.7, which both refer to the PHCS model, differ only slightly, but they qualitatively follow the trends of the Monte Carlo simulations (larger counterion concentration close to the surface for larger ion radius R).

We also discuss the behavior of $C^{diff}(\sigma_e)$ in Fig. 11.6 for large $|\sigma_e|$. In the limit $R \to 0$ both the Monte Carlo simulations (filled blue squares) and the PHB model (blue solid line) predict $C^{diff}(|\sigma_e|)$ to monotonically increase. This is reminiscent of the classical PB model (see Eq. 11.20). Indeed, as σ_e grows to large positive values, the anion-to-anion distances in the EDL decrease until they are small compared to $1/\kappa$, turning the Yukawa into a Coulomb interaction. The total anion-anion pair interaction is then $l_B/r + a/r$, which implies similarity of the simulation data and the PHB prediction to the classical PB model, yet with a rescaled Bjerrum length $l_B \to l_B + a$ for large σ_e. As R grows, the simulation data predict $C^{diff}(|\sigma_e|)$ to pass through a maximum, which is captured better by the PHLG model than by the PHCS model. For $R = 0.8\,\text{nm}$ (the orange star symbol in Fig. 11.6), $C^{diff}(|\sigma_e|)$ decreases monotonously, which the PHLG

model, but not the PHCS model, is able to reproduce. To understand the reason, we display in the middle and lower diagrams in Fig. 11.7 the local anion distribution $n_-(x)$ as predicted by Monte Carlo simulations (with $R = 0.2\,\text{nm}$ for the open black circles and $R = 0.6\,\text{nm}$ for the open green circles) and according to the PHLG model (dash-dotted lines in the middle diagram) and PHCS model (dashed lines in the lower diagram). The black and green colors refer to $R = 0.2\,\text{nm}$ and $R = 0.6\,\text{nm}$, respectively. In addition, all data in the middle and lower diagrams of Fig. 11.7 refer to $a = b = c = 0.6\,\text{nm}$ and to $\sigma_e = 1.0\,e/\text{nm}^2$. Regarding the Monte Carlo simulation data, we observe that the larger counterions are more condensed onto the surface and form a second layer near $x = 2\,\text{nm}$. The more pronounced condensation of the larger counterions results from the larger osmotic pressure of the ions in the bulk. Because at high ion concentrations in the EDL, ion-ion correlations become important, mean-field theory cannot be expected to even qualitatively capture the structural details of the counterion distribution $n_-(x)$. This is indeed not the case in Fig. 11.7, neither for the PHLG (middle diagram) nor the PHCS (lower diagram) model. However, the broader and more smeared out distribution for $n_-(x)$ predicted by the PHLG model appears to better account for the formation of a second (and other subsequent) ionic layers, thus placing the prediction for C^{diff} closer to the Monte Carlo simulation data than the PHCS model is able to accomplish.

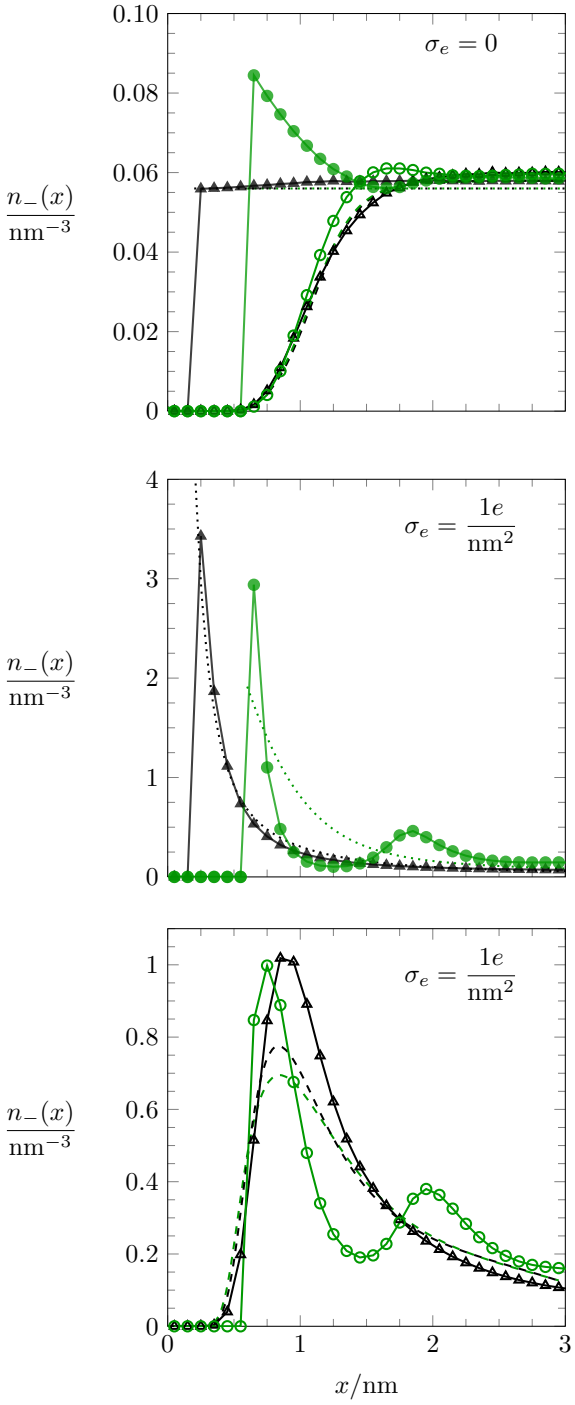

Figure 11.7. Counterion concentration profile $n_-(x)$ near the charged planar surface, located at $x = 0$, for $\sigma_e = 0$ (upper diagram) and $\sigma_e = 1.0\,e/\mathrm{nm}^2$ (middle and lower diagrams). Black and green circles/curves refer to $R = 0.2\,\mathrm{nm}$ and $R = 0.6\,\mathrm{nm}$, respectively. Monte Carlo simulation data are indicated by filled circles for $a = b = c = 0$ and by open circles for $a = b = c = 0.6\,\mathrm{nm}$. Note that the Monte Carlo simulation results in the middle and lower diagrams are identical. In the upper and lower diagrams, dashed lines refer to the PHCS model. In the middle diagram, dash-dotted lines correspond to the PHLG model. Dotted horizontal lines at $n = n_0 = 0.057/\mathrm{nm}^3$ in the upper diagram correspond to the PB-Stern model.

11.4. Conclusion

In this work we have expanded our theoretical approach of incorporating hydration-mediated interactions into the mean-field Poisson-Boltzmann formalism. We have not only incorporated distinct hydration-mediated interactions for each pair of interacting ions, i.e., anion-anion, anion-cation and cation-cation, but we have also taken into account the finite size of the ions by using two different mean-field approaches: the Carnahan-Starling equation of state and the lattice gas model.

We have studied the influence of hydration-mediated interactions on the differential capacitance using Monte Carlo simulations and compared them with our mean-field models. When hydration interactions are accounted for, a thin charge-depleted region that separates the surface from the diffuse part of the EDL emerges naturally [8]. The electric potential in this thin region drops linearly, as it does in a Stern layer. However, unlike the thickness of the classical Stern layer, the charge-depleted zone is able to adjust its spatial extension. As a result we find good agreement of our simulation results with the mean-field predictions, for small surface charge density if a non-ideal mixing entropy according to the Carnahan-Starling equation is employed and for large surface charge density on the basis of the lattice gas approach.

Thus far, we have applied our mean-field model to symmetric hydration-mediated interactions, where all ion pairs exhibit the same interactions irrespective of their chemical nature. We plan to also investigate asymmetric systems with three independent interaction parameters, a, b, and c. Note that, so far, no dielectric saturation effects are taken into account in our model; the assumption of a uniform dielectric background is, in fact, what enabled us to perform Monte Carlo simulations conveniently. Dielectric saturation effects further decrease the differential capacitance [448]. In the most simple case, for the PB-Stern model, the differential capacitance $C_{PB}^{diff} C_{Stern}/(C_{PB}^{diff} + C_{Stern})$ with $C_{Stern} = \varepsilon_{Stern}\varepsilon_0/d_{Stern}$ obviously decreases if the dielectric constant ε_{Stern} inside the Stern layer is reduced. In the future, the combined effects of hydration-mediated ion-ion interactions and concomitant changes in the local (or non-local) dielectric constant should also be addressed.

11.5. Acknowledgments

All simulations were performed by resources supplied by the Center of Scientific Computing (NCC/ GridUNESP) of the Sao Paulo State University (UNESP). Daniel L. Z. Caetano acknowl- edges the Sao

Paulo Research Foundation (FAPESP, Process Grant No. 2015/03549-9) for the financial support. Guilherme V. Bossa acknowledges a doctoral scholarship from CAPES Founda- tion/Brazil Ministry of Education (Grant No. 9466/13-4). Vini- cius M. de Oliveira was supported by the Conselho Nacional de Desenvolvimento Científico e Tecnológico (CNPq, Process Grant No. 141985/2013-5). Matthew A. Brown acknowledges the Swiss National Science Foundation for an International Short Visit travel grant (Grant No. 162320).

12. DIFFERENTIAL CAPACITANCE OF AN ELECTRIC DOUBLE LAYER WITH ASYMMETRIC SOLVENT-MEDIATED INTERACTIONS: MEAN-FIELD THEORY AND MONTE CARLO SIMULATIONS *

12.1. Introduction

The interaction of small mobile ions with electrodes and other macroions in an aqueous solution leads to the formation of an electric double layer (EDL), a diffuse cloud of counter- and co-ions that screen the surface charge of the macroion. The important role played by EDL in biology [456, 8, 457, 458], physico-chemical systems [459, 416, 460], and in technological applications [461, 462, 463, 464] continues to inspire the development of experimental methods and theoretical models. Clearly, the structure of the EDL is affected not only by bare electrostatic ion-ion and ion-macroion interactions, but also by structural features of the mobile ions, including their size, shape, polarizability, and the propensity to form hydration shells [64, 465, 66, 466, 68]. Although the study of these ion specific effects dates back to the pioneering works of Franz Hofmeister in the late 19th century [69], the influence of non-electrostatic interactions on EDL properties remains an area of active research. This concerns, for example, the questions how the electrostatic potential [467, 468, 469] and charge density [384, 385] on the surface of an electrode (or any type of macroion) is affected by hydration shells formed around the mobile ions in the EDL and how ion and surface hydration influence each other, especially how they modify the exponentially decaying force between two flat surfaces [65, 92, 93, 470].

The simultaneous presence of electrostatic and solvent-mediated interactions has been investigated in previous studies using theoretical models [446, 471, 472] and computer simulations [473, 474, 475,

*Reprinted from "D. L. Z. Caetano, G. V. V. Bossa, V. M. de Oliveira, M. Brown, S. J. de Carvalho, S. May, Differential capacitance of an electric double layer with asymmetric solvent-mediated interactions: Mean-field theory and Monte Carlo simulations, Phys. Chem. Chem. Phys. (19) (2017) 23971-23981.". Reproduced by permission of The Royal Society of Chemistry. Copyright 2016 The Royal Society of Chemistry. This paper can be accessed online at `http://pubs.rsc.org/-/content/articlelanding/2017/cp/c7cp04672c/unauth#!divAbstract` The material in this chapter was co-authored by Daniel L. Z. Caetano, Guilherme V. Bossa, Vinicius M. de Oliveira, Matthew A. Brown, Sidney J. de Carvalho, and Sylvio May. G. V. Bossa contributed to the project design and manuscript writing. G.V.B. was responsible for the mathematical development, numerical and analytical solution of the equations, mathematical processing of simulation data, figures preparation, and discussion of the results.

476, 477]. One specific theoretical approach is the incorporation of solvent-mediated interactions into the mean-field Poisson-Boltzmann framework. Classical Poisson-Boltzmann theory accounts exclusively for Coulomb interactions between any pair of mobile ions in a uniform dielectric background. Hydration effects result from the ordering of solvent molecules near the mobile ions and macroion surfaces. This ordering, which is of non-electrostatic origin and is thus not captured by the classical Poisson-Boltzmann approach, can be described by an additional non-electrostatic ion-ion interaction potential. Monte Carlo simulations suggest that this potential is short-ranged and exhibits damped oscillations [65, 67]. An approximate but nevertheless appealing representation of solvent-mediated interactions is the Yukawa potential. Although it ignores the presence of damped oscillations, the short-ranged nature of the interaction is described in a manner that is mathematically straightforward to be included into the Poisson-Boltzmann formalism. In addition, the Yukawa potential is consistent with the phenomenological hydration model suggested by Marčelja and Radić [353] and introduces the hydration-specificity of given ion-ion interactions through just one single parameter. It is hardly a surprise that variants of this idea have appeared frequently in the literature [361, 446, 73, 74, 222]. A systematic characterization of the corresponding mean-field formalism and a comparison with simulation results is, however, still missing.

The differential capacitance C^{diff} is an experimentally accessible quantity that reflects the properties of the EDL and has recently attracted considerable attention regarding new applications such as supercapacitors, which have applications, for example, in regenerative braking and as a source of backup power with long-term reliability [478]. Two of the experimentally observed features of C^{diff} have inspired a cascade of theoretical modeling efforts [428, 454, 454, 453]: the first is the camel-shape to bell-shape transition [479], where the minimum of the function $C^{diff}(\sigma_e)$ at small surface charge density σ_e switches to a maximum as a function of the salt concentration or ion size. The second is the asymmetry $C^{diff}(\sigma_e) \neq C^{diff}(-\sigma_e)$, which is a manifestation of how ion-specific interactions affect the structure of the EDL [480, 481]. The latter is the focus of the present work.

Most of the attempts to rationalize and model the asymmetry $C^{diff}(\sigma_e) \neq C^{diff}(-\sigma_e)$ have focused on excluded volume effects, where monovalent cations and anions of different steric sizes form EDLs with distinct properties. Specifically, there are multiple approaches to incorporate steric interactions of size-asymmetric electrolytes into extended versions of mean-field electrostatics based on a suitable equation of state for the uncharged system (often based on a lattice gas instead of an ideal gas). Examples include the addition of a volume exclusion term to the Boltzmann distribution [482], the adjustment of Stern layer thick-

ness to the ionic radius [483], the generalization of the lattice gas approach to size-asymmetric ionic mixtures by using a voltage-dependent packing parameter [406, 484], the introduction of sublattices [485, 486], and the usage of the Flory-Huggins equation of state [487], the Boublik-Mansoori-Carnahan-Starling-Leland equation of state [90, 487], and a van der Waals equation of state for a mixture of size-asymmetric hard spheres [88]. Other models to study the implications of ionic size asymmetry on C^{diff} employ density functional theory [488, 489, 452, 490] or self-consistent field theory [491]. Besides excluded volume interactions, there are additional physical mechanisms that can render C^{diff} asymmetric: one is the presence of different excess polarizabilities for mobile cations and anions [88] and another one results from solvent-mediated ion-ion interactions that are different for cation-cation and anion-anion pairs [222].

We have recently proposed [9] a mean-field formalism that incorporates both excluded volume interactions into the translational entropy of the mobile ions and a combination of Coulomb and Yukawa potentials [31, 78] to model the ion-ion pair interaction. Ion specificity in the model arises from assigning distinct cation-cation, anion-anion, and cation-anion interaction strengths to the Yukawa potential. Predictions of the model for the differential capacitance $C^{diff}(\sigma_e)$ as function of the surface charge density σ_e of a planar electrode were compared with Monte Carlo simulations. The additional soft Yukawa potential greatly improves the degree of agreement with Monte Carlo simulations and removes the need to add a Stern layer. Although a mean-field theory was developed in our previous work [9] for the most general case of an asymmetric electrolyte, only the symmetric case, $C^{diff}(\sigma_e) = C^{diff}(-\sigma_e)$ was analyzed so far. In the present work, we therefore focus on the case of asymmetric solvation-mediated interactions that lead to $C^{diff}(\sigma_e) \neq C^{diff}(-\sigma_e)$ even for a symmetric 1:1 electrolyte with spherical ions of the same steric size.

12.2. Theoretical Model

Consider a flat electrode that carries a fixed density σ_e of electric surface charges and is immersed in a symmetric $1:1$ electrolyte of cation and anion bulk concentrations n_0. We represent the electrode by an extended planar surface, located normal to the x-axis of a Cartesian coordinate system. The electrolyte extends from the electrode ($x = 0$) along the positive x-direction into the bulk and is modeled as an aqueous solvent with uniform dielectric constant $\varepsilon_w = 80$.

We assume all mobile ions in the electrolyte are spherical, with the same radius R, and hence volume $\nu = 4\pi R^3/3$ for each individual ion. Ions interact with each other through a composite pair potential: an

excluded volume potential, a Coulomb potential, and a Yukawa potential. Denote the pair potential between two anions as $U_{aa}(r)$, that between an anion and a cation as $U_{ac}(r)$, and that between two cations as $U_{cc}(r)$. All three potentials are infinitely large when the center-to-center distance r between two ions is smaller than $2R$. For $r > 2R$, we express the potentials as

$$\begin{aligned} \frac{U_{aa}(r)}{k_BT} &= \frac{l_B}{r} + \frac{a}{r} e^{\kappa(a-r)}, \\ \frac{U_{ac}(r)}{k_BT} &= -\frac{l_B}{r} + \frac{b}{r} e^{\kappa(b-r)}, \\ \frac{U_{cc}(r)}{k_BT} &= \frac{l_B}{r} + \frac{c}{r} e^{\kappa(c-r)}, \end{aligned} \tag{12.1}$$

where k_B denotes Boltzmann's constant and T the absolute temperature. The first contribution – the Coulomb interaction – involves the Bjerrum length in water, $l_B = e^2/(4\pi\varepsilon_0\varepsilon_w k_B T) = 0.7\,\text{nm}$, where e is the elementary charge and ε_0 the permittivity of free space. The plus and minus signs in front of each Coulomb term specify electrostatic ion-ion repulsion and attraction, respectively. The second contribution – the Yukawa interaction – is expressed in terms of the spatial decay length $1/\kappa \approx 0.3\,\text{nm}$ of the water ordering [492]. The three parameters a, b, and c characterize the strengths associated with the hydration interactions. For later use, we cast these parameters into a hydration interaction matrix

$$\mathscr{M}_h = \begin{pmatrix} ae^{\kappa a} & be^{\kappa b} \\ be^{\kappa b} & ce^{\kappa c} \end{pmatrix}. \tag{12.2}$$

The 1 : 1 electrolyte, which is symmetric with respect to the electrostatic and excluded volume interactions, becomes asymmetric with respect to hydration interactions when $a \neq c$ at any arbitrary b. Our preceding work [9] has presented a mean-field theory for the general case with arbitrary choices of a, b, c, but has then compared the prediction of the theory with Monte Carlo simulations only for the specific case $a = b = c$. Other earlier mean-field approaches [31, 78] have focused entirely on the case $\det(\mathscr{M}_h) = 0$, where the underlying theory simplifies significantly. The present work is the first one to systematically investigate electrolytes that acquire their asymmetry through an arbitrary set of parameters a, b, c, and to compare mean-field predictions with Monte Carlo simulations.

The presence of an electrolyte with asymmetric hydration interactions generally leads to $C^{diff}(\sigma_e) \neq C^{diff}(-\sigma_e)$. Asymmetry of $C^{diff}(\sigma_e)$ can also arise – even with $a = c$ – through different solvent-mediated

interactions of the mobile anions and cations with the electrode. This possibility is also covered by our two modeling approaches. In the following, we briefly recapitulate our mean-field model for an electrolyte with ion-ion interactions according to Eq. 12.1 and outline our Monte Carlo simulation method.

12.2.1. Mean-Field Model

To calculate the differential capacitance, we employ a mean-field model for a 1 : 1 electrolyte with ion-ion interactions according to Eq. 12.1. The underlying theoretical framework was developed in previous work [9] but has only been used so far to calculate C^{diff} for the specific case $a = b = c$. Briefly, the model introduces three different potentials, the commonly used dimensionless electrostatic potential $\Psi_e = e\Phi/k_BT$, where Φ is the regular electrostatic potential (measured in Volt), and two hydration potentials, Ψ_a and Ψ_c, that describe the presence of the solvent-mediated interaction. The two hydration potentials are defined at any given position $\mathbf{r}$ according to

$$\begin{pmatrix} \Psi_a(\mathbf{r}) \\ \Psi_c(\mathbf{r}) \end{pmatrix} = \int d^3\mathbf{r}' \, \frac{e^{-\kappa|\mathbf{r}-\mathbf{r}'|}}{|\mathbf{r}-\mathbf{r}'|} \, \mathscr{M}_h \begin{pmatrix} n_-(\mathbf{r}') - n_0 \\ n_+(\mathbf{r}') - n_0 \end{pmatrix}, \tag{12.3}$$

where n_- and n_+ denote the local anion and cation concentrations. The matrix $\mathscr{M}_h$ is specified in Eq. 12.2, and the integration in Eq. 12.3 runs over the entire electrolyte. For the present geometry of a single planar surface, the three potentials $\Psi_e = \Psi_e(x)$, $\Psi_a = \Psi_a(x)$ and $\Psi_c = \Psi_c(x)$ as well as the local concentrations $n_- = n_-(x)$ and $n_+ = n_+(x)$ are all functions of only their distance x from the surface. The local concentrations can be computed from the three potentials via

$$\begin{aligned} n_-(x) &= \frac{[\pi/(6\nu)]\, e^{\Psi_c(x)+\Psi_e(x)}}{e^{\Psi_c(x)+\Psi_e(x)} + e^{\Psi_a(x)-\Psi_e(x)} - \left(2 - \frac{\pi}{6\nu n_0}\right) e^{\Psi_a(x)+\Psi_c(x)}}, \\ n_+(x) &= \frac{[\pi/(6\nu)]\, e^{\Psi_a(x)-\Psi_e(x)}}{e^{\Psi_c(x)+\Psi_e(x)} + e^{\Psi_a(x)-\Psi_e(x)} - \left(2 - \frac{\pi}{6\nu n_0}\right) e^{\Psi_a(x)+\Psi_c(x)}}. \end{aligned} \tag{12.4}$$

The three potentials must be determined in the region $0 < x < \infty$ from the following set of three differential equations,

$$\Psi_e''(x) = -4\pi l_B \, [n_+(x) - n_-(x)],$$

$$\begin{pmatrix} \Psi_a''(x) - \kappa^2 \Psi_a(x) \\ \Psi_c''(x) - \kappa^2 \Psi_c(x) \end{pmatrix} = -4\pi \mathscr{M}_h \begin{pmatrix} n_-(x) - n_0 \\ n_+(x) - n_0 \end{pmatrix}, \tag{12.5}$$

and six boundary conditions: $\Psi_e(x \to \infty) = \Psi_a(x \to \infty) = \Psi_c(x \to \infty) = 0$, $\Psi_e'(x)|_{x=0} = -4\pi l_B \sigma_e / e$, and

$$\begin{pmatrix} \Psi_a'(x) \\ \Psi_c'(x) \end{pmatrix}_{x=0} - \kappa \begin{pmatrix} \Psi_a(0) \\ \Psi_c(0) \end{pmatrix} = -4\pi \mathscr{M}_h \begin{pmatrix} \sigma_- \\ \sigma_+ \end{pmatrix}. \tag{12.6}$$

In Eqs. 12.5-12.6, a prime denotes the derivative with respect to the argument (for example, $\Psi_e''(x) = d^2\Psi_e/dx^2$, etc); σ_- and σ_+ are two surface densities that determine the strength of the solvent-mediated interaction of the mobile anions and cations, respectively, with the electrode. In other words, analogously to σ_e being the density of charges on the surface, σ_- and σ_+ are the densities of the sources on the surface for the solvent-mediated interaction. We finally note that Eq. 12.4 accounts for the excluded volume interactions between the mobile ions on the basis of a lattice gas equation of state [79, 80], where each ion's diameter $2R$ equals the lattice size so that that maximal volume fraction is $(4/3)\pi R^3/(2R)^3 = \pi/6$. Numerical solutions of Eqs. 12.5-12.6 yield the surface potential $\Phi_0 = \Phi(x = 0)$ from which, when being determined as function of the surface charge density σ_e, we can compute the differential capacitance (measured in $\mathrm{F/m^2}$)

$$C^{diff} \equiv \frac{d\sigma_e}{d\Phi_0}. \tag{12.7}$$

The differential capacitance will then be a function of σ_e, σ_-, σ_+, a, b, c, κ, l_B, n_0. Note that the bulk ion concentration n_0 determines the Debye screening length $l_D = (8\pi l_B n_0)^{-1/2}$.

12.2.2. Monte Carlo Simulations

As in our previous work [9], we have carried out Metropolis Monte Carlo simulations in the NVT ensemble for a symmetric $1:1$ electrolyte of bulk concentration n_0, confined between two planar impenetrable surfaces placed at $x = 0$ and $x = H$. The surface located at $x = 0$ carries not only a uniform surface charge density, σ_e, but also uniform surface densities of sources for solvent-mediated interaction, σ_- and σ_+. All simulations were performed in a rectangular cell of dimensions $H \times L \times L$, with $L = 10\,\mathrm{nm}$ and $H = 30\,\mathrm{nm}$. Periodic boundary conditions were applied in the perpendicular directions to the x-axis, and

overall electroneutrality was ensured by the addition of neutralizing counterions. A modified restricted primitive model is used to describe the electrolyte solution. That is, all ions are treated as charged hard spheres, each with radius $R = 0.2$ nm (and in some cases with $R = 0.6$ nm), immersed in a medium of uniform dielectric constant $\varepsilon_w = 80$ or, equivalently, Bjerrum length $l_B = 0.7$ nm. Electrostatic and solvent-mediated ion-ion pair interactions are modeled according to Eq. 12.1. The solvent-mediated anion-surface and cation-surface interaction energies (with the surface being a distance x away) are $2\pi k_B T a \sigma_- e^{\kappa(a-x)}/\kappa$ and $2\pi k_B T c \sigma_+ e^{\kappa(c-x)}/\kappa$, respectively. In addition, the electrostatic ion-surface interaction energy (again, with the surface being a distance x away from the ion) is

$$\pm k_B T l_B \sigma_e L \left[2 \ln \left(\frac{d+L}{d-L} \right) - \frac{4x}{L} \arctan \left(\frac{L^2}{2xd} \right) \right], \tag{12.8}$$

with $d = \sqrt{2L^2 + 4x^2}$. The plus and minus signs in Eq. 12.8 refer to cations and anions, respectively. To account for the long-range nature of the Coulomb interaction, we used, as in our previous work [9], the so-called External Potential Method (EPM), developed by Torrie and Valleau [440]. In this method, which is also known as Charged Sheet Method (CSM) [493, 494], each ion is allowed to interact with the image cells by means of the usual minimum image convention and with an external electrostatic potential, given by the ionic distributions in the image cells, including the charges located at the electrode (we assume that the ionic distributions in the image cells are identical to those evaluated in the central cell) [440, 495, 443]. This method is equivalent to considering the electrostatic potential generated by a set of infinite sheets of thickness dx and surface charge density $e[-n_-(x) + n_+(x)]dx$ from which the central square hole of dimensions $L \times L$ is removed. Computationally, this method can be summarized into calculating, in the first simulation, the charge density in the central cell considering the external electrostatic potential equal to zero. In the next simulation, the charge density obtained in the previous simulation is assigned to the image cells and the external electrostatic potential is calculated. Then a new charge density in the central cell is determined and this procedure is repeated self-consistently until there are no significant variations in the charge density in the central cell.

For each value of σ_e, our simulations yield the local ion concentrations, $n_-(x)$ and $n_+(x)$. We used the corresponding volume charge density $e[-n_-(x) + n_+(x)]$ to numerically solve the Poisson equation (the first of the equations in Eq. 12.5), resulting in the dimensionless electrostatic potential $\Psi_e(x)$. In order to determine the differential capacitance $C^{diff} = d\sigma_e/d\Phi_0$, we first created a list $\{\sigma_e, \Phi_0\}$ that represents the

surface charge density, σ_e, and the corresponding electrostatic surface potential, $\Phi_0 = k_B T\,\Psi_e(x=0)/e$. The numerical values of C^{diff} are then determined using the algorithm developed by Lamperski and Zydor [443].

12.3. Results

We present Monte Carlo simulation and mean-field results for distinct combinations of interaction strength parameters (a, b, c) and surface source densities (σ_- and σ_+). In all scenarios analyzed here, we use a bulk salt concentration $n_0 = 0.056/\mathrm{nm}^3$ (equivalent to 100 mM), corresponding to a Debye screening length of $l_D = 1.0\,\mathrm{nm}$. Recall that we also use $1/\kappa = 0.3\,\mathrm{nm}$ and $l_B = 0.7\,\mathrm{nm}$.

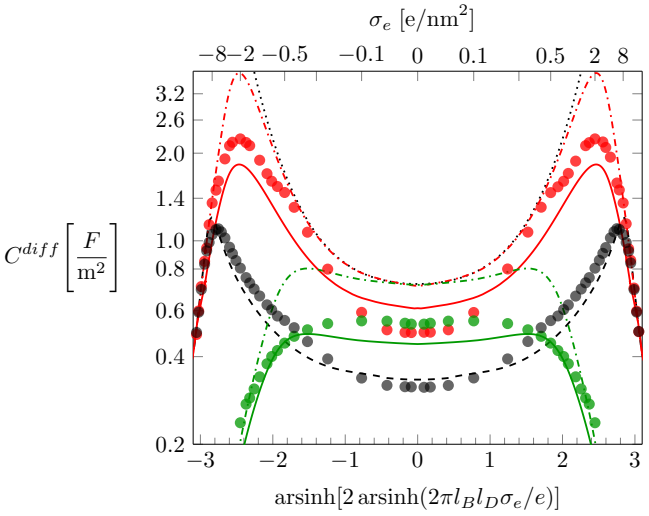

Figure 12.1. Differential capacitance, C^{diff}, as function of the surface charge density, σ_e. The dotted black line is the classical Poisson-Boltzmann result $C^{diff} = \varepsilon_w \varepsilon_0 \sqrt{1+w^2}/l_D$ with $w = 2\pi l_B l_D \sigma_e/e$. Curves colored red and green are calculated for $a = b = c = 0$, with ion radius $R = 0.2\,\mathrm{nm}$ (red) and $R = 0.6\,\mathrm{nm}$ (green) in the absence (dash-dotted lines) and presence (solid lines) of a Stern layer of thickness $d_S = R$. The color-matching bullets are corresponding results from Monte Carlo simulations. The black dashed line and the black bullets are mean-field and Monte Carlo simulation results, respectively, obtained for $R = 0.2\,\mathrm{nm}$, $a = b = c = 0.6\,\mathrm{nm}$, and $\sigma_- = \sigma_+ = 5.0\,\mathrm{nm}^{-2}$.

We first present results in Fig. 12.1 for $a = b = c = 0$ (colored red and green) and show that when solvent-mediated interactions are ignored, mean-field theory fails qualitatively in describing our Monte Carlo simulation results. The red and green bullets in Fig. 12.1 display Monte Carlo results for an ion radius of $R = 0.2\,\mathrm{nm}$ and $R = 0.6\,\mathrm{nm}$, respectively. The color-matching dash-dotted lines (red for $R = 0.2\,\mathrm{nm}$ and

green for $R = 0.6\,\text{nm}$) show the corresponding mean-field prediction. In fact, for $a = b = c = 0$ the lattice gas model, which we use to account for excluded volume interactions, yields the analytic expression [80, 431],

$$C^{diff} = \frac{\varepsilon_w \varepsilon_0}{l_D} \frac{\sqrt{\left(1 - e^{y w^2}\right)\left(1 - e^{y w^2} - y\right)}}{y\, w\, e^{y w^2}}, \tag{12.9}$$

with $y = 4 \times (2R)^3 n_0$ and $w = 2\pi l_B l_D \sigma_e / e$. The dash-dotted red and green lines are thus given by the expression in Eq. 12.9. Note that we prefer to display C^{diff} as nonlinear function of σ_e so as to highlight the regime of small $|\sigma_e|$. The function $\text{arsinh}[2\,\text{arsinh}(w)]$ is a convenient choice. For small $|\sigma_e|$, the finite ion size becomes irrelevant and the lattice gas model reproduces the prediction $C^{diff} = \varepsilon_w \varepsilon_0 \sqrt{1 + w^2}/l_D$ of the classical Poisson-Boltzmann model, which is shown by the black dotted line in Fig. 12.1. We note that the lattice gas model, but not the classical Poisson-Boltzmann model (which is based on an ideal gas instead of a lattice gas entropy for the mobile ions), predicts a camel-shape of C^{diff}, with two maxima that result from ion packing effects due to the non-vanishing ion size. More specifically, the camel-shape emerges from Eq. 12.9 (and also from Eq. 12.10 below) for sufficiently small ions $R < R^\star$ with $2R^\star = (6n_0)^{-1/3}$. For $R > R^\star$ the differential capacitance exhibits a bell-shape, with only a single maximum. Recall that in Fig. 12.1 we used $n_0 = 0.056/\text{nm}^3$, implying $R^\star = 0.72\,\text{nm}$. Hence, the green dash-dotted line, which is derived for $R = 0.6\,\text{nm} < R^\star$ is still in the camel-shape regime.

In order to account for the steric interaction between the flat surface and the mobile ions, it is common to add a Stern layer of fixed thickness $d_S = R$. This corresponds to adding in series a capacitor of fixed capacitance $C_{Stern} = \varepsilon_w \varepsilon_0 / R$, resulting in the total capacitance

$$C^{diff} = \varepsilon_w \varepsilon_0 \frac{1}{R + l_D \frac{y\, w\, e^{y w^2}}{\sqrt{\left(1 - e^{y w^2}\right)\left(1 - e^{y w^2} - y\right)}}}. \tag{12.10}$$

The prediction for C^{diff} according to Eq. 12.10 is shown in Fig. 12.1 by the solid red ($R = 0.2\,\text{nm}$) and solid green ($R = 0.6\,\text{nm}$) lines. Consider the specific point $\sigma_e = 0$: the thicker Stern layer for the larger ion leads to a smaller value of C^{diff}. More specifically, $C^{diff}(R = 0.6\,\text{nm}) = 0.44\,\text{F/m}^2$ and $C^{diff}(R = 0.2\,\text{nm}) = 0.59\,\text{F/m}^2$. However, the Monte Carlo simulations predict opposite behavior: $C^{diff}(R = 0.6\,\text{nm}) = 0.52\,\text{F/m}^2$ and $C^{diff}(R = 0.2\,\text{nm}) = 0.48\,\text{F/m}^2$. Clearly then, a mean-field model that is based on only excluded volume and Coulomb interactions is not able to qualitatively predict the behavior of C^{diff}.

We also display in Fig. 12.1 a mean-field prediction (black dashed line) and the corresponding Monte Carlo simulation results (black bullets), calculated in the presence of solvent-mediated interactions with $a = b = c = 0.6\,\mathrm{nm}$, $\sigma_- = \sigma_+ = 5.0\,\mathrm{nm}^{-2}$, and $R = 0.2\,\mathrm{nm}$. Note that because $a = c$ and $\sigma_- = \sigma_+$, the profile $C^{diff}(\sigma_e)$ must be symmetric so that $C^{diff}(\sigma_e) = C^{diff}(-\sigma_e)$. The choice $a = b = c = 0.6\,\mathrm{nm}$ implies that all mobile ions exhibit the same Yukawa-like solvent-mediated repulsion among each other irrespective of their electric charge, with an interaction strength of k_BT when the ion-ion distance is $r = 0.6\,\mathrm{nm}$. This widens the width of the EDL and thus decreases C^{diff}. In addition, each mobile ion experiences the same solvent-mediated repulsion with the electrode surface, as determined by $\sigma_- = \sigma_+ = 5.0\,\mathrm{nm}^{-2}$. The ion-surface repulsion leads to a charge-depleted region that separates the electrode surface from the diffuse ion cloud and further decreases C^{diff}. Unlike a Stern layer, the charge-depleted region emerges naturally from the inclusion of solvent-mediated interactions and has a self-adjusting thickness that minimizes the free energy [8]. The presence of the additional solvent-mediated interaction greatly improves the level of agreement between mean-field theory and Monte Carlo simulations. Fig. 12.1 exemplifies this for $R = 0.2\,\mathrm{nm}$: compare the mean-field and Monte Carlo simulation results with (the black dashed line and black bullets) and without (the red solid line and the red bullets) solvent-mediated interactions.

Asymmetric profiles of the differential capacitance, $C^{diff}(\sigma_e) \neq C^{diff}(-\sigma_e)$, emerge from asymmetric solvent-mediated interactions, where $a \neq c$. Fig. 12.2 demonstrates this for $a = c = 0.6\,\mathrm{nm}$ (black color), $a = 0.8\,\mathrm{nm}$ and $c = 0.4\,\mathrm{nm}$ (red color), as well as $a = 1.0\,\mathrm{nm}$ and $c = 0.2\,\mathrm{nm}$ (blue color). Dashed lines refer to mean-field prediction and the color-matching bullets to Monte Carlo simulations. All calculations apply to fixed $R = 0.2\,\mathrm{nm}$, $\sigma_- = \sigma_+ = 5.0\,\mathrm{nm}^{-2}$ and $b = 0.6\,\mathrm{nm}$. Increasing a and decreasing c renders anion-anion repulsion stronger and cation-cation repulsion weaker. Concomitantly, anions are repelled more strongly from the electrode, and cations are repelled less strongly from the electrode, irrespective of σ_e. For $\sigma_e > 0$, where the mobile anions are enriched in the diffuse part of the EDL, larger a leads to smaller C^{diff}. Conversely, for $\sigma_e < 0$, mobile cations accumulate near the electrode, implying an increase in C^{diff} for smaller c. Mean-field results agree well with Monte Carlo simulations, even better so when solvent-mediated interactions become stronger and thus decrease C^{diff}. For weak solvent-mediated interactions, when either a or c is comparable or smaller than R, excluded volume interactions continue to dominate at medium and large ion densities, implying no or only minor improvement (as compared to the absence of solvent-mediated interactions) in the ability of mean-field theory to describe Monte Carlo simulation results.

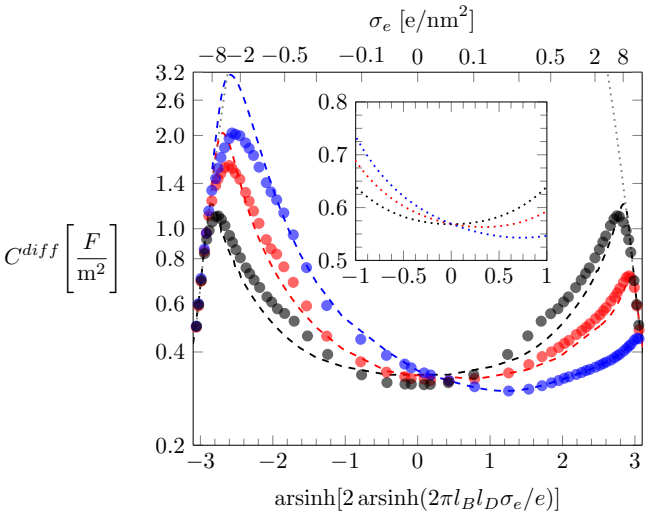

Figure 12.2. Differential capacitance, C^{diff}, as function of the surface charge density σ_e, for different combinations of the solvent-mediated interaction parameters a and c: $a = b = c = 0.6\,\text{nm}$ (black), $a = 0.8\,\text{nm}$ and $c = 0.4\,\text{nm}$ (red), and finally $a = 1.0\,\text{nm}$ and $c = 0.2\,\text{nm}$ (blue). Dashed lines and color-matching bullets refer to mean-field predictions and corresponding Monte Carlo simulation results. All results are derived for fixed $R = 0.2\,\text{nm}$, $\sigma_- = \sigma_+ = 5.0\,\text{nm}^{-2}$, and $b = 0.6\,\text{nm}$. The gray dotted line marks the limiting expression $C^{diff} = 2\varepsilon_w\varepsilon_0/[(2R)^3\sigma_e/e]$, valid for large $|\sigma_e|$. The inset displays model predictions for C^{diff} as function of arsinh[2arsinh($2\pi l_B l_D \sigma_e/e$)] according to Eq. 12.12, with $d_S = d_S^a = 0.2\,\text{nm}$ (black), $d_S = 0.132\,\text{nm}$ and $d_S^a = 0.266\,\text{nm}$ (red), as well as $d_S = 0.066\,\text{nm}$ and $d_S^a = 0.332\,\text{nm}$ (blue), all derived for $l_D = 1\,\text{nm}$.

We can qualitatively understand the emergence of the asymmetry $C^{diff}(\sigma_e) \neq C^{diff}(-\sigma_e)$ for $a \neq c$ based on the ion-surface interaction only while ignoring any non-electrostatic ion-ion interactions (including excluded volume interactions). To this end, recall the prediction of the classical Poisson-Boltzmann approach $C^{diff} = \varepsilon_w\varepsilon_0\sqrt{1+w^2}/l_D$ with the scaled surface charge density $w = 2\pi l_B l_D \sigma_e/e$. Adding a Stern layer of thickness $d_S \ll l_D$ reduces the differential capacitance according to

$$C^{diff} = (\varepsilon_w\varepsilon_0/l_D)\left[\sqrt{1+w^2} - (d_S/l_D)(1+w^2)\right] \tag{12.11}$$

while preserving the symmetry $C^{diff}(\sigma_e) = C^{diff}(-\sigma_e)$. The asymmetry $a > c$ can approximately be translated into the existence of a region $0 < x < d_S$ where all ions are excluded and another region $d_S < x < d_S^a$ where only anions (but not the cations) are excluded from. In this case, we obtain for the differential capacitance (valid up to first order in d_S/l_D and d_S^a/l_D) the expression

$$C^{diff} = \frac{\varepsilon_w\varepsilon_0}{l_D}\left\{\sqrt{1+w^2} - \left(\frac{d_S}{l_D}\right)(1+w^2) - \left(\frac{d_S^a - d_S}{l_D}\right)\left[1+w^2 - \frac{2+\frac{w}{\sqrt{1+w^2}}}{4(w+\sqrt{1+w^2})^2}\right]\right\}. \tag{12.12}$$

The Appendix, which derives Eq. 12.12, also shows a plot (Fig. 12.7) of both perturbation contributions, demonstrating that the additional zone of anion-exclusion further reduces C^{diff}, but does so in an asymmetric manner, giving rise to $C^{diff}(\sigma_e) < C^{diff}(-\sigma_e)$ as we observe in Fig. 12.2. To further demonstrate the usefulness of Eq. 12.12, we show in the inset of Fig. 12.2 the prediction of C^{diff} according to Eq. 12.12 as function of arsinh[2arsinh(w)] for $d_S = d_S^a = 0.2\,\text{nm}$ (black), $d_S = (0.2-0.066)\,\text{nm}$ and $d_S^a = (0.2+0.066)\,\text{nm}$ (red), as well as $d_S = (0.2-2\times 0.066)\,\text{nm}$ and $d_S^a = (0.2+2\times 0.066)\,\text{nm}$ (blue). Apparently, our simple phenomenological model gives rise to a similar asymmetry pattern for C^{diff} as that observed in the main figure. Note that the abscissa in the inset is the same as that in the main figure, yet extending only from -1 to $+1$ because the validity of Eq. 12.12 is confined to small $|\sigma_e|$.

We notice from Fig. 12.2 that for large $|\sigma_e|$ all predictions, mean-field and Monte Carlo, merge into a single line, irrespective of the solvent-mediated potential. This behavior reflects a state of dense ion packing due exclusively to their excluded volume interactions. If the maximal ion density is approximated by $(2R)^{-3}$, a differential capacitance $C^{diff} = 2\varepsilon_w\varepsilon_0/[(2R)^3\sigma_e/e]$ in the limit of large $|\sigma_e|$ emerges. This expression describes the limiting behavior well; see the gray dotted line in Fig. 12.2.

The parameter b determines the strength of the solvent-mediated interaction between anions and cations. For large $|\sigma_e|$ (or, more accurately, when $|2\pi l_B l_D \sigma_e/e| \gg 1$) the EDL consists predominantly of ions of one type, either anions or cations, rendering b irrelevant for C^{diff}. However, for $|2\pi l_B l_D \sigma_e/e| \ll 1$ both anions and cations will be present and b will affect C^{diff}. In Fig. 12.3 we compare mean-field prediction and Monte Carlo results for various values of b as indicated in the diagram, all for fixed $R = 0.2\,\text{nm}$, $\sigma_- = \sigma_+ = 5.0\,\text{nm}^{-2}$, $a = 0.8\,\text{nm}$, and $c = 0.4\,\text{nm}$. As expected, b influences C^{diff} only in the vicinity of small $|\sigma_e|$. Larger b leads to larger C^{diff} in that region. Recall from Fig. 12.2 that a larger a widens the width of the EDL near a positively charged electrode surface and thus decreases C^{diff}. Similarly, a larger c widens the width of the EDL near a negatively charged electrode surface and thus also decreases C^{diff}. In view of that, it might be unexpected that a larger b *increases* C^{diff} of a weakly charged electrode. To understand this finding, we display in Fig. 12.4 Monte Carlo simulation results (and the corresponding mean-field predictions) for the local concentrations of anions, $n_-(x)$, and cations, $n_+(x)$, as function of the distance x from the electrode surface, using the same set of values for b as in Fig. 12.3 and the specific choice $\sigma_e = -0.01\,e/\text{nm}^2$. All other parameters are the same as in Fig. 12.3 (that is, $R = 0.2\,\text{nm}$, $\sigma_- = \sigma_+ = 5.0\,\text{nm}^{-2}$, $a = 0.8\,\text{nm}$, and $c = 0.4\,\text{nm}$). Because the value of a is twice that of c, the anion-depleted region close to the surface is about twice as wide as the cation-depleted region. Cations are thus able to form a layer on their own

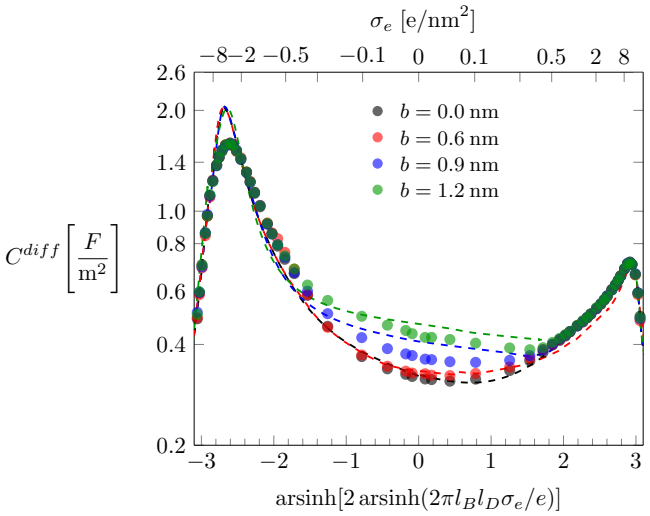

Figure 12.3. Differential capacitance, C^{diff}, as function of the surface charge density, σ_e, for different values of the anion-cation interaction strength b as indicated. Dashed lines and color-matching bullets refer to mean-field predictions and corresponding Monte Carlo simulation results. All results are derived for fixed $R = 0.2\,\text{nm}$, $\sigma_- = \sigma_+ = 5.0\,\text{nm}^{-2}$, $a = 0.8\,\text{nm}$, and $c = 0.4\,\text{nm}$.

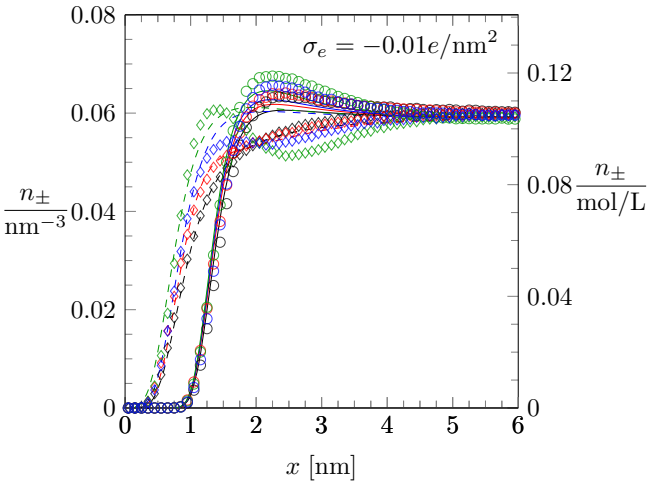

Figure 12.4. Ion concentration profiles $n_-(x)$ (open circles) and $n_+(x)$ (open diamonds) near the charged electrode as predicted by Monte Carlo simulations for $\sigma_e = -0.01\,e/\text{nm}^2$. Different colors refer to different values of b as specified in Fig. 12.3: $b = 0$ (black), $b = 0.6\,\text{nm}$ (red), $b = 0.9\,\text{nm}$ (blue), and $b = 1.2\,\text{nm}$ (green). The color-matching solid lines [for $n_-(x)$] and broken lines [for $n_+(x)$] display the corresponding mean-field predictions. All fixed parameters are the same as in Fig. 12.3, namely $R = 0.2\,\text{nm}$, $\sigma_- = \sigma_+ = 5.0\,\text{nm}^{-2}$, $a = 0.8\,\text{nm}$, and $c = 0.4\,\text{nm}$.

close to the surface, followed by a region of slightly enhanced anion concentration. With increasing b anion-cation interaction becomes more unfavorable. More cations then migrate into the anion-depleted layer and more anions accumulate in the region next to that. In other words, with increasing b cations and

anions tend to get more separated from each other, implying a larger response of the dimensionless surface potential $\Psi_e(x=0)$ to changes in σ_e. Note that besides our Monte Carlo simulation results, Fig. 12.4 also displays the corresponding mean-field predictions (color-matching solid and broken lines for anions and cations, respectively). With the exception of the oscillating behavior that emerges with growing b, the mean-field predictions agree with the qualitative trends of the simulation results. This includes, in particular, the depletion zones for anions and cations as well as the concentration changes as function of b.

In order to further rationalize the increase of C^{diff} with b we follow up on the simple model that gave rise to Eq. 12.12. Recall that based on the classical Poisson-Boltzmann model (thus assuming point-like ions that exhibit only Coulomb interactions), we assumed the existence of a region $0 < x < d_S$ where all ions are excluded from and another region $d_S < x < d_S^a$ where only anions are excluded from. This, in fact, is what we approximately observe in Fig. 12.4, with a and c translating into d_S and d_S^a. As b increases, more cations migrate to the region $d_S < x < d_S^a$. In our simple theoretical model we can enforce this migration by a Lagrangian multiplier λ, defined in such a way that $\lambda > 0$ induces the migration of additional cations from the region $x > d_S^a$ into the region $d_S < x < d_S^a$. Conversely $\lambda < 0$ leads to a depletion of cations from the region $d_S < x < d_S^a$. In other words, growing λ mimics the effect of growing b in Fig. 12.3. As we detail in the Appendix, the resulting differential capacitance of our model up to first order in d_S/l_D and d_S^a/l_D is

$$\begin{aligned} C^{diff} &= \frac{\varepsilon_w \varepsilon_0}{l_D}\left\{ \sqrt{1+w^2} - \left(\frac{d_S}{l_D}\right)(1+w^2) \right. \\ &- \left. \left(\frac{d_S^a - d_S}{l_D}\right)\left[1+w^2 - \frac{e^{\lambda}\left(2+\frac{w}{\sqrt{1+w^2}}\right)}{4(w+\sqrt{1+w^2})^2} \right] \right\}. \end{aligned} \tag{12.13}$$

For $\lambda = 0$ no constraint is imposed and we recover Eq. 12.12. For $\lambda \to -\infty$ all cations are forced to leave the region $d_S < x < d_S^a$, which recovers the simple Stern layer result

$$C^{diff} = (\varepsilon_w \varepsilon_0 / l_D)\left[\sqrt{1+w^2} - (d_S^a/l_D)(1+w^2) \right] \tag{12.14}$$

with an ion-depleted region $x < d_S^a$. Most importantly, growing λ in Eq. 12.13 increases C^{diff}, irrespective of the surface charge density σ_e (as expressed through $w = 2\pi l_B l_D \sigma_e / e$). This behavior clearly illustrates the mechanism of how the interaction parameter b increases C^{diff}, as observed in Fig. 12.3.

Asymmetric profiles of the differential capacitance, $C^{diff}(\sigma_e) \neq C^{diff}(-\sigma_e)$, can also emerge from

asymmetric solvent-mediated interactions between the ions and the surface as expressed through $\sigma_- \neq \sigma_+$. We illustrate the implications of such a mismatch in Fig. 12.5, which shows C^{diff} as function of σ_e for different choices of σ_+ as indicated in the legend. Mean-field predictions are displayed by broken lines and Monte Carlo simulations by the color-matching bullets. All cases are based on fixing $R = 0.2\,\text{nm}$, $a = b = c = 0.6\,\text{nm}$, and $\sigma_- = 5\,\text{nm}^{-2}$. Increasing σ_+ decreases C^{diff} in the region $\sigma_e < 0$ while leaving C^{diff} unchanged for $\sigma_e > 0$. Indeed, larger repulsion between the cations and the electrode surface increases the width of the ion charge-depleted region between the surface and the diffuse part of the EDL. This reduces C^{diff}. For $\sigma_e > 0$, the cation-surface interaction becomes increasingly irrelevant, leaving C^{diff} unaffected. Agreement between mean-field theory and Monte Carlo simulations is satisfying and becomes better for larger σ_+ (and analogously for σ_-). Here again we conclude that our mean-field approach qualitatively reproduces all Monte Carlo simulation results and does so even quantitatively when the additional solvent-mediated interactions are sufficiently large.

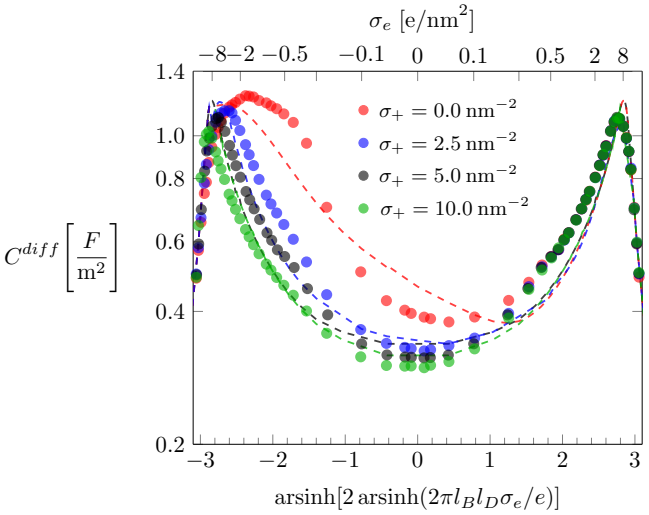

Figure 12.5. Differential capacitance, C^{diff}, as function of the surface charge density, σ_e, for different values of σ_+ as indicated in the figure legend. Dashed lines and color-matching bullets refer to mean-field predictions and corresponding Monte Carlo simulation results. All results are derived for fixed $R = 0.2\,\text{nm}$, $a = b = c = 0.6\,\text{nm}$, and $\sigma_- = 5\,\text{nm}^{-2}$.

Experimental data for the differential capacitance typically display a notable asymmetry $C^{diff}(\sigma_e) \neq C^{diff}(-\sigma_e)$. Fig. 12.6 shows a data set from Hamelin [7], obtained for a sodium fluoride (NaF) electrolyte of varying concentrations exposed to the 210 crystal face of a gold electrode, that exhibits both an asym-

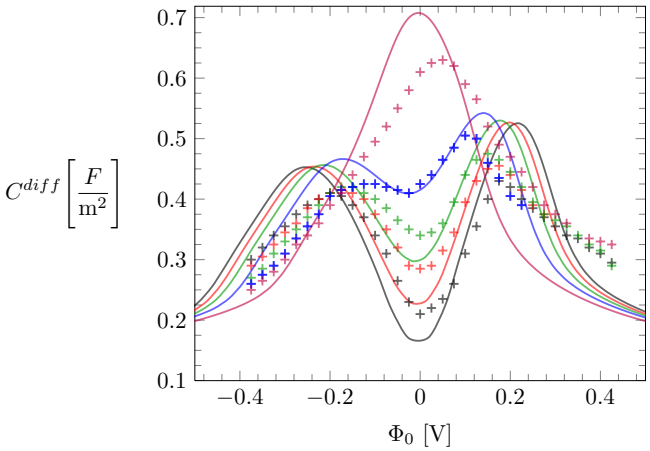

Figure 12.6. Differential capacitance, C^{diff}, as function of the electrostatic surface potential Φ_0, for different concentrations n_0 of a the electrolyte: $n_0 = 0.01$ M (black), $n_0 = 0.02$ M (red), $n_0 = 0.05$ M (green), $n_0 = 0.1$ M (blue), and $n_0 = 0.5$ M (purple). Experimental data points reported by Hamelin [7] are marked by crosses; solid lines represent mean-field results obtained for $a = 0.4\,\mathrm{nm}$, $b = 0.04\,\mathrm{nm}$, $c = 0.53\,\mathrm{nm}$, $\sigma_+ = 2.25\,\mathrm{nm}^{-2}$, $\sigma_- = 2.5\,\mathrm{nm}^{-2}$, and $R = 0.72\,\mathrm{nm}$.

metry and the camel-shape to bell-shape transition. Experimental data points are marked by crosses, with different colors corresponding to $n_0 = 0.01$ M (black), $n_0 = 0.02$ M (red), $n_0 = 0.05$ M (green), $n_0 = 0.1$ M (blue), and $n_0 = 0.5$ M (purple). The color-matching solid lines were calculated for $a = 0.4\,\mathrm{nm}$, $b = 0.04\,\mathrm{nm}$, $c = 0.53\,\mathrm{nm}$, $\sigma_+ = 2.25\,\mathrm{nm}^{-2}$, $\sigma_- = 2.5\,\mathrm{nm}^{-2}$, and $R = 0.72\,\mathrm{nm}$. The mean-field results clearly reproduce the qualitative trends of the experimental data sets, including the asymmetry and camel-shape to bell-shape transition as function of growing salt concentration. We note that Minton and Lue [88] have fitted the same experimental data set based on a mean-field model that introduces the asymmetry $C^{diff}(\sigma_e) \neq C^{diff}(-\sigma_e)$ through a combination of a van der Waals equation of state for a mixture of size-asymmetric hard spheres (supplemented by a Stern layer) and the account of excess polarizabilities for mobile cations and anions. As the authors have pointed out, additional effects like ion-ion correlations, field-induced dielectric decrement, and specific interactions can further modify the differential capacitance. While our present model continues to neglect changes in the local dielectric constant and also neglects ion polarizabilities (in contrast to the work of Minton and Lue [88]), it does account for specific interactions both between ion pairs and between ions and the surface through our use of Yukawa potentials. As a consequence, our model removes the need to add a Stern layer. The approaches by Minton and Lue [88] and ours thus complement each other in their ability to fit experimental data sets like the one in Fig. 12.6. Future work could merge both approaches.

12.4. Conclusions

In this work we have used our previously introduced mean-field formalism [9] to investigate how asymmetric solvent-mediated ion-ion and ion-surface interactions, modeled as Yukawa pair potentials, affect the differential capacitance C^{diff} of an EDL. In addition, we also carried out Metropolis Monte Carlo simulations and compared the results with our mean-field predictions. We demonstrate that in addition to asymmetries in ion valencies [496, 497] and sizes [482, 485, 486, 487], solvent-mediated non-electrostatic ion-ion interactions (modeled as Yukawa potentials) are also able to induce asymmetric profiles of the differential capacitance. Most significantly, the presence of the additional Yukawa potentials greatly improves the ability of mean-field theory to reproduce the simulation results, including the asymmetry $C^{diff}(\sigma_e) \neq C^{diff}(-\sigma_e)$ and the camel-shape to bell-shape transition. The improved agreement between mean-field model and simulation results from the softening of the composite ion-ion and ion-surface interaction potentials due to their additional Yukawa component. Softer potentials diminish the role of ion-ion correlations, which are accounted for in our Monte Carlo simulations but are neglected in mean-field theory.

Larger solvent-mediated anion-anion repulsion decreases C^{diff} of a positively charged electrode and shifts its maximum to more positively charged surfaces. Similarly, larger solvent-mediated cation-cation repulsion decreases C^{diff} of a negatively charged electrode and shifts its maximum to more negatively charged surfaces. Larger solvent-mediated anion-cation repulsion increases C^{diff} at small surface charge densities σ_e. We rationalize the latter finding using a simple phenomenological ion-depletion model that is based on the classical Poisson-Boltzmann model supplemented by two distinct Stern-like depletion layers for anions and cations.

In order to facilitate comparison of mean-field theory with Monte Carlo simulations, we have used a uniform dielectric background in both the mean-field model and Monte Carlo simulations. Imposing a uniform dielectric constant is one among a number of approximations in our work, including the neglect of ion polarizabilities and treating solvent-mediated interactions as simple Yukawa pair potentials. Nevertheless, we expect our findings about the role of solvent-mediated anion-anion, cation-cation, and anion-cation interactions to also apply for more detailed models of the EDL. This includes modeling the combined presence of asymmetries in steric size, ionic valence, and solvent interactions.

12.5. Acknowledgements

The authors thank Dr. Leo Lue for providing the experimental data used in our Figure 12.6. Daniel L. Z. Caetano acknowledges the Sao Paulo Research Foundation (FAPESP, Process Grant No. 2013/13151-7) for the financial support. Guilherme V. Bossa acknowledges a doctoral scholarship from CAPES Foundation/Brazil Ministry of Education (Grant No. 9466/13-4). Vinicius M. de Oliveira was supported by the Conselho Nacional de Desenvolvimento Científico e Tecnológico (CNPq, Process Grant No. 141985/2013-5). Matthew A. Brown acknowledges the Swiss National Science Foundation for an International Short Visit travel grant (Grant No. 162320). All simulations were performed by resources supplied by the Center of Scientific Computing (NCC/GridUNESP) of the Sao Paulo State University (UNESP).

12.6. Appendix

To derive Eq. 12.13 we consider the familiar functional [36] for the Poisson-Boltzmann free energy F, expressed in units of the thermal energy k_BT and unit area A

$$\begin{aligned}\frac{F}{Ak_BT} &= \int_0^\infty dx\left[\frac{\Psi_e'^2}{8\pi l_B}+n_-\ln\frac{n_-}{n_0}-n_-+n_+\ln\frac{n_+}{n_0}-n_+\right] \\ &+ \int_0^\infty dx(U_-n_-+U_+n_+)-\lambda\int_{d_S}^{d_S^a}dx\,n_+,\end{aligned} \tag{12.15}$$

where the charged electrode (modeled as a planar surface of surface charge density σ_e) is located at position $x=0$ and where the mobile anions (of local concentration n_-) and cations (of local concentration n_+) are assumed to be point-like, interacting only through the Coulomb potential. The first line in Eq. 12.15 represents the electrostatic energy as function of the dimensionless electrostatic potential $\Psi_e(x)$ and ideal gas entropy contribution of all mobile ions. The external potentials $U_-=\infty$ if $x\leq d_S^a$ and $U_-=0$ for $x>d_S^a$ as well as $U_+=\infty$ if $x\leq d_S$ and $U_+=0$ for $x>d_S$ (with $d_S^a\geq d_S$) ensure that anions and cations are excluded from the region $x<d_S$, whereas anions (but not the cations) are also excluded from the region $d_S<x<d_S^a$. Finally, λ is a constant Lagrangian multiplier that can be used to fix the number of cations in the region $d_S<x<d_S^a$. For $\lambda>0$ additional cations must enter that region. Minimization of Eq. 12.15 subject to Poisson's equation yields the Boltzmann distributions $n_-=n_+=0$ for $x<d_S$, $n_-=0$ and $n_+=n_0e^{\lambda-\Psi_e}$

for $d_S < x < d_S^a$, as well as $n_- = n_0 e^{\Psi_e}$ and $n_+ = n_0 e^{-\Psi_e}$ for $d_S^a < x$. Inserting these distributions into Poisson's equation $\Psi_e'' = 4\pi l_B(n_- - n_+)$ results in $\Psi_e'' = 0$ for $x < d_S$, $l_D^2\Psi_e'' = -e^{\lambda-\Psi_e}/2$ for $d_S < x < d_S^a$, and $l_D^2\Psi_e'' = \sinh\Psi_e$ for $d_S^a < x$. The potential $\Psi_e(x)$ must be continuous and smooth for $x > 0$, and it must fulfill $\Psi_e'(0) = -2w/l_D$ (with $w = 2\pi l_B l_D \sigma_e/e$) and $\Psi_e(x \to \infty) = 0$.

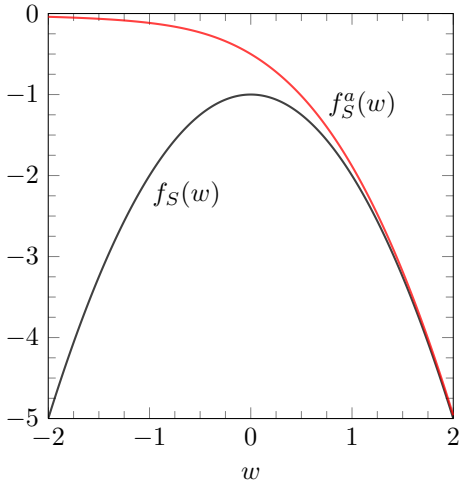

Figure 12.7. The two perturbation contributions $f_S(w)$ and $f_S^a(w)$ as function of $w = 2\pi l_B l_D \sigma_e/e$.

To find the differential capacitance we express the potential in the region $d_S < x < d_S^a$ as

$$\Psi_e(x) = \ln\left\{\frac{1}{a^2}\cos^2\left[\frac{a(x-d_S)}{2l_D}e^{\lambda/2} + \arctan\left(\frac{2w}{a}e^{-\lambda/2}\right)\right]\right\} \tag{12.16}$$

with $a = \sqrt{e^{-\tilde{\Psi}_e} - (2we^{-\lambda/2})^2}$. The potential $\Psi_e(x)$ in Eq. 12.16 then fulfills $\Psi_e(d_S) = \tilde{\Psi}_e$ and $\Psi_e'(d_S) = -2w/l_D$. Note that the potential is linear for $0 < x < d_S$, implying $\tilde{\Psi}_e = \Psi_e(0) - 2w\,d_S/l_D$. Integration of the classical Poisson-Boltzmann equation in the region $d_S^a < x$ yields the relation $l_D\Psi_e'(d_S^a) = -2\sinh[\Psi_e(d_S^a)/2]$. Inserting $\Psi_e(x)$ from Eq. 12.16 into that relation results in a transcendental relationship for the scaled surface charge density $w = 2\pi l_B l_D \sigma_e/e$ as function of the surface potential $\Psi_e(0)$. However, up to linear order in d_S/l_D and d_S^a/l_D we find the explicit relation

$$w = \sinh\frac{\Psi_e(0)}{2} - \frac{d_S^a}{l_D}\frac{1}{2}\sinh\Psi_e(0) - \frac{d_S^a - d_S}{l_D}\frac{1}{4}e^{\lambda-\Psi_e(0)}, \tag{12.17}$$

from which we can compute the differential capacitance $C^{diff} = (\varepsilon_w \varepsilon_0 / l_D)\, d(2w)/d\Psi_e(0)$. This leads to

$$C^{diff} = \frac{\varepsilon_w \varepsilon_0}{l_D} \left[\cosh \frac{\Psi_e(0)}{2} - \frac{d_S^a}{l_D} \cosh \Psi_e(0) + \frac{d_S^a - d_S}{l_D} \frac{1}{2} e^{\lambda - \Psi_e(0)} \right]. \tag{12.18}$$

We reiterate that Eq. 12.18 is valid up to linear order in d_S/l_D and d_S^a/l_D. Hence, to express C^{diff} as function of w in that order, we only need to solve the relationship in Eq. 12.17 for $\Psi_e(0)$ as function of w up to linear order in d_S/l_D and d_S^a/l_D and insert it back into Eq. 12.18. This then results in Eq. 12.13.

Clearly, for $\lambda = 0$ no constraint is imposed and Eq. 12.13 reduces to Eq. 12.12. The two perturbation contributions in Eq. 12.12, $f_S(w) = -(1+w^2)$ and

$$f_S^a(w) = -(1+w^2) + \frac{2 + \frac{w}{\sqrt{1+w^2}}}{4(w+\sqrt{1+w^2})^2} \tag{12.19}$$

are both negative for any choice of w, as shown in Fig. 12.7

REFERENCES

[1] B. J. Park, J. P. Pantina, E. M. Furst, M. Oettel, S. Reynaert, J. Vermant, Direct measurements of the effects of salt and surfactant on interaction forces between colloidal particles at water-oil interfaces, Langmuir 24 (5) (2008) 1686–1694.

[2] J. Zhang, B. Jing, V. Janout, S. L. Regen, Detecting cross talk between two halves of a phospholipid bilayer, Langmuir 23 (17) (2007) 8709–8712.

[3] U. Galicia-Pimentel, J. López-Lemus, P. Orea, Liquid–vapor interfacial properties of attractive Yukawa fluids, Fluid Phase Equilib. 265 (1) (2008) 205–208.

[4] E. El Mendoub, J.-F. Wax, N. Jakse, Evolution of the liquid-vapor coexistence of the hard-core yukawa fluid as a function of the interaction range, J. Chem. Phys. 132 (16) (2010) 164503.

[5] V. Weiss, W. Schröer, Corresponding-states analysis of the surface tension of simple, polar, and ionic fluids, Int. J. Thermophys. 28 (2) (2007) 506–519.

[6] D. Duh, L. Mier-y-Terán, An analytical equation of state for the hard-core Yukawa fluid, Mol. Phys. 90 (3) (1997) 373–380.

[7] A. Hamelin, Study of the (210) face of gold in aqueous solutions, J. Electroanal. Chem. Interfacial Electrochem. 138 (2) (1982) 395–400.

[8] D. F. Evans, H. Wennerström, The colloidal domain, where physics, chemistry, and biology meet, 2nd Edition, VCH publishers, 1994.

[9] A. J. Minn, P. Vélez, S. L. Schendel, H. Liang, S. W. Muchmore, S. W. Fesik, M. Fill, C. B. Thompson, Bcl-xl forms an ion channel in synthetic lipid membranes, Nature 385 (6614) (1997) 353.

[10] R. M. Epand, Do proteins facilitate the formation of cholesterol-rich domains?, Biochim. Biophys. Acta, Biomembr. 1666 (1) (2004) 227–238.

[11] K. Simons, W. L. Vaz, Model systems, lipid rafts, and cell membranes 1, Annu. Rev. Biophys. Biomol. Struct. 33 (2004) 269–295.

[12] H. M. McConnell, Structures and transitions in lipid monolayers at the air-water interface, Annu. Rev. Phys. Chem. 42 (1) (1991) 171–195.

[13] V. M. Kaganer, H. Möhwald, P. Dutta, Structure and phase transitions in langmuir monolayers, Rev. Mod. Phys. 71 (3) (1999) 779.

[14] H. M. McConnell, V. T. Moy, Shapes of finite two-dimensional lipid domains, J. Phys. Chem. 92 (15) (1988) 4520–4525.

[15] H. Brockman, Dipole potential of lipid membranes, Chem. Phys. Lipids 73 (1-2) (1994) 57–79.

[16] I. Sriram, D. K. Schwartz, Line tension between coexisting phases in monolayers and bilayers of amphiphilic molecules, Surf. Sci. Rep. 67 (6) (2012) 143–159.

[17] P. Pieranski, Two-dimensional interfacial colloidal crystals, Phys. Rev. Lett. 45 (7) (1980) 569.

[18] R. Aveyard, J. H. Clint, D. Nees, V. N. Paunov, Compression and structure of monolayers of charged latex particles at air/water and octane/water interfaces, Langmuir 16 (4) (2000) 1969–1979.

[19] F. Ravera, E. Santini, G. Loglio, M. Ferrari, L. Liggieri, Effect of nanoparticles on the interfacial properties of liquid/liquid and liquid/air surface layers, J. Phys. Chem. B 110 (39) (2006) 19543–19551.

[20] K. Du, E. Glogowski, T. Emrick, T. P. Russell, A. D. Dinsmore, Adsorption energy of nano-and microparticles at liquid- liquid interfaces, Langmuir 26 (15) (2010) 12518–12522.

[21] Y. Okado, Y. Nagata, N. Torikai, M. Kawaguchi, Adsorption behavior at the air/water interface for pnipam-adsorbed colloidal silica, Chem. Lett. 41 (10) (2012) 1168–1170.

[22] H. S. Wi, S. Cingarapu, K. J. Klabunde, B. M. Law, Nanoparticle adsorption at liquid–vapor surfaces: influence of nanoparticle thermodynamics, wettability, and line tension, Langmuir 27 (16) (2011) 9979–9984.

[23] H. Ma, M. Luo, L. L. Dai, Influences of surfactant and nanoparticle assembly on effective interfacial tensions, Phys. Chem. Chem. Phys. 10 (16) (2008) 2207–2213.

[24] D. C. Calzolari, D. Pontoni, M. Deutsch, H. Reichert, J. Daillant, Nanoscale structure of surfactant-induced nanoparticle monolayers at the oil–water interface, Soft Matter 8 (45) (2012) 11478–11483.

[25] B. J. Park, E. M. Furst, Attractive interactions between colloids at the oil–water interface, Soft Matter 7 (17) (2011) 7676–7682.

[26] C. L. Wirth, E. M. Furst, J. Vermant, Weak electrolyte dependence in the repulsion of colloids at an oil–water interface, Langmuir 30 (10) (2014) 2670–2675.

[27] E. Spohr, Some recent trends in computer simulations of aqueous double layers, Electrochimica Acta 49 (1) (2003) 23–27.

[28] G. Brannigan, F. L. Brown, Solvent-free simulations of fluid membrane bilayers, J. Chem. Phys. 120 (2) (2004) 1059–1071.

[29] I. R. Cooke, M. Deserno, Solvent-free model for self-assembling fluid bilayer membranes: stabilization of the fluid phase based on broad attractive tail potentials, J. Chem. Phys. 123 (22) (2005) 224710.

[30] S. Izvekov, G. A. Voth, Solvent-free lipid bilayer model using multiscale coarse-graining, J. Phys. Chem. B 113 (13) (2009) 4443–4455.

[31] K. Bohinc, A. Shrestha, S. May, The Poisson-Helmholtz-Boltzmann model, Eur. Phys. J. E: Soft Matter Biol. Phys. 34 (10) (2011) 1–10.

[32] D. Boda, D. Gillespie, W. Nonner, D. Henderson, B. Eisenberg, Computing induced charges in inhomogeneous dielectric media: application in a Monte Carlo simulation of complex ionic systems, Phys. Rev. E 69 (4) (2004) 046702.

[33] H. Yu, W. F. van Gunsteren, Accounting for polarization in molecular simulation, Comput. Phys. Commun. 172 (2) (2005) 69–85.

[34] K. Barros, D. Sinkovits, E. Luijten, Efficient and accurate simulation of dynamic dielectric objects, J. Chem. Phys. 140 (6) (2014) 064903.

[35] D. Andelman, Electrostatic properties of membranes: The Poisson-Boltzmann theory, in: R. Lipowsky, E. Sackmann (Eds.), Structure and Dynamics of Membranes, 2nd Edition, Vol. 1, Elsevier, Amsterdam, 1995, section 12, pp. 603–642.

[36] S. May, Lipid membranes: Mean-field continuum electrostatics, in: P. Somasundaran (Ed.), Encyclopedia of Surface and Colloid Science, 3rd Edition, Taylor and Francis, 2015, pp. 3792 –3806.

[37] R. Aveyard, B. P. Binks, J. H. Clint, Emulsions stabilised solely by colloidal particles, Adv. Colloid Interface Sci. 100 (2003) 503–546.

[38] A. D. Dinsmore, M. F. Hsu, M. G. Nikolaides, M. Marquez, A. R. Bausch, D. A. Weitz, Colloidosomes: Selectively permeable capsules composed of colloidal particles, Science 298 (5595) (2002) 1006–1009.

[39] M. E. Cates, P. S. Clegg, Bijels: a new class of soft materials, Soft Matter 4 (11) (2008) 2132–2138.

[40] J. Hiller, J. D. Mendelsohn, M. F. Rubner, Reversibly erasable nanoporous anti-reflection coatings from polyelectrolyte multilayers, Nat. Mater. 1 (1) (2002) 59–63.

[41] K. C. Krogman, T. Druffel, M. K. Sunkara, Anti-reflective optical coatings incorporating nanoparticles, Nanotechnology 16 (7) (2005) S338.

[42] F. H. Stillinger Jr, Interfacial solutions of the Poisson-Boltzmann equation, J. Chem. Phys. 35 (5) (1961) 1584–1589.

[43] A. J. Hurd, The electrostatic interaction between interfacial colloidal particles, J. Phys. A: Math. Gen. 18 (16) (1985) L1055.

[44] K. Masschaele, B. J. Park, E. M. Furst, J. Fransaer, J. Vermant, Finite ion-size effects dominate the interaction between charged colloidal particles at an oil-water interface, Phys. Rev. Lett. 105 (4) (2010) 048303.

[45] B. J. Park, J. Vermant, E. M. Furst, Heterogeneity of the electrostatic repulsion between colloids at the oil–water interface, Soft Matter 6 (21) (2010) 5327–5333.

[46] J. I. Park, T. D. Nguyen, G. de Queirós Silveira, J. H. Bahng, S. Srivastava, G. Zhao, K. Sun, P. Zhang, S. C. Glotzer, N. A. Kotov, Terminal supraparticle assemblies from similarly charged protein molecules and nanoparticles, Nat. Commun. 5.

[47] K. Simons, E. Ikonen, Functional rafts in cell membranes, Nature 387 (1997) 569–572.

[48] D. Lingwood, K. Simons, Lipid rafts as a membrane-organizing principle, Science 327 (5961) (2010) 46–50.

[49] K. Simons, D. Toomre, Lipid rafts and signal transduction, Nat. Rev. Mol. Cell Biol. 1 (1) (2000) 31.

[50] K. A. Melkonian, A. G. Ostermeyer, J. Z. Chen, M. G. Roth, D. A. Brown, Role of lipid modifications in targeting proteins to detergent-resistant membrane rafts many raft proteins are acylated, while few are prenylated, J. Biol. Chem. 274 (6) (1999) 3910–3917.

[51] A. Ono, E. O. Freed, Plasma membrane rafts play a critical role in hiv-1 assembly and release, Proc. Natl. Acad. Sci. U. S. A. 98 (24) (2001) 13925–13930.

[52] T. Baumgart, S. T. Hess, W. W. Webb, Imaging coexisting fluid domains in biomembrane models coupling curvature and line tension, Nature 425 (6960) (2003) 821–824.

[53] A. A. Bischof, N. Wilke, Molecular determinants for the line tension of coexisting liquid phases in monolayers, Chem. Phys. Lipids 165 (7) (2012) 737–744.

[54] A. Mangiarotti, B. Caruso, N. Wilke, Phase coexistence in films composed of dlpc and dppc: a comparison between different model membrane systems, Biochim. Biophys. Acta, Biomembr. 1838 (7) (2014) 1823–1831.

[55] P. Dhar, V. Prasad, E. R. Weeks, T. Bohlein, T. M. Fischer, Immersion of charged nanoparticles in a salt solution/air interface, J. Phys. Chem. B 112 (32) (2008) 9565–9567.

[56] G. V. Bossa, M. A. Brown, K. Bohinc, S. May, Modeling the electrostatic contribution to the line tension between lipid membrane domains using Poisson–Boltzmann theory, Int. J. Adv. Eng. Sci. App. Math. 8 (2) (2016) 101–110.

[57] A. Naydenov, P. A. Pincus, S. A. Safran, Equilibrium domains on heterogeneously charged surfaces, Langmuir 23 (24) (2007) 12016–12023.

[58] H. N. W. Lekkerkerker, Contribution of the electric double layer to the curvature elasticity of charged amphiphilic monolayers, Physica A. 159 (1989) 319–328.

[59] M. Winterhalter, W. Helfrich, Bending elasticity of electrically charged bilayers: coupled monolayers, neutral surfaces, and balancing stresses, J. Phys. Chem. 96 (1) (1992) 327–330.

[60] K. H. Kang, I. S. Kang, C. M. Lee, Electrostatic contribution to line tension in a wedge-shaped contact region, Langmuir 19 (22) (2003) 9334–9342.

[61] M. W. Lee, M. Han, G. V. Bossa, C. Snell, Z. Song, H. Tang, L. Yin, J. Cheng, S. May, E. Luijten, et al., Interactions between membranes and "metaphilic" polypeptide architectures with diverse side-chain populations, ACS Nano 11 (3) (2017) 2858–2871.

[62] S. M. K. Davidson, S. L. Regen, Nearest-neighbor recognition in phospholipid membranes, Chemical Reviews 97 (5) (1997) 1269–1279.

[63] H. T. Davis, Statistical mechanics of phases, interfaces, and thin films, Wiley-VCH, 1996.

[64] D. E. Smith, L. X. Dang, Computer simulations of nacl association in polarizable water, J. Chem. Phys. 100 (5) (1994) 3757–3766.

[65] I. Kalcher, J. Dzubiella, Structure-thermodynamics relation of electrolyte solutions, J. Chem. Phys. 130 (13) (2009) 134507.

[66] W. Kunz, R. Neueder, An attempt of a general overview, in: W. Kunz (Ed.), Specific Ion Effects, World Scentific, Singapore, 2010, chapter 1, pp. 3–54.

[67] I. Kalcher, J. C. F. Schulz, J. Dzubiella, Ion-specific Excluded-Volume Correlations and Solvation forces, Phys. Rev. Lett. 104 (9) (2010) 097802.

[68] J. Sala, E. Guardia, J. Marti, Effects of concentration on structure, dielectric, and dynamic properties of aqueous nacl solutions using a polarizable model, J. Chem. Phys. 132 (21) (2010) 214505.

[69] F. Hofmeister, Zur Lehre von der Wirkung der Salze., Arch. Exptl. Pathol. Pharmakol. 24 (1888) 247–260.

[70] X. F. Zhang, S. H. Yang, Nonspecific Adsorption of Charged Quantum Dots on Supported Zwitterionic Lipid Bilayers: Real-Time Monitoring by Quartz Crystal Microbalance with dissipation, Langmuir 27 (6) (2011) 2528–2535.

[71] R. R. Netz, D. Horinek, Progress in Modeling of Ion Effects at the Vapor/Water interface, Annu. Rev. Phys. Chem. 63 (2012) 401–418.

[72] J. R. Macdonald, Comparison and discussion of some theories of the equilibrium electrical double-layer in liquid electrolytes, J. Electroanalytical Chem. 223 (1-2) (1987) 1–23.

[73] E. Ruckenstein, M. Manciu, The coupling between the hydration and double layer interactions, Langmuir 18 (20) (2002) 7584–7593.

[74] F. Paillusson, R. Blossey, Slits, plates, and Poisson-Boltzmann theory in a local formulation of non-local electrostatics, Phys. Rev. E 82 (5) (2010) 052501.

[75] A. Abrashkin, D. Andelman, H. Orland, Dipolar Poisson-Boltzmann equation: Ions and dipoles close to charge interfaces, Phys. Rev. Lett. 99 (7) (2007) 077801.

[76] C. Azuara, H. Orland, M. Bon, P. Koehl, M. Delarue, Incorporating dipolar solvents with variable density in Poisson-Boltzmann electrostatics, Biophys. J. 95 (12) (2008) 5587–5605.

[77] D. H. Mengistu, K. Bohinc, S. May, Poisson-Boltzmann model in a solvent of interacting Langevin dipoles, Europhys. Lett. 88 (1) (2009) 14003.

[78] K. Bohinc, A. Shrestha, M. Brumen, S. May, Poisson-helmholtz-boltzmann model of the electric double layer: Analysis of monovalent ionic mixtures, Phys. Rev. E 85 (3) (2012) 031130.

[79] J. Bikerman, Structure and capacity of electrical double layer, Philos. Mag. (1798-1977) 33 (220) (1942) 384–397.

[80] I. Borukhov, D. Andelman, H. Orland, Steric effects in electrolytes: A modified Poisson-Boltzmann equation, Phys. Rev. Lett. 79 (3) (1997) 435–438.

[81] N. F. Carnahan, K. E. Starling, Equation of state for nonattracting rigid spheres, J. Chem. Phys. 51 (2) (1969) 635–636.

[82] T. Boublík, Hard-sphere equation of state, J. Chem. Phys. 53 (1) (1970) 471–472.

[83] G. Mansoori, N. Carnahan, K. Starling, T. Leland Jr, Equilibrium thermodynamic properties of the mixture of hard spheres, J. Chem. Phys. 54 (4) (1971) 1523–1525.

[84] G. A. Mansoori, N. Kioussis, A new thermodynamic model for the hard-core fluid with a Yukawa tail, J. Chem. Phys. 82 (4) (1985) 2076–2081.

[85] D. J. Griffiths, Introduction to electrodynamics, Prentice Hall, 1962.

[86] T. L. Hill, An introduction to statistical thermodynamics, Courier Corporation, 1960.

[87] K. Bohinc, G. V. Bossa, S. May, Incorporation of ion and solvent structure into mean-field modeling of the electric double layer, Adv. Colloid Interface Sci.doi:10.1016/j.cis.2017.05.001.

[88] G. Minton, L. Lue, The influence of excluded volume and excess ion polarisability on the capacitance of the electric double layer, Mol. Phys. 114 (16-17) (2016) 2477–2491.

[89] J. Dufreche, J. Simonin, P. Turq, Sedimentation of charged colloids in the gravitational field: Relaxation toward equilibrium., J. Mol. Liq. 79 (2) (1999) 137–149.

[90] L. Lue, N. Zoeller, D. Blankschtein, Incorporation of nonelectrostatic interactions in the Poisson-Boltzmann equation, Langmuir 15 (11) (1999) 3726–3730.

[91] P. Biesheuvel, M. Van Soestbergen, Counterion volume effects in mixed electrical double layers, J. Colloid Interface Sci. 316 (2) (2007) 490–499.

[92] J. I. Kilpatrick, S.-H. Loh, S. P. Jarvis, Directly probing the effects of ions on hydration forces at interfaces, J. Am. Chem. Soc. 135 (7) (2013) 2628–2634.

[93] I. Siretanu, D. Ebeling, M. P. Andersson, S. S. Stipp, A. Philipse, M. C. Stuart, D. Van Den Ende, F. Mugele, Direct observation of ionic structure at solid-liquid interfaces: a deep look into the Stern layer, Sci. Rep. 4 (2014) 4956.

[94] T. Baimpos, B. R. Shrestha, S. Raman, M. Valtiner, Effect of interfacial ion structuring on range and magnitude of electric double layer, hydration, and adhesive interactions between mica surfaces in 0.05–3 m li+ and cs+ electrolyte solutions, Langmuir 30 (15) (2014) 4322–4332.

[95] C. Duclairoir, A.-M. Orecchioni, P. Depraetere, F. Osterstock, E. Nakache, Evaluation of gliadins nanoparticles as drug delivery systems: a study of three different drugs, Int. J. Pharm. (Amsterdam, Neth.) 253 (1) (2003) 133–144.

[96] P. M. Ajayan, L. S. Schadler, P. V. Braun, Nanocomposite science and technology, John Wiley & Sons, 2006.

[97] A. E. Nel, L. Mädler, D. Velegol, T. Xia, E. M. Hoek, P. Somasundaran, F. Klaessig, V. Castranova, M. Thompson, Understanding biophysicochemical interactions at the nano–bio interface, Nat. Mater. 8 (7) (2009) 543–557.

[98] M. Lundqvist, J. Stigler, G. Elia, I. Lynch, T. Cedervall, K. A. Dawson, Nanoparticle size and surface properties determine the protein corona with possible implications for biological impacts, Proc. Natl. Acad. Sci. U. S. A. 105 (38) (2008) 14265–14270.

[99] B. P. Binks, T. S. Horozov, Colloidal particles at liquid interfaces, Cambridge University Press, 2006.

[100] M. Oettel, S. Dietrich, Colloidal interactions at fluid interfaces, Langmuir 24 (4) (2008) 1425–1441.

[101] R. Aveyard, B. Binks, J. Clint, P. Fletcher, T. Horozov, B. Neumann, V. Paunov, J. Annesley, S. Botchway, D. Nees, et al., Measurement of long-range repulsive forces between charged particles at an oil-water interface, Phys. Rev. Lett. 88 (24) (2002) 246102.

[102] K. D. Danov, P. A. Kralchevsky, Electric forces induced by a charged colloid particle attached to the water–nonpolar fluid interface, J. Colloid Interface Sci. 298 (1) (2006) 213–231.

[103] K. D. Danov, P. A. Kralchevsky, Forces acting on dielectric colloidal spheres at a water/nonpolar fluid interface in an external electric field. 2. charged particles, J. Colloid Interface Sci. 405 (2013) 269–277.

[104] K. D. Danov, P. A. Kralchevsky, M. P. Boneva, Electrodipping force acting on solid particles at a fluid interface, Langmuir 20 (15) (2004) 6139–6151.

[105] S. Uppapalli, H. Zhao, The influence of particle size and residual charge on electrostatic interactions between charged colloidal particles at an oil–water interface, Soft Matter 10 (25) (2014) 4555–4560.

[106] A. Majee, M. Bier, S. Dietrich, Electrostatic interaction between colloidal particles trapped at an electrolyte interface, J. Chem. Phys. 140 (16) (2014) 164906.

[107] D. Frydel, S. Dietrich, M. Oettel, Charge renormalization for effective interactions of colloids at water interfaces, Phys. Rev. Lett. 99 (11) (2007) 118302.

[108] A. Dominguez, D. Frydel, M. Oettel, Multipole expansion of the electrostatic interaction between charged colloids at interfaces, Phys. Rev. E 77 (2) (2008) 020401.

[109] V. Buch, A. Milet, R. Vácha, P. Jungwirth, J. P. Devlin, Water surface is acidic, Proc. Natl. Acad. Sci. U. S. A. 104 (18) (2007) 7342–7347.

[110] J. K. Beattie, A. M. Djerdjev, G. G. Warr, The surface of neat water is basic, Faraday Discuss. 141 (2009) 31–39.

[111] M. Paluch, Electrical properties of free surface of water and aqueous solutions, Adv. Colloid Interface Sci. 84 (1-3) (2000) 27–45.

[112] T. Gehring, T. M. Fischer, Diffusion of Nanoparticles at an Air/Water Interface Is Not Invariant under a Reversal of the Particle charge, J. Phys. Chem. C 115 (48) (2011) 23677–23681.

[113] S. M. Kathmann, I. F. W. Kuo, C. J. Mundy, Electronic Effects on the Surface Potential at the Vapor-Liquid Interface of water, J. Am. Chem. Soc. 130 (49) (2008) 16556–16561.

[114] J. D. Jackson, J. D. Jackson, Classical electrodynamics, Vol. 3, Wiley New York etc., 1962.

[115] W. Byerly, An elementary treatise on Fourier's series: and spherical, cylindrical, and ellipsoidal harmonics, with applications to problems in mathematical physics, New York: Dover Publications, 1959.

[116] T. S. Horozov, R. Aveyard, J. H. Clint, B. P. Binks, Order-disorder transition in monolayers of modified monodisperse silica particles at the octane-water interface, Langmuir 19 (7) (2003) 2822–2829.

[117] D. Frydel, M. Oettel, Charged particles at fluid interfaces as a probe into structural details of a double layer, Phys. Chem. Chem. Phys. 13 (9) (2011) 4109–4118.

[118] B. P. Binks, T. S. Horozov, Colloidal Particles at Liquid Interfaces, Cambridge University Press, 2006.

[119] F. Bresme, M. Oettel, Nanoparticles at fluid interfaces, J. Phys.: Condens. Matter 19 (41) (2007) 413101.

[120] I. A. Hamley, Introduction to Soft Matter, Wiley, 2008.

[121] B. S. Murray, R. Ettelaie, Foam stability: Proteins and nanoparticles, Curr. Opin. Colloid Interface Sci. 9 (5) (2004) 314–320.

[122] E. M. Herzig, K. A. White, A. B. Schofield, W. C. K. Poon, P. S. Clegg, Bicontinuous emulsions stabilized solely by colloidal particles, Nat. Mater. 6 (12) (2007) 966–971.

[123] Y. W. Kim, J. Yi, P. A. Pincus, Attractions between like-charged surfaces with dumbbell-shaped counterions, Phys. Rev. Lett. 101 (20) (2008) 208305.

[124] Y. Lin, H. Skaff, T. Emrick, A. Dinsmore, T. Russell, Nanoparticle assembly and transport at liquid-liquid interfaces, Science 299 (5604) (2003) 226–229.

[125] R. McGorty, J. Fung, D. Kaz, V. N. Manoharan, Colloidal self-assembly at an interface, Mater. Today 13 (6) (2010) 34–42.

[126] J. H. Fendler, Nanoparticles at air/water interfaces, Curr. Opin. Colloid Interface Sci. 1 (2) (1996) 202–207.

[127] C. Monat, P. Domachuk, B. Eggleton, Integrated optofluidics: A new river of light, Nat. Photonics 1 (2) (2007) 106–114.

[128] B. P. Binks, Particles as surfactants – similarities and differences, Curr. Opin. Colloid Interface Sci. 7 (1) (2002) 21–41.

[129] M. Oettel, S. Dietrich, Colloidal interactions at fluid interfaces, Langmuir 24 (4) (2008) 1425–1441.

[130] E. J. W. Verwey, J. T. G. Overbeek, Theory of the Stability of Lyophobic Colloids, Elsevier, Elsevier, New York, 1948.

[131] D. F. Evans, H. Wennerström, The colloidal domain, where physics, chemistry, and biology meet, 2nd Edition, VCH publishers, 1994.

[132] K. D. Danov, P. A. Kralchevsky, M. P. Boneva, Electrodipping force acting on solid particles at a fluid interface, Langmuir 20 (15) (2004) 6139–6151.

[133] G. V. Bossa, J. Roth, K. Bohinc, S. May, The apparent charge of nanoparticles trapped at a water interface, Soft Matter 12 (18) (2016) 4229–4240.

[134] S. Singer, G. Nicolson, The fluid mosaic model of the structure of cell membranes., Science 175 (4023) (1972) 720.

[135] D. Deamer, J. P. Dworkin, S. A. Sandford, M. P. Bernstein, L. J. Allamandola, The first cell membranes, Astrobiology 2 (4) (2002) 371–381.

[136] B. Alberts, D. Bray, K. Hopkin, A. Johnson, J. Lewis, M. Raff, K. Roberts, P. Walter, Essential Cell Biology, Garland Science, 2013.

[137] G. van Meer, Cellular lipidomics, EMBO J. 24 (18) (2005) 3159–3165.

[138] K. Jacobson, O. G. Mouritsen, R. G. Anderson, Lipid rafts: at a crossroad between cell biology and physics, Nat. Cell Biol. 9 (1) (2007) 7–14.

[139] A. J. García-Sáez, S. Chiantia, P. Schwille, Effect of line tension on the lateral organization of lipid membranes, J. Biol. Chem. 282 (46) (2007) 33537–33544.

[140] J. E. Vance, D. E. Vance, Biochemistry of Lipids, Lipoproteins and Membranes, Elsevier, 2008.

[141] S. L. Veatch, S. L. Keller, Miscibility phase diagrams of giant vesicles containing sphingomyelin, Phys. Rev. Lett. 94 (14) (2005) 148101.

[142] S. Chiantia, N. Kahya, J. Ries, P. Schwille, Effects of ceramide on liquid-ordered domains investigated by simultaneous afm and fcs, Biophys. J. 90 (12) (2006) 4500–4508.

[143] C. Dietrich, L. Bagatolli, Z. Volovyk, N. Thompson, M. Levi, K. Jacobson, E. Gratton, Lipid rafts reconstituted in model membranes, Biophys. J. 80 (3) (2001) 1417–1428.

[144] P. I. Kuzmin, S. A. Akimov, Y. A. Chizmadzhev, J. Zimmerberg, F. S. Cohen, Line tension and interaction energies of membrane rafts calculated from lipid splay and tilt, Biophys. J. 88 (2) (2005) 1120–1133.

[145] N. Wilke, Lipid monolayers at the air–water interface: A tool for understanding electrostatic interactions and rheology in biomembranes, Adv. in Planar Lipid Bilayers and Liposomes 20 (2014) 51.

[146] R. Lipowsky, Budding of membranes induced by intramembrane domains, J. Phys. II 2 (10) (1992) 1825–1840.

[147] D. Vind-Kezunovic, C. H. Nielsen, U. Wojewodzka, R. Gniadecki, Line tension at lipid phase boundaries regulates formation of membrane vesicles in living cells, Biochim. Biophys. Acta, Biomembr. 1778 (11) (2008) 2480–2486.

[148] J. B. Hutchison, R. M. Weis, A. D. Dinsmore, Change of line tension in phase-separated vesicles upon protein binding, Langmuir 28 (11) (2012) 5176–5181.

[149] F. Dumas, M. M. Sperotto, M.-C. Lebrun, J.-F. Tocanne, O. G. Mouritsen, Molecular sorting of lipids by bacteriorhodopsin in dilauroylphosphatidylcholine/distearoylphosphatidylcholine lipid bilayers., Biophys. J. 73 (4) (1997) 1940.

[150] E. C. Mbamala, A. Ben-Shaul, S. May, Domain formation induced by the adsorption of charged proteins on mixed lipid membranes, Biophys. J. 88 (3) (2005) 1702–1714.

[151] K. B. Towles, N. Dan, Line tension and coalescence in heterogeneous membranes, Langmuir 23 (26) (2007) 13053–13058.

[152] C. L. Baciu, S. May, Stability of charged, mixed lipid bilayers: effect of electrostatic coupling between the monolayers, J. Phys.: Condens. Matter 16 (26) (2004) S2455.

[153] M. K. Doeven, J. H. Folgering, V. Krasnikov, E. R. Geertsma, G. van den Bogaart, B. Poolman, Distribution, lateral mobility and function of membrane proteins incorporated into giant unilamellar vesicles, Biophys. J. 88 (2) (2005) 1134–1142.

[154] M. I. Kontorovich, N. N. Lebedev, On the one method of solution for some problems in diffraction theory and related problems, J. Exp. Theor. Phys. 8 (10) (1938) 1192–1206.

[155] A. Tian, C. Johnson, W. Wang, T. Baumgart, Line tension at fluid membrane domain boundaries measured by micropipette aspiration, Phys. Rev. Lett. 98 (20) (2007) 208102.

[156] S. May, Curvature elasticity and thermodynamic stability of electrically charged membranes, J. Chem. Phys. 105 (1996) 8314–8322.

[157] M. I. Kontorovich, N. N. Lebedev, On the application of inversion formulae to the solution of some electrodynamics problems, J. Exp. Theor. Phys. 9 (6) (1939) 729–742.

[158] N. D. Fowkes, M. J. Hood, Surface tension effects in a wedge, Q. J. Mech. Appl. Math. 51 (4) (1998) 553–561.

[159] B. Duplantier, Can one “hear”the thermodynamics of a (rough) colloid?, Phys. Rev. Lett. 66 (12) (1991) 1555.

[160] K. Simons, M. J. Gerl, Revitalizing membrane rafts: new tools and insights, Nat. Rev. Mol. Cell. Biol. 11 (10) (2010) 688–699.

[161] A. Kusumi, T. K. Fujiwara, N. Morone, K. J. Yoshida, R. Chadda, M. Xie, R. S. Kasai, K. G. Suzuki, Membrane mechanisms for signal transduction: the coupling of the meso-scale raft domains to membrane-skeleton-induced compartments and dynamic protein complexes, in: Semin. Cell Dev. Biol., no. 2, Elsevier, 2012, pp. 126–144.

[162] S. L. Veatch, S. L. Keller, Seeing spots: Complex phase behavior in simple membranes, Biochim. Biophys. Acta 1746 (3) (2005) 172–185.

[163] P. F. F. Almeida, Thermodynamics of lipid interactions in complex bilayers, Biochim. Biophys. Acta, Biomembr. 1788 (1) (2009) 72–85.

[164] W. D. Bennett, D. P. Tieleman, Computer simulations of lipid membrane domains, Biochim. Biophys. Acta, Biomembr. 1828 (8) (2013) 1765–1776.

[165] S. Komura, D. Andelman, Physical aspects of heterogeneities in multi-component lipid membranes, Adv. Colloid Interface Sci. 208 (2014) 34–46.

[166] P. F. F. Almeida, W. L. C. Vaz, T. E. Thompson, Lateral diffusion and percolation in two-phase, two-component lipid bilayers. topology of the solid-phase domains in-plane and across the lipid bilayer, Biochemistry 31 (31) (1992) 7198–7210.

[167] J. Korlach, P. Schwille, W. W. Webb, G. W. Feigenson, Characterization of lipid bilayer phases by confocal microscopy and fluorescence correlation spectroscopy, Proc. Nat. Acad. Sci. USA 96 (15) (1999) 8461–8466.

[168] M. D. Collins, S. L. Keller, Tuning lipid mixtures to induce or suppress domain formation across leaflets of unsupported asymmetric bilayers, Proc. Nat. Acad. Sci. USA 105 (1) (2008) 124–128.

[169] V. Kiessling, C. Wan, L. K. Tamm, Domain coupling in asymmetric lipid bilayers, Biochim. Biophys. Acta, Biomembr. 1788 (1) (2009) 64–71.

[170] I. Visco, S. Chiantia, P. Schwille, Asymmetric supported lipid bilayer formation via methyl-β-cyclodextrin mediated lipid exchange: influence of asymmetry on lipid dynamics and phase behavior, Langmuir 30 (25) (2014) 7475–7484.

[171] N. F. Hussain, A. P. Siegel, Y. Ge, R. Jordan, C. A. Naumann, Bilayer asymmetry influences integrin sequestering in raft-mimicking lipid mixtures, Biophys. J. 104 (10) (2013) 2212–2221.

[172] K. M. Spillane, J. Ortega-Arroyo, G. de Wit, C. Eggeling, H. Ewers, M. I. Wallace, P. Kukura, High-speed single-particle tracking of gm1 in model membranes reveals anomalous diffusion due to interleaflet coupling and molecular pinning, Nano Letters 14 (9) (2014) 5390–5397.

[173] M. R. Krause, S. L. Regen, The structural role of cholesterol in cell membranes: from condensed bilayers to lipid rafts, Acc. Chem. Res. 47 (12) (2014) 3512–3521.

[174] T. A. Daly, P. F. Almeida, S. L. Regen, Sorting of lipidated peptides in fluid bilayers: A molecular-level investigation, J. Am. Chem. Soc. 134 (41) (2012) 17245–17252.

[175] O. G. Mouritsen, M. Bloom, Mattress model of lipid-protein interactions in membranes, Biophys. J. 46 (2) (1984) 141–153.

[176] K. Jørgensen, M. M. Sperotto, O. G. Mouritsen, J. H. Ipsen, M. J. Zuckermann, Phase equilibria and local structure in binary lipid bilayers, Biochim. Biophys. Acta, Biomembr. 1152 (1) (1993) 135–145.

[177] J. B. Zhang, B. W. Jing, N. Tokutake, S. L. Regen, Transbilayer complementarity of phospholipids. A look beyond the fluid mosaic model, J. Am. Chem. Soc. 126 (35) (2004) 10856–10857.

[178] J. B. Zhang, B. W. Jing, S. L. Regen, Transbilayer complementarity of phospholipids. Proof of principle, Langmuir 21 (20) (2005) 8983–8986.

[179] M. J. Stevens, Complementary matching in domain formation within lipid bilayers, J. Am. Chem. Soc. 127 (44) (2005) 15330–15331.

[180] J. D. Perlmutter, J. N. Sachs, Interleaflet interaction and asymmetry in phase separated lipid bilayers: molecular dynamics simulations, J. Am. Chem. Soc. 133 (17) (2011) 6563–6577.

[181] K. Khanna, T. T. Chang, J. T. Kindt, Complementarity and clustering in a simple model mixed bilayer, J. Chem. Phys. 124 (3) (2006) 036102.

[182] J. de Joannis, Y. Jiang, F. C. Yin, J. T. Kindt, Equilibrium distributions of dipalmitoyl phosphatidylcholine and dilauroyl phosphatidylcholine in a mixed lipid bilayer: Atomistic semigrand canonical ensemble simulations, J. Phys. Chem. B 110 (51) (2006) 25875–25882.

[183] J. J. Williamson, P. D. Olmsted, Registered and antiregistered phase separation of mixed amphiphilic bilayers, Biophys. J. 108 (8) (2015) 1963–1976.

[184] P. Garidel, C. Johann, A. Blume, Thermodynamics of lipid organization and domain formation in phospholipid bilayers, J. Liposome Research 10 (2-3) (2000) 131–158.

[185] J. Skolnick, A. Godzik, L. Jaroszewski, A. Kolinski, Derivation and testing of pair potentials for protein folding. when is the quasichemical approximation correct?, Protein Sci. 6 (3) (1997) 676–688.

[186] A. D. Pelton, S. A. Degterov, G. Eriksson, C. Robelin, Y. Dessureault, The modified quasichemical model i—binary solutions, Metall. Trans. B 31 (4) (2000) 651–659.

[187] I. P. Sugár, G. Monticelli, Landau theory of two-component phospholipid bilayers: I. phosphatidylcholine/phosphatidylethanolamine mixtures, Biophys. Chemistry 18 (4) (1983) 281–289.

[188] T. L. Hill, Introduction to Statistical Thermodynamics, Addison-Wesley, New-York, 1960.

[189] H. T. Davis, Statistical Mechanics of Phases, Interfaces and Thin Films, VCH publishers, New-York, 1996.

[190] C. Tanford, The Hydrophobic Effect, 2nd Edition, Wiley-Interscience, New-York, 1980.

[191] E. Evans, D. Needham, Physical properties of surfactant bilayer membranes: Thermal transitions, elasticity, rigidity, cohesion, and colloidal interactions, J. Phys. Chem. 91 (1987) 4219–4228.

[192] M. D. Collins, Interleaflet coupling mechanisms in bilayers of lipids and cholesterol, Biophys. J. 94 (5) (2008) L32–L34.

[193] H. J. Risselada, S. J. Marrink, The molecular face of lipid rafts in model membranes, Proc. Nat. Acad. Sci. USA 105 (2008) 17367–17372.

[194] S. May, Trans-monolayer coupling of fluid domains in lipid bilayers, Soft Matter 5 (17) (2009) 3148–3156.

[195] C. F. Schmidt, Y. Barenholz, C. Huang, T. E. Thompson, Monolayer coupling in sphingomyelin bilayer systems, Nature (271) (1978) 775–777.

[196] L. O. Sillerud, R. E. Barnett, Lack of transbilayer coupling in phase transitions of phosphatidylcholine vesicles, Biochemistry 21 (8) (1982) 1756–1760.

[197] A. J. Wagner, S. Loew, S. May, Influence of monolayer-monolayer coupling on the phase behavior of a fluid lipid bilayer, Biophys. J. 93 (12) (2007) 4268–4277.

[198] G. G. Putzel, M. Schick, Phase behavior of a model bilayer membrane with coupled leaves, Biophys. J. 94 (3) (2008) 869–877.

[199] A. Zeiger, B. E. Layton, Molecular modeling of the axial and circumferential elastic moduli of tubulin, Biophys. J. 95 (8) (2008) 3606–3618.

[200] M. Guthold, W. Liu, E. Sparks, L. Jawerth, L. Peng, M. Falvo, R. Superfine, R. Hantgan, S. Lord, A comparison of the mechanical and structural properties of fibrin fibers with other protein fibers, Cell Biochem. Biophys. 49 (3) (2007) 165–181.

[201] F. Gittes, B. Mickey, J. Nettleton, J. Howard, Flexural rigidity of microtubules and actin filaments measured from thermal fluctuations in shape, J. Cell Biol. 120 (1993) 923–923.

[202] D. Vitkup, D. Ringe, G. A. Petsko, M. Karplus, Solvent mobility and the protein'glass' transition, Nat. Struct. Mol. Biol. 7 (1) (2000) 34–38.

[203] D. Ringe, G. A. Petsko, The 'glass transition'in protein dynamics: what it is, why it occurs, and how to exploit it, Biophys. Chem. 105 (2) (2003) 667–680.

[204] M. Zasloff, Antimicrobial peptides of multicellular organisms, nature 415 (6870) (2002) 389–395.

[205] K. A. Brogden, Antimicrobial peptides: pore formers or metabolic inhibitors in bacteria?, Nat. Rev. Microbiol. 3 (3) (2005) 238–250.

[206] R. E. Hancock, H.-G. Sahl, Antimicrobial and host-defense peptides as new anti-infective therapeutic strategies, Nat. Biotechnol. 24 (12) (2006) 1551–1557.

[207] M. W. Lee, S. Chakraborty, N. W. Schmidt, R. Murgai, S. H. Gellman, G. C. Wong, Two interdependent mechanisms of antimicrobial activity allow for efficient killing in nylon-3-based polymeric mimics of innate immunity peptides, Biochim. Biophys. Acta, Biomembr. 1838 (9) (2014) 2269–2279.

[208] Y. Shai, Mechanism of the binding, insertion and destabilization of phospholipid bilayer membranes by α-helical antimicrobial and cell non-selective membrane-lytic peptides, Biochim. Biophys. Acta, Biomembr. 1462 (1) (1999) 55–70.

[209] R. E. Hancock, R. Lehrer, Cationic peptides: a new source of antibiotics, Trends Biotechnol. 16 (2) (1998) 82–88.

[210] F. Milletti, Cell-penetrating peptides: classes, origin, and current landscape, Drug discovery today 17 (15) (2012) 850–860.

[211] E. Koren, V. P. Torchilin, Cell-penetrating peptides: breaking through to the other side, Trends Mol. Med. 18 (7) (2012) 385–393.

[212] C. Bechara, S. Sagan, Cell-penetrating peptides: 20years later, where do we stand?, FEBS Lett. 587 (12) (2013) 1693–1702.

[213] S. Futaki, T. Suzuki, W. Ohashi, T. Yagami, S. Tanaka, K. Ueda, Y. Sugiura, Arginine-rich peptides an abundant source of membrane-permeable peptides having potential as carriers for intracellular protein delivery, J. Biol. Chem. 276 (8) (2001) 5836–5840.

[214] P. A. Wender, W. C. Galliher, E. A. Goun, L. R. Jones, T. H. Pillow, The design of guanidinium-rich transporters and their internalization mechanisms, Adv. Drug Delivery Rev. 60 (4) (2008) 452–472.

[215] D. M. Copolovici, K. Langel, E. Eriste, U. Langel, Cell-penetrating peptides: design, synthesis, and applications, ACS Nano 8 (3) (2014) 1972–1994.

[216] M. Pooga, Ü. Langel, Classes of cell-penetrating peptides, Cell-Penetrating Peptides: Methods and Protocols (2015) 3–28.

[217] E. Y. Lee, B. M. Fulan, G. C. Wong, A. L. Ferguson, Mapping membrane activity in undiscovered peptide sequence space using machine learning, Proc. Natl. Acad. Sci. U. S. A. (2016) 201609893.

[218] N. W. Schmidt, A. Mishra, J. Wang, W. F. DeGrado, G. C. Wong, Influenza virus a m2 protein generates negative gaussian membrane curvature necessary for budding and scission, J. Am. Chem. Soc. 135 (37) (2013) 13710–13719.

[219] H. Yao, M. W. Lee, A. J. Waring, G. C. Wong, M. Hong, Viral fusion protein transmembrane domain adopts β-strand structure to facilitate membrane topological changes for virus–cell fusion, Proc. Natl. Acad. Sci. U. S. A. 112 (35) (2015) 10926–10931.

[220] M. Xiong, M. W. Lee, R. A. Mansbach, Z. Song, Y. Bao, R. M. Peek, C. Yao, L.-F. Chen, A. L. Ferguson, G. C. Wong, et al., Helical antimicrobial polypeptides with radial amphiphilicity, Proc. Natl. Acad. Sci. U. S. A. 112 (43) (2015) 13155–13160.

[221] S. J. Lam, N. M. O'Brien-Simpson, N. Pantarat, A. Sulistio, E. H. Wong, Y.-Y. Chen, J. C. Lenzo, J. A. Holden, A. Blencowe, E. C. Reynolds, et al., Combating multidrug-resistant gram-negative bacteria with structurally nanoengineered antimicrobial peptide polymers, Nature microbiology 1 (2016) 16162.

[222] H. Zhao, Influence of nonelectrostatic ion-ion interactions on double-layer capacitance, Phys. Rev. E 86 (5) (2012) 051502.

[223] A. F. Saleh, A. Arzumanov, R. Abes, D. Owen, B. Lebleu, M. J. Gait, Synthesis and splice-redirecting activity of branched, arginine-rich peptide dendrimer conjugates of peptide nucleic acid oligonucleotides, Bioconjugate Chem. 21 (10) (2010) 1902–1911.

[224] D. Mandal, A. Nasrolahi Shirazi, K. Parang, Cell-penetrating homochiral cyclic peptides as nuclear-targeting molecular transporters, Angew. Chem., Int. Ed. 50 (41) (2011) 9633–9637.

[225] A. M. Angeles-Boza, A. Erazo-Oliveras, Y.-J. Lee, J.-P. Pellois, Generation of endosomolytic reagents by branching of cell-penetrating peptides: tools for the delivery of bioactive compounds to live cells in cis or trans, Bioconjugate Chem. 21 (12) (2010) 2164–2167.

[226] J. H. Bilgram, Dynamics at the solid-liquid transition: experiments at the freezing point, Phys. Rep. 153 (1) (1987) 1–89.

[227] Y. Zhou, M. Karplus, Folding thermodynamics of a model three-helix-bundle protein, Proc. Natl. Acad. Sci. U. S. A. 94 (26) (1997) 14429–14432.

[228] D. C. Leslie, A. Waterhouse, J. B. Berthet, T. M. Valentin, A. L. Watters, A. Jain, P. Kim, B. D. Hatton, A. Nedder, K. Donovan, et al., A bioinspired omniphobic surface coating on medical devices prevents thrombosis and biofouling, Nat. Biotechnol. 32 (11) (2014) 1134–1140.

[229] N. MacCallum, C. Howell, P. Kim, D. Sun, R. Friedlander, J. Ranisau, O. Ahanotu, J. J. Lin, A. Vena, B. Hatton, et al., Liquid-infused silicone as a biofouling-free medical material, ACS Biomater. Sci. Eng. 1 (1) (2014) 43–51.

[230] M. Nosonovsky, Materials science: Slippery when wetted, Nature 477 (7365) (2011) 412–413.

[231] V. Muñoz, F. J. Blanco, L. Serrano, The hydrophobic-staple motif and a role for loop-residues in α-helix stability and protein folding, Nat. Struct. Mol. Biol. 2 (5) (1995) 380–385.

[232] K. Matsuzaki, A. Nakamura, O. Murase, K.-i. Sugishita, N. Fujii, K. Miyajima, Modulation of magainin 2- lipid bilayer interactions by peptide charge, Biochemistry 36 (8) (1997) 2104–2111.

[233] F. Chiti, M. Stefani, N. Taddei, G. Ramponi, C. M. Dobson, Rationalization of the effects of mutations on peptide andprotein aggregation rates, Nature 424 (6950) (2003) 805–808.

[234] Y. Chen, C. T. Mant, S. W. Farmer, R. E. Hancock, M. L. Vasil, R. S. Hodges, Rational design of α-helical antimicrobial peptides with enhanced activities and specificity/therapeutic index, J. Biol. Chem. 280 (13) (2005) 12316–12329.

[235] L. M. Yin, M. A. Edwards, J. Li, C. M. Yip, C. M. Deber, Roles of hydrophobicity and charge distribution of cationic antimicrobial peptides in peptide-membrane interactions, J. Biol. Chem. 287 (10) (2012) 7738–7745.

[236] H. Lu, J. Wang, Y. Bai, J. W. Lang, S. Liu, Y. Lin, J. Cheng, Ionic polypeptides with unusual helical stability, Nat. Commun. 2 (2011) 206.

[237] N. P. Gabrielson, H. Lu, L. Yin, D. Li, F. Wang, J. Cheng, Reactive and bioactive cationic α-helical polypeptide template for nonviral gene delivery, Angew. Chem. 124 (5) (2012) 1169–1173.

[238] H. Tang, L. Yin, K. H. Kim, J. Cheng, Helical poly (arginine) mimics with superior cell-penetrating and molecular transporting properties, Chemical science 4 (10) (2013) 3839–3844.

[239] B. Bechinger, Rationalizing the membrane interactions of cationic amphipathic antimicrobial peptides by their molecular shape, Current Opinion in Colloid & Interface Science 14 (5) (2009) 349–355.

[240] M. Dathe, M. Schümann, T. Wieprecht, A. Winkler, M. Beyermann, E. Krause, K. Matsuzaki, O. Murase, M. Bienert, Peptide helicity and membrane surface charge modulate the balance of electrostatic and hydrophobic interactions with lipid bilayers and biological membranes, Biochemistry 35 (38) (1996) 12612–12622.

[241] J. P. Segrest, H. De Loof, J. G. Dohlman, C. G. Brouillette, G. Anantharamaiah, Amphipathic helix motif: classes and properties, Proteins: Struct., Funct., Bioinf. 8 (2) (1990) 103–117.

[242] E. M. Tytler, J. Segrest, R. Epand, S.-Q. Nie, R. Epand, V. Mishra, Y. Venkatachalapathi, G. Anantharamaiah, Reciprocal effects of apolipoprotein and lytic peptide analogs on membranes. cross-sectional molecular shapes of amphipathic alpha helixes control membrane stability., J. Biol. Chem. 268 (29) (1993) 22112–22118.

[243] J. Zimmerberg, M. M. Kozlov, How proteins produce cellular membrane curvature, Nat. Rev. Mol. Cell. Biol. 7 (1) (2006) 9–19.

[244] F. Campelo, H. T. McMahon, M. M. Kozlov, The hydrophobic insertion mechanism of membrane curvature generation by proteins, Biophys. J. 95 (5) (2008) 2325–2339.

[245] A. Zemel, A. Ben-Shaul, S. May, Modulation of the spontaneous curvature and bending rigidity of lipid membranes by interfacially adsorbed amphipathic peptides, J. Phys. Chem. B 112 (23) (2008) 6988–6996.

[246] R. M. Epand, Y. Shai, J. P. Segrest, G. Anantharamiah, Mechanisms for the modulation of membrane bilayer properties by amphipathic helical peptides, Biopolymers 37 (5) (1995) 319–338.

[247] H.-C. Chen, J. H. Brown, J. L. Morell, C. Huang, Synthetic magainin analogues with improved antimicrobial activity, FEBS Lett. 236 (2) (1988) 462–466.

[248] S. E. Blondelle, R. A. Houghten, Design of model amphipathic peptides having potent antimicrobial activities, Biochemistry 31 (50) (1992) 12688–12694.

[249] G. Drin, B. Antonny, Amphipathic helices and membrane curvature, FEBS Lett. 584 (9) (2010) 1840–1847.

[250] N. W. Schmidt, M. Lis, K. Zhao, G. H. Lai, A. N. Alexandrova, G. N. Tew, G. C. Wong, Molecular basis for nanoscopic membrane curvature generation from quantum mechanical models and synthetic transporter sequences, J. Am. Chem. Soc. 134 (46) (2012) 19207–19216.

[251] A. Mishra, G. H. Lai, N. W. Schmidt, V. Z. Sun, A. R. Rodriguez, R. Tong, L. Tang, J. Cheng, T. J. Deming, D. T. Kamei, et al., Translocation of hiv tat peptide and analogues induced by multiplexed membrane and cytoskeletal interactions, Proc. Natl. Acad. Sci. U. S. A. 108 (41) (2011) 16883–16888.

[252] N. W. Schmidt, A. Mishra, G. H. Lai, M. Davis, L. K. Sanders, D. Tran, A. Garcia, K. P. Tai, P. B. McCray Jr, A. J. Ouellette, et al., Criterion for amino acid composition of defensins and antimicrobial peptides based on geometry of membrane destabilization, J. Am. Chem. Soc. 133 (17) (2011) 6720–6727.

[253] N. Schmidt, A. Mishra, G. H. Lai, G. C. Wong, Arginine-rich cell-penetrating peptides, FEBS Lett. 584 (9) (2010) 1806–1813.

[254] A. Mishra, V. D. Gordon, L. Yang, R. Coridan, G. C. Wong, Hiv tat forms pores in membranes by inducing saddle-splay curvature: Potential role of bidentate hydrogen bonding, Angew. Chem., Int. Ed. 47 (16) (2008) 2986–2989.

[255] G. Shearman, O. Ces, R. Templer, J. Seddon, Inverse lyotropic phases of lipids and membrane curvature, J. Phys.: Condens. Matter 18 (28) (2006) S1105.

[256] W. M. Gelbart, A. Ben-Shaul, D. Roux, Micelles, membranes, microemulsions, and monolayers, Springer Science & Business Media, 2012.

[257] T. Yeung, M. Terebiznik, L. M. Yu, J. Silvius, W. M. Abidi, M. Philips, T. Levine, A. Kapus, S. Grinstein, Receptor activation alters inner surface potential during phagocytosis, Science 313 (5785) (2006) 347–351.

[258] H. Jenssen, P. Hamill, R. E. Hancock, Peptide antimicrobial agents, Clin. Microbiol. Rev. 19 (3) (2006) 491–511.

[259] K. Hu, N. W. Schmidt, R. Zhu, Y. Jiang, G. H. Lai, G. Wei, E. F. Palermo, K. Kuroda, G. C. Wong, L. Yang, A critical evaluation of random copolymer mimesis of homogeneous antimicrobial peptides, Macromolecules 46 (5) (2013) 1908–1915.

[260] S. Hong, P. R. Leroueil, E. K. Janus, J. L. Peters, M.-M. Kober, M. T. Islam, B. G. Orr, J. R. Baker Jr, M. M. Banaszak Holl, Interaction of polycationic polymers with supported lipid bilayers and cells: nanoscale hole formation and enhanced membrane permeability, Bioconjugate Chem. 17 (3) (2006) 728–734.

[261] Y. Takechi, H. Yoshii, M. Tanaka, T. Kawakami, S. Aimoto, H. Saito, Physicochemical mechanism for the enhanced ability of lipid membrane penetration of polyarginine, Langmuir 27 (11) (2011) 7099–7107.

[262] H. D. Herce, A. E. Garcia, Molecular dynamics simulations suggest a mechanism for translocation of the hiv-1 tat peptide across lipid membranes, Proc. Natl. Acad. Sci. U. S. A. 104 (52) (2007) 20805–20810.

[263] H. D. Herce, A. E. Garcia, Cell penetrating peptides: how do they do it?, J. Biol. Phys. 33 (5) (2007) 345–356.

[264] H. Herce, A. Garcia, J. Litt, R. Kane, P. Martin, N. Enrique, A. Rebolledo, V. Milesi, Arginine-rich peptides destabilize the plasma membrane, consistent with a pore formation translocation mechanism of cell-penetrating peptides, Biophys. J. 97 (7) (2009) 1917–1925.

[265] K. Matsuzaki, O. Murase, K. Miyajima, Kinetics of pore formation by an antimicrobial peptide, magainin 2, in phospholipid bilayers, Biochemistry 34 (39) (1995) 12553–12559.

[266] M. Tang, A. J. Waring, M. Hong, Phosphate-mediated arginine insertion into lipid membranes and pore formation by a cationic membrane peptide from solid-state nmr, J. Am. Chem. Soc. 129 (37) (2007) 11438–11446.

[267] K. Matsuzaki, O. Murase, N. Fujii, K. Miyajima, Translocation of a channel-forming antimicrobial peptide, magainin 2, across lipid bilayers by forming a pore, Biochemistry 34 (19) (1995) 6521–6526.

[268] S. Deshayes, A. Heitz, M. C. Morris, P. Charnet, G. Divita, F. Heitz, Insight into the mechanism of internalization of the cell-penetrating carrier peptide pep-1 through conformational analysis, Biochemistry 43 (6) (2004) 1449–1457.

[269] E. Bárány-Wallje, J. Gaur, P. Lundberg, Ü. Langel, A. Gräslund, Differential membrane perturbation caused by the cell penetrating peptide tp10 depending on attached cargo, FEBS Lett. 581 (13) (2007) 2389–2393.

[270] A. Mirzoev, A. P. Lyubartsev, Effective solvent mediated potentials of na+ and cl- ions in aqueous solution: temperature dependence, Phys. Chem. Chem. Phys. 13 (13) (2011) 5722–5727.

[271] A. Walrant, A. Vogel, I. Correia, O. Lequin, B. E. Olausson, B. Desbat, S. Sagan, I. D. Alves, Membrane interactions of two arginine-rich peptides with different cell internalization capacities, Biochim. Biophys. Acta, Biomembr. 1818 (7) (2012) 1755–1763.

[272] S. Balayssac, F. Burlina, O. Convert, G. Bolbach, G. Chassaing, O. Lequin, Comparison of penetratin and other homeodomain-derived cell-penetrating peptides: interaction in a membrane-mimicking environment and cellular uptake efficiency, Biochemistry 45 (5) (2006) 1408–1420.

[273] V. Tiriveedhi, P. Butko, A fluorescence spectroscopy study on the interactions of the tat-ptd peptide with model lipid membranes, Biochemistry 46 (12) (2007) 3888–3895.

[274] J. C. Mai, H. Shen, S. C. Watkins, T. Cheng, P. D. Robbins, Efficiency of protein transduction is cell type-dependent and is enhanced by dextran sulfate, J. Biol. Chem. 277 (33) (2002) 30208–30218.

[275] S. E. Blondelle, K. Lohner, M.-I. Aguilar, Lipid-induced conformation and lipid-binding properties of cytolytic and antimicrobial peptides: determination and biological specificity, Biochim. Biophys. Acta, Biomembr. 1462 (1) (1999) 89–108.

[276] P. A. Wender, D. J. Mitchell, K. Pattabiraman, E. T. Pelkey, L. Steinman, J. B. Rothbard, The design, synthesis, and evaluation of molecules that enable or enhance cellular uptake: peptoid molecular transporters, Proc. Natl. Acad. Sci. U. S. A. 97 (24) (2000) 13003–13008.

[277] G. Tünnemann, G. Ter-Avetisyan, R. M. Martin, M. Stöckl, A. Herrmann, M. C. Cardoso, Live-cell analysis of cell penetration ability and toxicity of oligo-arginines, J. Pept. Sci. 14 (4) (2008) 469–476.

[278] D. J. Mitchell, L. Steinman, D. Kim, C. Fathman, J. Rothbard, Polyarginine enters cells more efficiently than other polycationic homopolymers, Chemical Biology & Drug Design 56 (5) (2000) 318–325.

[279] J. N. Israelachvili, D. J. Mitchell, B. W. Ninham, Theory of self-assembly of lipid bilayers and vesicles, Biochim. Biophys. Acta, Biomembr. 470 (2) (1977) 185–201.

[280] J. N. Israelachvili, H. Wennerstrom, Entropic forces between amphiphilic surfaces in liquids, J. Phys. Chem. 96 (2) (1992) 520–531.

[281] S. May, A molecular model for the line tension of lipid membranes, Eur. Phys. J. E: Soft Matter and Biological Physics 3 (1) (2000) 37–44.

[282] S. May, D. Harries, A. Ben-Shaul, The phase behavior of cationic lipid-DNA complexes, Biophys. J. 78 (4) (2000) 1681–1697.

[283] H. Lu, J. Cheng, Hexamethyldisilazane-mediated controlled polymerization of α-amino acid n-carboxyanhydrides, J. Am. Chem. Soc. 129 (46) (2007) 14114–14115.

[284] H. Lu, J. Cheng, N-trimethylsilyl amines for controlled ring-opening polymerization of amino acid n-carboxyanhydrides and facile end group functionalization of polypeptides, J. Am. Chem. Soc. 130 (38) (2008) 12562–12563.

[285] M. Zasloff, A. P. Adams, B. Beckerman, A. Campbell, Z. Han, E. Luijten, I. Meza, J. Julander, A. Mishra, W. Qu, et al., Squalamine as a broad-spectrum systemic antiviral agent with therapeutic potential, Proc. Natl. Acad. Sci. U. S. A. 108 (38) (2011) 15978–15983.

[286] J. Ilavsky, Nika: software for two-dimensional data reduction, J. App. Crystallogr. 45 (2) (2012) 324–328.

[287] The FIT2D home page, howpublished = `http://www.esrf.eu/computing/scientific/fit2d/`, note = Accessed November 21 2016.

[288] S. May, A. Ben-Shaul, A molecular model for lipid-mediated interaction between proteins in membranes, Phys. Chem. Chem. Phys. 2 (20) (2000) 4494–4502.

[289] W. Helfrich, Elastic properties of lipid bilayers: Theory and possible experiments, Z. Naturforsch. C 28 (1973) 693–703.

[290] J. Seddon, R. Templer, Polymorphism of lipid-water systems, Handbook of biological physics 1 (1995) 97–160.

[291] D. P. Tieleman, S.-J. Marrink, H. J. Berendsen, A computer perspective of membranes: molecular dynamics studies of lipid bilayer systems, Biochim. Biophys. Acta, Biomembr. 1331 (3) (1997) 235–270.

[292] G. Cevc, Membrane electrostatics, Biochim. Biophys. Acta 1031 (3) (1990) 311–382.

[293] V. Bloomfield, Dna condensation, Curr. Opin. Struct. Biol. 6 (3) (1996) 334–341.

[294] V. B. Teif, K. Bohinc, Condensed dna: Condensing the concepts, Prog. Biophys. Mol. Biol. 105 (2011) 208–222.

[295] J. C. Butler, T. Angelini, J. X. Tang, G. C. Wong, Ion multivalence and like-charge polyelectrolyte attraction, Phys. Rev. Lett. 91 (2) (2003) 028301.

[296] J. Tang, P. Janmey, A. Lyubartsev, L. Nordenskiold, Metal ion-induced lateral aggregation of filamentous viruses fd and m13, Biophys. J. 83 (1) (2002) 566–581.

[297] T. E. Angelini, H. Liang, W. Wriggers, G. C. Wong, Like-charge attraction between polyelectrolytes induced by counterion charge density waves, Proc. Natl. Acad. Sci. U. S. A. 100 (15) (2003) 8634–8637.

[298] I. Szilagyi, A. Sadeghpour, M. Borkovec, Destabilization of colloidal suspensions by multivalent ions and polyelectrolytes: from screening to overcharging, Langmuir 28 (15) (2012) 6211–6215.

[299] A. Sadeghpour, I. Szilagyi, M. Borkovec, Charging and aggregation of positively charged colloidal latex particles in presence of multivalent polycarboxylate anions, Z. Phys. Chem. 226 (7-8, SI) (2012) 597–612.

[300] E. F. Marques, O. Regev, A. Khan, M. d. G. Miguel, B. Lindman, Interactions between catanionic vesicles and oppositely charged polyelectrolytes phase behavior and phase structure, Macromolecules 32 (20) (1999) 6626–6637.

[301] F. Bordi, C. Cametti, S. Sennato, D. Viscomi, Polyion-induced liposomal vesicle aggregation: A radiowave dielectric relaxation study, J. Chem. Phys. 126 (2) (2007) 024902.

[302] A. Walter, C. J. Steer, R. Blumenthal, Polylysine induces ph-dependent fusion of acidic phospholipid vesicles: a model for polycation-induced fusion, Biochim. Biophys. Acta, Biomembr. 861 (1986) 319–330.

[303] D. Persson, P. E. Thorén, B. Nordén, Penetratin-induced aggregation and subsequent dissociation of negatively charged phospholipid vesicles, FEBS Lett. 505 (2) (2001) 307–312.

[304] W. M. Gelbart, R. F. Bruinsma, P. A. Pincus, V. A. Parsegian, Dna-inspired electrostatics, Phys. Today 53 (9) (2000) 38–44.

[305] J. O. Radler, I. Koltover, T. Salditt, C. R. Safinya, Structure of dna-cationic liposome complexes: Dna intercalation in multilamellar membranes in distinct interhelical packing regimes, Science 275 (5301) (1997) 810–814.

[306] S. Huebner, B. J. Battersby, R. Grimm, G. Cevc, Lipid-dna complex formation: reorganization and rupture of lipid vesicles in the presence of dna as observed by cryoelectron microscopy, Biophys. J. 76 (6) (1999) 3158–3166.

[307] L. Li, M. von Bergen, E. Mandelkow, E. Mandelkow, Structure, stability, and aggregation of paired helical filaments from tau protein and FTDP-17 mutants probed by tryptophan scanning mutagenesis, J. Biol. Chem. 277 (44) (2002) 41390–41400.

[308] N. Cuvillier, F. Rondelez, Breakdown of the Poisson-Boltzmann description for electrical double layers involving large multivalent ions, Thin Solid Films 327 (1998) 19–23.

[309] H. Boroudjerdi, Y.-W. Kim, A. Naji, R. R. Netz, X. Schlagberger, A. Serr, Statics and dynamics of strongly charged soft matter, Phys. Rep. 416 (3) (2005) 129–199.

[310] A. Naji, M. Kanduč, J. Forsman, R. Podgornik, Perspective: Coulomb fluids—weak coupling, strong coupling, in between and beyond, J. Chem. Phys. 139 (15) (2013) 150901.

[311] B. Hribar, V. Vlachy, Evidence of electrostatic attraction between equally charged macroions induced by divalent counterions, J. Phys. Chem. B 101 (18) (1997) 3457–3459.

[312] B. Shklovskii, Wigner crystal model of counterion induced bundle formation of rodlike polyelectrolytes, Phys. Rev. Lett. 82 (16) (1999) 3268–3271.

[313] A. Y. Grosberg, N. T. T, B. I. Shklovskii, Colloquium: The physics of charge inversion in chemical and biological systems, Rev. Mod. Phys. 74 (2) (2002) 329–345.

[314] R. Kjellander, S. Marcelja, Correlation and image charge effects in electric double-layers, Chem. Phys. Lett. 112 (1) (1984) 49–53.

[315] J. Wu, D. Bratko, J. Prausnitz, Interaction between like-charged colloidal spheres in electrolyte solutions, Proc. Natl. Acad. Sci. U. S. A. 95 (26) (1998) 15169–15172.

[316] P. Attard, D. Mitchell, B. Ninham, Beyond Poisson-Boltzmann - images and correlations in the electric double-layer .1. counterions only, J. Chem. Phys. 88 (8) (1988) 4987–4996.

[317] L. B. Bhuiyan, C. W. Outhwaite, Comparison of the modified Poisson–Boltzmann theory with recent density functional theory and simulation results in the planar electric double layer, Phys. Chem. Chem. Phys. 6 (13) (2004) 3467–3473.

[318] M. Stevens, M. Robbins, Density functional theory of ionic screening - when do like charges attract, Europhys. Lett. 12 (1) (1990) 81–86.

[319] A. G. Moreira, R. R. Netz, Binding of similarly charged plates with counterions only, Phys. Rev. Lett. 87 (7) (2001) 078301–078304.

[320] M. M. Hatlo, L. Lue, A field theory for ions near charged surfaces valid from weak to strong couplings, Soft Matter 5 (1) (2009) 125–133. doi:{10.1039/b815578j}.

[321] L. Belloni, O. Spalla, Attraction of pure electrostatic origin between small colloids, Ber. Bunsen-Ges. 100 (6) (1996) 905–908, 1st International Symposium on Polyelectrolytes/Discussion Meeting of Deutsche-Bunsen-Gesellschaft-fur-Physikalische-Chemie on Polyelectrolytes in Solution and at Interfaces, POTSDAM, GERMANY, SEP 18-22, 1995.

[322] J. Rescic, V. Vlachy, L. Bhuiyan, C. Outhwaite, Monte Carlo simulation studies of electrolyte in mixture with a neutral component, J. Chem. Phys. 107 (9) (1997) 3611–3618.

[323] L. Bhuiyan, C. Outhwaite, Thermodynamics and phase separation of a de-ionized colloidal system in the symmetric Poisson-Boltzmann and mean spherical approximation theories, J. Chem. Phys. 116 (6) (2002) 2650–2657.

[324] K. Bohinc, A. Iglič, S. May, Interaction between macroions mediated by divalent rod-like ions, Europhys. Lett. 68 (4) (2004) 494–500.

[325] S. May, A. Iglič, J. Reščič, S. Maset, K. Bohinc, Bridging like-charged macroions through long divalent rodlike ions, J. Phys. Chem. B 112 (6) (2008) 1685–1692.

[326] S. Maset, J. Rescic, S. May, J. I. Pavlic, K. Bohinc, Attraction between like-charged surfaces induced by orientational ordering of divalent rigid rod-like counterions: theory and simulations, J. Phys. A: Math. Theor. 42 (10).

[327] V. Démery, D. S. Dean, R. Podgornik, Electrostatic interactions mediated by polarizable counterions: weak and strong coupling limits, J. Chem. Phys. 137 (17) (2012) 174903.

[328] V. Freise, Zur theorie der diffusen doppeltschicht, Z. Elektrochem. 56 (1952) 822–827.

[329] M. Eigen, E. Wicke, The thermodynamics of electrolytes at higher concentrations, J. Phys. Chem. 58 (1952) 702–714.

[330] M. Manciu, E. Ruckenstein, Lattice site exclusion effect on the double layer interaction, Langmuir 18 (13) (2002) 5178–5185.

[331] C. O. S. Lamperski, Exclusion volume term in the inhomogeneous Poisson-Boltzmann theory for high surface charge, Langmuir 118 (1999) 3423–3424.

[332] R. Roth, R. Evans, A. Lang, G. Kahl, Fundamental measure theory for hard-sphere mixtures revisited: the white bear version, J. Phys.: Condens. Matter 14 (46) (2002) 12063.

[333] O. Stern, The theory of the electrolytic double-layer, Z. Elektrochem. 30 (508) (1924) 1014–1020.

[334] D. J. Bonthuis, S. Gekle, R. R. Netz, Profile of the static permittivity tensor of water at interfaces: Consequences for capacitance, hydration interaction and ion adsorption, Langmuir 28 (20) (2012) 7679–7694.

[335] S. May, K. Bohinc, Attraction between Like Charged Surfaces Mediated by Uniformly Charged Spherical Colloids in a Salt Solution, Croat. Chem. Acta 84 (2, SI) (2011) 251–257.

[336] P. Linse, Molsim, version 3.0 (2000).

[337] W. Poon, D. Andelman, Soft condensed matter physics in molecular and cell biology, Taylor and Francis, New York, 2005.

[338] R. Podgornik, Polyelectrolyte-mediated bridging interactions, J. Polym. Sci. B Polym. Phys. 42 (19) (2004) 3539–3556.

[339] M. M. Gudarzi, G. Trefalt, I. Szilagyi, P. Maroni, M. Borkovec, Forces between negatively charged interfaces in the presence of cationic multivalent oligoamines measured with the atomic force microscope, J. Phys. Chem. C 119 (27) (2015) 15482–15490.

[340] J. Rescic, D. Kovacevic, M. Tomsic, A. Jamnik, S. Ahualli, K. Bohinc, Experimental and theoretical study of the silica particle interactions in the presence of multivalent rod-like ions, Langmuir 30 (32) (2014) 9717–9725.

[341] P. Claesson, E. Poptoshev, E. Blomberg, A. Dedinaite, Polyelectrolyte-mediated surface interactions, Adv. Colloid Interface Sci. 114 (2005) 173–187.

[342] H. Yukawa, On the interaction of elementary particles. i, Proc. Phys. Math. Soc. Japan 17 (0) (1935) 48–57.

[343] A. Tardieu, A. Le Verge, M. Malfois, F. Bonneté, S. Finet, M. Ries-Kautt, L. Belloni, Proteins in solution: from x-ray scattering intensities to interaction potentials, J. Cryst. Growth 196 (2) (1999) 193–203.

[344] F. Sciortino, P. Tartaglia, E. Zaccarelli, One-dimensional cluster growth and branching gels in colloidal systems with short-range depletion attraction and screened electrostatic repulsion, J. Phys. Chem. B 109 (46) (2005) 21942–21953.

[345] Y. Bai, R. Das, I. S. Millett, D. Herschlag, S. Doniach, Probing counterion modulated repulsion and attraction between nucleic acid duplexes in solution, Proc. Natl. Acad. Sci. U. S. A. 102 (4) (2005) 1035–1040.

[346] T. D. Nguyen, B. A. Schultz, N. A. Kotov, S. C. Glotzer, Generic, phenomenological, on-the-fly renormalized repulsion model for self-limited organization of terminal supraparticle assemblies, Proc. Natl. Acad. Sci. U. S. A. 112 (25) (2015) E3161–E3168.

[347] S. Karanikas, J. Dzubiella, A. Moncho-Jordá, A. Louis, Density profiles and solvation forces for a Yukawa fluid in a slit pore, J. Chem. Phys. 128 (20) (2008) 204704.

[348] M. K. Tehrani, M. Jalali, Solvation force in a hard-sphere Yukawa fluid confined between walls, Int. J. Phys. Sci. 6 (10) (2011) 2572–2576.

[349] B. D'Aguanno, R. Klein, Structural effects of polydispersity in charged colloidal dispersions, J. Chem. Soc., Faraday Trans. 87 (3) (1991) 379–390.

[350] B. D'Aguanno, R. Klein, Integral-equation theory of polydisperse Yukawa systems, Phys. Rev. A 46 (12) (1992) 7652.

[351] Y.-X. Yu, F.-Q. You, Y. Tang, G.-H. Gao, Y.-G. Li, Structure and adsorption of a hard-core multi-Yukawa fluid confined in a slitlike pore: grand canonical Monte Carlo simulation and density functional study, J. Phys. Chem. B 110 (1) (2006) 334–341.

[352] X. Cao, H. Cummins, J. Morris, Hydrodynamic and interparticle potential effects on aggregation of colloidal particles, J. Colloid Interface Sci. 368 (1) (2012) 86–96.

[353] S. Marčelja, N. Radić, Repulsion of interfaces due to boundary water, Chem. Phys. Lett. 42 (1) (1976) 129–130.

[354] J. N. Israelachvili, D. Sornette, The interdependence of intra-aggregate and inter-aggregate forces, J. de Physique 46 (12) (1985) 2125–2136.

[355] Y. Rosenfeld, Free energy model for inhomogeneous fluid mixtures: Yukawa-charged hard spheres, general interactions, and plasmas, J. Chem. Phys. 98 (10) (1993) 8126–8148.

[356] F.-Q. You, Y.-X. Yu, G.-H. Gao, Structure of inhomogeneous attractive and repulsive hard-core Yukawa fluid: Grand canonical Monte Carlo simulation and density functional theory study, J. Phys. Chem. B 109 (8) (2005) 3512–3518.

[357] D. Di Caprio, J. Stafiej, M. Holovko, I. Kravtsiv, Yukawa fluid at a hard wall: field theory description, Mol. Phys. 109 (5) (2011) 695–708.

[358] A. Mkanya, G. Pellicane, L. L. Lee, Adsorption of Yukawa fluids on a hard wall, Mol. Phys. 113 (9-10) (2015) 1097–1107.

[359] I. Kravtsiv, T. Patsahan, M. Holovko, D. Di Caprio, Two-Yukawa fluid at a hard wall: Field theory treatment, J. Chem. Phys. 142 (19) (2015) 194708.

[360] D. D. Caprio, I. Kravtsiv, T. Patsahan, M. Holovko, Oscillating Yukawa fluid at a hard wall: field theory description, Mol. Phys. (2016) 1–16.

[361] R. D. Coalson, A. M. Walsh, A. Duncan, N. Ben-Tal, Statistical mechanics of a Coulomb gas with finite size particles: a lattice field theory approach, J. Chem. Phys. 102 (11) (1995) 4584–4594.

[362] S. Buyukdagli, C. V. Achim, T. Ala-Nissila, Ion size effects upon ionic exclusion from dielectric interfaces and slit nanopores, J. Stat. Mech.: Theory Exp. (2011) P05033.

[363] S. Buyukdagli, T. Ala-Nissila, Excluded volume effects in macromolecular forces and ion-interface interactions, J. Chem. Phys. 136 (7) (2012) 074901.

[364] V. C. Weiss, W. Schröer, Liquid–vapor asymmetry in mean-field theories of simple, polar and ionic fluids, J. Stat. Mech.: Theory Exp. 2008 (04) (2008) P04020.

[365] V. C. Weiss, Mean-field theoretical analysis of the corresponding-states behavior of model fluids with variable interaction range, Fluid Phase Equilib. 286 (1) (2009) 62–71.

[366] O. H. Scalise, D. Henderson, On the fluid phase behaviour of fluid binary mixtures using the Yukawa fluid molecular model, Fluid Phase Equilib. 293 (1) (2010) 59–65.

[367] P. Orea, S. Varga, G. Odriozola, A heuristic rule for classification of classical fluids: Master curves for mie, Yukawa and square-well potentials, Chem. Phys. Lett. 631 (2015) 26–29.

[368] D. Henderson, L. Blum, J. P. Noworyta, Inverse temperature expansion of some parameters arising from the solution of the mean spherical approximation integral equation for a Yukawa fluid, J. Chem. Phys. 102 (12) (1995) 4973–4975.

[369] E. El Mendoub, J.-F. Wax, N. Jakse, Phase diagram of the hard-core Yukawa fluid within the integral equation method, Phys. Rev. E 74 (5) (2006) 052501.

[370] E. Schöll-Paschinger, A. L. Benavides, R. Castañeda-Priego, Vapor-liquid equilibrium and critical behavior of the square-well fluid of variable range: A theoretical study, J. Chem. Phys. 123 (23) (2005) 234513.

[371] D. Fu, J. Wu, A self-consistent approach for modelling the interfacial properties and phase diagrams of Yukawa, Lennard-Jones and square-well fluids, Mol. Phys. 102 (13) (2004) 1479–1488.

[372] M. Ginoza, Simple MSA solution and thermodynamic theory in a hard-sphere Yukawa system, Mol. Phys. 71 (1) (1990) 145–156.

[373] M. Ginoza, Solution of the Ornstein-Zernike equation in a hard-sphere Yukawa liquid containing an arbitrary-size hard sphere: a simple mean-spherical-approximation solution and free energy of forming a cavity, J. Phys.: Condens. Matter 6 (8) (1994) 1439.

[374] M. Gonzalez-Melchor, A. Trokhymchuk, J. Alejandre, Surface tension at the vapor/liquid interface in an attractive hard-core Yukawa fluid, J. Chem. Phys. 115 (8) (2001) 3862–3872.

[375] C. Tapia-Medina, P. Orea, L. Mier-y Terán, J. Alejandre, Surface tension of associating fluids by Monte Carlo simulations., J. Chem. Phys. 120 (5) (2004) 2337–2342.

[376] Y. Duda, A. Romero-Martínez, P. Orea, Phase diagram and surface tension of the hard-core attractive Yukawa model of variable range: Monte Carlo simulations, J. of Chem. Phys. 126 (22) (2007) 224510.

[377] P. Orea, Y. Duda, On the corresponding states law of the Yukawa fluid, J. Chem. Phys. 128 (13) (2008) 134508.

[378] S. K. Singh, Effect of surface-screening parameter of the Yukawa potential model on vapour–liquid phase coexistence and critical-point properties of confined Yukawa fluid, Mol. Simul. 42 (5) (2016) 413–419.

[379] G. Odriozola, M. Bárcenas, P. Orea, Vapor–liquid surface tension of strong short-range Yukawa fluid, J. Chem. Phys. 134 (15) (2011) 154702.

[380] B. Widom, Theory of phase equilibrium, J. Phys. Chem. 100 (31) (1996) 13190–13199.

[381] J.-P. Hansen, I. R. McDonald, Theory of simple liquids, Elsevier, 1990.

[382] I. Borukhov, D. Andelman, H. Orland, Steric effects in electrolytes: A modified Poisson-Boltzmann equation, Phys. Rev. Lett. 79 (3) (1997) 435–438.

[383] M. Plischke, B. Bergersen, Equilibrium statistical physics, World Scientific, 2006.

[384] J. Sonnefeld, Surface charge density on spherical silica particles in aqueous alkali chloride solutions, Colloid Polym. Sci. 273 (10) (1995) 932–938.

[385] M. Porus, C. Labbez, P. Maroni, M. Borkovec, Adsorption of monovalent and divalent cations on planar water-silica interfaces studied by optical reflectivity and Monte Carlo simulations, J. Chem. Phys. 135 (6) (2011) 064701.

[386] G. V. Franks, Zeta potentials and yield stresses of silica suspensions in concentrated monovalent electrolytes: isoelectric point shift and additional attraction, J. Colloid Interface Sci. 249 (1) (2002) 44–51.

[387] M. Kosmulski, Positive electrokinetic charge of silica in the presence of chlorides, J. Colloid Interface Sci. 208 (2) (1998) 543–545.

[388] D. J. Tobias, J. C. Hemminger, Chemistry. getting specific about specific ion effects., Science 319 (5867) (2008) 1197–1198.

[389] M. Boström, D. Williams, B. Ninham, Specific ion effects: why dlvo theory fails for biology and colloid systems, Phys. Rev. Lett. 87 (16) (2001) 168103.

[390] Y. J. Zhang, P. S. Cremer, Interactions between macromolecules and ions: the Hofmeister series, Curr. Opin. Chem. Biol. 10 (6) (2006) 658–663.

[391] I. Larson, P. Attard, Surface charge of silver iodide and several metal oxides. are all surfaces nernstian?, J. Colloid Interface Sci. 227 (1) (2000) 152–163.

[392] L. Pilon, H. Wang, A. d'Entremont, Recent advances in continuum modeling of interfacial and transport phenomena in electric double layer capacitors, J. Electrochem. Soc. 162 (5) (2015) A5158–A5178.

[393] J. Lyklema, Fundamentals of interface and colloid science: soft colloids, Vol. 5, Academic press, 2005.

[394] L. Bhuiyan, C. Outhwaite, Comparison of exclusion volume corrections to the Poisson–Boltzmann equation for inhomogeneous electrolytes, J. Colloid Interface Sci. 331 (2) (2009) 543–547.

[395] P. Alijó, F. Tavares, E. Biscaia Jr, Double layer interaction between charged parallel plates using a modified Poisson–Boltzmann equation to include size effects and ion specificity, Colloids Surf., A 412 (2012) 29–35.

[396] J. J. López-García, J. Horno, C. Grosse, Poisson–Boltzmann description of the electrical double layer including ion size effects, Langmuir 27 (23) (2011) 13970–13974.

[397] Y. Burak, D. Andelman, Hydration interactions: Aqueous solvent effects in electric double layers, Phys. Rev. E 62 (4) (2000) 5296–5312.

[398] M. Manciu, E. Ruckenstein, Specific ion effects via ion hydration: I. surface tension, Adv. Colloid Interface Sci. 105 (1) (2003) 63–101.

[399] J. N. Israelachvili, P. M. McGuiggan, Forces between surfaces in liquids, Science 241 (4867) (1988) 795–800.

[400] K. A. Dill, T. M. Truskett, V. Vlachy, B. Hribar-Lee, Modeling water, the hydrophobic effect, and ion solvation, Annu. Rev. Biophys. Biomol. Struct. 34 (2005) 173–199.

[401] D. F. Parsons, M. Boström, P. L. Nostro, B. W. Ninham, Hofmeister effects: interplay of hydration, nonelectrostatic potentials, and ion size, Phys. Chem. Chem. Phys. 13 (27) (2011) 12352–12367.

[402] J. Kielland, Individual activity coefficients of ions in aqueous solutions, J. Am. Chem. Soc. 59 (9) (1937) 1675–1678.

[403] J.-W. Shen, C. Li, N. F. van der Vegt, C. Peter, Transferability of coarse grained potentials: Implicit solvent models for hydrated ions, J. Chem. Theory Comput. 7 (6) (2011) 1916–1927.

[404] T. T. Duignan, D. F. Parsons, B. W. Ninham, A continuum solvent model of ion–ion interactions in water, Phys. Chem. Chem. Phys. 16 (40) (2014) 22014–22027.

[405] Y. Gur, I. Ravina, A. J. Babchin, On the electrical double layer theory. ii. the Poisson—Boltzmann equation including hydration forces, J. Colloid Interface Sci. 64 (2) (1978) 333–341.

[406] M. V. Fedorov, A. A. Kornyshev, Ionic liquid near a charged wall: structure and capacitance of electrical double layer, J. Phys. Chem. B 112 (38) (2008) 11868–11872.

[407] V. L. Shapovalov, The interaction of electric field and hydrostatic pressure in an electrical double layer: A simple "first principle" model that accounts for the finite sizes of counterions, J. Colloid Interface Sci. 454 (2015) 187–191.

[408] M. S. Kilic, M. Z. Bazant, A. Ajdari, Steric effects in the dynamics of electrolytes at large applied voltages. i. double-layer charging, Phys. Rev. E 75 (2) (2007) 021502.

[409] F. Booth, The dielectric constant of water and the saturation effect, J. Chem. Phys. 19 (4) (1951) 391–394.

[410] H. Wang, J. Varghese, L. Pilon, Simulation of electric double layer capacitors with mesoporous electrodes: Effects of morphology and electrolyte permittivity, Electrochim. Acta 56 (17) (2011) 6189–6197.

[411] M. C. Wander, A. E. Clark, Structural and dielectric properties of quartz- water interfaces, J. Phys. Chem. C 112 (50) (2008) 19986–19994.

[412] R. Podgornik, G. Cevc, B. Žekš, Solvent structure effects in the macroscopic theory of van der waals forces, J. Chem. Phys. 87 (10) (1987) 5957–5967.

[413] J. N. Israelachvili, P. M. McGuiggan, Forces between surfaces in liquids, Science 241 (4867) (1988) 795–800.

[414] A. G. Volkov, Liquid interfaces in chemical, biological and pharmaceutical applications, CRC Press, 2001.

[415] R. J. Hunter, Foundations of colloid science, Oxford University Press, 2001.

[416] B. Hou, W. Bu, G. Luo, P. Vanỳsek, M. L. Schlossman, Ion distributions at electrified water-organic interfaces: Pb-pmf calculations and impedance spectroscopy measurements, J. Electrochem. Soc. 162 (12) (2015) H890–H897.

[417] H. Ohshima, Theory of electrostatics and electrokinetics of soft particles, Sci. Technol. Adv. Mater. (2016) 1–13.

[418] R. Parsons, The electrical double layer: recent experimental and theoretical developments, Chem. Rev. (Washington, DC, U. S.) 90 (5) (1990) 813–826.

[419] D. Brogioli, R. Zhao, P. Biesheuvel, A prototype cell for extracting energy from a water salinity difference by means of double layer expansion in nanoporous carbon electrodes, Energy Environ. Sci. 4 (3) (2011) 772–777.

[420] A. Härtel, M. Janssen, S. Samin, R. van Roij, Fundamental measure theory for the electric double layer: implications for blue-energy harvesting and water desalination, J. Phys.: Condens. Matter 27 (19) (2015) 194129.

[421] F. Mugele, B. Bera, A. Cavalli, I. Siretanu, A. Maestro, M. Duits, M. Cohen-Stuart, D. van den Ende, I. Stocker, I. Collins, Ion adsorption-induced wetting transition in oil-water-mineral systems, Sci. Rep. 5 (2015) 10519.

[422] B. E. Conway, Electrochemical supercapacitors: scientific fundamentals and technological applications, Springer Science & Business Media, 2013.

[423] C. Largeot, C. Portet, J. Chmiola, P.-L. Taberna, Y. Gogotsi, P. Simon, Relation between the ion size and pore size for an electric double-layer capacitor, J. Am. Chem. Soc. 130 (9) (2008) 2730–2731.

[424] P. Attard, Electrolytes and the electric double layer, Adv. Chem. Phys. 92 (1996) 1–160.

[425] G. Gouy, Constitution of the electric charge at the surface of an electrolyte, J. Phys. 9 (4) (1910) 457–467.

[426] D. L. Chapman, Li. a contribution to the theory of electrocapillarity, London, Edinburgh Dublin Philos. Mag. J. Sci. 25 (148) (1913) 475–481.

[427] G. Valette, Double layer on silver single-crystal electrodes in contact with electrolytes having anions which present a slight specific adsorption: part i. the (110) face, J. Electroanal. Chem. Interfacial Electrochem. 122 (1981) 285–297.

[428] A. A. Kornyshev, Double-layer in ionic liquids: paradigm change?, J. Phys. Chem. B 111 (20) (2007) 5545–5557.

[429] G. Valette, Double layer on silver single crystal electrodes in contact with electrolytes having anions which are slightly specifically adsorbed: Part ii. the (100) face, J. Electroanal. Chem. Interfacial Electrochem. 138 (1) (1982) 37–54.

[430] M. Z. Bazant, M. S. Kilic, B. D. Storey, A. Ajdari, Towards an understanding of induced-charge electrokinetics at large applied voltages in concentrated solutions, Adv. Colloid Interface Sci. 152 (1) (2009) 48–88.

[431] Y. Nakayama, D. Andelman, Differential capacitance of the electric double layer: The interplay between ion finite size and dielectric decrement, J. Chem. Phys. 142 (4) (2015) 044706.

[432] C. W. Outhwaite, L. B. Bhuiyan, An improved modified Poisson–Boltzmann equation in electric-double-layer theory, J. Chem. Soc., Faraday Trans. 2 79 (5) (1983) 707–718.

[433] S. Lamperski, C. W. Outhwaite, Exclusion volume term in the inhomogeneous Poisson-Boltzmann theory for high surface charge, Langmuir 18 (2002) 3423–3424.

[434] V. Kralj-Iglič, A. Iglič, A simple statistical mechanical approach to the free energy of the electric double layer including the excluded volume effect, J. Phys. II 6 (4) (1996) 477–491.

[435] V. K.-I. K. Bohinc, A. I. c, Thickness of electrical double layer. effect of ion size, Electrochimica Acta 46 (2001) 3033–3040.

[436] D. Henderson, L. Blum, J. L. Lebowitz, An exact formula for the contact value of the density profile of a system of charged hard spheres near a charged wall, J. Electroanal. Chem. Interfacial Electrochem. 102 (3) (1979) 315–319.

[437] S. L. Carnie, D. Y. Chan, D. J. Mitchell, B. W. Ninham, The structure of electrolytes at charged surfaces: the primitive model, J. Chem. Phys. 74 (2) (1981) 1472–1478.

[438] A. Martín-Molina, M. Quesada-Pérez, R. Hidalgo-Álvarez, Electric double layers with electrolyte mixtures: Integral equations theories and simulations, J. Phys. Chem. B 110 (3) (2006) 1326–1331.

[439] D. Antypov, M. C. Barbosa, C. Holm, Incorporation of excluded-volume correlations into Poisson-Boltzmann theory, Phys. Rev. E 71 (6) (2005) 061106.

[440] G. Torrie, J. Valleau, Electrical double layers. i. Monte Carlo study of a uniformly charged surface, J. Chem. Phys. 73 (11) (1980) 5807–5816.

[441] M. Valiskó, D. Henderson, D. Boda, Competition between the effects of asymmetries in ion diameters and charges in an electrical double layer studied by Monte Carlo simulations and theories, J. Phys. Chem. B 108 (42) (2004) 16548–16555.

[442] P. Zarzycki, Monte Carlo simulation of the electrical differential capacitance of a double electrical layer formed at the heterogeneous metal oxide/electrolyte interface, J. Colloid Interface Sci. 297 (1) (2006) 204–214.

[443] S. Lamperski, A. Zydor, Monte Carlo study of the electrode— solvent primitive model electrolyte interface, Electrochim. Acta 52 (7) (2007) 2429–2436.

[444] P. Koelsch, P. Viswanath, H. Motschmann, V. L. Shapovalov, G. Brezesinski, H. Mohwald, D. Horinek, R. R. Netz, K. Giewekemeyer, T. S. Alditt, H. Schollmeyer, R. von Klitzing, J. Daillant, P. Guenoun, Specific ion effects in physicochemical and biological systems: Simulations, theory and experiments, Colloids Surf., A 303 (1-2) (2007) 110–136.

[445] D. Ben-Yaakov, D. Andelman, D. Harries, R. Podgornik, Beyond standard Poisson-Boltzmann theory: ion-specific interactions in aqueous solutions, J. Phys.: Condens. Matter 21 (42) (2009) 424106.

[446] J. Stafiej, D. Di Caprio, J. Badiali, A simple model to investigate the effects of non-Coulombic interactions on the structure of charged interfaces, J. Chem. Phys. 109 (9) (1998) 3607–3618.

[447] J. Israelachvili, D. Sornette, The interdependence of intra-aggregate and inter-aggregate forces, J. Phys. (Paris) 46 (12) (1985) 2125–2136.

[448] C. W. Outhwaite, S. Lamperski, L. B. Bhuiyan, Influence of electrode polarization on the capacitance of an electric double layer at and around zero surface charge, Mol. Phys. 109 (1) (2011) 21–26.

[449] T. L. Hill, An introduction to statistical thermodynamics, Courier Corporation, 2012.

[450] B. Jönsson, H. Wennerstroem, B. Halle, Ion distributions in lamellar liquid crystals. a comparison between results from Monte Carlo simulations and solutions of the Poisson-Boltzmann equation, J. Phys. Chem. 84 (17) (1980) 2179–2185.

[451] S. Lamperski, D. Henderson, Simulation study of capacitance of the electrical double layer of an electrolyte near a highly charged electrode, Mol. Simul. 37 (4) (2011) 264–268.

[452] D. Jiang, D. Meng, J. Wu, Density functional theory for differential capacitance of planar electric double layers in ionic liquids, Chem. Phys. Lett. 504 (4) (2011) 153–158.

[453] D. Henderson, S. Lamperski, Z. Jin, J. Wu, Density functional study of the electric double layer formed by a high density electrolyte, J. Phys. Chem. B 115 (44) (2011) 12911–12914.

[454] S. Lamperski, C. W. Outhwaite, L. B. Bhuiyan, The electric double-layer differential capacitance at and near zero surface charge for a restricted primitive model electrolyte, J. Phys. Chem. B 113 (26) (2009) 8925–8929.

[455] S. Lamperski, M. Płuciennik, C. W. Outhwaite, The planar electric double layer capacitance for the solvent primitive model electrolyte, Phys. Chem. Chem. Phys. 17 (2) (2015) 928–932.

[456] J. N. Israelachvili, P. M. McGuiggan, Forces between surfaces in liquids, Science 241 (4867) (1988) 795–800.

[457] P. Kralchevsky, K. Nagayama, Capillary interactions between particles bound to interfaces, liquid films and biomembranes, Adv. Colloid Interface Sci. 85 (2-3) (2000) 145–192.

[458] R. J. Hunter, Foundations of colloid science, Oxford University Press, 2001.

[459] A. G. Volkov, Liquid interfaces in chemical, biological and pharmaceutical applications, CRC Press, 2001.

[460] H. Ohshima, Theory of electrostatics and electrokinetics of soft particles, Sci. Technol. Adv. Mater. (2016) 1–13.

[461] R. Parsons, The electrical double layer: recent experimental and theoretical developments, Chem. Rev. (Washington, DC, U. S.) 90 (5) (1990) 813–826.

[462] D. Brogioli, R. Zhao, P. Biesheuvel, A prototype cell for extracting energy from a water salinity difference by means of double layer expansion in nanoporous carbon electrodes, Energy Environ. Sci. 4 (3) (2011) 772–777.

[463] N.-S. Choi, Z. Chen, S. A. Freunberger, X. Ji, Y.-K. Sun, K. Amine, G. Yushin, L. F. Nazar, J. Cho, P. G. Bruce, Challenges facing lithium batteries and electrical double-layer capacitors, Angew. Chem., Int. Ed. 51 (40) (2012) 9994–10024.

[464] A. Härtel, M. Janssen, S. Samin, R. van Roij, Fundamental measure theory for the electric double layer: implications for blue-energy harvesting and water desalination, J. Phys.: Condens. Matter 27 (19) (2015) 194129.

[465] I. Kalcher, J. Dzubiella, Structure-thermodynamics relation of electrolyte solutions, J. Chem. Phys. 130 (13) (2009) 134507.

[466] I. Kalcher, J. C. Schulz, J. Dzubiella, Ion-specific excluded-volume correlations and solvation forces, Phys. Rev. Lett. 104 (9) (2010) 097802.

[467] R. Pashley, J. Israelachvili, Dlvo and hydration forces between mica surfaces in mg2+, ca2+, sr2+, and ba2+ chloride solutions, J. Colloid Interface Sci. 97 (2) (1984) 446–455.

[468] M. A. Brown, A. Beloqui Redondo, M. Sterrer, B. Winter, G. Pacchioni, Z. Abbas, J. A. van Bokhoven, Measure of surface potential at the aqueous–oxide nanoparticle interface by xps from a liquid microjet, Nano Lett. 13 (11) (2013) 5403–5407.

[469] M. A. Brown, Z. Abbas, A. Kleibert, R. G. Green, A. Goel, S. May, T. M. Squires, Determination of surface potential and electrical double-layer structure at the aqueous electrolyte-nanoparticle interface, Phys. Rev. X 6 (1) (2016) 011007.

[470] M. Kanduč, A. Schlaich, E. Schneck, R. R. Netz, Hydration repulsion between membranes and polar surfaces: Simulation approaches versus continuum theories, Adv. Colloid Interface Sci. 208 (2014) 142–152.

[471] A. Trokhymchuk, D. Henderson, D. T. Wasan, A molecular theory of the hydration force in an electrolyte solution, J. Colloid Interface Sci. 210 (2) (1999) 320–331.

[472] R. Ramirez, D. Borgis, Density functional theory of solvation and its relation to implicit solvent models, J. Phys. Chem. B 109 (14) (2005) 6754–6763.

[473] M. Holovko, M. Druchok, T. Bryk, Computer modelling of hydration structure of highly charged ions and cationic hydrolysis effects, Curr. Opin. Colloid Interface Sci. 9 (1) (2004) 64–66.

[474] M. Holovko, M. Druchok, T. Bryk, A molecular dynamics modelling of cation hydrolysis effects, J. Electroanal. Chem. 582 (1) (2005) 50–56.

[475] S. Lamperski, A. Zydor, Monte Carlo study of the electrode— solvent primitive model electrolyte interface, Electrochim. Acta 52 (7) (2007) 2429–2436.

[476] R. R. Netz, D. Horinek, Progress in modeling of ion effects at the vapor/water interface, Annu. Rev. Phys. Chem. 63 (2012) 401–418.

[477] S. Hocine, R. Hartkamp, B. Siboulet, M. Duvail, B. Coasne, P. Turq, J.-F. Dufrêche, How ion condensation occurs at a charged surface: A molecular dynamics investigation of the Stern layer for water–silica interfaces, J. Phys. Chem. C 120 (2) (2016) 963–973.

[478] P. Sharma, T. Bhatti, A review on electrochemical double-layer capacitors, Energy Convers. Manage. 51 (12) (2010) 2901–2912.

[479] L. Daniels, M. Scott, Z. Mišković, The role of Stern layer in the interplay of dielectric saturation and ion steric effects for the capacitance of graphene in aqueous electrolytes, J. Chem. Phys. 146 (9) (2017) 094101.

[480] V. Lockett, R. Sedev, J. Ralston, M. Horne, T. Rodopoulos, Differential capacitance of the electrical double layer in imidazolium-based ionic liquids: influence of potential, cation size, and temperature, J. Phys. Chem. C 112 (19) (2008) 7486–7495.

[481] V. Lockett, M. Horne, R. Sedev, T. Rodopoulos, J. Ralston, Differential capacitance of the double layer at the electrode/ionic liquids interface, Phys. Chem. Chem. Phys. 12 (39) (2010) 12499–12512.

[482] S. Lamperski, C. Outhwaite, Differential capacitance of the solvent primitive model diffuse layer using the inhomogeneous Poisson–Boltzmann theory with an exclusion volume term, J. Electroanal. Chem. 567 (2) (2004) 263–267.

[483] A. Velikonja, V. Kralj-Iglič, A. Iglič, On asymmetric shape of electric double layer capacitance curve, Int. J. Electrochem. Sci 10 (2015) 1–7.

[484] M. V. Fedorov, A. A. Kornyshev, Ionic liquids at electrified interfaces, Chem. Rev. (Washington, DC, U. S.) 114 (5) (2014) 2978–3036.

[485] M. Popović, A. Šiber, Lattice-gas Poisson-Boltzmann approach for sterically asymmetric electrolytes, Phys. Rev. E 88 (2) (2013) 022302.

[486] Y. Han, S. Huang, T. Yan, A mean-field theory on the differential capacitance of asymmetric ionic liquid electrolytes, J. Phys.: Condens. Matter 26 (28) (2014) 284103.

[487] A. Maggs, R. Podgornik, General theory of asymmetric steric interactions in electrostatic double layers, Soft Matter 12 (4) (2016) 1219–1229.

[488] U. M. B. Marconi, J. Wiechen, F. Forstmann, The structure of size-asymmetric electrolytes at charged surfaces: The unrestricted primitive model in the hnc/msa approximation, Chem. Phys. Lett. 107 (6) (1984) 609–612.

[489] J. Wu, T. Jiang, D.-e. Jiang, Z. Jin, D. Henderson, A classical density functional theory for interfacial layering of ionic liquids, Soft Matter 7 (23) (2011) 11222–11231.

[490] A. Härtel, S. Samin, R. van Roij, Dense ionic fluids confined in planar capacitors: in-and out-of-plane structure from classical density functional theory, J. Phys.: Condens. Matter 28 (24) (2016) 244007.

[491] M. Ma, S. Zhao, Z. Xu, Investigation of dielectric decrement and correlation effects on electric double-layer capacitance by self-consistent field model, Commun. Comput. Phys. 20 (02) (2016) 441–458.

[492] J. N. Israelachvili, H. Wennerstrom, Entropic forces between amphiphilic surfaces in liquids, J. Phys. Chem. 96 (2) (1992) 520–531.

[493] P. S. Crozier, R. L. Rowley, E. Spohr, D. Henderson, Comparison of charged sheets and corrected 3d ewald calculations of long-range forces in slab geometry electrolyte systems with solvent molecules, J. Chem. Phys. 112 (21) (2000) 9253–9257.

[494] D. Henderson, D. Boda, Insights from theory and simulation on the electrical double layer, Phys. Chem. Chem. Phys. 11 (20) (2009) 3822–3830.

[495] A. Martín-Molina, M. Quesada-Pérez, R. Hidalgo-Álvarez, Electric double layers with electrolyte mixtures: Integral equations theories and simulations, J. Phys. Chem. B 110 (3) (2006) 1326–1331.

[496] D. Di Caprio, M. Valiskó, M. Holovko, D. Boda, Anomalous temperature dependence of the differential capacitance in valence asymmetric electrolytes. comparison of Monte Carlo simulation results and the field theoretical approach, Mol. Phys. 104 (22-24) (2006) 3777–3786.

[497] T. Nagy, M. Valiskó, D. Henderson, D. Boda, Behavior of 2: 1 and 3: 1 electrolytes at polarizable interfaces, J. Chem. Eng. Data 56 (4) (2011) 1316–1322.